Studies on Liquid Crystals and Nanocomposites at Interfaces

THESIS

Submitted in partial fulfillment
of the requirements for the degree of

DOCTOR OF PHILOSOPHY

by

KEERTI CHOUDHARY

Under the Supervision of

Prof. V. MANJULADEVI

BITS Pilani
Pilani | Dubai | Goa | Hyderabad

BIRLA INSTITUTE OF TECHNOLOGY AND SCIENCE, PILANI
2016

BIRLA INSTITUTE OF TECHNOLOGY & SCIENCE, PILANI -333031 (RAJASTHAN) INDIA

CERTIFICATE

This is to certify that the work reported in the Ph.D. thesis entitled "**Studies on Liquid Crystals and Nanocomposites at Interfaces**" submitted by **KEERTI CHOUDHARY**, ID No **2011PHXF025P** at Physics Department, BITS-Pilani, Pilani Campus for the award of the degree of Doctor of Philosophy (Ph.D.), is a bonafide record of her original work carried out under my supervision. This work has not been submitted elsewhere for any other degree or diploma.

…..……..

Signature of Supervisor
Dr. V. Manjuladevi

Associate Professor
Department of Physics
BITS-Pilani, Pilani Campus

Date:……..

Dedicated to my Parents

and

my husband. . .

Acknowledgements

During these five years of my life (2011-2016) there have been many challenges, excitement and everything in between that moulded the person who I am now and gave me the strength to accomplish what today is the proudest achievement in my academic career. This achievement was not one man's work, but the collaboration of all the people present in my life during the last half decade. With this said, I would like to mention, in no particular order, the people whose support and help was indispensable:

My supervisor, Prof. V. Manjuladevi who is not only just a great academic guide, but also a good life mentor and friend, with all the people who have been working with her. I feel highly privileged to thank first and foremost my supervisor, Prof. V. Manjuladevi for her expert guidance, suggestions and continuous encouragement to me at all phases of my work during the entire course of my research. I would also like to say special thanks to her for believing in me during my hard time also. She had put all her efforts and advised me so many times professionally and personally. I am also grateful to Prof. R. K. Gupta for his immense guidance and constant motivation throughout my PhD work. He is very supportive and I am indebted to him for the help rendered to me. I thank GOD for giving me such a patient and caring, mentor couple. I got to learn so much from them during the entire course of my work. Their constant support, understanding and involvement in the minutest details have given this thesis the present form

I deeply acknowledge the invaluable support of my DAC members Prof. R.R. Mishra and Prof. R. K. Gupta for reviewing my work and giving valuable suggestions, feedback and constructive comments during the course of my research work.

I am grateful to Vice-Chancellor, Directors, Deputy Directors, Deans and Unit Chiefs of Birla Institute of Technology & Science (BITS), Pilani for providing me the opportunity to pursue my doctoral studies by providing necessary facilities and financial support.

I am thankful to Prof. S. K. Verma, Dean, Academic research division, BITS, Pilani, Prof. Hemant Jadhav, Associate Dean, Academic research division, BITS, Pilani for their co-operation and encouragement at every stage of my PhD programme. I overwhelmingly acknowledge the

office staff of ARD, Mr. Raghuveer and Mr. Mahipal whose secretarial assistance helped me in submitting the various evaluation documents in time.

I sincerely thank Prof. Anshuman Dalvi, Head of Department and Prof. Navin Singh Convenor, Departmental Research Committee (DRC), Department of Physics, BITS Pilani, Pilani Campus for their official support and encouragement. I would also like to thank all the faculty members of Physics Department for their support and encouragement during my PhD tenure. I deeply acknowledge BITS, Pilani for the financial assistance throughout my PhD tenure.

I wish to place on record my special thanks to Raman Research Institute (RRI), Bengaluru for providing the experimental facilities for my research work. I am grateful to our collaborators Prof. Sadashiva, Prof. Pratibha and Prof. Sandeep Kumar of RRI, Bengaluru for providing us molecules used for carrying out the research work. I would like to thank Material Research Center, MNIT Jaipur, central laboratory and department of chemical engineering, BITS Pilani for providing the experimental facilities for my research work. These were the most important inputs for my present research study. I would like to thank BITS, Pilani for providing central facilities to carry out my research work.

I would like to extend my thanks to my Lab-mates C. Karthik, Monika, Jitendra, Devnarayanan for their refreshing company and helping me to carry out my research work. I would like to thank my friends Amar Singh, Sunita Joshi, Munesh Rathore and Tej Verma for helping and motivation. I would like to acknowledge my sincere thanks to all my friends of Physics Department, BITS, Pilani and of other departments too.

I express my thanks to the office staff of Physics Department, BITS, Pilani, including Mr. Srikant Sharma, Mr. Rajiv Gaur , Mr. Kundan for providing all the necessary support whenever needed.

I owe this doctorate degree especially to my parents and my mother-in-law whose dreams have come true with my achievement of this stage in education. This has been possible because of prayers and sacrifices made by them, their love, affection and blessings. I owe this doctorate degree to my husband Naresh for his unconditional love, sacrifices, care and support. He has always been with me. Thank you for everything. Your motivation and warm encouragement helped me in overcoming tough times. I would like to thank my uncle Mr. O.P. and Mr. M. P. Suhag and my aunt Mrs. Rajbala for their motivation and blessings. I would like to thank to all my family members for their direct and indirect support.

Lastly, I wish to apologize if I forgot the names of persons who had helped me in any way. Finally, I wish to express my gratitude to all those who have directly or indirectly assisted me and whose help and cooperation made this research work get accomplished.

Keerti Choudhary

Abstract

Liquid crystals (LCs) are the fourth state of matter whose order lies between that of 3-dimensioanlly (3D) ordered solids and completely disordered fluids. There are two types of LCs: thermotropic and lyotropic LCs. The thermotropic LCs exhibit mesophases as a function of temperature whereas lyotropic LCs exhibit mesophases as a function of concentration, ion-contents, pH, temperature and humidity. The thermotropic mesophases are dependent on various factors including the molecular interaction and molecular shape anisotropy. Several thermotropic LCs are amphiphilic in nature and can form stable Langmuir monolayer (LM). LM is a stable film of single layer of amphiphilic molecules at the air-water (A/W) interface. A single layer of molecules onto the substrate can be considered as thin film. The thin films of LC exhibit interesting properties. The surface to volume ratio of a material increases enormously when spread on to a substrate to form thin film. Such huge increase in surface-to-volume ratio increases the activities of the material enormously and thereby the material properties like catalysis, reactivity, adhesion, etc are enhanced remarkably. Such changes in the material properties in the state of thin films promises a wide range of applications starting from the basic science research to various device fabrications. The surface morphology and the nanostructure in the thin film can govern the growth of the bulk material deposited over it. Therefore, this provides an opportunity to alter the alignment of bulk LC molecules by altering the morphology and functionality of the interfacial layer. The formation of nanostructure in the thin film is governed by molecular interaction and external parameters like temperature, surface density etc. The surface can be patterned and the nanostructures can be controlled by an appropriate choice of thin film forming materials e.g. LCs, nanomaterials and its nanocomposites. The LC based devices consist of alignment layer for aligning the bulk LC materials within a confined geometry. Such alignment layer can determine the alignment of bulk material and thus regulates the performance of LC based devices. The study on the role of alignment layer on the bulk LCs is essential. The alignment layer can be fabricated using different techniques including a precisely controlled Langmuir-Blodgett (LB) technique for ultrathin film deposition.

This thesis mainly focuses on the LM and Langmuir-Blodgett (LB) films of LCs, nanomaterials and their composites at A/W and air-solid (A/S) interfaces. The monolayer in a particular phase at the A/W interface can be transferred layer-by-layer onto a solid substrate by

using the LB and inverse Langmuir-Schaefer (ILS) methods in a highly controlled manner. LC cells fabricated using LB and ILS film deposited substrates can influence the overall performance of the device, as the anchoring can play a major role in switching the bulk LC medium. Substrates prepared using the LB and ILS techniques are used for the fabrication of LC cell. LC sample was filled in cells in isotropic phase through capillary action. The alignment of LCs in these cells was observed under a Polarizing Optical Microscope (POM).

This thesis comprises of the results of studies on thin films of LCs, nanomaterials and its nanocomposites. The titanium dioxide (TiO_2) nanomaterials, nanocomposites of TiO_2 with discotic LC (DLC), different bent-core LCs (BCLCs) and calamitic LCs have been used for our studies.

We fabricated a Langmuir film (LF) of TiO_2 nanoparticle at A/W interface and transferred the ultrathin film of TiO_2 nanoparticles onto solid substrate using LB technique. The LB film of TiO_2 was characterized using field emission scanning electron microscopy (FESEM), atomic force microscopy (AFM) and ultraviolet-visible spectroscopy. The LB films of TiO_2 deposited at higher target surface pressure (π_t) reveal a higher surface coverage, thereby yielding a higher density of crystalline defect sites. We observed an Arrhenius behavior of charge transport for LB film of TiO_2. The ultrathin film LB film of TiO_2 shows an appreciable and recoverable response toward ethanol sensing. The monolayer of DLC hexa-alkoxy triphenylene (HAT5) at the A/W interface was doped with TiO_2 nanoparticles. We found condensation effect on the monolayer of HAT5+TiO_2 nanocomposites due to the presence of TiO_2 nanoparticles. We observed reduction in the energy gap of the HAT5 system in a controlled manner on doping the system with TiO_2 nanoparticles. The conductivity and activation energy of discotic system increases with doping of TiO_2 nanoparticles.

The surface manometry on carboxylated graphene (G-COOH), HAT5 and their composites was performed. The LM of G-COOH exhibits gas and a liquid-like phase. Structurally similar organic DLC HAT5 molecule was incorporated in the monolayer matrix of G-COOH. The surface manometry of such mixed monolayer system indicated the evidence of repulsive interaction or complex formation between the components. The LB films of these nanocomposites were deposited onto solid substrates. The UV-Vis spectroscopy on the LB films of the nanocomposite reveals red shift in the characteristic peak and thereby leading to a decrease in energy gap due to incorporation of HAT5 in G-COOH monolayer matrix. The

charge-transport mechanism shows that the in-plane conductivity of the LB films of the nanocomposites enhances as compared to that of pure components. The surface morphology obtained using FESEM shows uniform film over the 2D surface. The LC cells were fabricated using LB and ILS films of such nanocomposites deposited on indium tin oxide (ITO) coated glass plates and used as alignment layers. The DLC decyloxytriphenylene (TP10) was filled in these LC cells and dielectric constant was measured. The dielectric measurements indicate that the LB film of the nanocomposites provide better alignment of discotic liquid crystals as compared to some other mechanism of obtaining the alignment layer in the LC cells.

The effect of different stress in the LM on the morphology of the LB films of stearic acid deposited at same π_t with different orientation angle of substrate normal w.r.t. the monolayer compression direction was studied. We present the effect of surface morphology of LB films of stearic acid deposited at same π_t =15mN/m , but in different direction of substrate normal relative to the compression direction on the alignment of a nematic LC (NLC). The LB film of stearic acid deposited at $\theta = 0^o$ shows granular texture with very large size and compact grains. The large grains change to smaller size and finally vanish due to reduction of the stress by changing θ from 0° to 45^o and then 90^o. The LC cells were fabricated using such LB films deposited substrates. These LC cells show different alignments (planar to homeotropic) due to difference in morphology of stearic acid in the LB films.

The surface behavior of different unsymmetrical BC molecules 4-((4-(tetradecyloxy) benzoyl) oxy) phenyl 3-((4-((4-cyanobenzoyl)oxy) benzoyl) oxy) benzoate, 4-((4-(tetradecyloxy) phenoxy) carbon) phenyl 3-((4-((nitrobenzoyl) oxy) benzoyl)oxy) benzoate and 4-((4-(octadecyloxy) phenoxy) carbonyl) phenyl 3-((4-((4-nitrobenzoyl)oxy) benzoyl) oxy) benzoate (we referred these molecules as B-CN, BN1 and BN2, respectively) were studied at A/W interface. The LM of these BCLCs at A/W interface were found to be stable. We transferred the LM of B-CN molecule onto Si/SiO_2 substrate using both LB and ILS method at different π_t. Both LB and ILS film of B-CN molecule on Si/SiO_2 substrate was found to be uniform. The LB film of BN1 molecules on Si/SiO_2 substrate shows the uniform texture at different π_t. The topographic images of LB film of BN2 deposited on Si/SiO_2 substrate shows triangular shaped domains with some defects. With increases in π_t , the density of these triangular shaped domains increases and film becomes more uniform. LB film of banana molecules deposited onto ITO plate shows granular texture with partial bilayer formation of the molecules on substrate. Using the force -

distance spectroscopy of AFM, the adhesion force between LB film of BN2 molecules on Si/SiO_2 substrate with hydrophilic Si/Si_3N_4 tip and hydrophobic functionalized tip was calculated. We proposed a model for the orientation of BN2 molecules in the LB film on Si/SiO_2 substrate. Both LB and ILS film of BCLCs on different substrates (ITO, microscopic glass plate) were employed as alignment layer for the fabrication of LC cell. The alignment of bulk NLC is studied using POM. The ILS film of B-CN molecules on ITO and glass plates exhibit the planar alignment of E7 at lower π_t = 10 mN/m and at higher π_t = 30 mN/m, it shows homeotropic alignment. The uniform LB film of BN1 molecules deposited onto ITO substrate supports the homeotropic alignment where as the LB film of BN2 molecule supports the planar alignment of NLC in the LC cell.

The surface behavior of a mixed monolayer system of two different shape anisotropic LC molecules viz calamitic LC 4-octyloxy-4-cyanobiphenyl (8OCB) and achiral symmetric BC molecules ((5-cyano-1, 3-phenylene) bis(oxy)) bis(carbonyl))bis(2-fluoro-4,1-phenylene) bis(4'-nonyl-[1,1'-biphenyl]-4-carboxylate (referred as 5CNBC). The surface pressure- area per molecule ($\pi - A_m$) isotherms of the mixed system were recorded by varying mole fraction (X_M) of 8OCB in 5CNBC. The variation of excess area (A_{ex}) and excess Gibbs free energy versus X_M shows negative values for all composition in the π range of 1 to 3 mN/m. This suggests the system to be miscible and stable. The miscibility may arise due to attractive interaction between the component molecules. The LB films of the mixed monolayer system were deposited and the morphology was obtained using AFM. The AFM image shows the miscible nature of the components on the solid substrates. These LB films were employed as alignment layer for the fabrication of LC cell. The alignment of bulk 8OCB LC is observed using POM and the dielectric measurement was performed. The value of dielectric constant of 8OCB measured in LC cell treated with LB film of 5CNBC molecules in liquid - expanded phase is enhanced. This indicates homeotropic alignment of 8OCB. The nematic phase of 8OCB is suppressed in LC cells prepared using LB film of mixed monolayer.

The thin films of LCs, nanomaterials and their composites on solid substrates exhibit better performance than the bulk materials. Such properties of thin films of organic LC materials and their nanocomposites can be employed for fabrication of better performing devices.

Contents

List of Figures

List of Tables

Abbreviations

A/W	Air Water
A/S	Air Solid
AFM	Atomic Force Microscopy
ATR	Attenuated Total Reflectance
BAM	Brewster Angle Microscope
BC	Bent-Core
CIP	Current-In-Plane
CNTs	Carbon Nanotubes
CP	Close-Packing Phase
DLC	Discotic Liquid Crystal
ECG	Edge-Carboxylated Graphene
FESEM	Field Emission Scanning Electron Microscopy
FLC	Ferroelectric Liquid Crystal
FTIR	Fourier Transform Infrared Spectroscopy
G-COOH	Carboxylic Acid Functionalized Graphene
HAT5	Hexa-Alkoxy Triphenylene
HMDS	Hexamethyldisilazane
HPB	Hydrophobic
HPL	Hydrophilic
HPLC	High Performance Liquid Chromatography
ILS	Inverse Langmuir-Schafer
IR	Infrared
ITO	Indium Tin Oxide
I-V	Current-Voltage
LB	Langmuir-Blodgett
LC	Liquid Crystal
LCD	Liquid Crystal Display

LED	Light Emitting Diode
LF	Langmuir Film
LM	Langmuir Monolayer
LP	Loose-Packing Phase
MFC	Mass Flow Controller
N	Nematic
NLC	Nematic Liquid Crystal
POM	Polarizing Optical Microscope
PPM	Parts Per Million
QD	Quantum Dot
RAIRS	Reflection Absorption Infrared Spectra
SmA	Smectic-A Phase
SmA_d	Partial Bilayer Smectic A Phase
SmA_dP_a	Partial Bilayer Biaxial Antiferroelectric Smectic A Phase
SmC	Smectic-C Phase
SmC^*	Smectic C^*(Chiral)
SmC_A^*	Antiferroelectric Smectic C Phase
SEM	Scanning Electron Microscopy
SPM	Scanning Probe Microscopy
SRI	Spreading Resistance Imaging
STM	Scanning Tunneling Microscopy
TEM	Transmission Electron Microscope
TiO_2	Titanium Dioxide
UV-Vis	Ultraviolet-Visible Spectroscopy
XRD	X-Ray Diffraction
1D	1-Dimensional
2D	2-Dimensional
3D	3-Dimensional

Symbols

A	Area
A_{ex}	Excess area per molecule
A_i	Lift off area
A_L	Area of monolayer from water
A_m	Area per molecule
A_o	Limiting area per molecule
A°	Armstrong
A_S	Area of the substrate covered with monolayer
A_w	Area per micro gram
a.u.	Arbitrary unit
c	Velocity of light
dI/dV, G	Differential conductance
ΔG	Gibbs free energy
ε	Dielectric Constant
E	Elastic modulus
E_g	Energy Gap
E_A	Activation energy
h	Planck`s constant
γ_0	Surface tension of water without monolayer
γ	Surface tension of water with monolayer
H_2O_2	Hydrogen Peroxide
H_2SO_4	Sulfuric acid
I	Current
k_B	Boltzmann constant
L_1	Liquid expanded or low density liquid phase
L_2	Liquid condensed or high density liquid phase
λ	Wavelength
μm	Micrometer

µl	Microlitre
µm	Microgram
mM	Millimolar
mN/m	Milli newton per meter
N_a	Avogadro number
$\hat{n}$	Director
n_1	Refractive index of medium
n_2	Refractive index of reflecting material
π	Surface pressure
π_c	Collapse surface pressure
π_t	Target surface pressure
R_a	Initial sensor resistance in air
R_g	Measured resistance with exposure to a target gas or vapor
S_a	Average roughness
Si	Silicon
Si_3N_4	Silicon nitride
SiO_2	Silicon dioxide
T	Temperature
T_R	Transfer ratio
θ_B	Brewster angle
X_M	Mole fractions
V	Voltage

Chapter-1
Introduction

1.1 Liquid Crystal

In 1888, Australian Botanist Friedrich Reinitzer identified a new phase which was different from existing solid, liquid and gas phases of matter. This was an intermediate phase that lies between the disordered liquid and 3-dimensionally (3D) ordered crystalline solid phase. This is popularly called as the **Liquid Crystal** (LC) phase. The LC phases are also known as mesophases since their properties lie between an isotropic liquid and 3D ordered solid crystal phase [1, 2]. They can flow like liquids and their properties such as refractive indices, dielectric constant and diamagnetic susceptibilities are anisotropic, similar to that of crystalline solid. Reinitzer [1] gave the first systematic description of the LC phase.

LCs are classified into two categories viz., thermotropic and lyotropic. Many organic compounds exhibit mesophases as a function of temperature. Such LC are called **thermotropic** LCs [2]. Thermotropic LCs find applications in electro-optic devices e.g. liquid crystal displays (LCD), smart windows [3], temperature and pressure sensors [4].

Organic compounds exhibiting mesophases as a function of both concentration and temperature are known as **lyotropic** LCs. Lyotropic LCs can be observed in biological system, paints and colloids.

1.2 Classification of Liquid crystals

Some organic molecules with shape anisotropy exhibit liquid crystalline phase. Depending on the shape anisotropy of the molecule thermotropic LCs are classified into:

1. **Calamitic** liquid crystals made up of rod-like molecules
2. **Discotic** liquid crystals made up of disc-like molecules
3. **Banana** liquid crystals made up of bent-core molecules

1.2.1 Calamitic LC: The rod shaped (calamitic LCs) are the most common type of organic molecules that form mesophase. Most of the rod-shaped molecules consist of a rigid core of two or more aromatic ring systems, linked together directly or through connecting groups and one or two flexible chains attached at the end. Here, we have described the few common phases exhibited by calamitic LCs.

(a) Nematic Phase (N): Nematic phase is the most fundamental phase among LCs. The word nematic came from the greek word "NEMA" which means thread like. The nematic phase exhibits a thread like texture on observation under the microscope between the crossed polarizers. In the nematic phase, the molecules have a long range orientational order but no translational order. The molecules in this phase are free to move along the long molecular axis but maintain on an average their original orientation.

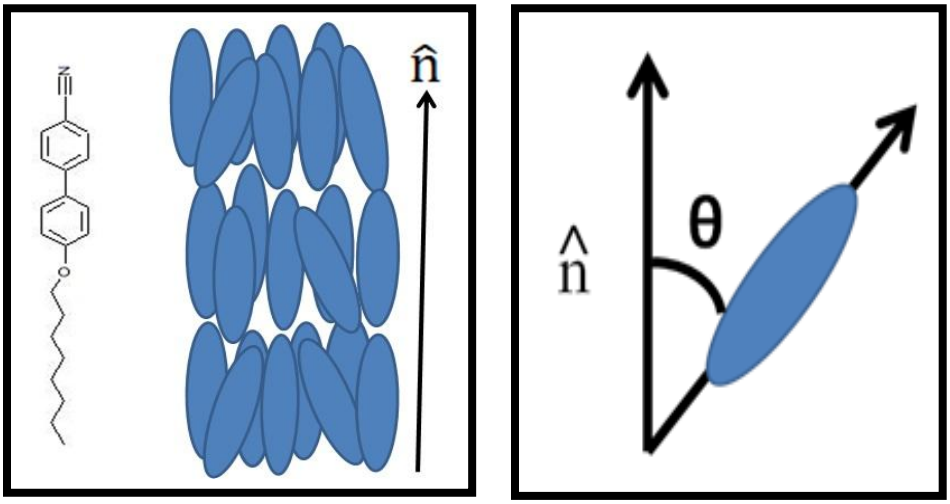

(a) (b)

Figure 1.1: Schematic diagram of the (a) molecular structure of rod shaped molecule and nematic phase exhibited by rod shaped molecules (b) the director n̂ ; here θ indicates the angle between the director n̂ and the long axis of molecule.

In the nematic phase of rod-shaped molecules, on an average the long axes of the molecules are oriented along a particular direction called the director n̂ (in figure 1.1(a)). The director n̂ is a dimensionless apolar unit vector which means n̂ and -n̂ are physically equivalent. The schematic diagram of molecular arrangement of rod shaped molecules in the nematic phase is shown in figure 1.1(a).

The degree of orientational order of the molecules in nematic phase is defined by an order

parameter S. The order parameter is defined as: $S = (1/2) < 3\cos^2\theta - 1 >$ Here, θ is the angle between the director and the long axis of each molecule (in figure 1.1(b)) and the brackets indicate an average over all of the molecules. The order parameter is a function of temperature. For an isotropic liquid, S = 0. For LC mesophases, usually S varies from 0.3 to 0.9 [5].

(b) Smectic Phase (Sm): In addition to long range orientational order, there exists 1D or 2D translational order in smectic phase (Sm) which arises from a layered arrangement of the molecules. There are several types of smectic LC phases, which are characterized by a variety of molecular arrangements within the layers. Based on the molecular arrangement and orientation of molecules within the layers, the different smectics phases (Smectic – A, B, C, D, E, F, ……) are known to exist in literature[5]. Among these smectic phases, two most commonly observed smectic phases are: smectic-A phase (SmA) and smectic-C phase (SmC). Smectic phases are higher ordered mesophases than nematic, possessing long-range orientational order along with additional layer ordering [5].

Smectic A Phase (SmA): In SmA phase, the LC molecules are arranged in layers, and there is no positional order within each layer. The long axes of molecules are parallel on an average to the layer normal $\hat{z}$ i.e. $\hat{n}$ is parallel to $\hat{z}$ (shown in figure 1.2(a)) [5].

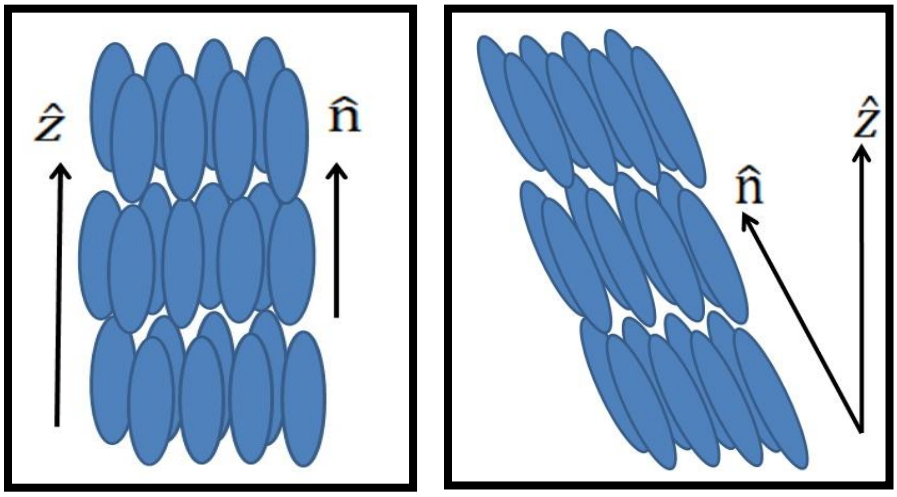

(a) (b)

Figure 1.2: Schematic diagram of the molecules in the (a) Smectic A phase and (b) Smectic C phase.

Smectic C Phase (SmC): SmC phase has layer structure closely related to SmA phase. In SmC phase, the long axes of the molecules are tilted with respect to layer normal $\hat{z}$ as shown in

figure 1.2 (b). The SmC phase is "biaxial" in nature. Due to anisotropic polarizability, SmC becomes optically biaxial [2].

(c) Smectic C*(Chiral) - Ferroelectric Phase: The layered structure of the molecules in SmC phase changes to a helical pattern, if the molecules are chiral or if we add an optically active (chiral) dopant molecule to a LC material exhibiting SmC phase. The helix is formed by precession of the tilt direction about an axis perpendicular to the layer. This configuration is known as chiral SmC or SmC* [6].

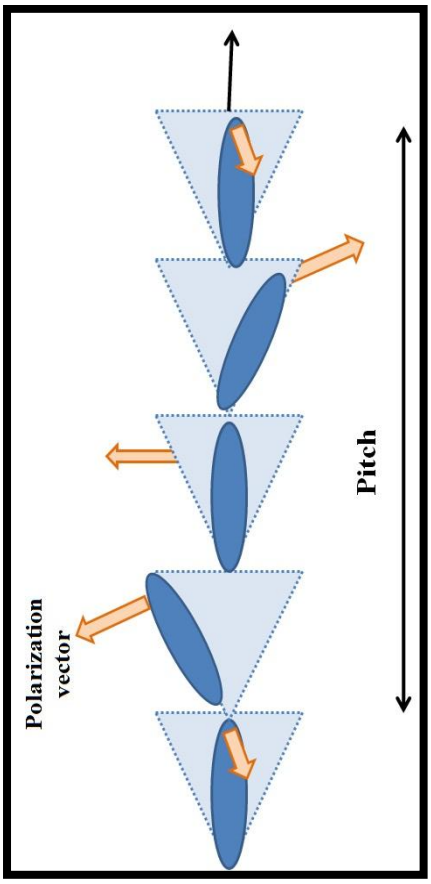

Figure 1.3: Schematic diagram of the molecules in the Smectic C phase.*

The helix can be either left-handed or right-handed, depending on the chirality of the molecule. The pitch is the distance after which the molecules have the same average orientation (shown in figure 1.3). The symmetry of the SmC* layers allows them to be transversely polarized and hence the SmC* is also referred to as a ferroelectric LC (FLC) [7]. The molecules exhibit a spontaneous polarization along the symmetry axis.

(d) Antiferroelectric Phase: In an anti ferroelectric SmC phase (SmC_A*) the constituent molecules tilt in opposite directions in successive layers as shown in figure 1.4. The direction of polarization in each layer is opposite from that the adjacent layer [8].

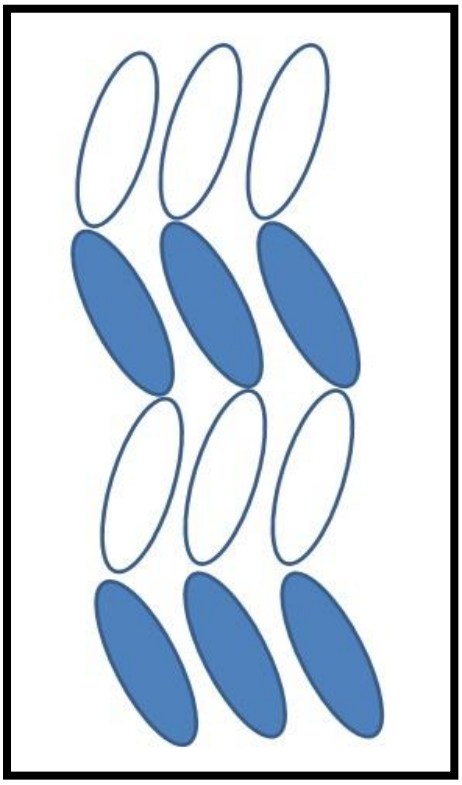

Figure 1.4: Schematic diagram of molecules in Anti-ferroelectric Smectic C (SmC_A*) *phase.*

1.2.2 Disc-shaped LC

In 1977 Chandrasekhar et al. [4] discovered the first discotic LC (DLC). These molecules are disk like in shape. Usually the discotic core is made of flat aromatic ring attached with flexible parts like alkyl chains. The most common core groups are benzene, triphenylene, hexabenzocoronene, anthracene and anthraquinone [9] etc. Figure 1.5(a) shows the molecular structure of DLC. DLCs exhibits stable thermotropic liquid crystalline phase. The phases exhibited by DLCs can be classified into two categories, nematic discotic and columnar discotic phases [10].

(a) Nematic Discotic Phase: This phase is similar to the nematic phase exhibited by rod shaped LCs. This is the least order mesophase in which the molecules have only long-range orientational order but no positional order [11]. Discotic molecules exhibit a variety of nematic phases such as discotic nematic, cholesteric discotic nematic, columnar nematic and lateral

nematic phase [12]. Figure 1.5 (b) shows the schematic representation of nematic phase exhibited by DLCs. In this phase, the molecular axis perpendicular to disc-plane align on average in one particular direction, known as director $\hat{n}$.

(b) Columnar discotic: In this phase, the disk like mesogens pack into stacks to form column like structures. The molecules are arranged in a 2D lattice with the column axes being parallel to each other. The schematic representation of columnar phase exhibited by DLC is shown in figure 1.5(c). Depending on the lattice formed by the columns; the columnar phase can be classified into different categories like: hexagonal, rectangular, oblique and lamellar phases. In columnar hexagonal phase, the columns organize in a 2D hexagonal lattice. The columnar rectangular phase is characterized by the rectangular lattice formed by the columns. In columnar oblique phase, the columns organize in a lattice with oblique unit cell. The columnar lamellar phase has the columns arranged in the layered structure. [12].

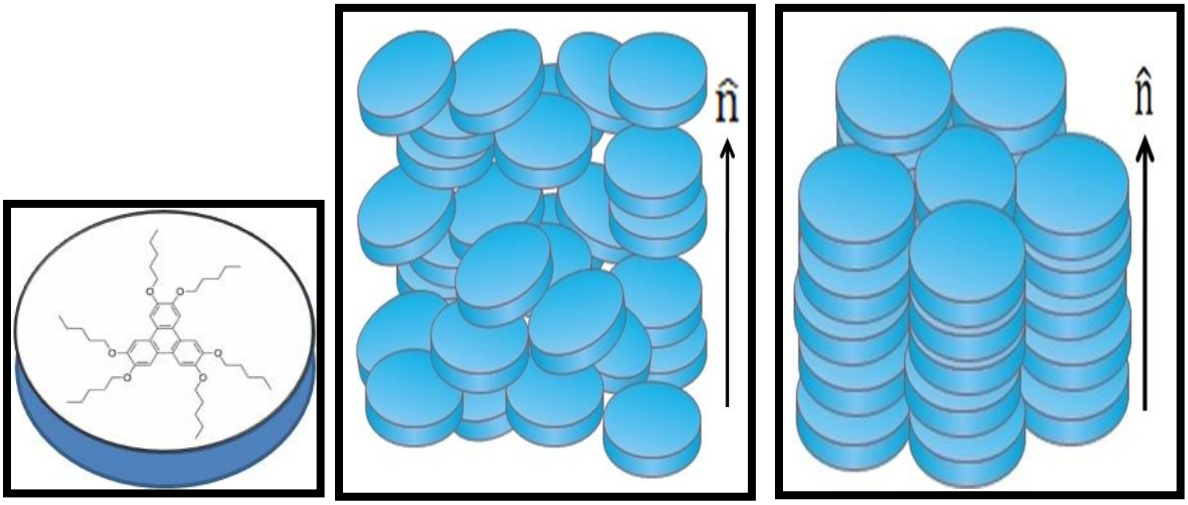

(a) (b) (c)

Figure 1.5: (a) The chemical structure of a discotic liquid crystal. Schematic diagram of the molecular arrangement molecules in the (b) Nematic phase (c) Columnar discotic phase exhibited by discotic liquid crystal.

The molecules in a column exhibit only short-range positional order. The molecules with their rigid, relatively flat cores can self-organize into columns. This is due to steric packing and π-π interactions between the cores [12]. There is high charge mobility along the column axis as compared to the charge mobility in the direction perpendicular to the column axis due to the strong π–π interaction between the cores. This high anisotropy in the charge mobility results in

quasi-one dimensional of conductivity [11]. Because of this property, DLCs find applications in devices like field effect transistor, light emitting diode, photo voltaic solar cell, liquid crystal displays, sensors and memory devices [13-14].

In this thesis, we have used DLC exhibiting hexagonal columnar phase with triphenylene core.

1.2.3 Bent-Core LC

The first LC compound made up of bent-core (BC) molecules was synthesized by D. Vorlander [15] in 1903. BC molecules consist of a rigid, highly conjugated core and flexible hydrocarbon tails with a large bend angle ≥ 120°. BC molecules are typically composed of aromatic rings with an angular central ring, various side linkages to the core and terminal chains at one or both ends. These molecules may be symmetric or asymmetric and the linkages between the aromatic rings may vary in position and size. Due to the bent shape and close packing of BC molecules, it is convenient to define three orthogonal unit vectors $\hat{n}$, $\hat{m}$ and $\hat{p}$. The vector $\hat{n}$ is the unit vector along the long axis (the director), $\hat{m}$ is perpendicular to the molecular plane and $\hat{p}$ is along the kink direction [16].

The molecular structure and the symbolic representation of BC molecule are shown in figure 1.6 (a) and (b) respectively.

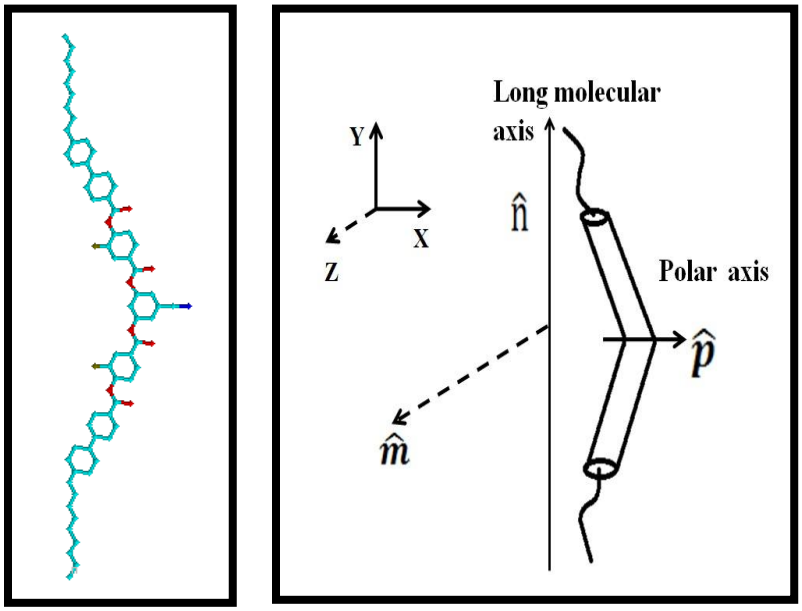

(a) (b)

Figure 1.6: (a) The chemical structure and (b) symbolic representation of bent-core liquid crystal [16].

BC molecules exhibit a rich variety of phases. BCLCs form a large number of smectic and columnar phases which are denoted by B_1, B_2,…...B_8. The letter B stands for banana or BC molecules and the number shows the chronological order of their discovery of the different B phases [17, 18]. In this thesis, we have described some of the BCLC phases which are employed for our studies.

(a) B_1 Phase: B_1 phase is exhibited by BC compounds having short terminal alkyl chains. This phase is categorized as a columnar phase. In this phase the banana molecules are arranged in 2D rectangular columnar structure as shown in figure 1.7. The lattice parameter 'a' provides an approximate number of molecules in the lattice and the parameter 'b' corresponds to the length of the molecule [19-20]. Aromatic cores and alkyl chains of the molecules overlap only near column boundaries. Antiferroelectric order is observed between neighbouring columns.

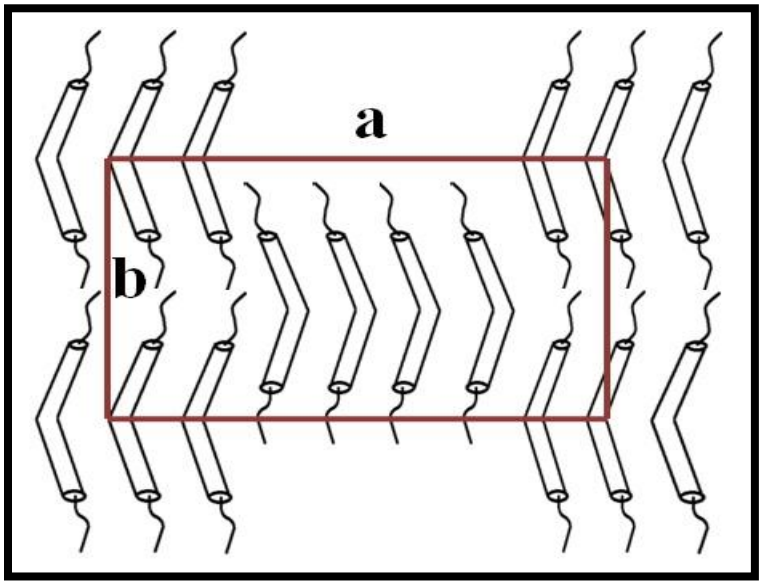

Figure 1.7: Schematic diagram of molecules in the B_1 phase exhibited by bent-core liquid crystals.

(b) **B_2 Phase:** The B_2 phase is the most interesting banana phase because of its polar switching. This mesophase is generally observed in BC compounds with long terminal alkyl chains. The BC compounds with long terminal alkyl chains exhibit layered structure. Figure 1.8 shows the schematic diagram of a smectic layer in B_2 phase. Due to packing constraints, the molecules cannot rotate about the long axes and this gives rise to layer polarization. The layer has no mirror planes and becomes chiral even though the molecules are achiral.

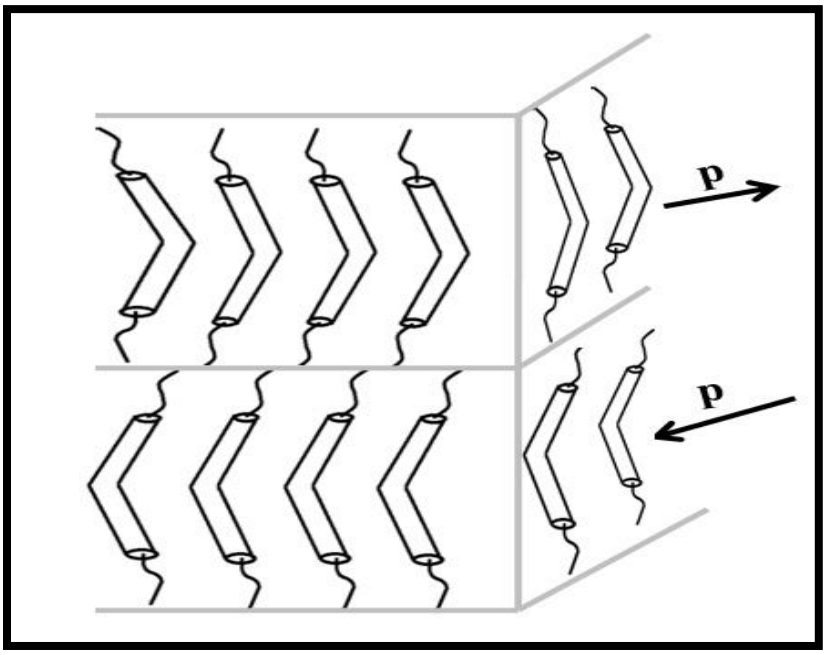

Figure 1.8: Schematic diagram of smectic layers in B_2 phase.

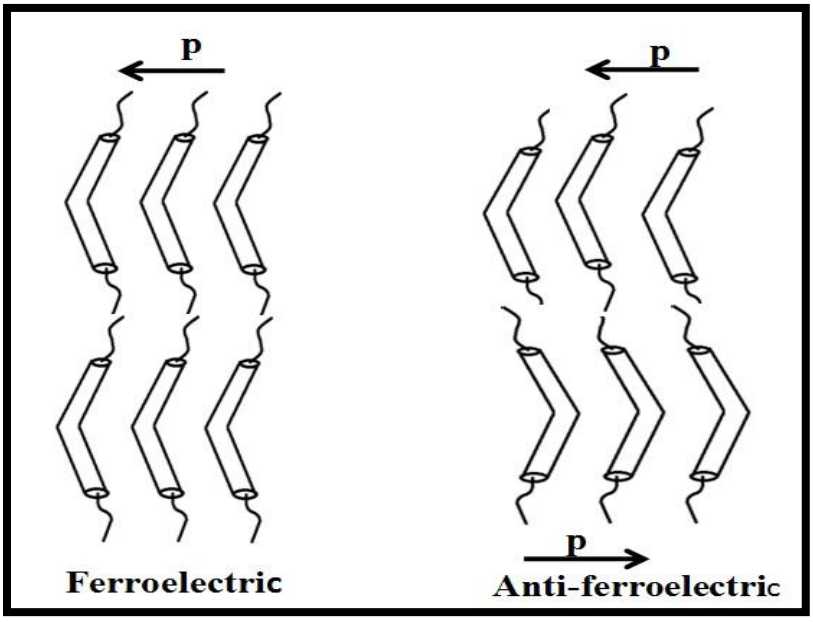

Figure 1.9: Schematic representation of the ferroelectric and antiferroelectric in polar smectic phases.

This phase is similar to the SmA phase of calamitic LCs, except that the layers are polar. This difference is labeled by adding the letter P (for polar) to SmA. Depending on the direction of the polar order in adjacent layers, SmAP phase can organize into two different structures:

ferroelectric (polar direction parallel $SmAP_F$) and antiferroelectric (polar direction antiparallel $SmAP_A$) [16]. Figure 1.9 shows the schematic of $SmAP_A$ and $SmAP_F$ for the polar smectic phase. There are four different phase structures formed in B_2 phase which differ in chirality and polarity depending on the tilt in molecular long axis $\hat{n}$ by θ from the smectic layer normal $\hat{m}$.

Niori et al., in 1996 [21] first observed the ferroelectric switching behaviour due to spontaneous polarization and they explained the polar order based on close packing of molecules in a smectic layer with a bending direction along a symmetry axis. They reported achiral BC molecules can also form polar smectic layer and exhibit ferroelectric and anti-ferroelectric switching behavior [21].

The BC molecules are strongly polar and biaxial in shape and thus strongly deviate from cylindrical symmetry. BC molecules not only can induce polar order but also chiral superstructures in some of their liquid crystalline mesophases, despite the fact that constituent molecules of these mesophases were achiral [16]. The unique properties of BC molecule like chirality, ferroelectricity and anti-ferroelectricity make them very attractive for practical applications such as electro-mechanical devices [22], electro-optical display devices [23], switching and in storage devices [24].

1.3 Nanomaterials

Nanomaterials are defined as materials having dimension in the range of 1-1000nm [25]. The field of nanoscience and nanotechnology is developing due to possibility of its vast industrial applications. The materials exhibit different properties when it scaled down to the nanometer length scale as compared to its bulk state. The surface to volume ratio of nanomaterials increases with decreasing the particle size. Nanomaterials have large surface area to volume ratio than their conventional forms, which can lead to greater chemical reactivity and affect their strength. Researchers are interested in these nanomaterials due to their special and unique properties. Shape and size of the nanoclusters play an important role in defining the properties of nanomaterials [26-27].

Nanomaterials can be classified into different categories according to their chemical and physical properties. Common types of nanomaterials are nanoparticles, composites, dendrimers, quantum dots and carbon based materials like: carbon nanotubes, graphene, fullerene etc [26].

Nanoparticles have a small size in the range of few nm, that they actually lie between the bulk materials and the molecular structures. As a result they possess some of the properties of the bulk materials as well as molecular structures. The physical, chemical and biological properties of nanomaterials differ from the properties of bulk materials. Nanoparticles are formed using variety of materials like; metals, semiconductors or oxides [26]. In this thesis we have used titanium dioxide (TiO_2) nanoparticles for the formation of thin film.

Nanocomposites are materials prepared by combining one or more nanomaterial component into a bulk material in order to obtain the best properties of each component [26, 27]. Nanocomposites are materials that incorporate nano-sized particles into a matrix of standard material. The effectiveness of nanoparticles are based on the amount of material (mostly 0.5 to 5% by weight) added. The result of the addition of nanoparticles leads to a drastic improvement in properties like: mechanical (strength, modulus and dimensional stability), electrical conductivity, thermal stability, chemical resistance, surface appearance, optical clarity etc. The properties of nanocomposite materials depend not only on the properties of their individual component, but also on their combined morphology and interfacial characteristics. The large surface to volume ratio of nanoparticles changes their properties in comparison to material in bulk and it also changes the way in which the nanoparticles bond with the bulk material. The electrical and optical properties of nanoparticles are size dependent; hence it is important to control the particle size, shape and distribution [26, 28]. So by using combinations of these unique properties a number of multi functional nanostructures can be produced with precise control of their composition. Some nanocomposites materials have been shown to be 1000 times tougher than the bulk component materials. Various fields (thin-film, drug delivery systems, UV protection gels, nano-wires, sensors etc) are using nanocomposites in order to develop new applications [27].

Quantum dots (QDs) are semiconductor nanomaterials ranging from 2 to 10 nm in diameter with a core - shell structure [29]. The core and shell of QDs is usually composed of elements from groups II–VI, III–V and IV–VI with configurations (core/shell) such a CdSe/ ZnS, CdS/ ZnS, InAs/CdSe etc [30, 31]. The properties of QDs changes as a function of both the size and shape. QDs are mostly used to manufacture transistors, solar cells, light emitting diodes (LEDs), diode lasers and second - harmonic generation devices.

Carbon based Nanomaterials: There are different types of carbon-based nanomaterials like single or multiwall nanotubes, fullerenes and graphene. Carbon nanotubes (CNTs) can be described as seamless hollow tubes composed of rolling graphite sheet. CNTs can be further divided into single-walled carbon nanotubes and multi-walled carbon nanotubes depending upon the layer number of graphite sheet. CNTs have attracted a great deal of attention due to their unique structural, electrical and mechanical properties [32].

Graphene is a single layer of sp_2 hybridized carbon atoms arranged in a honeycomb-shaped lattice [32]. It is another class of carbon nanomaterials which is gaining tremendous scientific attention due to its unique physicochemical properties such as high surface area, excellent thermal and electrical properties, strong mechanical strength [33-36]. The unique electrical, optical and mechanical properties of graphene have led to enormous possibilities of innovative applications including light emitting diodes, solar cells, optoelectronics, sensors etc [37-40].

The thin films of LCs and nanomaterials on solid substrates exhibit remarkable properties. Such properties can be potentially employed for device fabrication. In order to improve the device performance, nanomaterials should be aligned onto the active area of the device.

For the device fabrication the alignment of LC at interfaces play crucial role. The ability to control the alignment of the LC molecules at interface is very important for the fabrication of LC display devices. The conventional method such as rubbed polyimide (PI) and silane pretreated substrates give either an alignment of molecules parallel or perpendicular to substrate for the dielectric anisotropy calamitic LC materials. However, we cannot rely on then conventional method for the alignment of BCLC and discotic LCs. Alignment layer in any LC based device is the main driving point which determines the switching behavior on application and removal of external electric and magnetic fields. The morphology of thin film on the solid substrate controls the alignment of LCs. Langmuir - Blodgett (LB) technique provides a precise control over the orientation and ordering of the molecules at the substrate.

The experimental techniques for formation of thin film of nanomaterials and LCs are briefly explained in the next chapter.

References

1. F. Reinitzer, W. Monatsh, Chem. 9, 421, **1888.**
2. S. Chandrasekhar, "*Liquid Crystals"* Cambridge University Press, Cambridge, **1992**.
3. D. W. Bruce, J. W. Goodby, J. R. Sambles, H. J. Coles, Phil. Trans. R. Soc. A. 364, 2567, **2006**.
4. S. Chandrasekhar, B. K. Sadashiva, K. A. Suresh, Pramana Journal of Physics 9, 5, 471, **1977.**
5. P. G. de Gennes, J. Prost, "*The Physics of Liquid Crystals"* Clarendon Press, Oxford, **1993.**
6. V. Manjuladevi, "*Experimental Studies on Phase Diagrams of Liquid Crystals* " [Ph.D. Thesis], Raman Research Institute, Bangalore, **2004**.
7. R. B. Meyer, L. Liebert, L. Strzelecki, P. Keller, J. Physique Lett. 36, 3, 69,**1975**.
8. L. A. Beresnev, "*Ferroelectric Liquid Crystals"* Gordon and Breach, New York, **1988.**
9. S. Kumar, Liquid Crystals 36, 607, **2009.**
10. S. Chandrasekhar, G.S. Ranganath, "*Discotic liquid Crystals Rep Prog Phys"* 53, 57, **1990.**
11. S. Kumar, Chem. Soc. Rev. 35, 83, **2006**.
12. T. Wohrle, I. Wurzbach, J. Kirres, A. Kostidou, N. Kapernaum, J. Litterscheidt, J. C. Haenle, P. Staffeld, A. Baro, F. Giesselmann, S. Laschat, Chem. Rev. 116, 1139, **2016**.
13. S. Sergeyev, W. Pisula, Y. H. Geerts, Chem. Soc. Rev. 36, 12, 1902, **2007**.
14. S. Kumar, S. K. Varshney, Angew. Chem. Int. Ed. 39, 3140, **2000.**
15. D. Vorlander, A. Apel, Ber. Dtsch. Chem. Ges. 65, 1101, **1932.**
16. R. A. Reddy , C. Tschierske, J. Mater. Chem. 16, 907, **2006.**
17. D.R. Link, G. Natale, R. Shao, J. E. Maclennan, N.A. Clark, E. Korblova, D. M. Walba, Science 278, 5345, 1924,**1997.**
18. H. Takezoe, Y. Takanishi, Japanese, J. Appl. Phy. 45, 597, **2006.**
19. K. Pelz, W. Weissflog, U. Baumeister, S. Diele, Liquid Crystals 30, 10,1151, **2003**.
20. J. Szydlowska, J. Mieczkowski, J. Matraszek, D. W. Bruce, E. Gorecka, D. Pociecha , D. Guillon, Phys. Rev. E. 67, 031702, **2003.**
21. T. Niori, T. Sekine, J. Watanbe, T. Furukawa, H. Takezoe, J. Mater. Chem. 6, 1231, **1996.**

22. A. Jakli, D. Kruerke, G. G. Nair, Phys. Rev. E. 67, 5,051702, **2003**.
23. Y. Tong, Y. Wang, G. Wang, H. Wang, L. Wang, D. Yan, J. Phys. Chem. B 108, 34,12921, **2004.**
24. J. Wang, L. Qiu, A. Jakli , W. Weissflog, E. K. Mann, Liquid Crystals, 37, 10, 1229, **2010.**
25. K. T. Ramesh, "*Nanomaterials Mechanics and Mechanisms*", Springer, Science + Business Media, LLC, USA, **2009**.
26. M. Tuominen, E. Schultz "*Environmental aspects related to nanomaterials"* A literature survey. 26, **2010.**
27. P. M. Ajayan, L. S. Schadler, P. V. Braun "*Nanocomposite Science and Technology* ", Weinheim: Wiley-VCH, **2003.**
28. P. J. Alivisatos, J. Phys. Chem. 100, 13226, **1996**.
29. I. L. Medintz, H.T. Uyeda, E.R. Goldman, H. Mattoussi, Nat. Mater. 4, 6, 435, **2005.**
30. T. Jamieson, R. Bakhshi, D. Petrova, R. Pocock, M. Imani, A. M. Seifalian, Biomaterials 28, 31, 4717, **2007**.
31. X. Michalet, F. Pinaud, L. Bentolila, Science 307, 5709,538, **2005.**
32. H. O. Pierson, "*Handbook of Carbon, Graphite, Diamond, and Fullerenes: Properties, Processing, and Applications"* Noyes Publications: Park Ridge, NJ, **1993.**
33. A. K. Geim, K. S. Novoselov, Nat Mater 6, 183, **2007**
34. R. F. Service, Science 324, 875, **2009.**
35. A. A. Balandin , S. Ghosh,W. Bao, I. Calizo, D.Teweldebrhan, F. Miao, C. N. Lau, Nano Lett. 8, 902, **2008** .
36. C. Lee, X. Wei, J. W. Kysar, J. Hone, Science 321, 385, **2008.**
37. K. S. Novoselov, V. I. Falko, L. Colombo, P. R. Gellert, M. G. Schwab, K. Kim, Nature 490, 192, **2012**.
38. F. Bonaccorso, Z. Sun, T. Hasan, A. C. Ferrari, Nat Photon 4, 611, **2010**.
39. Y. Dan, Y. Lu, N. J. Kybert, Z. Luo, A. T. C. Johnson, Nano Lett. 9, 1472, **2009**.
40. S. Borini , R. White, D. Wei, M. Astley, S. Haque, E. Soigone, N. Harris, J.Kivioja, T. Ryhanen, ACS Nano 7, 11166 , **2013**.

Chapter-2
Experimental and Characterization Techniques

Liquid Crystal (LC) and nanocomposites have to be aligned on a surface for device fabrication. In this thesis, we have used Langmuir-Blodgett (LB) technique for the alignment of LCs and nanocomposites. The atomic force microscopy (AFM) & field emission scanning electron microscopy (FESEM) are used for studying surface topography and morphology. In this chapter, we have discussed the experimental methods and characterization techniques used for investigation in detail.

2.1 Introduction

Certain organic molecules orient themselves at an interface to minimize their free energy between a gas and a liquid phase (or between two liquid phases). When the surface film is one molecule in thickness, it is called a monolayer or monomolecular layer [1]. Organic thin film of thickness of few nm or a monolayer is useful component in many applications like: detectors, sensors, displays and electronic circuit components [2-4]. The surface to volume ratio of a material increases enormously when spread on to a substrate to form a thin film. So, there is an improvement in the sensitivity and efficiency of thin film devices. The physicochemical properties of a thin film may depend on the nature of molecular aggregation onto the substrate. The structures of the thin films on a surface can lead to the growth of bulk material; so by manipulating the structures of the thin films material structural properties can be controlled [5]. The molecule-substrate and intermolecular interactions play vital role in the formation of such structures of thin films.

A thin film can be transferred onto a solid substrate by various techniques like: thermal evaporation, sputtering, electro deposition, molecular beam epitaxy, chemical vapour deposition, physical vapour deposition, dip coating, spin coating, drop casting, self-assembly and LB

technique. Among all these techniques, the LB technique is one of the most promising techniques for the formation of monolayer of molecules at the air-water (A/W) interface and a specific phase of monolayer can be transferred onto solid substrate [6], as it allows for

(i) the precise control of the monolayer thickness,

(ii) control over surface density of the molecules in the film

(ii) homogeneous deposition of the monolayer over large areas and

(iii) the possibility to make multilayer structures with varying layer compositions.

The LB technique was introduced by Irving Langmuir [7] and extensively applied by Katharine Blodgett [8] for the deposition and characterization of thin films. Irwing Langmuir was awarded Nobel Prize in 1932 for his studies on floating monolayer on water surface. These monolayer assemblies are known as **Langmuir-Blodgett (LB)** films. The term "Langmuir Film" (LF) is reserved for a floating monolayer on water subphase, known as "Langmuir monolayer" (LM). The LB technique is used for the fabrication of monolayer and multilayer on solid surface by vertical dipping method [8].

2.2 Experimental Techniques

2.2.1 Langmuir Monolayer (LM)

LM is a single layer of insoluble amphiphilic molecules at the A/W interface. An amphiphilic molecule, which is organic in nature possess two parts: hydrophilic (HPL) and hydrophobic (HPB) part; HPL is water loving/polar head and HPB is water hating/non polar tail as shown in figure 2.1.

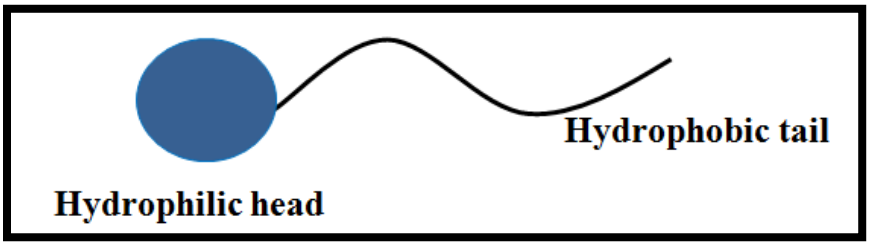

Figure 2.1: Schematic representation of an amphiphilic molecule.

Table 2.1 shows a list of possible HPL head groups and HPB tail groups of amphiphilic molecules. Amphiphilic molecules consisting of such HPL and HPB parts may form a stable monolayer at the A/W interface [5].

Table 2.1: The hydrophilic and hydrophobic groups of the molecules.

Hydrophilic part	**Hydrophobic part**
-COOH	Fluorocarbon chains,
-OH	Phenyl,
$-NO_2$	Polycyclic,
$-NH_2$	Hydrocarbon chains
$-CN_2$	

The hydrophilic part of the molecule can easily form hydrogen bond with water. On the other hand, the hydrophobic part does not form hydrogen bond with water and prefers to stay away from the water. When these amphiphilic molecules with a proper balance between hydrophilic and hydrophobic parts are spread on the water surface, the hydrophobic part stays away from the water surface whereas the hydrophilic part gets anchored to the water surface (figure 2.2). This gives rise to a monomolecular thick stable film at the A/W interface. Such stable film at A/W interface is known as LM [9]. A boundary surface between two different phases is called an interface. Generally, the thickness of the interface is only of the order of few angstrom (A°). Therefore, an interface can be approximated to two-dimensional (2D) surface. The most important feature of an interface is the sudden change in both density and composition that gives rise to an excess free energy at the interface. The monolayer at the A/W interface can be considered as a 2D system.

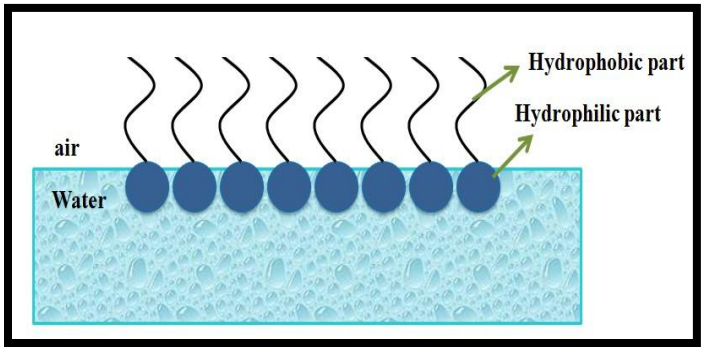

Figure 2.2: A schematic diagram of amphiphilic molecules at air- water interface.

The stability of the monolayer at the A/W interface is determined by the strength of polarity of the head group and the hydrophobicity of tail group of the molecules [9]. It has been found that the monolayer of fatty acid ($C_nH_{2n+1}COOH$) with n in the range of 12 to 24 can form stable film

at A/W interface [10]. If n > 24, the hydrophobicity dominates and molecules aggregate to form crystallites on water surface. If n < 12, the hydrophilicity dominates, and the molecules dissolve in water to form various concentration dependent structures [11]. Such structures are dependent on molecular interaction, temperature, pH and ion contents of the aqueous medium.

At very low concentration of the hydrophilically dominant amphiphilic molecules, the molecules adsorb and desorb from the interface and establish a dynamical equilibrium. Such monolayer at A/W interface is known as Gibb's monolayer [9]. Above a certain concentration, called the critical aggregation concentration (CAC), the molecules self-assemble into different structures e.g., rods, discs, spheres, bilayers and vesicles. At concentrations much higher than the CAC, amphiphiles may form diverse liquid-crystalline phases, e.g., bilayer stacks (lamellar phase) and hexagonal phases [12].

2.2.2 Langmuir Monolayer at Air-Water Interface

LM shows different 2D phases, depending on the thermodynamic condition [5]. Surface manometry is a standard method to study the thermodynamics and the surface phases in a LM. In surface manometry technique, the monolayer is uniformly compressed and surface pressure (π) as a function of surface density is measured at constant temperature. At the A/W interface, the presence of a monolayer reduces the surface tension of water. Such reduction in the surface tension is defined as π. It is given by

$$\boldsymbol{\pi = \gamma_o - \gamma} \qquad 2.1$$

where $\boldsymbol{\gamma_o}$ is the surface tension of water without monolayer and $\boldsymbol{\gamma}$ is the surface tension with monolayer. The surface pressure can be measured using a Wilhelmy plate. In surface manometry, the surface density of amphiphilic molecules is varied and change in surface tension relative to pure aqueous subphase is recorded. The surface density can be varied either by changing number of molecules in a given area or by changing area for a given number of molecules. Practically, it is convenient to change area available for a fixed number of molecules. At a constant temperature, the variation of surface pressure as a function of area per molecule (A_m) is known as π - A_m isotherm [9].

A schematic diagram of the LB trough for obtaining π - A_m isotherm is shown in figure 2.3.The LB trough (LB2007 DC, Apex Instrument) is kept inside a glass box to avoid any thermal or air drift. The trough (1) and barriers (4) are made up of teflon. Teflon is hydrophobic and

oleophobic in nature which ensures no deposition of material onto the trough and barriers. The subphase is ultrapure ion free water (2) with resistivity ≥ 18.2MΩ cm from Millipore (DQ5, Milli-Q) filtering system.

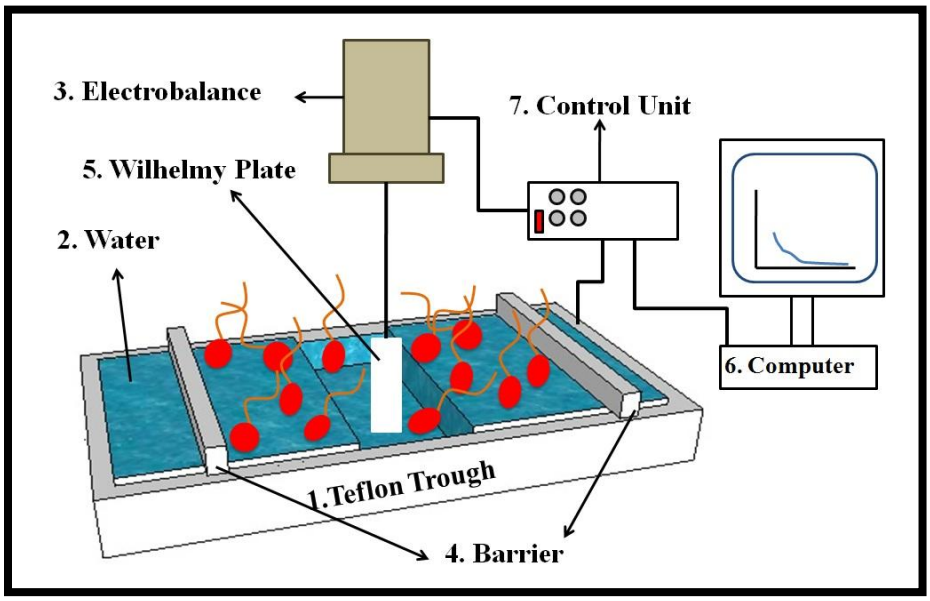

Figure 2.3: A schematic diagram of a Langmuir Blodgett trough. The components are: (1) Teflon Trough (2) Liquid Subphase water (3) Electro balance (4) Barriers (5) Wilhelmy Plate (6) Computer (7) Control unit.

Wilhelmy plate (5) is partially immersed into the water subphase. We have used filter paper of appropriate size as the Wilhelmy plate. The benefit of the filter paper is that the wetting is more efficient due to the porosity, low cost comparative to a Platinum-plate and the light weight of filter paper increases its sensitivity towards the surface pressure. The filter paper is suspended from the pressure sensor and is made just to touch the surface of the water. The filter paper is allowed to soak water fully and reading of the sensor is made zero. Filter paper is connected to the electro-balance (3) which is used to measure the value of π. The barriers are driven by motor connected to the control unit (7) which is interfaced with a computer (6). Electro balance and LB trough are also connected to the control unit.

Formation of Monolayer

Before forming the monolayer proper cleaning of the trough is essential. For this, the usual approach is to fill the trough with dilute sulphuric acid and leave it for 10-12 hours. Then the dilute sulphuric acid is suctioned out through a pump and the trough is rinsed thoroughly with

ultrapure ion-free water followed by cleaning using organic solvents like acetone and chloroform. The sample (amphiphilic molecules) is dissolved in an appropriate solvent to obtain a solution of known concentration. The solvent should be chemically inert and volatile so as to evaporate within a reasonable time period to leave no trace on the water surface. We have used mostly chloroform (high performance liquid chromatography (HPLC) grade purchased from Merck) and alcohol (HPLC grade, purity ≥ 99.8% purchased from Sigma-Aldrich,) as the dispersing solvent for our research work. The known quantity of solution is spread drop by drop on the water subphase between the barriers using a micro syringe (from Hamilton). The total available area in the trough is 1200 cm^2 and the subphase volume is 1.75 L.

Before starting the compression, the solvent is allowed to evaporate for about 20-30 minutes. As the solvent evaporates, a monolayer gets formed as dictated by the amphiphilic nature of the molecules. The head groups of amphiphilic molecules get anchored to the water surface and the tail groups stay away from the water surface. The barriers are controlled by a computer which is driven by motors. These barriers are coupled to each other to ensure a symmetric compression of the monolayer. By moving the barriers laterally the area available for the molecules on the water subphase can be changed. This helps in varying the surface density of the molecules in the monolayer. The π is measured using a Wilhelmy plate method [9, 13]. At a constant temperature, the π and A_m are recorded simultaneously using a computer. This recorded curve is the π - A_m isotherm of the spread molecules. The isotherm provides the information about the different phases and phase transitions in LM at A/W interface [14, 15].

The typical π - A_m isotherm of LM at A/W interface exhibiting different phases and their possible molecular arrangement is shown in figure 2.4. On compression at A/W interface, the monolayer passes through several different phases which can be identified by discontinuities in the isotherm. The isotherm shows the rise in π with decreasing A_m. The kink in the isotherm indicates a phase transition. A plateau in the isotherm shows the coexistence of two phases.

At large A_m, there is a gas phase. In this phase the molecules do not interact and there is neither orientational nor positional order. The A_m at which the isotherm indicates very small and finite values of the π (*e.g.* 0.2 mN/m) is known as lift-off area per molecule (A_i). As the A_m is reduced the liquid phase is formed, is generally called the expanded phase (L_1). It is an intermediate phase between gas and condensed phase. Upon further compression the L_1 phase undergoes a transition to the liquid condensed phase (L_2). In this phase the molecules are closely packed with

quasi-long range positional order.

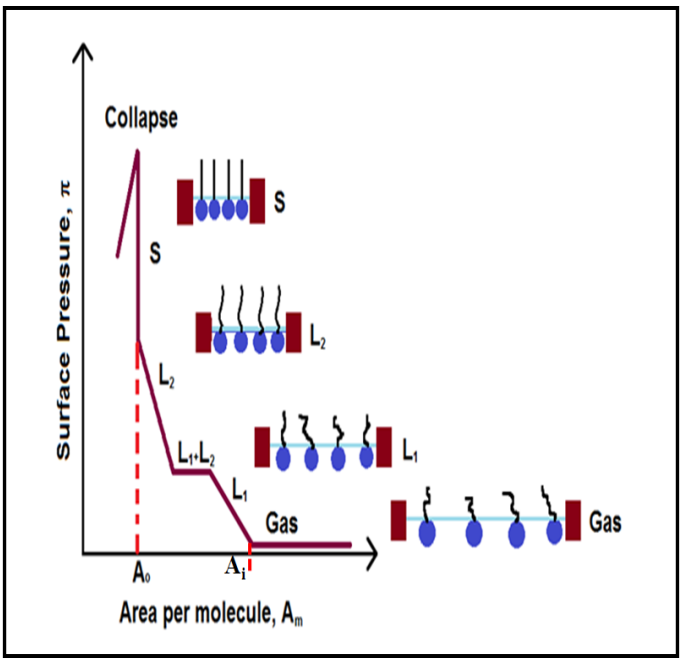

Figure 2.4: A schematic representation of surface pressure (π) - area per molecule (A_m) isotherm of LM at A/W interface indicating the different phases and possible molecular arrangement therein. The symbols L_1, L_2, S and A_0 represent liquid-expanded, liquid-condensed, solid phases and limiting area, respectively.

On further reduction of A_m, a high density liquid phase or 2D solid phase is obtained. The monolayer collapses on further decrease in A_m. Generally the collapsed state is indicated by a sharp drop in π or a plateau in the isotherm [1]. In the collapsed state, monolayer destabilizes and the molecules go to the third dimension. A plateau in the collapse state may indicate the formation of multilayer, whereas a sharp decrease may indicate a random crystallization into the 3D crystals. The nature of collapse varies from molecules to molecules and also depends on the experimental conditions. The monolayer may fold or bend in the collapsed state [16-20].

The average area occupied by the molecules in a phase is calculated by extrapolating the corresponding region of the isotherm to the zero π on the A_m axis. The extrapolation of the sharp region of the isotherm to zero π is called limiting area per molecule (A_o). This is the minimum area to which the molecules can be compressed on the water surface without collapse of the monolayer. The orientational states (tilt or untilt) of the molecules in a phase can be estimated

qualitatively by comparing the extrapolated A_m with that of molecular cross- sectional area in the bulk single crystal [5].

The LM of fatty acid is known to exhibit 17 different phases. These phases are dependent on surface density, temperature and ion content of the aqueous subphase [15, 21-23]. The kinks and plateau in the isotherm indicate the phase transitions. Sometimes the weak phase transitions do not appear as prominent kinks or plateaus in the isotherm due to experimental limitations. Such weak phase transition can be studied by calculating the in-plane elastic modulus (E) from the isotherm. The isothermal E is an appropriate quantity for distinguishing very weak phase transitions and the elastic nature of the monolayer [5] in a given phase. The E is defined as

$$\boldsymbol{E = -(A_m)\frac{d\pi}{dA_m}} \qquad 2.2$$

To check the stability of LM at A/W interface isocycles are recorded. The isocycles of LM can be obtained by repeated compression and expansion of the monolayer. Small hysteresis and retraceable isocycles indicate stable and reversible phases of the LM. A large shift in the isocycle curves towards the lower or higher A_m indicates unstable LM. The instability may arise due to dissolution of the molecules or the formation of irreversible aggregates on the water surface [1].

The LM at the A/W interface can be imaged by Brewster angle microscopy (BAM). We have explained this microscopy technique in the characterization section.

2.2.3 Thin Film at Air-Solid interface:

2.2.3.1 Langmuir- Blodgett Technique

The monolayer in a particular phase at the A/W interface can be transferred layer by layer onto a solid substrate (air - solid interface) by vertically moving the substrate in and out of the aqueous subphase in a highly controlled manner. This technique is known as LB technique. The schematic diagram of experimental setup for LB film formation is shown in figure 2.5. The setup is similar to that of the Langmuir trough except it possesses a dipper with electro-balance. LB technique exhibits numerous advantages over any other thin film deposition techniques. It provides precise control over the film thickness and intermolecular separation. A thin film of organic and inorganic materials can be fabricated on solid substrates by LB deposition technique [2, 8].

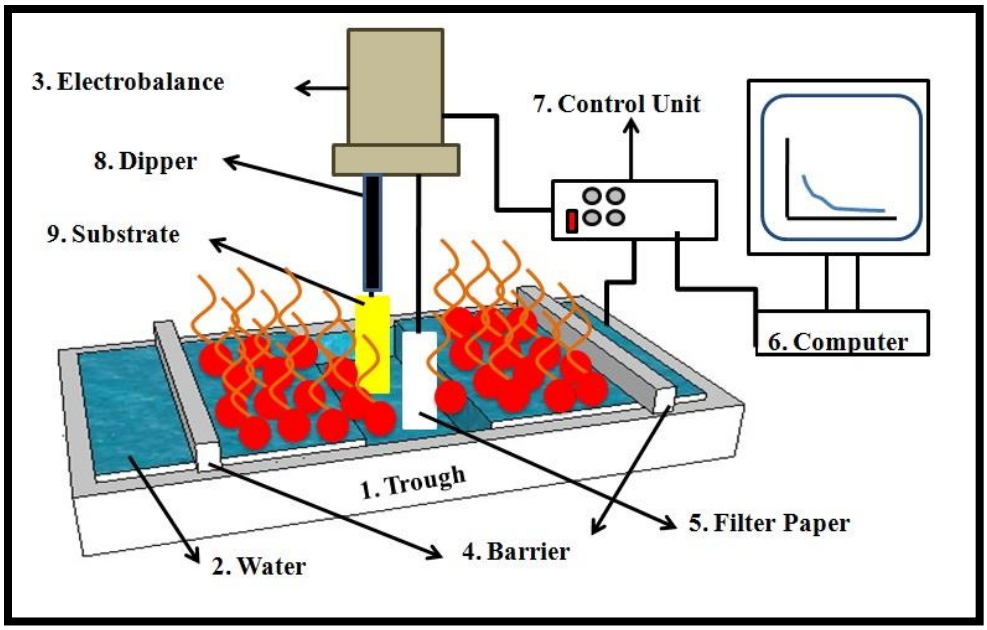

Figure 2.5: A schematic diagram showing the experimental setup for formation of LB films. The parts are as follows; (1) Teflon trough (2) Water (3) Electro balance (4) Barriers made of teflon (5) Filter paper (6) Computer (7) Control unit (8) Dipper and (9) Substrate.

In order to transfer LM at a specific phase, the monolayer is held at target surface pressure (π_t) and the solid substrate is immersed and withdrawn by vertical motion of the dipper [5]. Each stroke of the dipper may deposit a single layer of molecules onto the substrate. Various substrates like silicon (Si/SiO_2) wafer, indium tin oxide (ITO) coated glass plate, quartz plate, glass coverslip and glass plate were used for LB deposition. Before deposition, substrates like glass coverslip, glass plate and Si wafer are treated hydrophilically by boiling them in piranha solution (3:1, conc Sulfuric acid (H_2SO_4): Hydrogen peroxide (H_2O_2)), and then rinsed successively with ion-free water, absolute alcohol and acetone solvents. Concentrated H_2SO_4 (Guaranteed Reagent (GR) grade), H_2O_2 (International Standards Organization (ISO) grade) and acetone (Guaranteed Reagent (GR) grade) were procured from Merck. The substrates were then dried by blowing hot air at ~ 70º C. The substrates like glass and silicon are treated hydrophobically by immersing the hydrophilically treated substrates in a solution (1:9, Hexamethyldisilazane (HMDS) : Chloroform) for 12 hours. Then substrates are rinsed with chloroform thoroughly and stored in ultrapure water. The ITO and quartz substrates are cleaned

thoroughly by ultrapure ion-free water, absolute alcohol and HPLC grade chloroform, successively. The substrates were dried by blowing hot air at ~ 70°C.

In LB films, molecules orient differently on the solid surface depending on the nature of the solid substrate. When hydrophilic substrate is used (in fig 2.6(a)), the hydrophilic polar head group adheres to the substrate thereby yielding a hydrophobic surface. When hydrophobic substrate is used (in fig 2.6(b)), the hydrocarbon chain adheres to the substrate thereby yielding a hydrophilic surface.

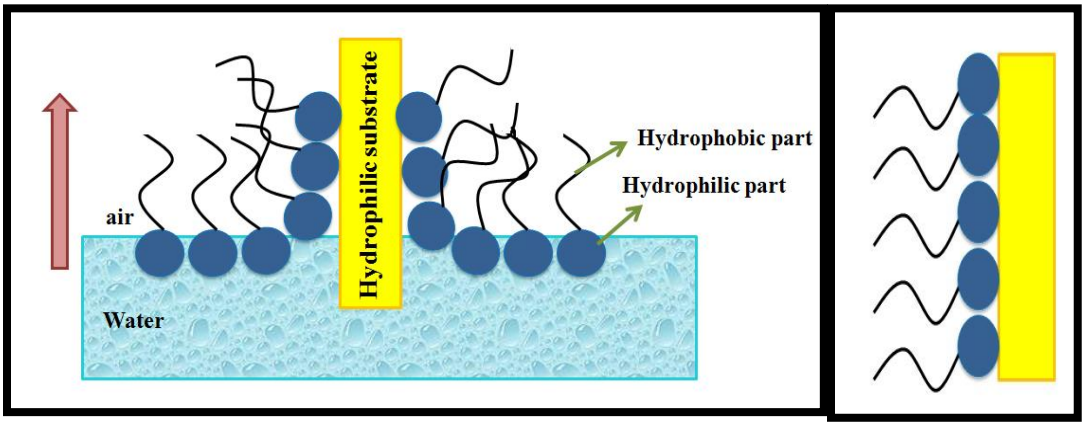

Figure 2.6: (a) Scheme for the LB transfer of the monolayer by upstroke on hydrophilic substrate.

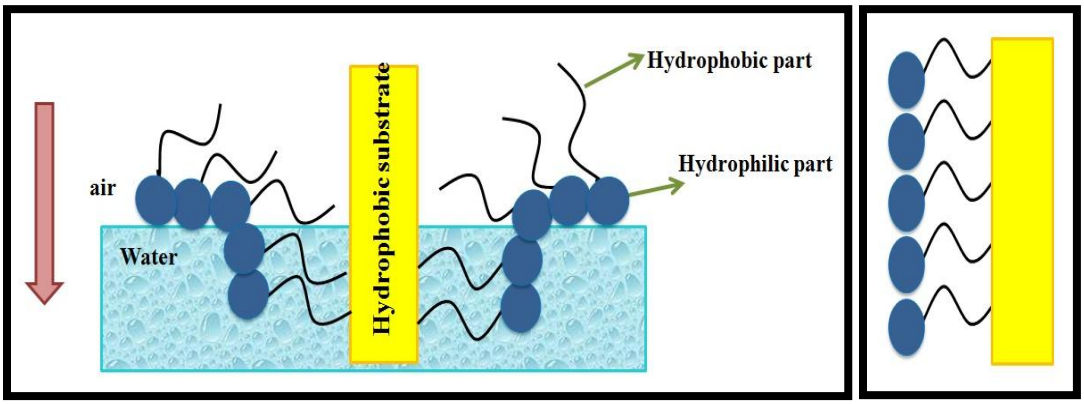

Figure 2.6: (b) Scheme for the LB transfer of the monolayer by downstroke on hydrophobic substrate.

In case of multilayer deposition, if the monolayer transfers during both the upstroke and down stroke of the dipper, such deposition is known as Y-type (figure 2.7 (b)) of LB deposition. On the other hand, if the deposition takes place only with either down strokes or up strokes, they are termed as X (figure 2.7(a)) or Z-type (figure 2.7 (c)) of LB deposition, respectively[2].

The nature of LB deposition depends on various experimental conditions including ion-contents in the subphase, temperature, pH, humidity and molecule-substrate interaction.

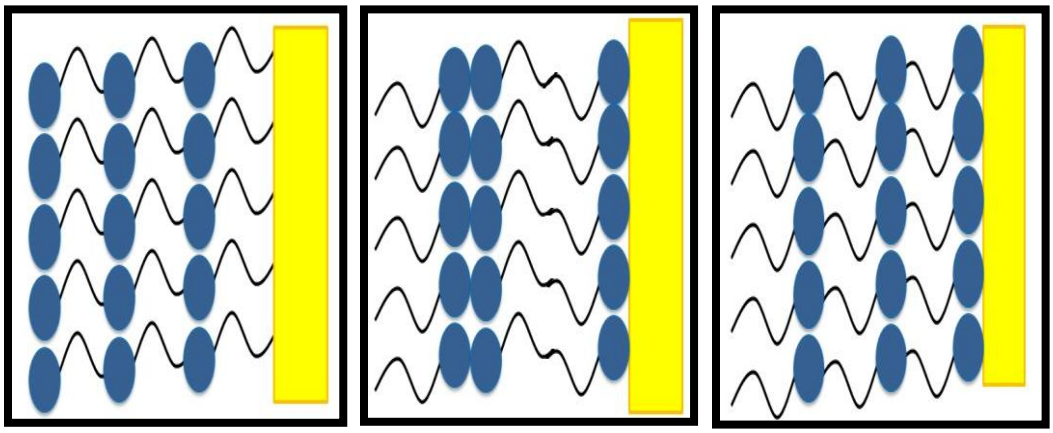

(a) X type (b) Y type (c) Z type

Figure 2.7: Schemes for the multilayer deposition during (a) downstroke only X type deposition (b) both upstroke and downstroke Y type deposition (c) upstroke Z type deposition.

The transfer efficiency of LB film can be quantified by measuring the transfer ratio (T_R) of the monolayer area (A_L) from the water surface to the area of the substrate (A_S) which is covered by the monolayer.

$$\mathbf{T_R = A_L / A_s} \qquad 2.3$$

Here, A_L is the decrease in monolayer area from the water surface during the deposition and A_s is the area of the substrate to be covered by the monolayer. The value $T_R = 1$ indicates defect-less LB film whereas $T_R = 0$ indicates no deposition. The negative value of the T_R indicates desorption of the LB film from the substrate [2].

2.2.3.2 Horizontal Transfer and Schaefer's Method

The horizontal transfer method and schaefer's method are two different techniques utilized for transferring the monolayer at the A/W interface onto substrates.

In the horizontal transfer method, first the hydrophilic substrate is dipped horizontally in the water subphase and then the monolayer is formed by spreading the molecules on water subphase. After achieving the target surface pressure (π_t), the aqueous subphase is siphoned out very slowly from the other side of the barriers. The monolayer gets adsorbed onto the substrate as the water drains out as shown in figure 2.8(a).

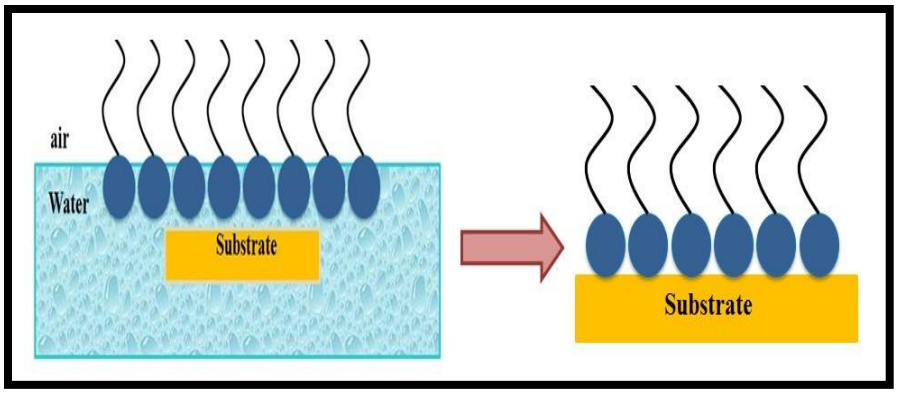

(a)

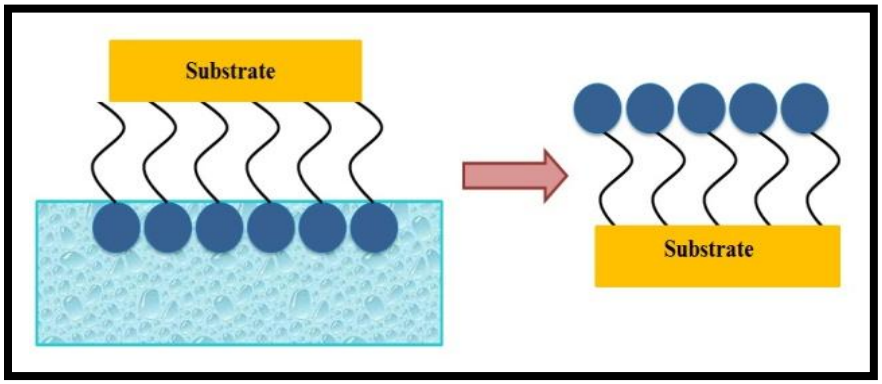

(b)

Figure 2.8: Schematic diagrams of (a) horizontal transfer (b) Langmuir Schaefer's method of deposition of Langmuir monolayer onto a solid substrate.

In the schaefer's method, first the monolayer is formed on water subphase then a hydrophobic substrate is touched onto the monolayer at A/W interface (figure 2.8(b)). The hydrophobic part of the molecules gets adsorbed to the substrate. To facilitate the drainage of water, the substrates in either case can be tilted by a small angle prior to the adsorption [5].

2.2.3.3 Spin Coating Method

Another method for the thin film deposition is spin coating. Spin coating is a fast and easy method to form thin and homogenous organic films on substrates. The substrate is mounted on a sample holder and the known quantity of a solution (molecules dissolved in solvent) is placed on the substrate. The solution was spread over the surface of substrate through centrifugal force generated while rotating the sample holder with a high speed (few thousand rounds per minute) and thus a thin film gets deposited. The thickness of the film can be varied by changing the spin

time or speed. Here, the interactions between substrate and layer solution are stronger than the interactions between surface solution and air.

2.3 Characterization Techniques

The LM at the A/W interface can be imaged by Brewster angle microscopy (BAM) and epifluorescence microscopy. There are numerous techniques to characterize the thin films on solid substrates. LB film can be characterized by various techniques like Atomic Force Microscopy (AFM), Field Emission Scanning Electron Microscopy (FESEM), UV visible Spectroscopy (UV-Vis), Fourier Transform Infrared Spectroscopy (FTIR) and X-Ray diffraction (XRD) technique. Table 2.2 shows a list of the techniques used for the formation and characterization of thin films.

Table 2.2: Experimental techniques used for the formation and characterization of thin films.

Instrument	**Company and Model**	**Purpose**
Langmuir Blodgett Trough	LB2007DC, Apex Instrument Co.	Obtaining surface pressure-area per molecule isotherm and fabrication of LB film on solid substrate
Spin Coating Unit	SCU2007, Apex Instrument Co.	Deposition of thin film on solid substrate
Brewster Angle Microscopy	MiniBAM Plus Nanofilm technolgie	Imaging of monolayer phase, phase co-existence, domain formation exhibited on A/W interface in real-time
Atomic Force Microscopy	NT-MDT, Solver Pro.	Obtaining topography of thin films on solid substrate and related spectroscopy
Field Emission Scanning Electron Microscopy	ZEISS, Sigma	Surface texture and surface morphology of thin film
UV-Vis Spectroscopy	Jasco Kyoto Japan V530	Band structure of the system and material species
Fourier Transform Infrared Spectroscopy	Perkin Elmer	Functional group in LB film

X-Ray Diffraction	PANalytical XPERT-PRO powder and Rigaku Miniflex II	Grain size and phase identification of a crystalline material
Current-Voltage Measurement	Keithley sourcemeter 2400	Charge transport mechanism

2.3.1 Langmuir monolayer at Air-Water interface:

Brewster angle microscopy (BAM)

A microscope which works on the principle of Brewster angle is known as the Brewster angle microscope (BAM). BAM gives the real-time image of phase exhibited by the LM at A/W interface [24-27]. The angle of incidence at which an unpolarized light acquires a linearly polarized state after reflection from the plane of an interface is known as Brewster angle of the reflecting material. The state of polarization of the reflected light at the Brewster angle (θ_B) is perpendicular (s-polarized) to the plane of incidence. At Brewster angle of incidence

$$tan\,(\theta_B) = n_2/n_1 \qquad 2.4$$

where n_2 is the refractive index of the reflecting material and n_1 is the refractive index of the medium through which the light is incident. BAM is used to monitor the changes in the phase of the material at A/W interface as the monolayer is compressed and decompressed [26, 27].

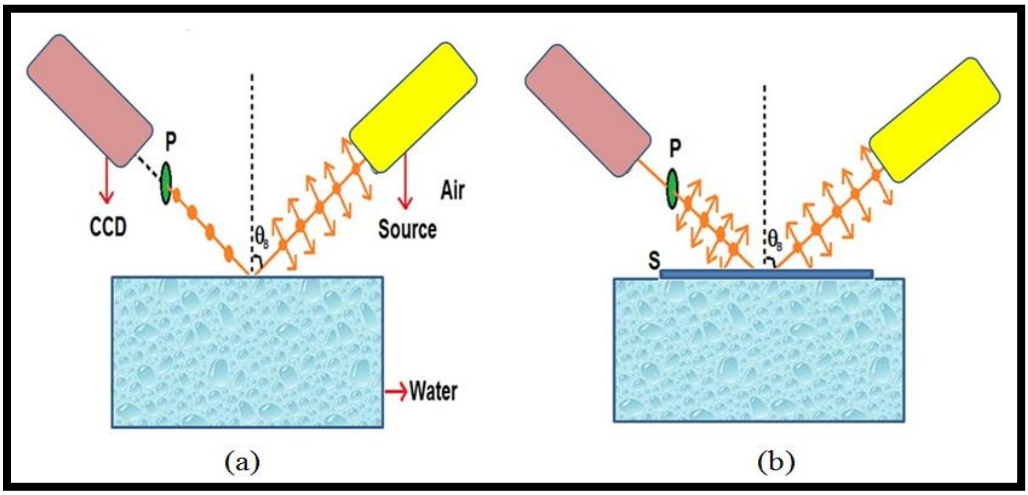

Figure 2.9: Schematic diagrams showing the working principle of a BAM. θ_B is the Brewster angle for water with respect to air and S is the monolayer at the A/W interface. The BAM setup is (a) without and (b) with monolayer at the A/W interface, respectively.

The schematic diagram of BAM is shown in figure 2.9. In the microscope, a polarized light source falls on the water surface. We have used a 30mW laser of wavelength 660nm as a light source. The reflected light is allowed to pass through a polarizer (P) which allows only the p-component of the reflected light to enter a charge coupled device (CCD) camera. For the A/W interface, θ_B is ~ 53° and the reflected image of pure water looks nearly black under this condition. The refractive index changes at the interface with the addition of material, so the θ_B for A/W interface is also changed. This in turn reflects some light which is collected by the CCD to form the images of the monolayer of material. The intensity of the reflected light varies with the thickness of the film and the surface density of the molecules. The BAM imaging of a LM reveals dark region for the gas phase due to very low surface density of the molecules. The BAM image shows a uniform texture for liquid expanded phase and uniform bright texture for liquid condensed phase.

In our research work, we have used MiniBAM Plus (Nanofilm Technologie at RRI, Bengaluru) for the study of the changes in the phase of material at A/W interface.

2.3.2 Langmuir-Blodgett film at Air-Solid interface: To characterize the film at air-solid (A/S) interface different microscopy techniques have been used.

2.3.2.1. Scanning Probe Microscopy

Scanning Probe Microscopy (SPM) can be used to obtain the surface morphology and topography information. In SPM, a physical interaction is established between a sharp probe and the sample under scan. With a precise control of the motion of the probe in raster motion, the various properties related to the sample film can be extracted. Two important types of SPM; scanning tunneling microscopy (STM) and atomic force microscopy (AFM) are used for investigation of samples.

In STM, the tunneling current between the conducting tip and the sample is measured as a function of the position. In 1981, Binnig et al. developed the first STM at IBM Zurich Research Laboratory, Switzerland [28]. It gives the topography and conductivity information of the sample surface but it can be used only for conducting surfaces. To overcome this disadvantage, Binnig et al. developed AFM in 1985 [29].

By sensing the atomic forces between a sharp tip and the sample AFM provides the topographic images. Unlike in STM, AFM does not require the conducting surface. It is useful in the study of

the surface topography, electronic properties of the film, film growth, adhesion, friction, lubrication, dielectric and magnetic properties. This makes AFM a versatile tool to carry out the studies in the fields of surface science. Among the various SPM tools, STM [29] and AFM [30] are used to study LB films.

The schematic diagram of working principle of AFM is shown in figure 2.10. In AFM, the tip and cantilever are usually made up of silicon or silicon nitride (Si_3N_4). The tip is mounted on a cantilever that moves over the sample in a raster scan. The radius of the tip on the cantilever is few tens of nanometers. The back side of the cantilever is coated with a reflecting material like gold. The cantilever is illuminated by a laser light. The reflected light is collected on a quadrant photodiode.

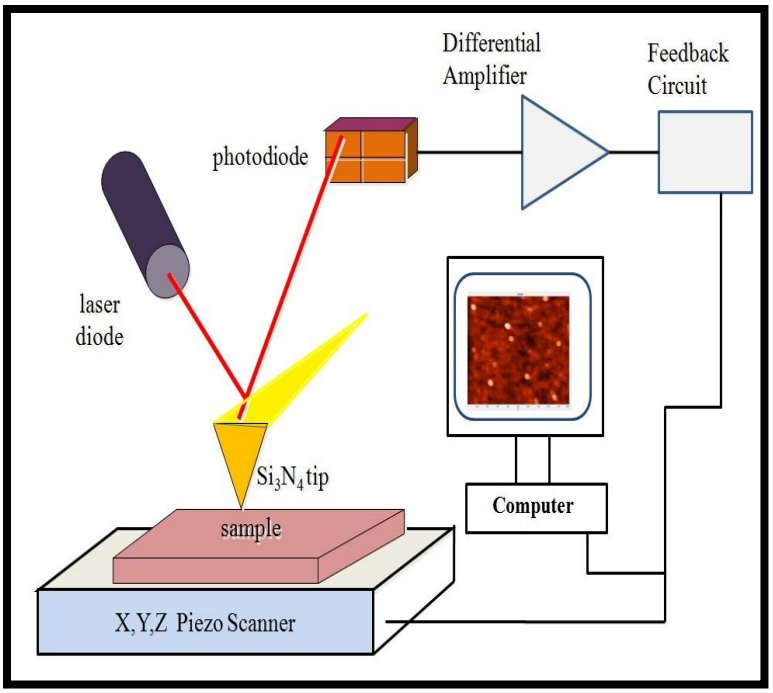

Figure 2.10: A schematic diagram showing the working principle of atomic force microscope.

The force between the tip and the sample is calculated from the deflection of cantilever. Due to the tip and sample interaction, there is a deflection in the tip. That deflection is monitored by measuring a distribution of light intensity in the photodiode. The deflection in the cantilever is given by Hooke's law, $F = -kz$ where F is the force between tip and sample, k is the stiffness of cantilever and z is the cantilever deflection. The amplitude and phase of oscillation of the tip change due to the interaction between tip and sample. The change in amplitude gives a

topographic image and change in phase gives the information about the chemical nature of the sample [29].

Depending on the interaction between the tip and the sample like Van der Waals attractive forces, electrostatic forces, magnetic forces, adhesion forces and frictional forces, there are many modes of AFM to characterize various properties of a sample like electrical [31], mechanical [32] and chemical [33] properties, in addition to the surface morphology characterization. The modes are: contact mode, noncontact mode, tapping mode.

In contact mode, the AFM tip is in direct contact with the sample surface. The force between the tip and sample surface is measured by feedback loop. In this mode, the interaction between the tip and sample surface is due to repulsive forces. This mode is also known as constant force mode. Here, the force between the tip and the sample is kept constant and a topographic image can be obtained by monitoring the bending of the cantilever. The contact mode also gives the information about lateral force between the tip and the sample.

In non-contact mode, long range attractive forces are used to monitor the tip - sample interaction. These attractive forces are weaker than the repulsive forces detected in the contact mode [34]. In the non-contact mode, the tip is oscillated at a distance from the sample. The oscillating tip never touches the sample surface.

In the tapping mode, the tip bounces up and down (taps) nearly to its resonant frequency on the sample surface with given amplitude and frequency. In this mode, the interaction between the tip and sample is dominated by the repulsive forces. Due to this interaction between the tip and the sample, the amplitude and phase of oscillation of the cantilever change. The change in amplitude can be used for obtaining the topography of the sample. Generally this mode is used for imaging soft and poorly immobilized samples.

AFM investigation of all the samples were carried out using commercial scanning probe microscope (model: Solver Pro, NTMDT).

2.3.2.2. Field Emission Scanning Electron Microscopy (FESEM)

In scanning electron microscope (SEM), generally electrons are generated by “heating” a tungsten filament (electron gun). The resolution of an SEM is therefore limited by the wavelength of electrons. In SEM, the electron source is focused into a fine point which is used for scanning the surface of the sample. The scanning electrons hit the sample surface and the

secondary electrons are emitted. These emitted secondary electrons are collected by a detector. The image of the sample is formed by using the information gathered from secondary electrons [35]. The main difference between the SEM and FESEM is the emitter type (thermionic emitter and field emitter, respectively). Thermionic sources have relative low brightness, evaporation of cathode material and thermal drift during operation. Field emission is one way of generating electron to avoid these problems. Field emission is the emission of electrons from the surface of a conductor caused by a strong electric field. A thin and sharp tungsten needle (tip diameter 10 - 100nm) is employed as a cathode. The field emission source reasonably combines with SEM. The acceleration voltage between cathode and anode is commonly ~ 0.5 kV to 30 kV, and the system requires a vacuum of ~ 10^{-6} Pa. The image quality is improved, due to the electron beam emitted by the field emission source which is 1000 times smaller than that of thermal electron gun in a standard microscope.

FESEM is a very important device for high resolution surface imaging in the fields of nanomaterial science. The FESEM gives the morphology of thin film at A/S interface. In our research work, we have used FESEM instrument from ZEISS, Sigma (RRI, Bengaluru) for obtaining the surface morphology of thin film at solid substrates.

2.3.2.3. UV-Vis Spectroscopy

The UV-Vis spectroscopy gives valuable information about material species and the band structure of the system. The UV-Vis spectrum reveals the absorption related to the surface plasmon resonance oscillation in the nanomaterials. Such data can be analyzed to elucidate the size and band structure of the nanomaterials [36]. We used double beam UV-Vis spectrophotometers from Jasco, Kyoto Japan (model V530), which is available in the central analytical laboratory of our institute. In spectrophotometer, tungsten (W-lamp) for the 1100 to 350 nm region and a deuterium (D_2 lamp) for the 350 - 200 nm are commonly used light sources supporting the 200 - 1100 nm wavelength range covered in it. The light detectors are Si-photodiodes with 0.2 nm resolution.

2.3.2.4. Fourier Transform Infrared (FTIR) Spectroscopy

FTIR spectroscopy is an important tool to detect the molecular species and its structural states. FTIR has been extensively used for detecting the molecular orientation in LB films of organic

molecules. FTIR is based on the interaction (vibrations of the atoms of a molecule) of the infrared (IR) radiation with sample (liquid/solid). In infrared spectroscopy, IR radiation is passed through a sample. Some of the IR radiation is absorbed by the sample and some of it is passed through (transmitted). The resulting IR spectrum represents a fingerprint of a sample with absorption peaks which correspond to the frequencies of vibrations between the bonds of the atoms making up the material. The FTIR spectrometer has IR source, a detector and Michelson interferometer. The source emits the IR rays and these rays enter the interferometer where the "spectral encoding" takes place and it is transmitted or reflected from the surface of the sample, depending on the type of analysis being accomplished. The specific frequencies of energy are absorbed, which are uniquely characteristic of the sample. The detector is used for detecting the changes in the IR radiation [37].

We have used FTIR from Perkin Elmer (model Frontier) in attenuated total reflectance (ATR) mode. The ATR crystal consists of an IR transparent material with a high refractive index and has polished surfaces. It operates by measuring the changes into contact with a sample. The infrared beam is directed onto ATR crystal with a high refractive index at an angle of typically 45° (relative to the crystal surface) and is totally reflected at the crystal to sample interface. The fraction of the light wave that reaches into the sample is called the evanescent wave. In those spectral regions where the sample absorbs energy, the evanescent wave will be attenuated. After one or several internal reflections, the IR beam exits the ATR crystal and is directed to the IR detector.

In our research work, we have used Perkin Elmer Frontier FTIR which is available in the analytical laboratory of Chemical Engineering department of our institute.

2.3.2.5. X-Ray Diffraction Technique

X-ray diffraction is used to investigate microscopic structure of the material. XRD is based on constructive interference of monochromatic X-rays and a crystalline sample [38]. The constructive interference occurs due to the interaction between the incident X-rays and sample. Distance between planes of the atoms can be calculated by applying Bragg`s law, $n\lambda = 2d \sin\theta$. The crystalline property of nanoparticle and the positional and orientational ordering in the liquid crystal (LC) phases can be investigated using X-ray diffractometer.

2.3.2.6. Current-Voltage Measurement

Electrical characterization of thin film of materials and devices were carried out using a Keithley source meter (model 2400-SCS). The charge - transport mechanism in the LB films was studied by recording current (I) - voltage (V) curves. For I-V characterization of LB film of nanoparticle and LCs, LB film was fabricated onto a 100 μm gap between two gold electrodes on Si wafer. The voltage is applied across the gold electrodes and the corresponding current is measured using the source meter.

2.4 Fabrication of Liquid Crystal Cell

Substrates prepared using the techniques as discussed earlier are used for the fabrication of LC cell. The LC cells were fabricated using these substrates in such a way that two substrates deopsited at same π_t are placed one above the other in such a manner that their deposition directions remain parallel to each other as shown in figure 2.11.

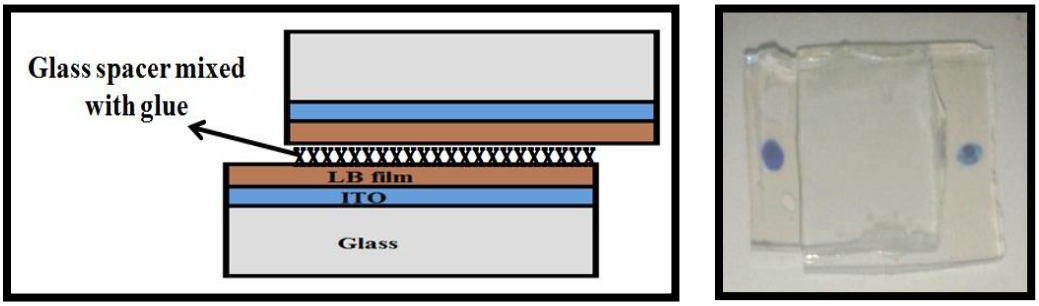

(a) (b)

Figure 2.11: (a) Schematic diagram of fabrication of liquid crystal cell (b)photograph of Liquid crystal cell.

A little gap is left at both ends so that electrical connections for application of the electric field can be made. The sides of LC cell are sealed using a special kind of glue viz. epoxy glue meant for liquid crystal displays (LCD) which does not react with LCs [39]. Cells of definite thickness were prepared using glass spacer. The sealed cell is cured for about an hour at 100°C. LC sample was filled in cells in isotropic phase through capillary action. The alignment of LCs in these cells was observed under a Polarizing Optical Microscope (POM).

2.5 Polarizing Optical Microscopy (POM)

Polarizing optical microscopy (POM) is an important technique in LC field and is used for

identification of different LC phases [40, 41]. In POM, there are two polarizers and the angle between polarizer and analyzer can be changed. The LC cell filled with sample is placed on the stage between two crossed polarizers of POM (Model OLYMPUS BX51). The LC textures were captured through a digital camera (AmScope FMA050) fitted onto POM and connected to a computer. A suitable software (Amscope) was used to obtain the images.

The alignment layer on the substrate plays a crucial role in determining the bulk orientation of LC molecules. In LCD devices, the substrates are treated with certain organic or inorganic film. The interaction between the LC molecules and the surface is strong enough to align the director in a particular direction at the boundaries. In an unaligned sample, the director $\hat{n}$ varies from point to point. In general the director is aligned either parallel or perpendicular to the plane of the glass substrate known as planar and homeotropic alignment. In planar state, the LC molecules lie parallel to the plane of substrate and exhibits color texture between crossed polarizer. In homeotropic alignment the long axis of the LC molecules is perpendicular to the substrate and looks uniformly dark between the crossed polarizer. The schematic diagrams of different alignment geometries of LCs are shown in figure 2.12.

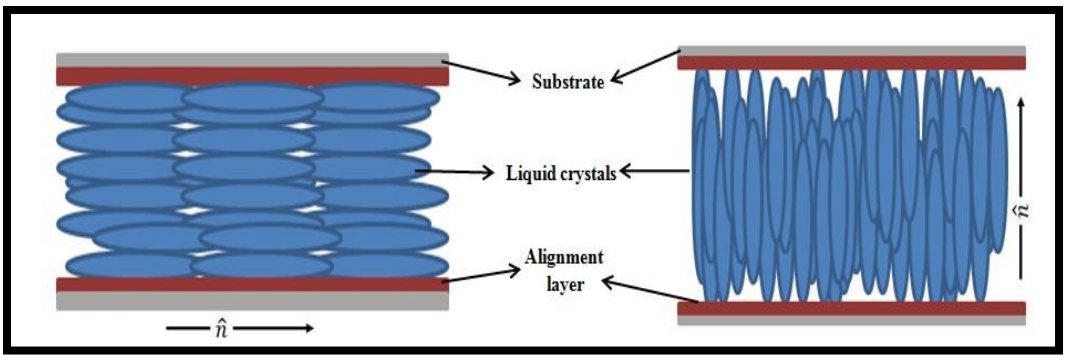

Figure 2.12: Schematic diagrams of the (a) planar and (b) homeotropic alignment of the LC molecules.

2.6 Dielectric Constant Measurement

For display device, dielectric constant (ε) is a very important material property as it determines the degree of coupling between applied electric field and LC molecules. Dielectric constant depends on the intrinsic properties of the material like distribution of the charges in the molecules and intermolecular interactions. Due to the anisotropic shape of LC molecules, the dielectric permittivity measured along the direction of long axis of LC molecules (ε||) is different from that measured perpendicular to the long axis of LC molecules (ε⊥). For the dielectric

measurement of LCs, ε|| and ε⊥ represent the dielectric constants measured with an electric field parallel and perpendicular to the director $\hat{n}$, respectively [39]. The dielectric constant (ε) is given by the ratio C_S /C_0 , where C_0 is the capacitance of the empty cell, and C_S is the capacitance of the cell filled with LC sample.

Most of LC materials are not free of ionic impurities and exhibit finite resistances. The equivalent electrical circuit of a LC cell can hence be considered to be a capacitor of capacitance (C_S) connected in parallel with resistor of resistance (R_S) (Figure 2.13(a)). A lock-in amplifier (Stanford Research System, SRS 830) is connected to the cell in series with a standard capacitor of capacitance value $C_m \sim 1\mu F$ to measure the impedance of the cell. C_m is chosen to be large, so that a large part of the voltage drops across the cell and only a small voltage is measured by lockin amplifier [39].

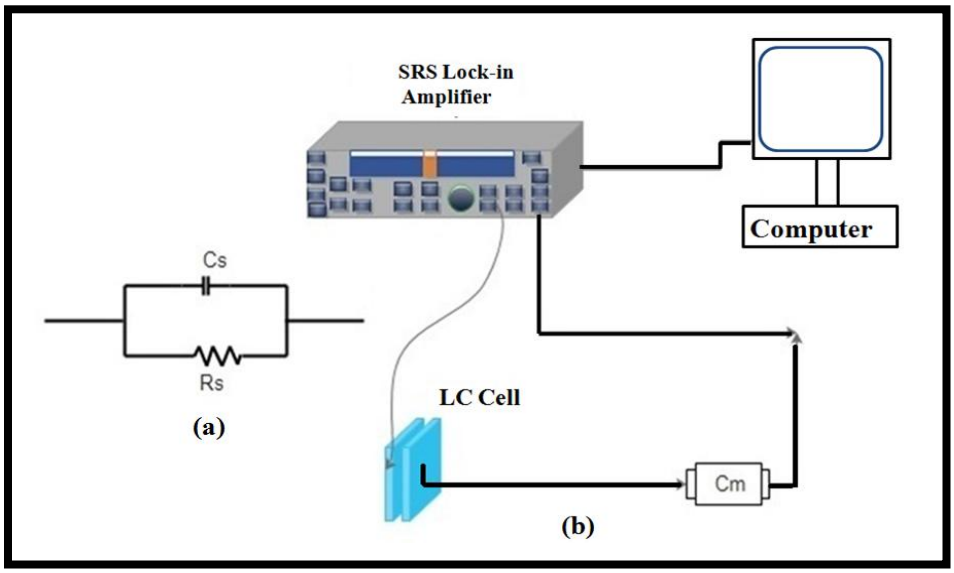

Figure 2.13: Schematic diagram of (a) electrical circuit equivalent of the LC cell and (b) the dielectric constant measurement set up.

2.7 Background and Literature Survey

Research on water-supported thin film dates back to the nineteenth century [42]. In this thesis, we describe the formation of stable LM of different LCs, nanomaterials and nanocomposites. These LM transfer onto different solid substrate and the films were characterized by different techniques. The thin films of LC exhibit interesting properties. The formation of nanostructure in the thin film is governed by molecular interaction and external parameters like temperature, surface density etc. The surface can be patterned and the nanostructures can be controlled by an

appropriate choice of molecules.

LB technique has been used for fabrication of thin films of different types of LC molecules and nanomaterials [1]. There are plenty of materials which can form stable LM (shown in table 2.3 and 2.4) and can be transferred onto solid substrates by LB technique. Conventionally, lyotropic LC (amphiphilic molecules), thermotropic LCs of different shape anisotropy form LM at the A/W interface and have been widely studied.

Table 2.3: Materials forming stable Langmuir Monolayer.

	Materials	**References**
Lyotropic Liquid crystal	Fatty acids	43-48
	Cholesterol and its derivatives	49-52
Thermotropic Liquid crystal	Rod shaped LC	53, 54-56
	Disk shaped LC	55,57 - 63
	Banana LC	64-69
	H Type LC	70-71

Amphiphilic molecules form a stable LM at an A/W interface and can be transferred onto solid substrates by LB technique. Stearic acid is the most commonly studied molecule. Monolayer of stearic acid exhibits a great stability. Deposition of stearic acid molecule at a different π (in different phases) on a substrate has shown interesting results [72-73]. The LB deposition of different types of amphiphilic molecule like pyramidic, bowl shaped, star like, disk like, spherical shaped and plate like amphiphilic molecules have been reported [74]. The steric effect and intermolecular interactions play an essential role in determination of their structural arrangement in thin films formed using these amphiphilic molecules. For a given amphiphilic molecule, deposition pressure, subphase composition and temperature can be varied in order to establish optimum LB deposition conditions [74].

The LM of a calamitic LC, octylcyanobiphenyl (8CB) has been studied and it is observed, that at collapse pressure molecules tend to align themselves in smectic multilayer [55]. To investigate the collapse of a monolayer of the 8CB, Xue et al. [56] employed surface balance measurements, ellipsometry and optical second-harmonic-generation technique .

Many compounds composed of disc-shaped molecules, known as discotic liquid crystal (DLC) exhibit stable LC phase. DLCs at A/W and A/S interface show interesting properties. There are numerous studies on the LM of the DLCs at the A/W interface and has been found that the molecular organizations within these monolayer which are quite different from those of classical amphiphilic molecule depend on the chemical nature of the disk-shaped cores [75]. Such systems are known to exhibit monolayer phases where the disk-plane of the molecules are either planar to the water surface (face-on conformation) or it is perpendicular to the water surface (edge-on conformation) [54, 59-63]. Thin films of DLCs find potential industrial application in the fields of opto-electronics and photovoltaic devices such as light emitting diodes [76-77], field-effect transistors [78], solar cells [79] and sensors [80].

Most of the research on bent-core (BC) molecules has been focused on the study of their organization in the mesomorphic phases. Thin films of simplest, three-ring, BC molecules were vacuum-deposited on mica substrates by Tang et al. (2005). Using AFM and Transmission Electron Microscopy (TEM), the investigation on the morphologies, structures and phase behavior of the films indicated the anti-ferroelectricity nature of the films [81]. A series of five-ring, BC molecules (same cores, different end-chains) were self-assembled on highly oriented pyrolytic graphite (HOPG) and studied using STM and well-organized stripes were observed [82].

The studies of LF of BC molecules have been focused on the behavior of such molecules at the A/W interface [68-69, 83-86]. In addition, a few promising results have been obtained in the study of the optical and electrical properties of the LB films of these molecules.

Kinoshita et al. studied the LM formed by a single BC molecule with long hydrophobic side chains. In 1998, they reported that LM and LB film could be formed from BC molecule. The LM of 1,3-phenylene bis[4-(((4-dodecylphenyl) imino) methyl) benzoate] was prepared by the LB technique. The molecular orientation in the LB films was investigated by using the surface second harmonic generation measurements and they found the optical symmetries and the nonlinear optical susceptibility of the BC molecular monolayer [64]. Blinov et al. investigated the dielectric, ferroelectric and antiferroelectric properties of LB films of similar BC molecules [65-67].

The LF of five different symmetric BCLCs was studied at A/W interface by Zou et al. in 2004. In that study both the core and the end-chains were varied but the molecular symmetry was

maintained. They observed that the properties of these layers are dependent on the type of molecules: the molecules with amphiphilic chains lie quite flat on the surface, the molecules with hydrophobic end chains formed multilayer structures [68]. LF of a symmetric BC molecule with hydrocarbon end chains and two chlorine atoms substituted on the central phenyl ring of the BC were characterized by isotherms, BAM and surface potential measurement by Wang et al. in 2006. These LFs were found to be optically anisotropic [69].

In 2009, Scheres et al. for the first time have reported the covalently attached BC mesogen to a silicon surface in order to achieve monolayer. These studies showed that interactions between the molecules and molecule-substrate interactions, both play important roles in the formation of uniform films [87]. In 2010, Wang et al. fabricated the Inverse Langmuir-Schafer (ILS) films of BC molecules. They found that ILS films of a symmetric BC molecule can serve as effective planar alignment layer for a nematic bent-core LC cell [88-89]. The BCLC can be useful in switching devices, storage device [90], electromechanical devices [91], electro-optical display devices [92].

Other non-traditional materials like nanoparticles, quantum dots (QDs) and carbon based nanomaterials form LM and can be transferred onto different solid substrates by LB technique. Synthesis and processing of nanomaterials and nanostructures are the essential aspects of nanotechnology. Studies on new physical properties and applications of nanomaterials and nanostructures are possible only when nanostructured materials are made available with desired size, morphology, microstructure and chemical composition. Such nanomaterials when spread on the water surface yield a stable LM and show a variety of phases and can be deposited onto solid substrate by using the LB technique. Table 2.4 shows examples of different nanomaterials and nanostructures forming stable LM.

A composite thin film of nanomaterials can also be fabricated by LB deposition technique. Such composite thin films can be potentially employed for several technological applications [2, 8]. Table 2.5 shows examples of different nanocomposites forming stable LM. The fabrication of nanocrystalline films and the significant triumph of the nano super structure creation have provided prospective in the field of nanomaterials with superior performance for the applications in advanced magnetic recording media, light-emitting devices, biological tags, catalysts and solar cells [127-130].

Table 2.4: Nanomaterials forming stable Langmuir Monolayer.

	Materials	**References**
Nanoparticles	CdSe	93
	Fe_3O_4	94
	Ag	95-98
	Au	99-101
	Pt	102
	TiO_2	103
Nanorods	Au, $BaCrO_4$ and $BaWO_4$	104
Nanowires	Ag	105
	Si	106
	$Mo_3Se_3^-$	107
	ZnSe	108
	WO_x	109
	Ge	110
Quantum dots (QDs)	quantum dots (QDs)	111-113
Carbon based nanomaterials	carbon nanotubes (CNT)	114-118
	graphene	119-121

Table 2.5: Different nanocomposites forming stable Langmuir Monolayer.

Materials	**References**
Multiwalled carbon nanotubes with poly(*o*-anisidine) and o-toluidine	122-123
poly(maleic monoester) with Fe_3O_4 nanoparticles	124
HAT5 with TiO_2 nanoparticles	125
Polyaniline with TiO_2	126

2.8 Gaps in existing research

From device point of view, rod shaped LC have been a major interest of research community for a long time. BCLC and DLCs can be suitable candidates from the point of fabrication of many devices. The fabrication of nanocomposites of these LCs is potential candidates from the point of future upcoming switching devices. There are very few reports on such research reported till now. Alignment layer in any LC based device is the main driving point which decides the switching behavior on applying and removing external electric and magnetic fields. LB technique is the only technique in which a thin film of these LCs or their nanocomposites and any other nanomaterials can be deposited onto substrates in a highly controlled manner. By depositing thin films at different surface pressure we can have a control over the molecular conformation and their density at the substrate. LC cells fabricated by LB and ILS film deposited substrates can influence the overall performance of the material as the anchoring can play a major role in switching devices. LC displays are fabricated in many geometries viz, planar, homeotropic, twisted nematic, in plane etc [39, 131]. Usually different aligning agents are used for fabrication of such cells of different geometries. Aligning DLC and BCLC using these commercially available agents most often do not result in monodomain samples. Dielectric as well as electro - optic measurements need monodomain sample and even from device point of view, monodomain sample would be the best candidate. By depositing the host BCLC or DLC or their nanocomposites at different π will result in different orientation at substrate. The possibilities of obtaining monodomain samples become possible by using these LB and ILS deposited substrate. As there are not many studies available in literature, so our efforts towards these studies will throw more insight into such possibilities which would be of importance from device fabrication point of view.

The prime objective of the thesis is to fill this gap to an extent, in existing investigations. Objectives of our research work are the following.

- ❖ Surface manometry of LCs and nanocomposites
- ❖ Fabrication of thin films of LCs and nanocomposites on different kinds of substrates.
- ❖ Characterization of these thin films on solid substrates using different techniques.
- ❖ Applications of such films primarily as alignment layers for aligning bulk LCs in the LC cell.

Our studies are focused on the LF of BC molecules on solid substrates as an aligning layer for the alignment of LCs. We can control the alignment of LC using the LM as aligning layer by depositing on substrate at various π_t. LC cells were fabricated using these LB and ILS film deposited substrates. Alignments of LC in these cells were observed under a POM. Our studies are relevant for the alignment of LCs in device fabrication and display devices.

A brief introduction of the LCs and LC phases exhibited by mesogens with different shape and nanocomposites are discussed in chapter 1. Chapter 2 deals with the experimental methods for the fabrication of thin film of LCs and nanocomposites and characterization techniques. The fabrication of LC cell has been discussed.

In chapter 3, we present the results of our investigation on a mixture of anatase and rutile (ca. 80:20) phases of titanium dioxide (TiO_2) nanoparticles which are in the form of 2D layer fabricated using the LB technique. The LB film of TiO_2 nanoparticles was characterized using AFM, FESEM, FTIR UV-Vis spectroscopy. The LB films deposited at higher π_t reveal a higher surface coverage, thereby yielding a higher density of crystalline defect sites. The UV-Vis spectroscopy reveals that with the increase in π_t of deposition the optical property more closely approaches that of the bulk sample. The charge-transport mechanism in the LB film of TiO_2 nanoparticles was studied. We observed an Arrhenius behavior of charge transport for LB film of TiO_2 nanoparticles.

Development of sensors for detecting various chemical species in many industrial, medicinal, environmental pollution control and commercial applications is in great need. In this regard, TiO_2 nanoparticle is a promising candidate for sensing application due to its catalytic behavior, stability at high temperature and high tolerance for harsh environments. Both the LB and spin coated film of TiO_2 nanoparticles are employed for ethanol (CH_3 CH_2OH) sensing applications. The LB film of TiO_2 nanoparticles shows an appreciable and recoverable response toward ethanol sensing as compared to the thick film obtained using the spin-coating technique. The enhanced sensing performance of the LB film is due to the availability of the large surface density of crystalline defect sites for ethanol adsorption and subsequent reduction.

In this chapter, we also present the investigations on doped DLC with TiO_2 nanoparticles. We doped DLC hexa-alkoxytriphenylene (HAT5) with TiO_2 nanoparticles. We found a condensation effect on the monolayer of HAT5+TiO_2 nanocomposites due to the presence of TiO_2

nanoparticles. We transferred the LB film of pure HAT5 and HAT5+TiO_2 nanocomposites onto HPL substrates characterized using AFM, UV-Visible spectroscopy and I-V measurement. We observed reduction in the energy gap of the HAT5 system in a controlled manner on doping the system with TiO_2 nanoparticles. We observed that the even with 10 wt.% TiO_2 nanoparticles doped into HAT5 DLC lead to a change the charge-transport behavior of HAT5. The conductivity and activation energy (E_A) of HAT5+TiO_2 nanocomposites increases with increasing concentration of TiO_2 nanoparticles. The charge-transport mechanism in thin film of HAT5 can be controlled precisely by altering the π_t of LB film deposition of HAT5+ TiO_2 nanocomposites

In Chapter 4, we present our investigation on the carboxylated graphene (G-COOH) doped with a DLC, at interfaces. The surface manometry on HAT5, G-COOH and their composites shows interesting results. The LM of G-COOH exhibits gas and a liquid-like phase. Structurally similar organic DLC molecule HAT5 was incorporated in the monolayer matrix of G-COOH. The surface manometry of such mixed monolayer system indicated the evidence of repulsive interaction or complex formation between the components. The LB films of G-COOH+HAT5 nanocomposites were deposited on solid substrate and characterized using UV-Vis spectroscopy. The UV-Vis spectroscopy on the LB films of the nanocomposite reveals red shift in the characteristic peak. The charge - transport mechanisms in the LB film of G-COOH+HAT5 nanocomposites were studied. The in-plane conductivity of the LB films of the nanocomposites enhances as compared to that of pure components. The surface morphology obtained using FESEM shows uniform film over the 2D surface. The signature of both HAT5 and G-COOH were seen from the images.

LC cells were fabricated by using LB and ILS film of G-COOH+HAT5 nanocomposites deposited indium tin oxide (ITO) coated glass plates. A DLC decyloxytriphenylene (TP10) exhibiting rectangular columnar phase was filled in these LC cells. Dielectric constant measurement was carried out. The dielectric measurements indicate that the LB film of the nanocomposites provide better alignment of discotic liquid crystals as compared to some other mechanism of obtaining the alignment layer in the LC cells.

In chapter 5, we present result of investigation on the effect of different stress on the morphology of the LB films of stearic acid deposited at the same π_t with different orientation angle of

substrate normal with respect to the monolayer compression direction. The morphology of LB film of stearic acid was studied using AFM. The LB films show a morphological transformation from granular texture with large and compact grains to granular texture with very small grains to completely uniform texture. We present the effect of surface morphology of LB films of stearic acid deposited at a same π_t, but in different direction of substrate normal relative to the compression direction on the alignment of a nematic LC (NLC).

The LC cells were fabricated using such LB films deposited substrates. Alignments of NLCs in these cells were observed under a POM. These LC cells show different alignments (planar to homeotropic) due to difference in morphology of stearic acid in the LB films. The transmittance intensity measurement was also performed.

In chapter 6, we have presented the results of detailed study of a stable monolayer of different unsymmetrical BC molecules4-((4-(tetradecyloxy)benzoyl)oxy)phenyl 3-((4-((4-cyanobenzoyl) oxy)benzoyl) oxy) benzoate (we referred this molecule as B-CN),4-((4-(tetradecyloxy) phenoxy) carbon) phenyl 3-((4-((nitrobenzoyl) oxy) benzoyl)oxy) benzoate (we referred this molecule as BN1) and 4-((4-(octadecyloxy) phenoxy) carbonyl) phenyl 3-((4-((4-nitrobenzoyl)oxy) benzoyl) oxy) benzoate (we referred this molecule as BN2) at A/W interface. The LM of B-CN, BN1 and BN2 at A/W interface were found to be stable.

We transferred the LM of B-CN molecule onto Si/SiO_2substrate using both LB and ILS method at different π_t and characterized them using AFM and FESEM. Both LB and ILS film of B-CN molecule on Si/SiO_2 substrate was found to be uniform. The LB film of BN1 molecules on Si/SiO_2 substrate shows the uniform texture at different π_t. The topographic images of LB film of BN2 deposited on Si/SiO_2 substrate shows triangular shaped domains with some defects With increases in π_t, the density of these triangular shaped domains increases and film becomes more uniform. LB film of banana molecules deposited onto ITO plate shows granular texture with partial bilayer formation of the molecules on substrate.

Using the force - distance spectroscopy, the adhesion force between LB film of BN2 molecules on Si/SiO_2 substrate with hydrophilic Si/Si_3N_4 tip and hydrophobic functionalized tip was calculated. On the basis of the value of adhesion force we propose a model for the orientation of BN2 molecules in the LB film on substrate.

Both LB and ILS film of BCLCs on different substrates (ITO, microscopic glass plate) were

employed as alignment layer for the fabrication of LC cell. The alignment of bulk NLC is studied using POM.

The ILS film of B-CN molecules on ITO and glass plates exhibit the planar alignment of NLC at lower π_t =10 mN/m and at higher π_t = 30 mN/m, it shows homeotropic alignment. The uniform LB film of BN1 molecules deposited onto ITO substrate supports the homeotropic alignment whereas the LB film of BN2 molecule supports the planar alignment of NLC in the LC cell.

In chapter 7, we investigated the surface behavior of a mixed monolayer system of two different shape anisotropic LC molecules viz 4-octyloxy-4-cyanobiphenyl (8OCB calamitic LC) and bent-core ((5-cyano-1, 3-phenylene) bis(oxy)) bis(carbonyl))bis(2-fluoro-4,1-phenylene) bis(4'-nonyl-[1,1'-biphenyl]-4-carboxylate(referred as 5CNBC). The $\pi - A_m$ isotherms of the mixed system were recorded by varying mole fraction (X_M) of 8OCB in 5CNBC. The variation of excess area (A_{ex}) and excess Gibbs free energy versus X_M (in figure 8.4) shows negative values for all composition in the π range of 1 to 3 mN/m. This suggests the system to be miscible and stable. The miscibility may arise due to attractive interaction between the component molecules. The LB films of the mixed monolayer system were deposited and the morphology was obtained using AFM. The AFM image shows the miscible nature of the components on the solid substrates.

These LB films were employed as alignment layer for the fabrication of LC cell. The alignment of bulk 8OCB LC is observed using POM and the dielectric measurement was performed. The value of dielectric constant of 8OCB measured in LC cell treated with LB film of 5CNBC molecules in L_2 phase is enhanced. This indicates homeotropic alignment of 8OCB. The nematic phase of 8OCB is suppressed in LC cells prepared using LB film of mixed monolayer.

In summary, we developed the protocols to control the alignment of LCs by fabricating LB and ILS films of different LCs, nanoparticles and their nanocomposites on a variety of substrates under extremely controlled experimental conditions. The developed protocol for aligning LCs will be useful for device applications.

References

1. M. C. Petty, "*Langmuir-Blodgett Films: An Introduction",* Cambridge University Press: Cambridge, U. K. **1996.**
2. G. Roberts, Ed. "*Langmuir-Blodgett Films*", Plenum Press, New York, **1990.**
3. J. D. Swalen, D. L. Allara, J. D. Andrade, E. A. Chandross, S. Garoff, J. Israelachvili, T. J. McCarthy, R. Murray, R. F. Pease, J. F. Rabolt, K. J. Wynne, H. Yu, Langmuir 3, 932, **1987.**
4. M. Breton, J. Macromol, Sci., Rev. Macromol. Chem. C, 21, 61, **1981.**
5. R. K. Gupta and V. Manjuladevi, "*Molecular Interactions at Interfaces*", InTech, Croatia, Ch 4, **2012**.
6. M. C. Petty, "*Thin Solid Films"*, 210, 417, **1992**.
7. I. Langmuir, K. B. Blodgett, Kolloid-Z, 73, 258, **1935.**
8. K. B. Blodgett, J. Am. Chem. Soc. 57, 1007, **1935.**
9. G. L. Gaines, " *Insoluble Monolayers at Gas-Liquid Interfaces*", Wiley, New York, **1966**.
10. S. Kundu, D. Langevin, Colloids and Surfaces A: Physicochemical and Engineering Aspects 325, 81, **2008.**
11. R. E. Heikkila, D. W. Deamer, D. G. Cornwell, Journal of Lipid Research 11, 195, **1970.**
12. G. Gompper, M. Schick, C. Domb, J. L. Lebowitz, editors, "*Self-Assembling Amphiphilic Systems"*, Phase Transitions and Critical Phenomena, Academic Press, 16, **1994.**
13. A. W. Adamson, "*Physical Chemistry of Surfaces*", Wiley-Interscience, New York, **1990.**
14. H. Mohwald, Ann. Rev. Phys. Chem. 41, 441, **1990.**
15. H. M. McConnell, Rev. phys. Chem. 42, 171, **1991.**
16. H. E. Ries, Nature 281, 287, **1979.**
17. R. Seoane, J. Minones, O. Conde, J. Minones, Jr., M. Casas, E. Iribarnegaray, J. Phys. Chem. B 104,32, 7735, **2000**.
18. M. J. Hwang, K. Kim, Langmuir 15, 3563, **1999.**
19. C. Mc. Fate, D. Ward, J.O.III, Langmuir 9 1036, **1993.**
20. K. S. Birdi, D. T. Vu, Langmuir 10, 623, **1994.**
21. C. M. Knobler , R. C. Desai, A. Rev. phys. Chem. 43, 207, **1992.**
22. H. Schwickert, G. Strobl, Kimmig, J. Chem. Phys. 95, 2800, **1991**.
23. V. M. Kaganer, H. Mohwald, and P. Dutta, Rev. Mod. Phys. 71, 779, **1999.**

24. G. A. Overbeck, D. Honig, D. Mobius, Langmuir 9, 555, **1993.**
25. E. Teer, C. M. Knobler, S. Siegel, D. Vollhardt, G. Brezesinski, J. Phys. Chem. B 104, 10053, **2000.**
26. S. Henon, J. Meunier, Rev. of Sci. Inst. 62, 936, **1991.**
27. D. Honig, D. Mobius, J. Phys. Chem. 95, 4590, **1991**
28. G. Binnig, H. Rohrer, Ch. Gerber, E. Weibel, Phys. Rev. Lett. 49, 57, **1982.**
29. G. Binnig, C. F. Quate, C. Gerber, Phys. Rev. Lett. 56, 930, **1986.**
30. Q. Huo, S. Russev, T. Hasegawa, J. Nishijo, J. Umemura, G. Puccetti, K. C.Russell, R. M. Leblanc, J. Am. Chem. Soc. 122, **2002.**
31. C. Ionescu-Zanetti, A. Mechler, S. A. Carter, R. Lal, Adv. Mater. 16, 385, **2004.**
32. E. W. Wong, P. E. Sheehan, C. M. Lieber, Science 277, 1971, **1997**.
33. Y. Sugimoto, P. Pou, M. Abe, P. Jelinek, R. Perez, S. Morita, O. Custance, Nature 446, 64, **2007.**
34. V. J. Morris, A. R. Kirby, A. P. Gunning, "*Atomic Force Microscopy for Biologists"*, Imperial College Press: London, **1999**.
35. T. Pradeep, "*NANO:The Essentials understanding Nanoscience and Nanotechnology"* McGrawHill, New Delhi, **2007.**
36. D. A. Skoog, F. J. Holler, S.R. Crouch *"Principles of Instrumental Analysis*" 6th ed. Thomson Brooks Cole.,169, **2007**.
37. P.R.G.J.A.D. Haseth, "*Fourier Transform Infrared Spectrometry"*, Wiley-interscience, 1656, 3, **1986**.
38. D. M. Moore, Jr. R. C. Reynolds, "*X-Ray diffraction and the identification and analysis of clay minerals"* 2nd ed. Oxford University Press, New York, **1997.**
39. ManjulaDevi V. "*Experimental Studies on Phase Diagrams of Liquid Crystals*" [Ph.D. Thesis], Raman Research Institute, Bangalore, **2004**
40. I. Dierking, Textures of Liquid Crystals 33, **1999**.
41. A.J. Nicastro, American Laboratory 14, 12, **1982**
42. A. Pockels, Surface Tension Nature 43, 437, **1891.**
43. J. B. Peng, G. T. Barnes, I. R. Gentle, Adv. Coll. Inter. Sci. 91, 163, **2001.**
44. K. Takeshi, J. Umemura, T. Takenaka, Langmuir 5, 1378, **1989.**
45. G. Veale, I. R. Girling, I. R. Peterson, Thin Solid Films 127, 293, **1985.**

46. S. Ye, H. Noda, S. Morita, K. Uosaki, M. Osawa, Langmuir 19, 2238, **2003**.
47. F. Kimura, J. Umemura, T. Takenaka, Langmuir 2, 96, **1986.**
48. S. Ye, H. Noda, T. Nishida, S. Morita, M. Osawa, Langmuir 20, 357, **2004.**
49. R. K. Gupta, K. A. Suresh, Euro. Phys. J. E 14, 35, **2004**.
50. M. Zimple, G. Sumana, S. K. Arya, S. P. Singh, V. Gupta, B. D. Malhotra, Langmuir 23, 13188, **2007**.
51. O. Hitoshi, R. Honjo, H. Endo, T. Imakubo, M. Izumi, Thin Solid Films, 518, 596, **2009.**
52. M. Tsuyoshi, S. Shinoda, T. Nakanishi, J. P. Hill, K. Fujii, T. N. Player, H. Tsukube, K. Ariga, J. Ame. Chem. Soc. 128, 14478, **2006.**
53. M. F. Danier, O. C. Lettington, S. M. Small, Thin Solid Films 99, 61, **1983.**
54. R. K. Gupta, V. Manjuladevi , C. Karthik,, S. Kumar, J. Phys. conference series 417, 012068, **2013**.
55. A. Bhattacharyya, K. A. Suresh, Europhys. Lett. 41, 641, **1998.**
56. J. Xue, C. S. Jung, M. W. Kim, Phys. Rev. Lett. 69, 474, **1992.**
57. Y. Tabe, N. Shen, E. Mazur, H. Yokoyama, Phys. Rev. Lett. 82, 759, **1999.**
58. F. Rondelez, D. Koppel, B. K. Sadashiva, J. Phys. (Paris), 43, 1361, **1982**.
59. A. Albrecht, W. Cumming, W. Kreuder, A. Laschewsky, H. Ringsdorf, Col. Polym. Sci. 264, 659, **1986**.
60. N. C. Maliszewskyj, P. A. Heiney, J. K. Blasie, J. P. McCauley Jr., A. B. Smith III, J. Phys. II (France) 2, 75, **1992.**
61. D. Gidalevitz, O. Y. Mindyuk, P. A. Heiney, B. M. Ocko, P. Henderson, H. Ringsdorf, N. Boden, R. J.Bushby, P. S. Martin, J. Strzalka, J. P. McCauley Jr., A. B. Smith III, J. Phys. Chem. B 101, 10870, **1997**.
62. N. C. Maliszewskyj, P. A. Heiney, J. Y. Josefowicz, J. P. McCauley Jr., A. B. Smith III, Science 77, 264, **1994.**
63. A. Nayak, K. A. Suresh, S. K. Pal, S. Kumar, J. Phys. Chem. B 11, 11157, **2007**.
64. Y. Kinoshita, B. Park, H. Takezoe, T. Niori, J. Watanabe, Langmuir 14, 6256, **1998.**
65. L. M. Blinov, A. R. Geivandov, V. V. Lazarev, S. P. Palto,S. G. Yuding, G. Pelzl, W. Weissflog, Appl. Phys. Lett. 87, 241913, **2005.**
66. L. M. Blinov, P. Palto, V. B. Lazarev, A. R. Geivandov, S. G. Yuding, Crystallography, 51, 843 **2006.**

67. A. R. Geivandov, S. P. Alto, S. G. Yudin, L. M. Blinov, G. Pelzl, W. Weissflog, Ferroelectrics, 344, 1, 3 **2006.**
68. L. Zou, J. Wang, V. J. Beleva, E. Kooijman, S. V. Primak, J. Risse, W. Weissflog, A. Jakli, E. K. Mann, Langmuir 20, 2772, **2004.**
69. J. Wang, L. Zou, A. Jakli, W. Weissflog, E. K. Mann, Langmuir 22, 3198, **2006**.
70. C. Karthik, A. Gupta, A Joshi, V. Manjuladevi, R. K. Gupta, M. Varia, AIP Conference Proceedings, 1591, 1036, **2014**.
71. B. Kumar, A. K. Prajapati, M. C. Varia, K. A. Suresh, Langmuir 25, 839, **2008.**
72. S. Ye, H. Noda, S. Morita, K. Uosaki, M. Osawa, Langmuir 19, 2238, **2003.**
73. S. Ye, H. Noda, T. Nishida, S. Morita, M. Osawa, Langmuir 20, 357, **2004.**
74. A. Angelova, R. Ionov, Langmuir 12, 5643, **1996.**
75. D. Janietz, Langmuir 13, 305, **1997.**
76. G. Lussem, J. H. Wendroff, Polym. Adv. Technol. 9, 443, **1998.**
77. I. Seguy, P. Jolinat, P. Destruel, J. Farenc, R. Mamy, H. Bock, J. Ip, T. P. Nguyen, J. Appl. Phys. 89, 5442, **2001**.
78. N. Stutzmann, R. H. Friend, H. Sirringhaus, Science 299, 1881, **2003.**
79. L. Schmidt-Mende, A. Fechtenkotter, K. Mullen, E. Moons, R. H. Friend, J. D. MacKenzie, Science 293, 1119, **2001**.
80. N. Boden, R. J. Bushby, J. Clements, B. Movaghar, J. Mater. Chem. 9, 81, **1999.**
81. Y. Tang, Y. Wang, X. Wang , S. Xun , C. Mei, L. Wang, D. Yan, J. Phys. Chem. B 109, 8813, **2005**.
82. J. R. Gong, L. J. Wan, J. Phys. Chem. B 109,18733, **2005.**
83. T. Yamamoto, S. Oguchi, T. Manaka, M. Iwamoto, Thin Solid Films 499, 242, **2006.**
84. T. Yamamoto, T. Manaka, M. Iwamoto, Colloids and Surfaces A: Physicochem. Eng. Aspects 154, 284, **2006**.
85. N. Duff, L. Wang , E. K. Mann, D. J. Lacks, Langmuir 22, 9082, **2006.**
86. N. Duff, E. K.Mann, D. J. Lacks, Langmuir 24, 4456, **2008.**
87. L. Scheres, R. Achten, M. Giesbers, L.C.P.M. de Smet, A. Arafat, E. J. R. Sudholter, A.T.M. Marcelis, H. Zuilhof, Langmuir 25, 1529, **2009.**
88. J. Wang, L. Qiu, A. Jakli, W. Weissflog, E. K. Mann, Liquid Crystal 37, 1229, **2010**.
89. W. Iglesias, T. J. Smith, P. B. Basnet, S. R. Stefanovic, C. Tschierske, D. J. Lacks, A. Jakli,

E. K. Mann, Soft Matter 7, 9043, **2011**.

90. A. Jakli, D. Kruerke, H. Sawade, L. C. Chien, G. Heppke, Liquid Crystal 29, 377, **2002.**
91. A. Jakli, D. Kruerke, G. G. Nair, Phys. Rev. E 67, 051702, **2003**.
92. Y. Tong, Y. Wang, G. Wang, H. Wang, L. Wang, D. Yan, J. Phys. Chem. B 108, 12921, **2004.**
93. B. O. Dabbousi, C. B. Murray, M. F. Rubner, M. G. Bawendi, Chem. Mater. 6, 216, **1994.**
94. T. Fried, G. Shemer, G. Markovich, Adv. Mater. 13, 1158, **2001.**
95. L. Yu, G. L. Liu, L. P. Lee, Nano lett. 5, 5, **2005**.
96. C. P. Collier, R. J. Saykally, J. J. Shiang,S. E. Henrichs, J. R. Heath, Science 277, 1978, **1997.**
97. C. Xue, X. Chen, S. J. Hurst, C. A. Mirkin, Adv. Mater. 19, 4071, **2007.**
98. A. Tao, P. Sinsermsuksakul, P. Yang, Nature Nanotechnology. 2, 435, **2007.**
99. R. K. Gupta, K. A. Suresh, S. Kumar, Phys. Rev. E 78, 032601, **2008.**
100. S. Paul, P. Shashi, C. Pearson, A. Molloy, M. A. Cousins, M. Green, S. Kolliopoulou, P. Dimitrakis, P. Normand, D. Tsoukalas, M. C. Petty, Nano Lett. 3, 533, **2003**.
101. J. R. Heath, C. M. Knobler, D. V. Leff, J. Phys. Chem. B 101, 189, **1997.**
102. H. Song, F. Kim, S. Connor, G. A. Somorjai, P. Yang, J. Phys. Chem. B 109, 188, **2005.**
103. K. Choudhary, V. Manjuladevi, R. K. Gupta, P. Bhattacharyya, A. Hazra, S. Kumar, Langmuir 31,1385, **2015.**
104. P. Yang, F. Kim, Chem. Phys. Chem. 3, 503, **2002.**
105. A. Tao, F. Kim, C. Hess, J. Goldberger, R. R. He, Y. G. Sun, Y. N. Xia, P. D. Yang, Nano Lett. 3, 1229, **2003.**
106. D. Whang, S. Jin, Y. Wu, C. Lieber, Nano Lett. 3, 1255, **2003**.
107. F. Kim, S. Kwan, J. Akana, P. Yang, J. Am. Chem. Soc. 123, 4360, **2001.**
108. S. Acharya, A. B. Panda, N. Belman, S. Efrima, Y. A. Golan, Adv. Mater. 18, 210, **2006.**
109. Y. S. Jong, L. J. Wan, S. Yung-Eun, J. Y. Hwa, C. H. Goo, K. D. Kyung, Appl. Phys. Lett. 90, 173126, **2007.**
110. D. Wang, Y. L. Chang, Z. Liu, H. Dai, J. Am. Chem. Soc. 127, 11871, **2005.**
111. A. Marc, M. A. Petruska, S. A. Crooker, V. I. Klimov, J. Phys. Chem. B 107, 13782, **2003**.
112. B. O. Dabbousi, C. B. Murray, M. F. Rubner, M. G. Bawendi, Chem. Mat. 6, 216, **1994**.

113. A. Milekhin, M. Friedrich, D. R. T. Zahn, L. Sveshnikova, S. Repinsky, App. Phys. A 69, 97, **1999.**
114. M. Poonia, R. K. Gupta, V. Manjuladevi, S. K. Gupta, J. Akhtar, J. Nanopart. Res. 16, 1, **2014**.
115. G. Yinzhong, N. Minami, S. Kazaoui, J. Peng, M. Yoshida, T. Miyashita, Physica B: Cond. Matt. 323, 235, **2002**.
116. K. Vojislav, G. S. Duesberg, J. Muster, M. Burghard, S. Roth, Chem. Mat. 10, 2338, **1998**.
117. K. Yeji, N. Minami, W. Zhu, S. Kazaoui, R. Azumi, M. Matsumoto, Jap. J. App. Phys. 42, 7629, **2003.**
118. X. Li, L. Zhang, X. Wang, I. Shimoyama, X. Sun, W. S. Seo, H. Dai, J. Am. Chem. Soc. 129, 4890, **2007.**
119. L. Xiaolin, G. Zhang, X. Bai, X. Sun, X. Wang, E. Wang, H. Dai, Nat. Nanotech. 3, 538, **2008**.
120. Z. Qingbin, W. Hing, X. Lin, N. Yousefi, K. K. Yeung, Z. Li, J. K. Kim, ACS Nano 5, 6039, **2011**.
121. K. Jaemyung, L. J. Cote, F. Kim, W. Yuan, K. R. Shull, J. Huang, J. Ame. Chem. Soc. 132, 8180, **2010.**
122. B. Valter, M. K. Ram, C. Nicolini, Langmuir 18, 1535, **2002.**
123. B. Valter, S. Carrara, M. K. Ram, C. Nicolini, Langmuir 20, 969, **2004.**
124. D. K. Lee, Y. S. Kang, C. S. Lee, P. Strove, J. Phys. Chem. B 29,106, 7267, **2002**
125. C. Karthik, K. Choudhary, A. Joshi, A. Gupta, V. Manjuladevi, R. K. Gupta, S. Kumar, Adv. Sci. Lett. 20, 1138, **2014.**
126. G. K. Bhular, R. Kaur, K.K. Raina J. Appl. Polym. Sci. 132, 41386, **2015**.
127. H. P. Zhou, C. Zhang, C. H. Yan, Langmuir 25, 12914, **2009.**
128. S. Coe, W. K. Woo, M. Bawendi, V. Bulovic, Nature 420, 800, **2002**.
129. J. M. Nam, C. S. Thaxton, C. A. Mirkin, Science 301, 1884, **2003.**
130. W. U. Huynh, J. J. Dittmer, A. P. Alivisatos, Science 295, 2425, **2002.**
131. J. Cognard, Molecular Crystal and Liquid Crystal Supp. 1, 1, **1982.**

Chapter - 3

Ultrathin Films of TiO_2 Nanoparticles and Discotic Liquid Crystal Doped with TiO_2 Nanoparticles

3.1 Introduction

Titanium dioxide (TiO_2) is considered to be a versatile material exhibiting interesting electrical and optical properties. It can be utilized for the development of applications, namely, gas sensors, solar cells, photocatalytic devices and optical coatings for filters and waveguides [1, 2]. TiO_2 is one of the ideal functional materials for gas-sensing applications because of its catalytic behavior, stability at high temperature and high tolerance for harsh environments [3].

The most abundantly available forms of TiO_2 are anatase and rutile [4]. Because of lower resistance and a strong response to gas adsorbents, the anatase phase can be used for gas-sensing applications; however it is unstable at higher temperature. The rutile phase exhibits stable semiconducting behavior at higher temperature; however, it is less sensitive to gas adsorbents. Due to the possibility of separating electrons and holes at the interface between the phases, mixed-phase of TiO_2 can be more effective than the single phase. At the transition point between the two phases of TiO_2, a rapid transfer of electrons can occur, and thereby the mixed phase creates a catalytic hot spot at the rutile - anatase interface [5]. It was suggested that the morphology of the hot-spot nanoclusters of mixed-phase titania is such that the rutile crystallites are interwoven with the anatase crystallites [5, 6]. Such rutile - anatase interface can be considered to be crystalline defects.

In this chapter, we are presenting the results of our investigation on ultrathin films of the TiO_2 nanoparticles at different interfaces. Our investigation reveals that Langmuir film (LF) of the mixture of anatase and rutile (ca. 80:20) phases of TiO_2 nanoparticles at the air-water (A/W)

interface is stable and can be transferred to solid substrates by the Langmuir-Blodgett (LB) technique for any device application. Such finding facilitates the formation of ultrathin film of nanocomposites of discotic liquid crystals (DLC) doped with TiO_2 nanoparticles at different interfaces. We found that the TiO_2 nanoparticles in the ultrathin film regime exhibit promising ethanol (CH_3CH_2OH) gas sensing capability as compared to the thick film obtained using the spin-coating technique. The enhanced sensing performance of the LB film is due to the availability of the large surface density of crystalline defect sites for ethanol adsorption and subsequent reduction. There are few reports on the LF and LB films of titania in the form of nanosheets [7, 8] or macroporous material [9]. Furthermore, the LB film template is being used for the synthesis of TiO_2 nanoparticles at the given interface [10-12]. However, there are no studies on the LF and LB films of the mixed phases of TiO_2 nanocrystalline particles.

In this chapter, we report the formation of a stable and reversible LF of mixed phases of TiO_2 nanoparticles at the A/W interface. We fabricated a single layer of LB films of the TiO_2 nanoparticles onto hydrophilically (HPL) treated substrates at different target surface pressures (π_t). The topography and morphology of such LB films were characterized by using the atomic force microscope (AFM) and field emission scanning electron microscope (FESEM). The LB films deposited at higher π_t reveal a higher surface coverage, thereby yielding a higher density of crystalline defect sites. The UV-Vis spectroscopy reveals that with the increase in π_t of deposition the optical property more closely approaches that of the bulk sample. The electrical properties of LB films were characterized by using current - voltage (I-V) measurement. The LB film of TiO_2 nanoparticles are employed for ethanol sensing applications. The LB film of TiO_2 nanoparticles shows an appreciable and recoverable response toward ethanol sensing.

In this chapter we are also presenting the results of our investigation on the LB film of DLC molecules doped with TiO_2 nanoparticles. DLCs have large band gap of about 4 eV, so they are insulators like any other organic material but they can be conducting on doping with a small amount of electron donor or acceptor, depending on the electronic nature of the core. DLC act as semiconducting material on its alignment with proper doping. Since most DLC material possess characteristics of an acceptor and exhibit high mobility due to their columnar arrangement, they may become a potential candidate for photovoltaic devices [13]. When DLC is doped with p-type or n-type material, it finds application in light emitting diodes and organic solar cells [14]. It has been reported that, when electron-rich hexa-alkoxy triphenylene discotics are doped with

$NOBF_4$, the conductivity increases significantly [15]. Similarly, the doping of electron-deficient tricycloquinazoline discotic with potassium metal enhances the dc electrical conductivity from 10^{-7} S/m to 10^{-4} S/m [16]. It has been observed that the LB films of a polymer possessing triphenylene moieties in the side groups show in-plane conductivity [17]. The efficiency and sensitivity of a device increases manifold, if the functional material is spread to form ultrathin films. Such enhancement occurs due to increase in surface-to-volume ratio of the material. There are some studies on the ultrathin films of DLC materials [18- 23].

We doped a DLC, hexa-alkoxy triphenylene (HAT5) with TiO_2 nanoparticles. Our investigation revealed the formation of a stable LF of HAT5 and different wt.% of TiO_2 in HAT5 at A/W interface. LB films of HAT5 and HAT5+TiO_2 nanocomposites are transferred onto HPL treated substrates. These LB films were characterized using UV-Vis spectroscopy. The charge- transport mechanism in the LB film of HAT5 and HAT5+TiO_2 (10 wt.%) nanocomposites at different π_t were also studied. This is the first report on incorporation of TiO_2 nanoparticles in discotic liquid-crystalline matrix. We studied the conductivity properties of triphenylene-based DLC doped with TiO_2 nanoparticles. Our study reveals enhancement in conductivity of the DLC by doping with TiO_2 nanoparticles.

3.2 Materials and Experimental Methods

3.2.1 Materials

TiO_2 (anatase : rutile (ca. 80:20)) nanoparticles were procured from Sigma-Aldrich. The Brunauer - Emmet - Teller (BET) surface area of the material was 90 ± 25 m^2/g.

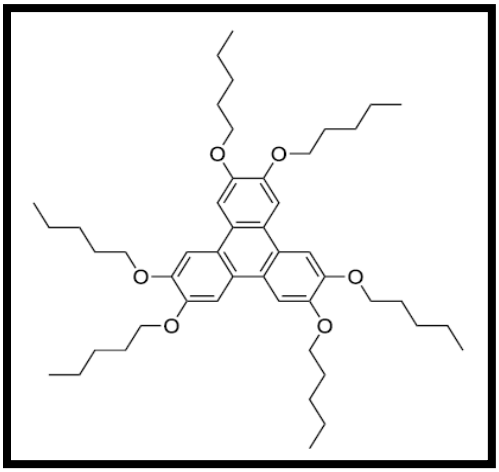

Figure 3.1: Chemical structure of Hexa-alkoxytriphenylene (HAT5) discotic liquid crystal molecule.

Hexa-alkoxy triphenylene (HAT5) molecule was synthesized by Prof. Sandeep Kumar, Raman Research Institute, Bengaluru [24]. The molecular structure of HAT5 is shown in figure 3.1.

3.2.2 Surface manometry and thin film deposition

A solution of TiO_2 nanoparticles was prepared in absolute alcohol with a concentration of 0.5 mg/ml. The solution (500 μl) was spread on the surface of ultrapure ion-free water between the two barriers of an LB trough. About 60 min was allowed for the solvent to evaporate from or dissolve into the subphase, leaving behind dispersed nanoparticles on the water surface. The two barriers were compressed symmetrically at a speed of 47 cm^2/min and simultaneously the surface pressure (π) as a function of area (A) isotherm was recorded. The LF of TiO_2 nanoparticles at A/W interface was imaged in real time using a Brewster angle microscope (BAM).

The LB films of TiO_2 nanoparticles were deposited at different π_t onto HPL glass coverslip and Si/SiO_2 substrates. The silicon ⟨100⟩ p-type substrates were procured from Institute of Electronic Materials Technology, Poland. A single-layer of LB film was deposited onto such substrates by one upstroke of the dipper at a withdrawal speed of 2 mm/min. We wait for about 2 min for drying the film after the deposition. The transfer ratio of the LB film deposition was found to be 1 ± 0.2. Thin film of TiO_2 nanoparticles was also formed using the spin coating unit. For spin coating, 100 μl volume of TiO_2 nanoparticles solution in alcohol was spread on substrate. Deposition was done at a spinning rate of 3000 rotations per minute.

3.2.3 Characterization

The topography of the LB films of TiO_2 nanoparticles and spin coated film of TiO_2 nanoparticles were obtained by using AFM. The morphology of the aggregation of the TiO_2 nanoparticles in the LB film was obtained by using FESEM. LB films of TiO_2 nanoparticles deposited onto optical-quality quartz substrates at different π_t was characterized using UV-Vis spectrophotometer. The charge-transport mechanism in the LB film of TiO_2 nanoparticles was studied by using I-V characteristic measurement. The LB films deposited at different π_t onto Si/SiO_2 substrates were scanned using a Fourier transform infrared (FTIR) spectrometer in reflection absorption mode. The LB and spin coated films of TiO_2 nanoparticles were employed as a functional material for ethanol gas sensing. The detailed description of I-V characteristic and the gas sensing are given below.

3.2.3.1 Current-Voltage measurement

The in-plane charge-transport mechanism in the LB films was studied by recording I-V curves at different temperatures using a Keithley (model 2400) source meter. For I-V measurement, we used gold electrodes fabricated on silicon substrates having an interelectrode separation of ~ 100 μm. The LB film of TiO_2 nanoparticles was transferred on to the gold electrode coated Si substrate. The film deposited on gold electrode on Si substrate is mounted in a hot stage whose accuracy of temperature is around 0.01°C. The schematic diagram of I-V measurement setup is shown in figure 3.2.

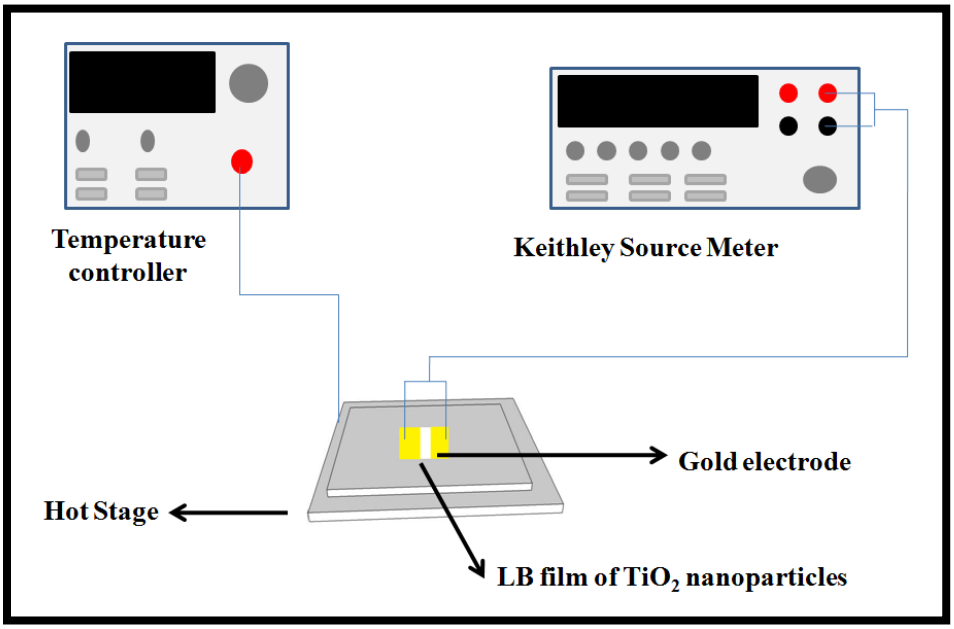

Figure 3.2: The schematic diagram of I-V measurement setup.

3.2.3.2 Gas Sensing

The LB film of TiO_2 nanoparticles was employed as a functional material for ethanol gas sensing in resistive mode. A resistive-type sensor device was fabricated over an 8 mm × 8mm thermally oxidized SiO_2/p-Si substrate. The LB film of TiO_2 nanoparticles was deposited over the substrate at π_t = 10 mN/m and annealed for ~ 2 hour at 200°C in ambient air. The sensing performance of a spin-coated film of TiO_2 nanoparticles is measured and compared to that of the LB film. Two palladium (Pd) catalytic electrode contacts of 3 mm × 8 mm were taken over the TiO_2 film surface, maintaining a separation of 2 mm between contacts. The 50 nm Pd electrodes were deposited by e-beam evaporation (vacuum pressure ~ 10^{-6} mbar). Figure 3.3 shows the schematic diagram of gas sensor measurement setup [25]. There are two cylinders of nitrogen

(N_2) gas. The saturated ethanol vapour was achieved by passing the carrier gas (N_2) through ethanol. These saturated ethanol vapor was mixed with additional IOLAR grade N_2 (carrier gas) in desired proportion in the mixing chamber to get the desired parts per million (ppm) of ethanol vapor. The flow rate was controlled by mass flow controller (MFC) from Alicat Scientific. The sensor sample was inserted in the central portion of the sensing chamber from one side which was heated with a resistive heating coil (~7 cm of constant heating zone, temperature maintained to an accuracy of ±1°C).

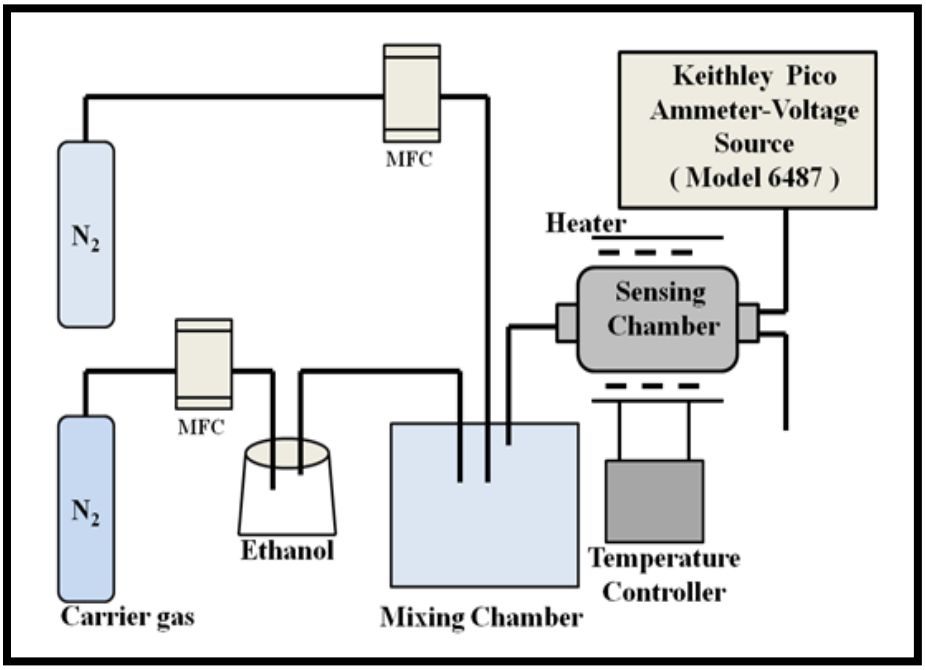

Figure 3.3: Schematic diagram of gas sensor set-up.

A Keithley picoammeter (model 6487) with a built-in programmable voltage source was connected for resistance measurements. The detection principle of resistive sensors is based on change of the resistance of a thin film upon adsorption of the gas molecules on the surface. The gas-solid interactions affect the resistance of the film because of the density of electronic species in the film. The sensor response magnitude is represented as $\Delta R/R_g \times 100\%$, ($\Delta R = R_g - R_a$) where R_a is the initial sensor resistance in air and R_g is the resistance measured with exposure to a target gas or vapor (ethanol diluted with air) [26]. The response time and the recovery time of the sensor are calculated as the time taken by the sensor signal to reach 90% of its saturation response value (with exposure of ethanol vapor) and to return to 10% from the saturation response value upon cutting off the ethanol pulse [27, 28].

3.3 Results and Discussion

3.3.1 X-ray diffraction of TiO_2 nanoparticles

The crystalline property of the TiO_2 nanoparticles was studied using X-ray diffraction. The intensity vs 2θ data is shown in figure 3.4. The 2θ scan rate was maintained at 0.33° per minute. The X-ray data clearly indicate the presence of both forms of TiO_2 (i.e., anatase and rutile) [29].

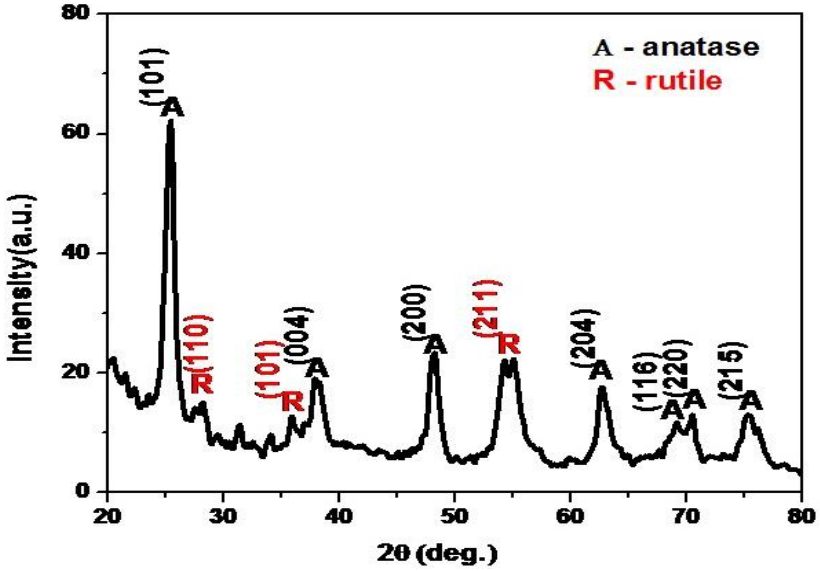

Figure 3.4: X-ray diffraction data of the TiO_2 nanoparticles.

The sharp peaks indicate the highly crystalline nature of the TiO_2 nanoparticles. The average size of the TiO_2 nanoparticles was estimated using the Debye-Scherrer equation [30].

$$D = k\lambda/\beta\cos\theta \qquad 3.1$$

Where, k = 0.9 is a constant; λ =1.54A° is wavelength, β is the full width half maximum of the peak. The estimated average particle size of TiO_2 nanoparticles was about 5 nm.

3.3.2 Surface manometry of the TiO_2 nanoparticles

The surface manometry of the TiO_2 nanoparticles is studied at A/W interface. The π-*A* isotherm of the LF of TiO_2 nanoparticles at the A/W interface is shown in figure 3.5. The corresponding in-plane elastic modulus (*E*) as a function of *A* is also plotted in same figure 3.5. The isotherm shows negligible π at large *A* until the film is compressed to 450 cm^2. This is the loose-packing (LP) phase of the LF of TiO_2 nanoparticles. The π rises sharply thereafter until the film is compressed completely in the trough. The sharp rise in π indicates the onset of a close - packing (CP) phase of the TiO_2 nanoparticles. The isotherm shows a maximum π of about ~ 24 mN/m.

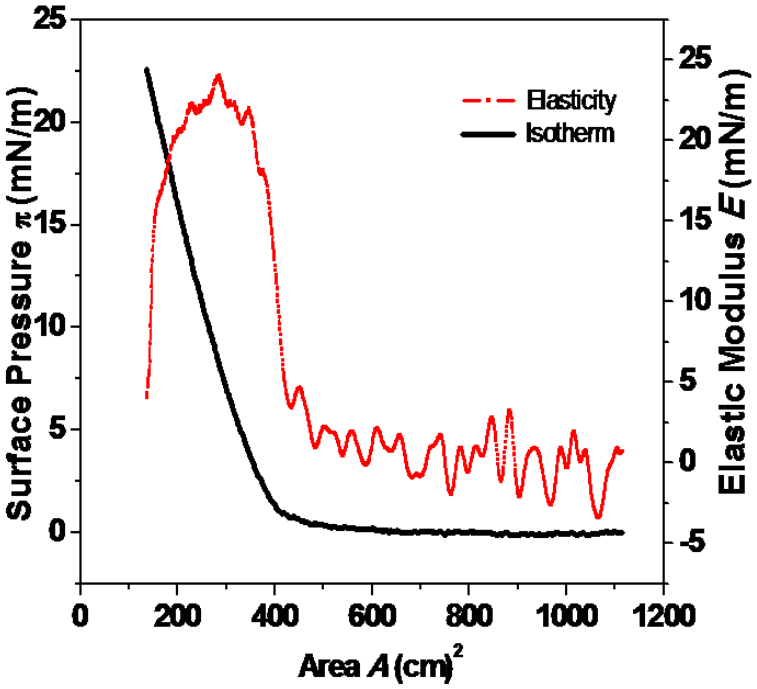

Figure 3.5: Surface pressure (π) - area (A) isotherm and the variation of the in-plane elastic modulus (E) as a function of A of the TiO_2 nanoparticles at the air-water interface.

The signature of the collapse is not evident from the isotherm. The variation of *E* as a function of *A* not only provides insight into the elastic nature of the LF but also reveals the weak phase transition in the LF at the A/W interface. *E* as a function of *A* is estimated using the relation 2.2. The variation of *E* indicates the onset of the CP phase of the LF of TiO_2 nanoparticles at around 460 cm^2. The maximum value of *E* in the CP phase is obtained as ~ 22 mN/m. This value of *E* for the LF of TiO_2 nanoparticles lies within the range for that of the liquid like phase of LF of some reported molecules, namely, octadecanoic acid, octadecanol, and octadecylamine [31-33]. The CP phase destabilizes upon further compression, leading to a decrease in the value of *E*. Such a destabilization of *E* is an indication of the initiation of the collapse of the film. Though the collapse of the LF of TiO_2 nanoparticles was not evident from the isotherm, the indication of the collapse can be seen from the elastic modulus curves.

The stability and reversibility of the LF of TiO_2 nanoparticles is studied by recording the isocycles of the film at the A/W interface. The isocycles are obtained by repeated compression and expansion of the LF. The maximum π was maintained at 10 mN/m. Figure 3.6 shows the isocycles of the LF of TiO_2 nanoparticles at the A/W interface. The curves for the second and third cycles are shifted vertically by 5 mN/m relative to each other for visual clarity.

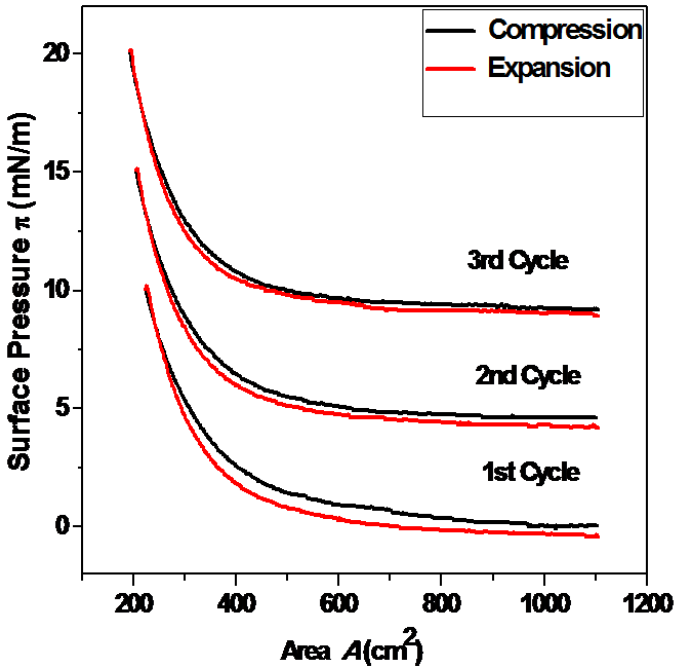

Figure 3.6: Isocycles of the LF of TiO_2 nanoparticles at the air-water interface. The film was compressed to the maximum surface pressure of 10 mN/m.

The isocycles measurement shows negligible hysteresis in the compression and expansion curves of a given cycle. The observed minute hysteresis is due to some reorganization of the clusters of TiO_2 nanoparticles at the A/W interface. The isocycles curves indicate that the film of TiO_2 nanoparticles at the A/W interface is stable and almost reversible, though the TiO_2 nanoparticles do not possess any functional organic ligands to exhibit an amphiphilic nature. The stability of LF of the nanoparticles is achieved by attractive Van der Waals interaction and steric repulsion between the particles as reported in the case of some non-amphiphilic nanoparticles at the A/W interface [34-38]. Several reports in the literature indicate a stable Langmuir monolayer (LM) formed by non-amphiphilic organic molecules [32, 39-41]. Such systems attain stability because of entropic reasons.

3.3.3 Characterization of Langmuir Film of TiO_2 nanoparticles at the A/W interface using BAM

The LF of TiO_2 nanoparticles at the A/W interface was imaged in real time using a BAM. The BAM images of TiO_2 nanoparticles at the A/W interface are shown in figure 3.7. The BAM image obtained at A = 700 cm^2 (figure 3.7(a)) shows very loosely packed bright tiny elliptical

domains in the dark background. The bright tiny domains represent the clusters of the TiO_2 nanoparticles at the A/W interface. The dark background represents the water surface. The surface density of the bright domain increases with the compression of the LF.

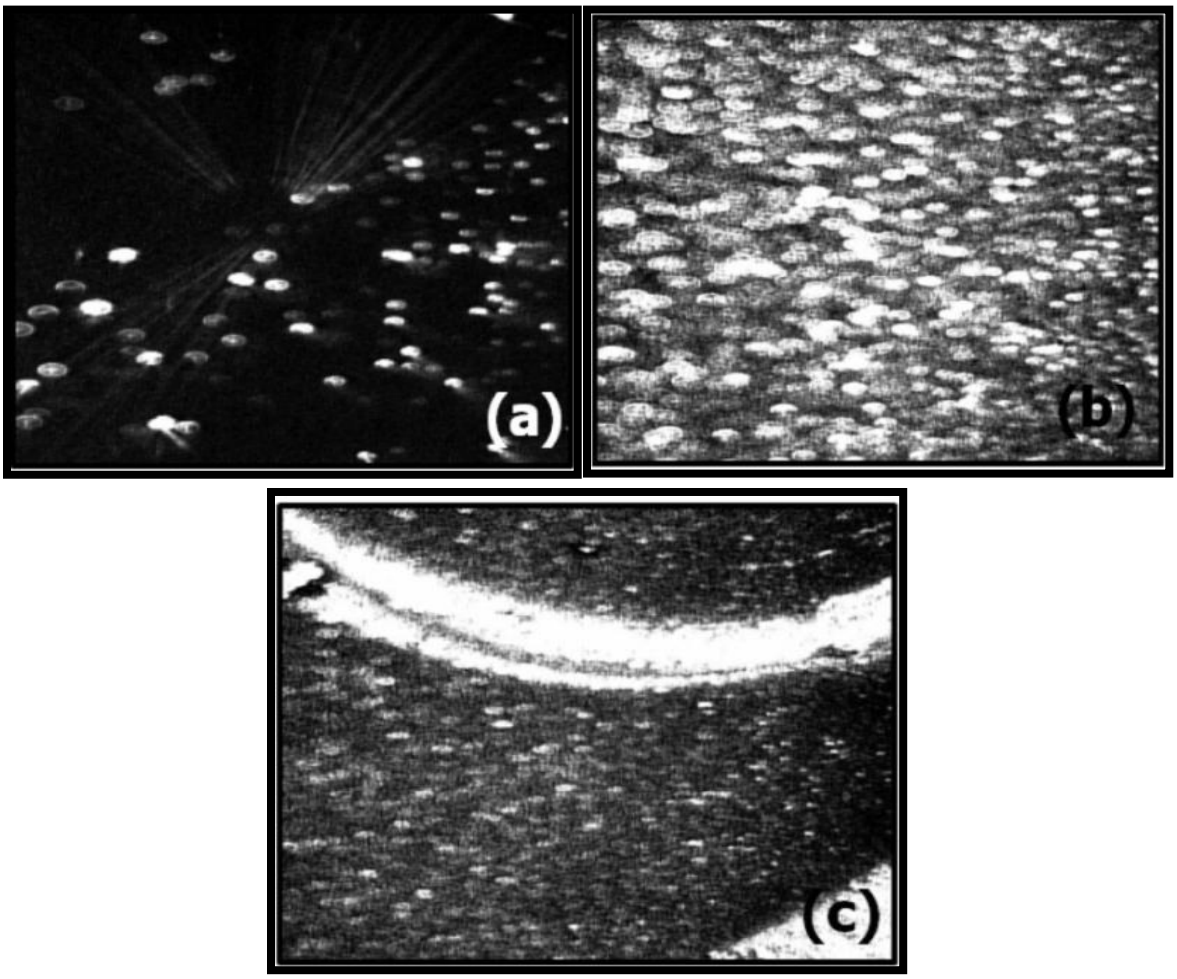

Figure 3.7: Brewster angle microscope images of LF of TiO_2 nanoparticles at the air-water interface. Images (a)-(c) were captured over film areas (A) of 700, 300 and 140 cm^2. The size of each image is 6.4 × 4.8 mm^2.

The BAM image (figure 3.7 (b)) captured in the CP phase shows the complete coverage of the water surface with the TiO_2 nanoparticles leading to a very bright texture composed of very dense tiny elliptical domains. The BAM image (figure 3.7(c)) in the collapsed state shows streaks of very thick and bright domain. In a separate experiment, the compression barriers were held in the CP phase of the TiO_2 nanoparticles and the evolution of the domains was observed for about 30 min. The BAM images did not reveal either the dark region or very bright thick domains during such observation. This indicates that the CP phase of the LF of TiO_2 nanoparticle

is very stable and does not yield an LP phase or tend toward a collapsed state on holding the barriers in such a phase.

3.3.4 Characterization of LB films of TiO_2 on solid substrate

3.3.4.1 Reflection Absorption Infrared Spectroscopy

The data from reflection absorption infrared spectroscopy (RAIRS) of the LB films of TiO_2 nanoparticles deposited at π_t = 1, 5 and 10 mN/m onto Si/SiO_2 substrates are shown in figure 3.8(a). The absorption bands corresponding to Ti-O-Ti bending, Ti-O-Ti stretching, Si-O-Ti stretching and Ti-O stretching are observed at 481, 785, 1007 and 1152 cm^{-1} respectively [42,43].

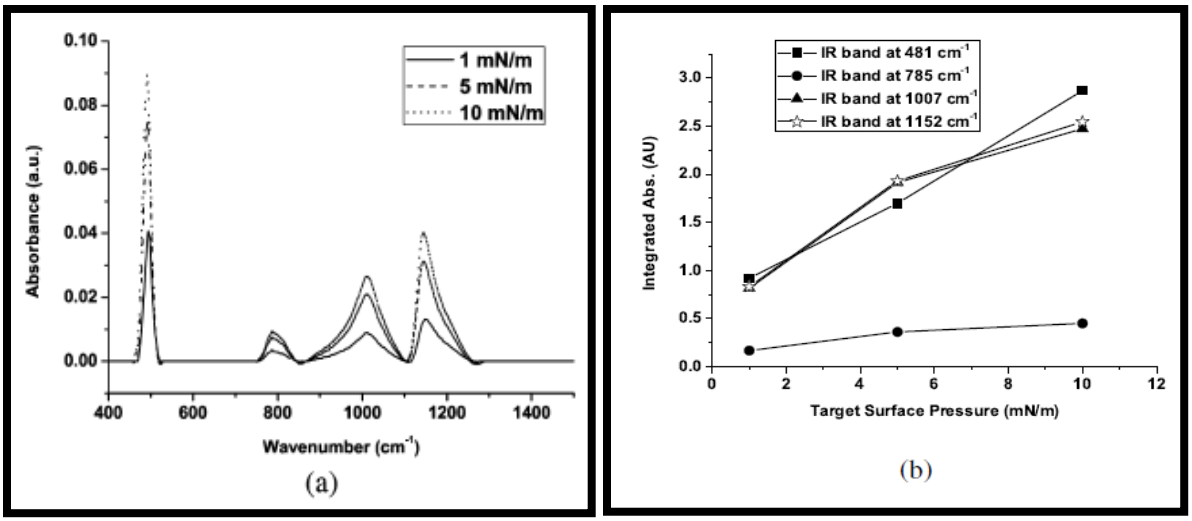

Figure 3.8: (a) Reflection absorption infrared spectra of the LB films of TiO_2 nanoparticles deposited onto Si/SiO_2 substrates at target surface pressures of 1, 5 and 10 mN/m. (b) Variation of integrated absorption for different modes as a function of target surface pressure of LB deposition.

The variation of integrated absorbance for the different modes as a function of π_t of LB film deposition is shown in figure 3.8(b). The integrated absorbance increases monotonically with the increase in π_t, indicating an increase in surface density for the TiO_2 nanoparticles in the single layer of LB films.

3.3.4.2 Field Emission Scanning Electron Microscopy

The morphology of aggregation of the nanoparticles in such LB films was obtained using a

FESEM (figure 3.9). The FESEM images show a 2-dimensional (2D) layer of the TiO_2 nanoparticles. It is noteworthy that with increase in π_t of deposition the surface coverage of the TiO_2 nanoparticles increases. With increase in surface coverage of TiO_2 nanoparticles, it is most likely that the density of crystalline defect sites will increase. Therefore, the activity of the films deposited at higher π_t is expected to be higher than for those deposited at lower π_t. This is in agreement with the observation of the RAIRS result.

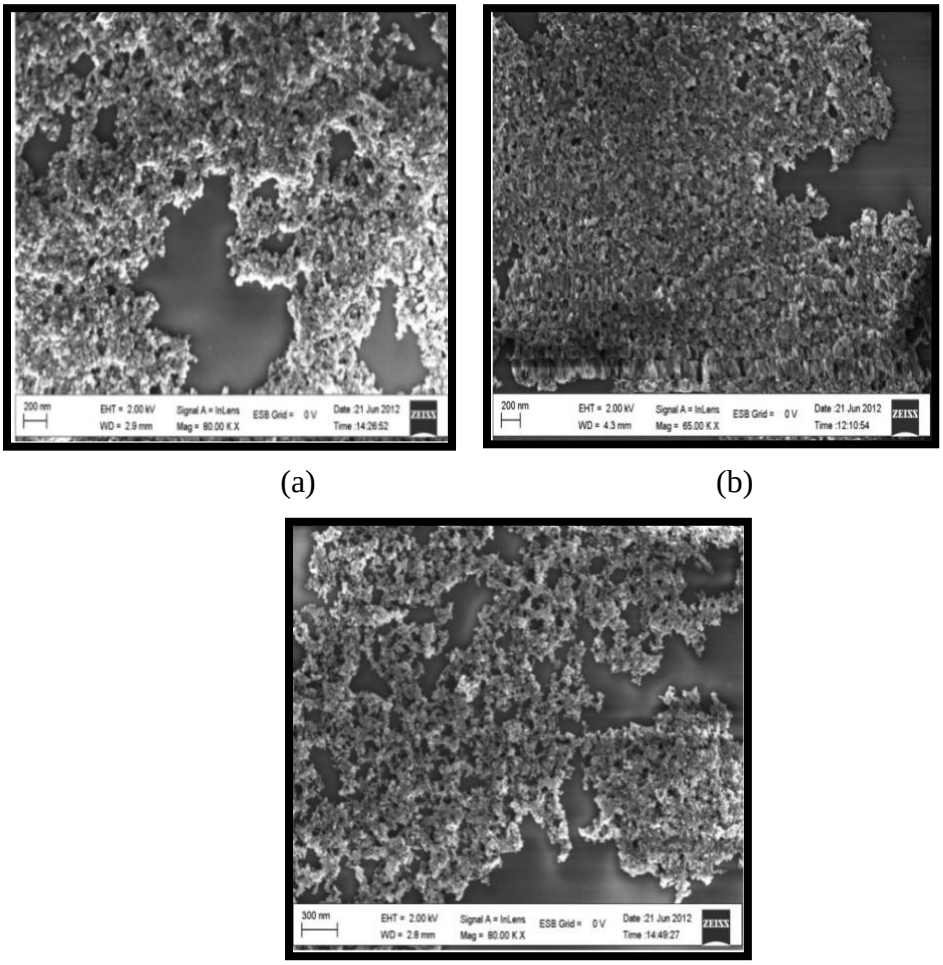

Figure 3.9: FESEM images of the LB films of TiO_2 nanoparticles deposited onto Si/SiO_2 substrates at target surface pressure (π_t) of (a) 1, (b) 5 and (c) 10 mN/m.

3.3.4.3 Atomic Force Microscopy

The surface topography of films deposited onto glass coverslip was obtained using AFM. The topography images of LB film of TiO_2 nanoparticles transferred on HPL coverslip at π_t = 5 and 15 mN/m are shown in figure 3.10(a) & (b). The topographic image of LB film of TiO_2

nanoparticles shows the clusters of TiO_2 nanoparticles on HPL coverslip. The density of these clusters increases on substrate with increasing π_t. The average thickness of the LB film of TiO_2 nanoparticles was measured and was found to be ~ 70 nm. The topographic image of spin coated film of TiO_2 nanoparticles on HPL coverslip is shown in figure 3.10(c). It shows the uniform film of aggregation of TiO_2 nanoparticles on substrate. The thickness of the spin-coated film was estimated to be ~ 4000 nm which is many times higher than that of LB film of TiO_2 nanoparticles.

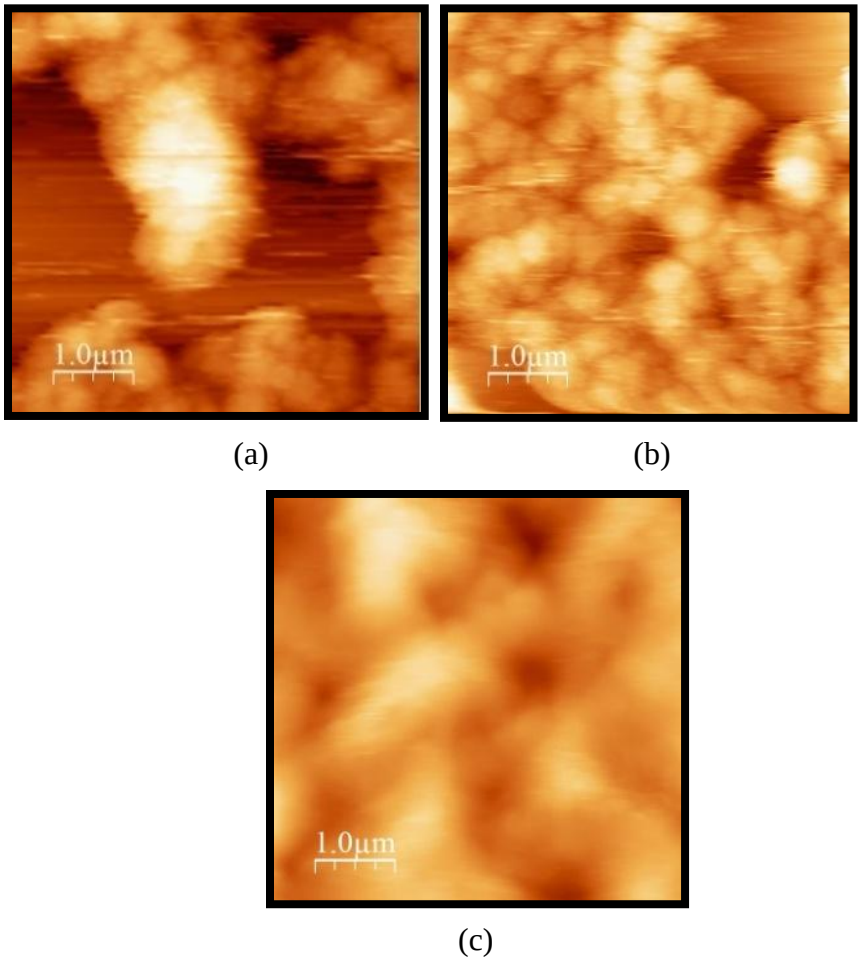

(a) (b)

(c)

Figure 3.10: Atomic force microscope images of LB of TiO_2 nanoparticles transferred at target surface pressure (π_t) of (a) 5 and (b) 15 mN/m (c) Spin coated film of TiO_2 nanoparticles.

3.3.4.4 UV−Vis Spectroscopy

The optical property of the LB films of TiO_2 nanoparticles deposited at different π_t onto quartz substrates was investigated using UV-Vis spectroscopy. The spectra of the LB films are shown in figure 3.11. The bulk sample of the TiO_2 nanoparticles was prepared by spin coating the

solution. The spectrum of the bulk sample shows a broad peak at 290 nm (inset of figure 3.11). The broad peak may indicate poly-dispersity due to different degrees of aggregation of the TiO_2 nanoparticles in the spin-coated film. The peak positions of the films deposited at π_t values of 1, 5, 10, 15, and 20 mN/m are estimated to be 301, 298.5, 297.1, 295.5, and 294.5 nm, respectively as shown in table 3.1

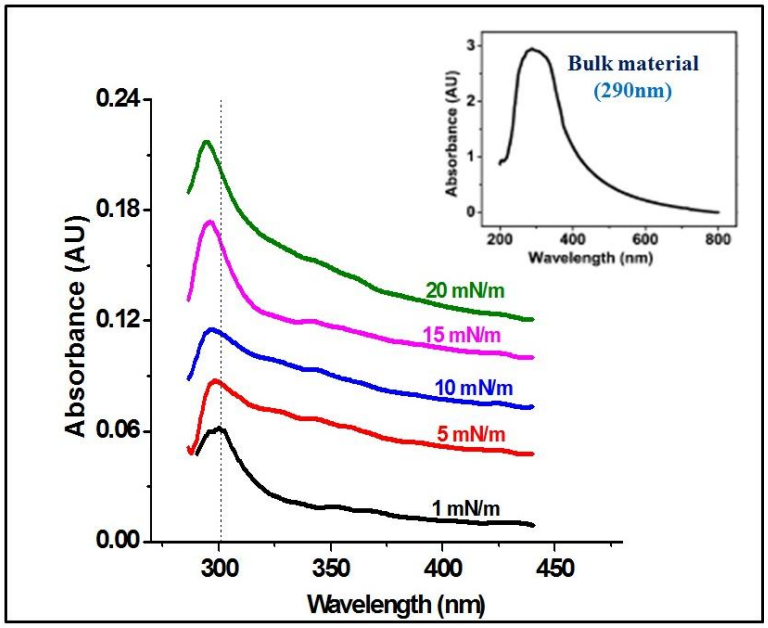

Figure 3.11: UV−Vis spectra of the LB films of the TiO_2 nanoparticles deposited at different target surface pressures (π_t) onto quartz substrates. The vertical line is shown to indicate the blue shift of the peak with the increase in π_t of deposition. The UV−Vis spectrum for the bulk sample (TiO_2) is shown in inset.

.

Table 3.1: The peak positions of the LB films of TiO_2 nanoparticles deposited at different π_t values and for the bulk material.

Surface Pressure (mN/m)	**Peak Position (nm)**
1	301
5	298.5
10	297.1
15	295.5
20	294.5
Bulk material	290

The variation of peak position due to increasing π_t indicates a blue shift with respect to the LB film deposited at 1 mN/m. This is due to the fact that as the π_t increases to approach the collapsed surface pressure (π_c) more closely, the deposited LB films approach the proximity of the 3D bulk material. Hence, the optical property of the LB films of TiO_2 nanoparticles varies systematically with the increase in π_t of deposition and approaches the bulk material more closely (shown in figure 3.12).

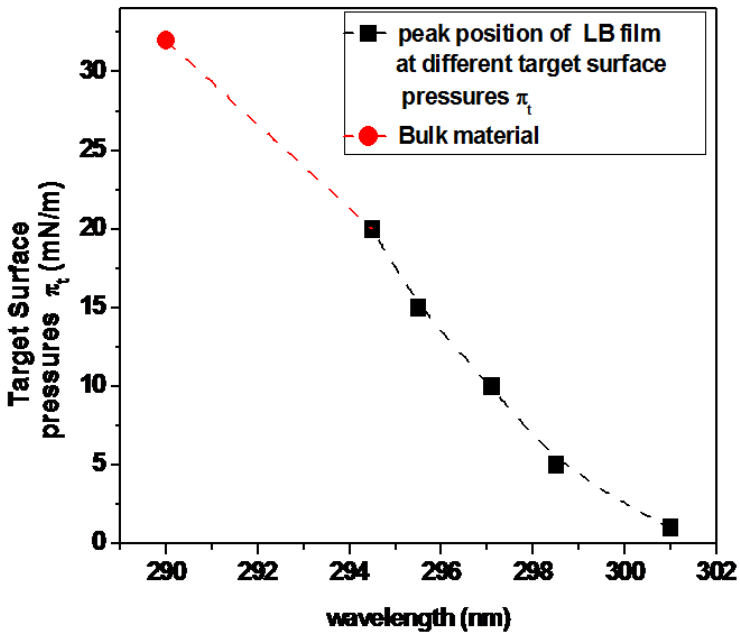

Figure 3.12: The peak positions of the absorbance of LB films of TiO_2 nanoparticles deposited at different target surface pressures (π_t) values and for the bulk material.

3.3.4.5 Current-Voltage (I-V) Characteristics

The charge-transport mechanism in the LB film of TiO_2 nanoparticles was investigated by the I - V measurement in current-in-plane (CIP) geometry. The I - V curves for the LB film of TiO_2 nanoparticles recorded at different temperature (T) are shown in figure 3.13. The figure 3.13 (a) shows the nonlinear behavior of current (I) as a function of applied voltage (V) and the trend remains same with increasing temperature. The slope of I vs V increases with increasing temperature. The differential conductance (G = dI/dV) was calculated for different temperature at V = 0 volt. A plot of ln (G) versus 1/T for both LB film and spin coated film of TiO_2 nanoparticles is as shown in figure 3.13(b). A linear fit to the data corresponding to an LB film indicates the Arrhenius behavior of the charge transport.

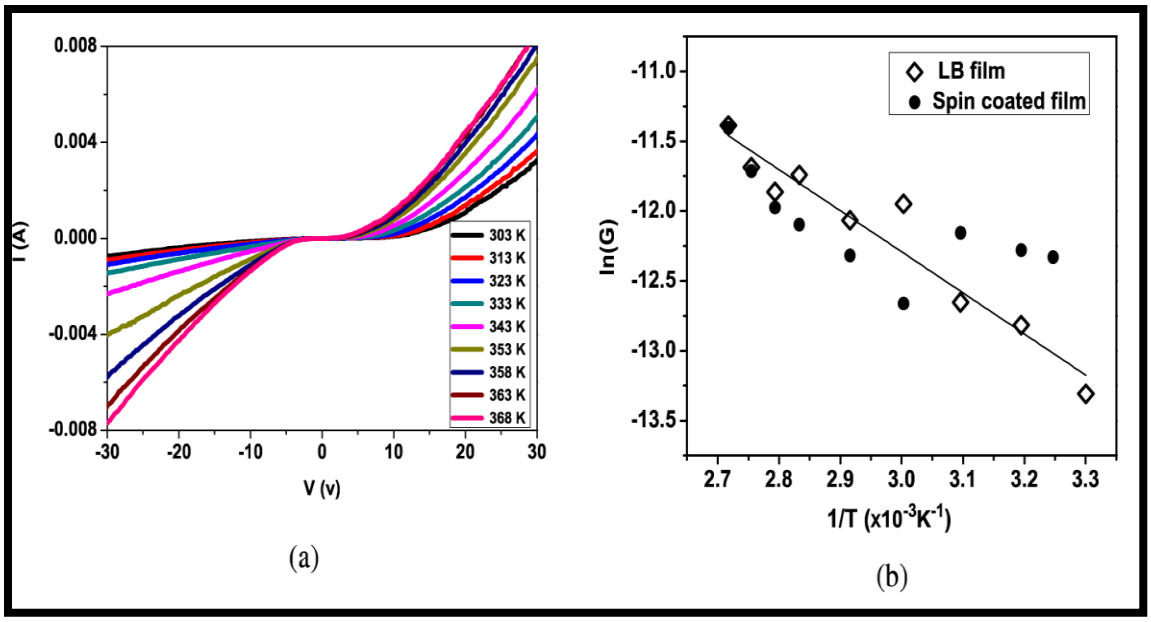

Figure 3.13: (a) Current-voltage (I-V) curves of the LB films of TiO_2 nanoparticles (π_t = 10 mN/m) at different temperature. (b) Arrhenius plot. The solid line is a linear fit to the data points for the LB film.

At high temperature, the temperature dependence of the dc and ac conductivity shows a simply activated behavior according to the Arrhenius relation:

$$G(T)= G_0 +\exp(-E_A /k_B T) \qquad 3.2$$

where G(T) is the differential conductance, E_A is the activation energy and k_BT is the characteristic thermal energy. This reflects classical hopping transport of individual charges between nearest neighboring particles. At temperature above room temperatures, where k_BT becomes comparable to the charging energy E_c of the particle, thermally excited extra charge carriers are participating in the hopping process. So, at high temperature, above the room temperature, the E_A reflects the energy needed to transfer one electron from an electrically neutral particle to another.

The LB film of TiO_2 nanoparticles shows the Arrhenius behavior of the charge transport, i.e., classical hopping of individual charges between nearest neighbor particles [44]. The slope of the curve yield E_A. The E_A was found to be 0.25 eV, which is 1 order of magnitude larger than the thermal energy (at 300 K = 0.025 eV).

At high temperature (around room temperature), thermally excited extra charge carriers are participating in the hopping process. This indicates that the transport mechanism is

predominantly governed by the hopping of the charges between the nearest-neighbor sites. The plot of ln G versus 1/T of the spin-coated film of TiO_2 nanoparticles shows nonlinear behavior and therefore indicates some complex mechanism of charge transport.

3.3.4.6 Ethanol sensing using TiO_2 film

The highest surface coverage of the TiO_2 nanoparticles on the solid substrates was found at π_t = 10 mN/m (Figure 3.9(c)). Because of the increase in surface coverage, the defect density in the film increases and therefore the activity of such a film is expected to be the highest. Therefore, the LB films of TiO_2 nanoparticles deposited at π =10 mN/m are employed for ethanol (CH_3CH_2OH) sensing applications. The ethanol sensing mechanism by the LB film of TiO_2 nanoparticles can be explained by the classical gas sensing theory where the surface adsorbed ionized oxygen species (O^-, O_2^-, etc.) readily react with the reducing vapor ethanol in different temperature ranges [45]. Initially, the ethanol molecules are adsorbed to the TiO_2 nanoparticle surface and become oxidized or dehydrogenated by the surface - adsorbed oxygen. Because of the chemical reactions as indicated by equations 3.3 to 3.6, either acetaldehyde (CH_3CHO) or the final product of CO_2 and H_2O is released at elevated temperature by releasing free electrons onto the oxide surface, which effectively reduces the sensor resistance [45, 46].

$$CH_3CH_2OH_{(gas)} \rightarrow CH_3CH_2OH_{(ads)} \quad 3.3$$

$$CH_3CH_2OH_{(ads)} + O^-_{(ads)} \rightarrow CH_3CHO_{(gas)} + H_2O_{(gas)} + e^- \quad 3.4$$

$$CH_3CH_2OH_{(ads)} + 5O^-_{(ads)} \rightarrow 2CO_{2\,(gas)} + 2H_2O_{(gas)} + 5e^- \quad 3.5$$

$$CH_3CH_2OH_{(ads)} + 6O^-_{(ads)} \rightarrow 2CO_{2\,(gas)} + 3H_2O_{(gas)} + 6e^- \quad 3.6$$

The sensing capability of the LB films (thickness ~70 nm) of TiO_2 is compared to that of thick (~ 4000 nm) film obtained by the spin-coating technique. The gas-sensing performance of the films is obtained in terms of the dynamic change in the resistance and the gas-sensing response time [3]. The thick spin coated film of the TiO_2 nanoparticle-based sensor had a continuously decreasing nature with large fluctuations in the sensor resistance in the temperature range of 200-350°C with the exposure of both air and 500 ppm ethanol.

Figure 3.14(a) represents the resistance profile of the sensor at 300°C. The ethanol sensing using a spin-coated TiO_2 nanoparticle thick film does not show any systematic trend in resistance and

hence cannot be employed for any sensing application. At the same time, the LB film of TiO_2 nanoparticles offered promising sensing performance toward ethanol at 300°C with very stable baseline characteristics. The transient response curve of the LB film of TiO_2 nanoparticle-based sensors shows a very stable response ((ΔR/Rg) × 100%) of 18.52% in the exposure of 500 ppm at 300°C as shown in figure 3.14 (b). The response and recovery times of the sensor are found to be 55 and 134 sec., respectively.

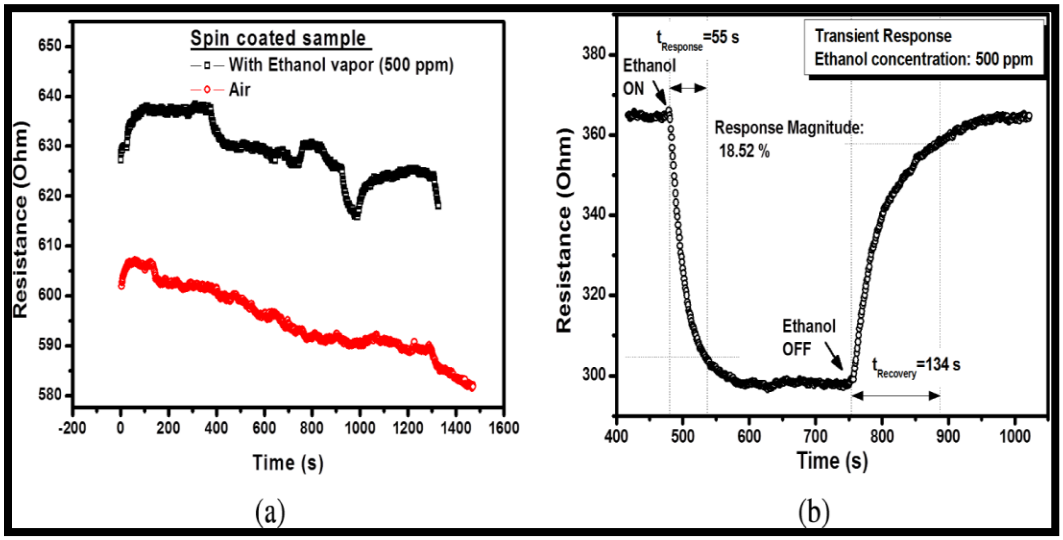

Figure 3.14: Transient response of the TiO_2 nanoparticle-based ethanol sensor at 300°C at a 500ppm concentration fabricated using (a) a spin-coated thick film of TiO_2 nanoparticles and (b) an LB film of TiO_2 nanoparticles deposited at 10 mN/m.

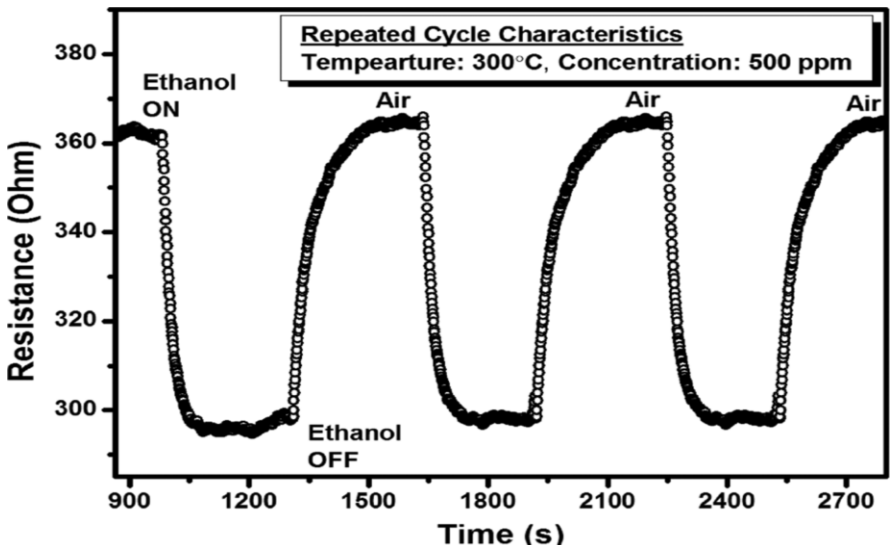

Figure 3.15: Repeated cycles of transient response due to the interaction of ethanol with the LB film of TiO_2 nanoparticles.

The repeated cycles of the characteristic curve for the LB film-based sensor is shown in figure 3.15. The response of the sensor appears to be very stable and recoverable with excellent baseline stability.

The magnitude of the response was increased monotonically with increasing ethanol concentration up to 1000 ppm and becomes saturated after 1000 ppm. The sensing performance remains invariant for temperature higher than 300°C. No promising sensing performance was observed below 300°C and below 500 ppm ethanol concentration. We believe that the best sensing performance at and above 300°C is due to favorable conditions for reactions as indicated by eqs 3.3 to 3.6. Though both spin-coated thick films and LB-deposited thin films carry almost similar material properties, sensor results shows an enormous deviation between their sensing performances possibly because of the variation of their structural properties and the nonavailability of ethanol gas to the deeply embedded defect sites in the bulk spin-coated film. The mixed phase of titania possesses a morphological structure wherein the rutile crystallites are interwoven with anatase crystallites [3, 47]. The interface of the two phases acts as the catalytic hot spot. We believe that the LB film of TiO_2 nanoparticles deposited at π_t = 10 mN/m exhibits a large number of such reaction sites. Because of an enormous gain in the surface to volume ratio in the ultrathin LB film of TiO_2 nanoparticles; such reaction sites will be available for the adsorption and reduction of ethanol gas.

3.4. DLC doped with TiO_2 nanoparticle

We found that TiO_2 is suitable nanomaterial for the fabrication of ultrathin film. We also demonstrated a potential sensing application of the film. TiO_2 nanoparticles can be incorporate into DLC which can be employed for photovoltaic application. As we discussed earlier that the DLC can be conducting on doping with a small amount of electron donor or acceptor, depending on the electronic nature of the core. We doped DLC with TiO_2 nanoparticle and studied the properties at interfaces. HAT5 acts as acceptor molecule (p-type) having high charge mobility. The TiO_2 nanoparticles act as n-type dopant [48] to the HAT5 monolayer.

3.4.1 Surface manometry of HAT5 and HAT5+ TiO_2 nanocomposites

The surface manometry of HAT5 and HAT5+TiO_2 nanocomposites (with 5, 10, 15 & 20 wt.% of TiO_2 nanoparticles) is studied at A/W interface. We found stable LF of HAT5 and

HAT5+TiO_2 nanocomposites at A/W interface as shown in figure 3.16. We found condensation effect on the film of HAT5+TiO_2 nanocomposites due to the presence of TiO_2 nanoparticles. The π - *A* isotherm shifts towards lower area on increasing the wt.% of TiO_2 in HAT5. The shift in the isotherms towards lower area on incorporation of TiO_2 nanoparticles can be either due to complexation of HAT5 with TiO_2 or 3D aggregates of TiO_2 nanoparticles in the monolayer matrix of HAT5 [49].

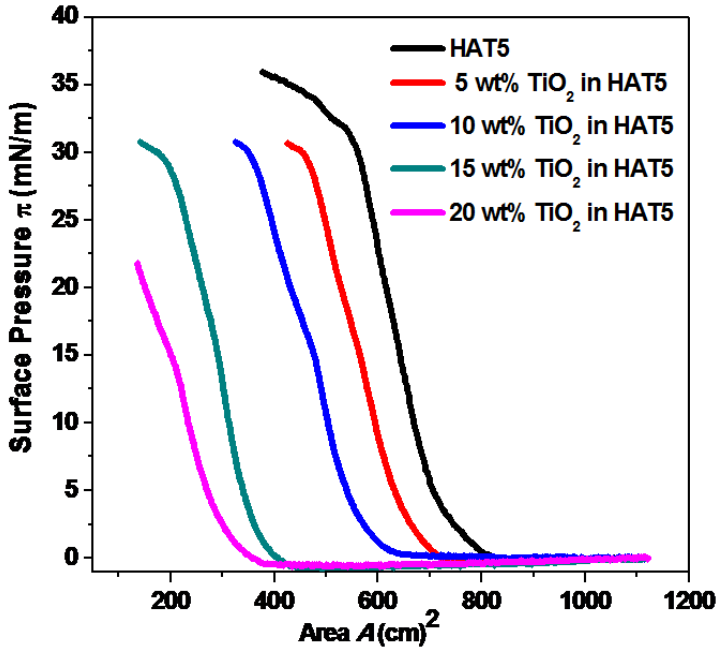

Figure 3.16: Surface pressure (π) - Area (A) isotherms of Langmuir monolayer of pure HAT5 and HAT5+TiO_2 nanocomposites at air-water interface.

The isotherm of HAT5+TiO_2 (10 wt.%) nanocomposites shows the kink at π = 15 mN/m. It shows the behavior of both HAT5 DLC and TiO_2 nanoparticles at A/W interface. We transferred a single layer of HAT5+TiO_2 (10 wt.%) nanocomposites at π_t = 5 and 20 mN/m using LB technique.

3.4.2 Characterization of thin film of HAT5 and HAT5+TiO_2 nanocomposites on solid substrate

LB films of DLC HAT5 and HAT5+TiO_2 nanocomposites deposited onto solid substrates at different π_t were characterized using AFM, UV-Vis spectrophotometer and I-V measurement. The AFM images of the LB films of HAT5 and HAT5+TiO_2 (10 wt.%) nanocomposites are

shown in figure 3.17. The AFM image of the LB film of HAT5 deposited at 20mN/m shows very uniform layer over an area of 5x5 μm^2 (figure 3.17(a)). The AFM image of the LB film of HAT5+TiO_2 (10 wt.%) mixed system shows small bright dots in the uniform background over an area of 2x2 μm^2. These bright dots are small clusters of TiO_2 nanoparticles embedded in the monolayer matrix of HAT5 (figure 3.17(b)).

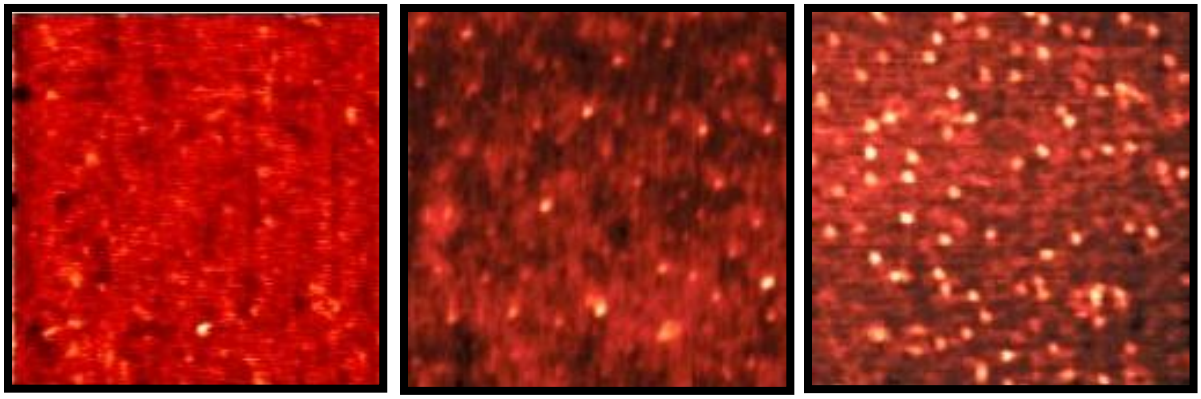

(a) (b) (c)

Figure 3.17: The AFM images of LB films of (a) HAT5 deposited at target surface pressure π_t = 20 mN/m, (b) HAT5+TiO_2(10 wt.%) nanocomposites deposited at π_t = 5 mN/m and (b) π_t = 20 mN/m. The size of the image (a) is 5x5 μm^2 and that of (b) and (c) is 2x2 μm^2.

On increasing the π_t of LB deposition from 5 to 20 mN/m, the size and density of bright dots increases (figure 3.17(c)). This is due to aggregation of TiO_2 nanoparticles to form relatively larger 3D clusters in the LB film. With increase in density of clusters of TiO_2 nanoparticles, the defect sites get increased [49].

A single layer of LB films of HAT5 and HAT5+TiO_2 nanocomposites on HPL coverslips was characterized using UV-Vis spectroscopy. The energy gap (E_g) [50] was calculated using the equation

$$E_g = hc/\lambda \qquad 3.7$$

where E_g is the energy gap, h is Planck's constant, c is the velocity of light in vacuum and λ is the absorption wavelength at which the peak is observed.

We observed a systemic reduction in the energy gap of the HAT5 system on doping it with TiO_2 nanoparticles as shown in figure 3.18.

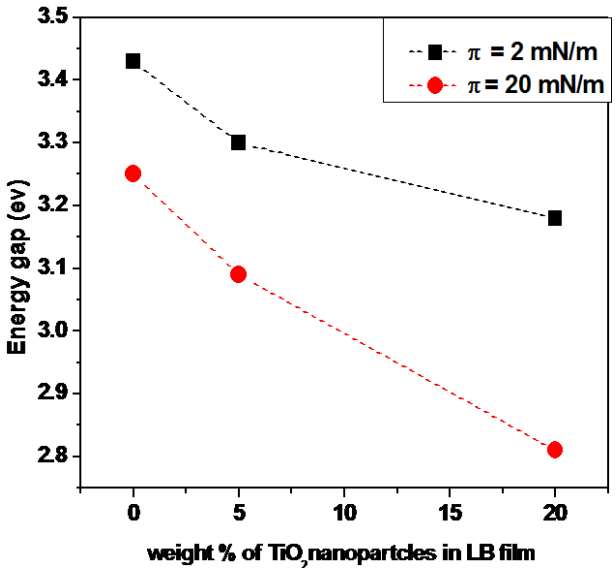

Figure 3.18: Decrease in energy gap (eV) value of HAT5 system on increasing the dopant concentration of TiO_2 in HAT5 at target surface pressure π_t = 2 and 20 mN/m.

The energy gap of HAT5 system decreases with increasing wt.% of TiO_2 nanoparticles in HAT5 [49]. Decrease in the energy gap value indicates better charge mobility which is an important factor in various devices e.g. photovoltaic cells [13]. There are some reports on enhancing conductivity of discotic system by doping it with p or n-type material [15-16]. In 2008, Lakshminarayanan et al. [51] have reported the conductivity properties of two triphenylene-based DLCs hexahexyloxytriphenylene and hexahexylthiotriphenylene doped with ferrocenium species and they observed the conductivity increment in the systems after addition of ferrocenium species.

DLC have large band gap but this can be reduced by doping it with a small quantity of electron acceptor or donor. The UV-Vis result shows reduction in the energy gap of HAT5 system on doping it with TiO_2 nanoparticles. The charge-transport mechanism in the LB film of pure HAT5 and HAT5+ TiO_2 (10 wt.%) nanocomposites were also studied by recording I-V curves at different temperatures.

The LB film of pure HAT5 and HAT5+TiO_2 (10 wt.%) nanocomposites were deposited on gold electrodes deposited Si substrate. The I-V curves of LB film of pure HAT5 deposited at π_t = 20 mN/m (figure 3.19) show nonlinear behavior of I as a function of applied V and the trend remains same with increasing temperature. This is similar to that of semiconductors. The change in slope of I-V increases with increasing temperature.

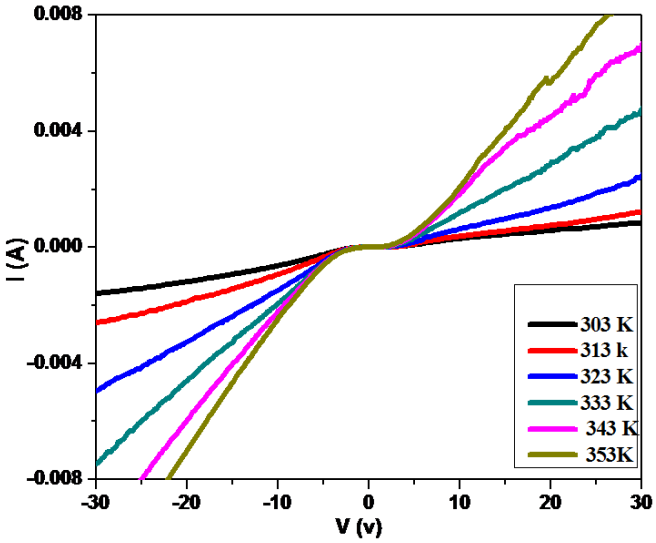

Figure 3.19: Current-Voltage (I-V) curves of the LB film of HAT5 molecules (π_t =20 mN/m) at different temperature.

We fabricated the LB film of HAT5+TiO_2 (10 wt.%) nanocomposites at different π_t (5 and 20 mN/m) on gold electrode deposited Si substrate and studied the charge - transport mechanism. The I-V curves of HAT5+TiO_2 (10 wt.%) nanocomposites deposited at different π_t are shown in figure 3.20(a) & (b).

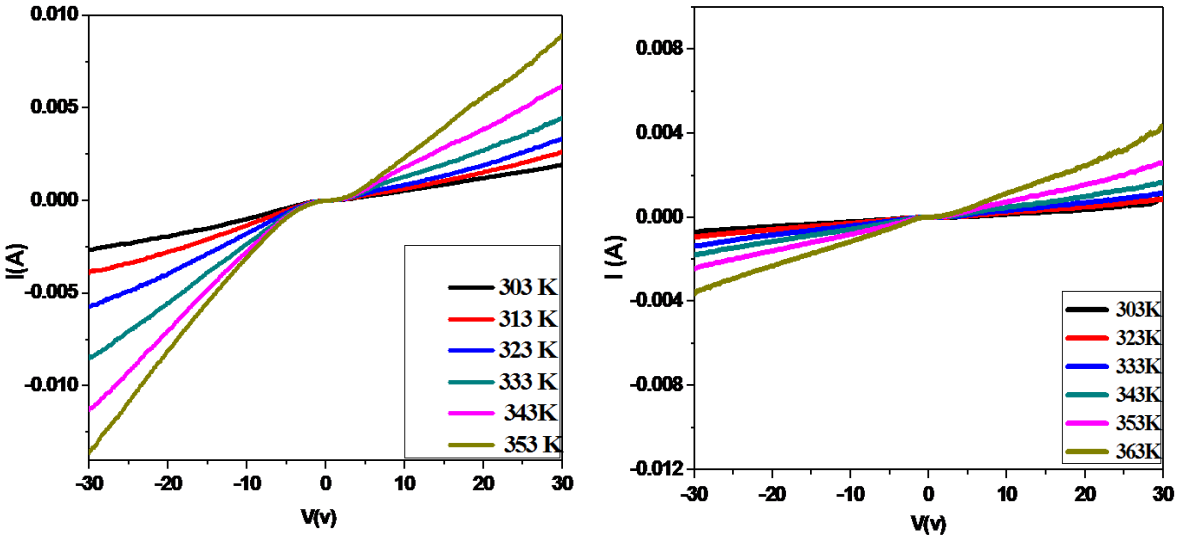

(a) (b)

Figure 3.20: Current-Voltage (I-V) curves for the LB film of HAT5+TiO_2 (10 wt.%) nanocomposites at target surface pressure (π_t) for (a) 5 mN/m (b) 20 mN/m at different temperature.

The I-V curves of HAT5+TiO_2 (10 wt.%) nanocomposites deposited at π_t = 5 and 20 mN/m also show the nonlinear behavior of I as a function of applied V and trend remains similar with increasing temperature (figure 3.20 (a) and (b)). The slope of I-V curves increases with increasing temperature. The change in slope for LB film of HAT5+TiO_2 (10 wt.%) nanocomposites deposited at π_t = 20 mN/m is less in comparison to LB film of TiO_2, HAT5 and HAT5+TiO_2 (10 wt.%) nanocomposites at π_t = 5 mN/m. So the LB film of HAT5+TiO_2 (10 wt.%) nanocomposites deposited at π_t = 5 mN/m is more conductive in comparison to that of LB film deposited at π_t = 20 mN/m. This is due to the nucleation of TiO_2 nanoparticles into large clusters at higher π_t and hence approaching closer to the pure TiO_2 film.

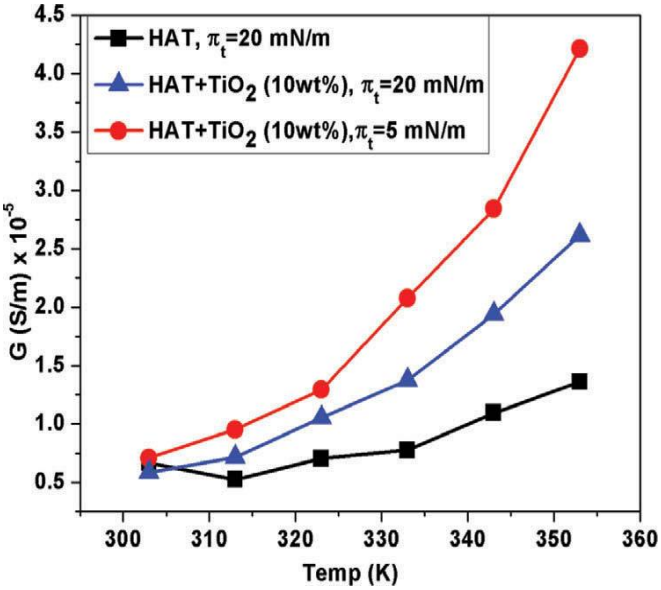

Figure 3.21: Conductivity curve as a function of temperature for the LB films of pure HAT5 and HAT5+TiO_2 (10 wt.%) nanocomposites deposited at different target surface pressure (π_t).

The conductivity (G) was calculated from I-V curves at different temperature for the LB films of pure HAT5 and HAT5+TiO_2 (10 wt.%) nanocomposites deposited at different π_t. The graph of G as a function of temperature for pure HAT5 and HAT5+TiO_2 (10 wt.%) nanocomposites at different π_t is plotted in figure 3.21. The value of G appears monotonically increasing with the increase in temperature. The curves show an increment in conductivity of HAT5 system after doping it with TiO_2 nanoparticles. The conductivity of HAT5 system increases even when a very small quantity of TiO_2 nanoparticle is doped in DLC.

The plot of ln G v/s 1/T for different temperatures shows an Arrhenius behavior of charge transport for LB film of pure HAT5 and HAT5+TiO_2 (10 wt.%) nanocomposites deposited at

different π_t as shown in figure 3.22.

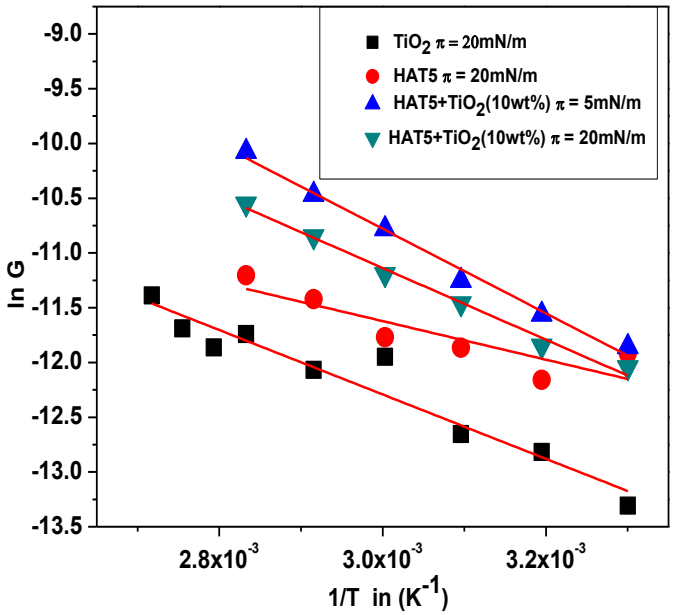

Figure 3.22: The plot of ln G as a function of 1/T for LB films of pure HAT5 and HAT5+TiO_2 nanocomposites (10 wt.%) at different target surface pressure (π_t). The solid line is a linear fit to the data points for the LB film of HAT5 and HAT5+TiO_2 (10 wt.%).

The trend of the Arrhenius plot is similar to the behavior of LB film of pure TiO_2 nanoparticles. The linear fit to the data corresponding to the LB film of HAT5 shows relatively some deviation from the linearity as compared to that for LB films of HAT+TiO_2. The E_A was calculated from slope of the curve. The E_A corresponding to LB films of pure HAT5 deposited at π_t = 20 mN/m and that of HAT5+TiO_2 (10 wt.%) deposited at π_t = 5 and 20 mN/m are 0.15, 0.33 and 0.28 eV, respectively. This indicates that due to incorporation of TiO_2 nanoparticles in the monolayer matrix of HAT5, not only the stability of the charge transport increases but also the activation energy increases. The E_A value decreases slightly with the increase in π due to nucleation of TiO_2 nanoparticles into large clusters at the higher π_t. This can be observed from the AFM images (figure 3.17) of LB film of pure HAT5 and HAT5+TiO_2 nanocomposites. The increase in E_A is also depends up on the concentration of the dopant and π_t. Here, TiO_2 is playing a role as a candidate for charge transport in organic material.

Our study reveals that the charge transport mechanism in ultrathin film of HAT5 can be controlled by altering the π_t of LB film deposition and may be the composition of HAT5 +TiO_2 nanoparticles. Such a control on the charge transport through the LB films may be very useful in optoelectronic device application.

3.5 Conclusion

The properties of the ultrathin film of a material are remarkably different as compared to those of its bulk form. We formed stable LF of TiO_2 nanoparticles at the A/W interface. A single layer of TiO_2 nanoparticles was fabricated onto HPL substrates. The morphological, optical, and electrical properties of such LB films were characterized. The LB films of TiO_2 deposited at higher π_t reveal a higher surface coverage, thereby yielding a higher density of crystalline defect sites. The UV-Vis spectroscopy of LB film of TiO_2 nanoparticles reveals that with the increase in π_t of deposition the optical property of LB film are closely approaches that of the bulk sample. The charge-transport mechanism in the LB film of TiO_2 nanoparticles shows an Arrhenius behavior of charge transport. Both the LB and spin coated film of TiO_2 nanoparticles are employed for ethanol sensing applications. The LB film of TiO_2 nanoparticles shows an appreciable and recoverable response toward ethanol sensing and spin-coated bulk material does not show any sensing toward the ethanol gas.

We doped HAT5 with TiO_2 nanoparticles and formed a stable LF of HAT5 and different wt.% of TiO_2 in HAT5 at A/W interface. We found condensation effect on the monolayer of HAT5+TiO_2 nanocomposites due to the presence of TiO_2 nanoparticles. A single layer of HAT5 and HAT5+ TiO_2 nanocomposites were fabricated onto HPL substrates. We observed a systematic reduction in the energy gap of the HAT5 system due to doping the system with TiO_2 nanoparticles. We observed an Arrhenius behavior of charge transport for LB film of HAT5 and HAT5+TiO_2 (10 wt.%) nanocomposites. We observed that the fewer amounts of TiO_2 nanoparticles (10 wt.%) in HAT5 can change the charge - transport behavior of HAT5. The conductivity and E_A of HAT5 increases with doping TiO_2 nanoparticles. The charge transport mechanism in thin film of HAT5 can be controlled by altering the π_t of LB film deposition in the composition of the HAT5 and TiO_2 nanoparticles. The LB films of HAT5+TiO_2 nanocomposites can be employed for some applications e.g. photovoltaic, sensing etc.

In the next chapter, we present our studies on the thin films of DLC doped with graphene.

References

1. L. Sang, Y. Zhao, C. Burda, Chem. Rev. 114, 9283, **2014**.
2. L. Liu, X. Chen, Chem. Rev. 114, 9890, **2014**.
3. A. Wisitsoraat, A. Tuantranont, E. Comini, G. Sberveglieri, W. Wlodarski, Thin Solid Films 517, 2775, **2009**.
4. D. R. Coronado, G. R. Gattorno, M. E. E. Pesqueira, C. Cab, R. D. Coss, G. Oskam,. Nanotechnology 19, 145605, **2008**.
5. D.C. Hurum, A. G. Agrios, K. A. Gray, T. Rajh, M. C. Thurnauer, J. Phys. Chem. B 107, 4545, **2003**.
6. G. Li, K. A. Gray, Chem. Phys. 339, 173, **2007**.
7. K. Saruwatari, H. Sato, T. Kogure, T. Wakayama, M. Iitake, K. Akatsuka, M. Haga, T. Sasaki, A. Yamagishi, Langmuir 22, 10066, **2006**.
8. H. Yuan, R. Lubbers, R. Besselink, M. Nijland, J.E. Elshof, ACS Appl. Mater. Interfaces 16, 8567, **2014**.
9. C. E. McNamee, S. Yamamoto, H. J. Butt, K. Higashitani, Langmuir 27, 887, **2011**.
10. M.Takahashi, K. Kobayashi, K. Tajima, Thin Solid Films 519, 8077, **2011**.
11. P. J. G. Coutinho, M. T. C. Mm Barbosa, J. Fluoresc. 16, 387, **2006**.
12. I. Piwonski, A. Kisielewska, J. Marczak, J. Porous Mater. 20, 1395, **2013**.
13. A. Facchetti , Y. Deng, A. Wang, Y. Koide, H. Sirringhaus, T. J. Marks, R. H. Friend, Ang. Chemie International Edition 39, 4547, **2000**.
14. M. Pope and C. E. Swenberg, Ann. Rev. Phys. Chem. 35, 613, **1984.**
15. E.O. Arikainen, N. Boden, R. J. Bushby, J. Clements, B. Movaghar, A. Wood, J. Mater. Chem. 5, 2161, **1995.**
16. N. Boden, R. C. Borner, R. J. Bushby, J. J, Clements, J. J. Am. Chem. Soc. 116, 10807, **1994**.
17. C. Catry, M. V. der Auweraer, F. C. De Schryver, H. Bengs, L. Haussling, O. Karthaus, H. Ringsdorf, Mac. Chem. Phy. 194, 2985, **1993**.
18. R. K. Gupta, V. Manjuladevi, C. Karthik, S. Kumar, K. Suresh, Coll. Surf. A 410, 91, **2012**.
19. R. K. Gupta, V. Manjuladevi, C. Karthik, S. Kumar, Journal of Physics. 417, 012068, **2013**.

20. O. Albrecht, W. Cumming, W. Kreuder, A. Laschewsky , H. Ringsdorf, Coll. Polym. Sci. 264, 8, 659, **1986**.
21. N. C. Maliszewskyj, P. A. Heiney, J. K. Blasie, J. P. McCauley Jr, A. B. Smith III, J. de Phys. II (France) 2, 75, **1992**.
22. A. Nayak, K. Suresh, S. Kumar Pal, and S. Kumar, J. Phys. Chem. B 111, 11157, **2007**.
23. D. Gidalevitz, O. Y. Mindyuk, P. A. Heiney, B. M. Ocko, P. Henderson, H. Ringsdorf, N. Boden, R. J. Bushby, P. S. Martin, J. Strzalka, J. Phys. Chem. B 101, 10870, **1997**.
24. S. Kumar, "*Chemistry Of Discotic Liquid Crystals: From Monomers To Polymers",* Taylor and Francis, US, **2010**
25. N. Banerjee, S. Roy, C. K. Sarkar, P. Bhattacharyya, IEEE Sens. J. 13, 1669, **2013**.
26. A. Hazra, S. Das, J. Kanungo, C. K. Sarkar, S. Basu, Sens. Actuators, B 183, 87, **2013**.
27. M. Babaei, N. Alizadeh Sens. Actuators, B 183, 617, **2013**.
28. P. P. Sahay, R. K. Nath, Sens. Actuators, B 134, 654, **2008**.
29. S. Ngamta, N. Boonprakob, N. Wetchakun, K. Ounnunkad, S. Phanichphant, B. Inceesungvorn, Mater. Lett. 105, 76, **2013**.
30. S. Paul, A. Choudhury, Appl. Nanosci. 4, 839, **2014**.
31. P. He, K. Fang, G. Zou, J. P. K. Peltonen, J. B. Rosenholm, Colloids Surf. A 201, 265, **2002**.
32. D. Langevin, F. Monroy, Curr. Opin. Colloid Interface Sci.15, 283, **2010**.
33. R. K. Gupta, V. Manjuladevi, "*Molecular Interaction at Interfaces"* Intech: Croatia, **2012**.
34. M. Poonia, R. K. Gupta, V. Manjuladevi, S. K. Gupta, J. Akhtar, J. Nanopart. Res. 16, 2572, **2014**.
35. C. P. Collier, R. J. Saykally, J. J. Shiang, S. E. Henrichs, J. R. Heath, Science 277, 1978, **1997**.
36. J. R. Heath, C. M. Knobler, D. V. Leff, J. Phys. Chem. B, 101,189, **1997**.
37. G. Markovich, C. P. Collier, J. R. Heath, Phys. Rev. Lett., 80, 3807, **1998**.
38. B. Lin, D.G. Schultz, X.-M. Lin, D. Li, J. Gebhardt, M. Meron, P. J. Viccaro, Thin Solid Films 515, 5669, **2007**.
39. M. Y. Lee, A. A. Acero, Z. Huang, S. A. Rice, Nature 367, 151, **1994**.
40. Y. Tabe, T. Yamamoto, I. Nishiyama, K. M. Aoki, M. Yoneya, H. Yokoyama, J. Phys.

Chem. B 106, 12089, **2002**.

41. F. Monroy, F. Ortega, R. G. Rubio, M. G. Velarde, Adv. Colloid Interface Sci. 134, 175, **2007**.
42. S. A. Ananthan, R. Suresh, K. Giribabu, V. Narayanan, J. Chem. Sci. 125, 1365, **2013**.
43. H. Pan, X. D. Wang, S. S. Xiao, L. G. Yu, Z. J. Zhang, Ind. J. Eng. Mater. Sci. 20, 561, **2013.**
44. G. Schmid, U. Simon, Chem. Commun. 6, 697, **2005**.
45. A. Hazra, K. Dutta, B. Bhowmik, P. Bhattacharyya, IEEE Sens. J. 15, 408, **2014**.
46. Y. Kwon, H. Kim, S. Lee, I. Chin, T. Seong, W. Lee, C. Lee, Sens. Actuators, B 173, 441, **2012**.
47. R. I. Bickley, T. G. Carreno, J. S. Lees, L. Palmisano, R. J. D. Tilley, J. Solid State Chem. 92, 178, **1991**.
48. C. Di Valentin, G. Pacchioni , A. Selloni, J. Phys. Chem. C 113, 20543, **2009**.
49. C. Karthik, K. Choudhary, A. Joshi, A. Gupta, Manjuladevi V., R. K. Gupta, S. Kumar, Adv. Sci. Lett. 20, 11382, **2014.**
50. L. S. Murov, L. G. Hug, I. Carmichael, "*Handbook of photochemistry*", CRC Press, US, **1963**.
51. P. S. Kumar, S. Kumar, V. Lakshminarayanan, J. Phys. Chem. B 112, 4865, **2008.**

Chapter-4

Study on Ultrathin Film of Discotic Liquid Crystal Doped with Graphene

4.1 Introduction

In the previous chapter, we have discussed about the ultrathin films of titanium dioxide (TiO_2) nanoparticles and discotic liquid crystal (DLC) doped with TiO_2 nanoparticles. We characterized the system and found that the in-plane conductivity increases due to incorporation of TiO_2 in DLC hexa-alkoxy triphenylene (HAT5) monolayer matrix. It will be interesting to study the surface behavior of the nanocomposite of DLC mixed with another shape compatible nanomaterial viz. graphene. In this chapter, we report the results of our studies on the surface behavior of DLC doped with graphene.

Graphene is a single layer of two-dimensional (2D) sp^2-hybridized carbon network which is gaining tremendous scientific attention due to its unique physicochemical properties such as charge transport mobility, tunable band gap, high elasticity [1,2], huge surface area [3], high electrical and thermal properties [4,5] and strong mechanical strength [6]. These unique properties of graphene have led to enormous possibilities of innovative applications including light emitting diodes (LEDs), solar cells, optoelectronics, sensors [7-10], nano-electronics [12-14] and spintronics [1,15].

Graphene and their functionalized form have been used for different applications in photovoltaics [7], optoelectronics [8], sensors [9-10] and electrochemistry [16, 17]. Functionalization and dispersion of graphene sheets are crucial for their end applications. Firstly, chemical functionalization of graphene enables this material to be processed by solvent-assisted techniques, such as layer-by-layer assembly, spin-coating and filtration [18]. Secondly, surface functionalization can improve the solubility of graphene in organic solvents. Carboxylic acid functionalized graphene (G-COOH) is easily dispersible in various polar solvents. The edge-modified functional groups tend to repel each other to effectively open up the edges of the G-

COOH, leading to self-exfoliation in solvent [19].

The presence of -COOH groups on the of graphene sheets provides hydrophilicity while the basal graphene plane remains largely hydrophobic. G-COOH monolayer may thus possess an overall amphiphilic character, which makes it possible to spread them and form stable Langmuir monolayer (LM) at air-water (A/W) interface. Such LM can be easily transferred onto solid substrate using Langmuir-Blodgett (LB) technique. Thin film of G-COOH is preferred in various applications due to its interesting properties [20]. The possible synthesis strategies of edge-carboxylated graphene (ECG) through a high energy ball milling and ECG nano-flakes from nitric acid oxidized arc-discharge material has been reported [21, 22]. Myung et al. [23] have reported the ECG nanoplatelets as oxygen-rich metal free cathodes for organic dye-sensitized solar cells.

Recently, Avinash et al. [24] have reported the self-assembly of DLC-graphene nanocomposites. They have used the discotic 1,5-dihydroxy- 2,3,6,7-tetrakis(3,7-dimethyloctyloxy) -9,10-anthraquinone for self-assembly in the presence of octadecylamine functionalized graphene (f-graphene) into an ordered sandwich like structure. They found that these composites are mutually ordered into a sandwich like structure and composites show higher conductivity compared to pure DLC. The f-graphene fillers act as bridges across defects resulting in efficient charge transport. The potential of discotic LC materials as active components has been demonstrated in organic semiconductor devices such as LEDs, field effect transistors [25], solar cells [26], photovoltaic cells [27]. DLCs behave as insulators in normal conditions. DLCs may be converted into semiconductors by doping with either electron rich or electron deficient molecules into the supramolecular order of the liquid crystalline phase [28].

Hexasubstituted triphenylene derivatives are the most broadly examined discotic materials because they have a strong tendency to form columnar mesophases, which are of interest in one-dimensional (1D) energy and electron transport devices [29]. It has been observed that the LB films of a polymer possessing triphenylene moieties in the side groups show in plane conductivity [30]. The efficiency and sensitivity of a device increases manifold, if the functional material is spread to form ultrathin films. Such enhancement occurs due to increase in surface-to-volume ratio of the material. There are some studies on the ultrathin films of DLC materials [31-35].

In this chapter, we have presented the results of our studies on a system of DLC, hexa-alkoxy triphenylene (HAT5) doped with G-COOH at A/W and air-solid (A/S) interfaces. We obtained a stable LF for different wt.% of HAT5 in G-COOH+HAT5 nanocomposites at A/W interface.

A single layer of LB films of pure HAT5, G-COOH, and G-COOH+HAT5 nanocomposites is transferred onto hydrophilically treated coverslips and silicon (Si/SiO_2) wafer at different target surface pressure (π_t). The LB films were characterized using ultraviolet-visible (UV-Vis) spectroscopy and spectro-fluorometer. We found that the energy gap of G-COOH decreases with doping of HAT5. The charge - transport mechanism in the LB film of G-COOH and G-COOH+HAT5 nanocomposites at different π_t were also studied. The conductivity of G-COOH+HAT5 nanocomposites was studied. Our study reveals enhancement in conductivity of the G-COOH+HAT5 nanocomposites by doping with HAT5.The topography and morphology of such LB films were characterized by using the atomic force microscope (AFM) and field emission scanning electron microscope (FESEM).

Monolayer of G-COOH+HAT5 nanocomposites was deposited on solid substrate using the LB and Inverse Langmuir Schaefer (ILS) techniques. Liquid crystal (LC) cells were made by sandwiching the LC between two indium tin oxide coated (ITO) glass plates on which G-COOH+HAT5 (50 wt.%) nanocomposites LB films were deposited. DLC decyloxytriphenylene (TP10) was filled in these LC cells and the dielectric constant was measured.

4.2 Materials and Experimental Methods

4.2.1 Materials

Hexa-alkoxy triphenylene (HAT5) molecule was synthesized by Prof. Sandeep Kumar, Raman Research Institute, Bengaluru [36]. The carboxylated graphene (G-COOH) was purchased commercially from Redex Technologies Pvt. Ltd and was used without further purification. The hexakis(decyloxy) triphenylene (TP10) was also synthesized by Prof. S. Kumar of Raman Research Institute, Bengaluru. Molecular structures of G-COOH, HAT5 and TP10 are shown in figure 4.1.

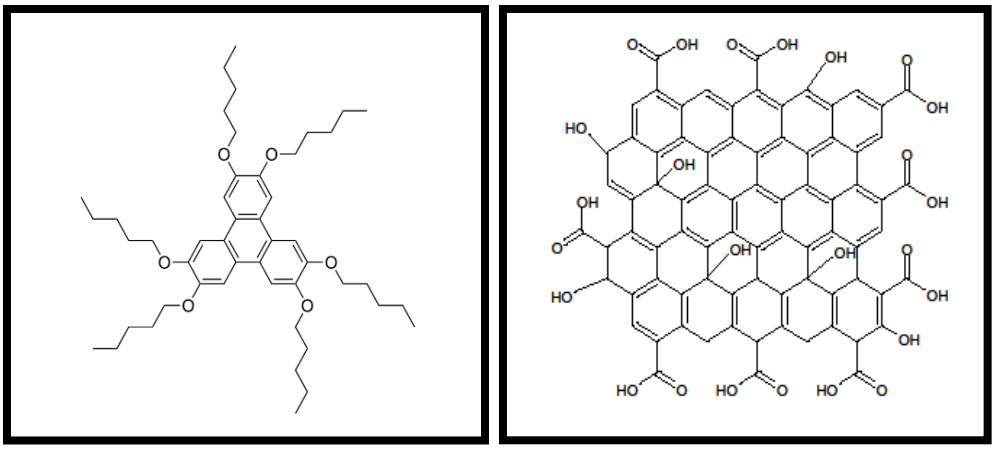

Figure 4.1: Chemical structure of (a) Hexa-alkoxytriphenylene (HAT5) (b) carboxylated graphene (G-COOH) and (c) hexakis(decyloxy)triphenylene (TP10) discotic liquid crystal molecule.

4.2.2 Experimental Methods

The solution of HAT5 was prepared in chloroform with a concentration of 0.5 mg/ml. The solution of G-COOH was also prepared in chloroform having a concentration of 0.05 mg/ml. The solution of uniformly dispersed G-COOH is obtained by ultra-sonicating the G-COOH-chloroform solution for around 45 minutes. The solutions were mixed appropriately so as to obtain G-COOH+HAT5 nanocomposites of 5, 10, 20 and 50 wt. % of HAT5 in G-COOH and an appropriate quantity was spread on water surface. The LF of pure HAT5, G-COOH and G-COOH+HAT5 nanocomposites were formed in a LB trough by spreading appropriate volume of

these solutions very slowly using a microsyringe onto ultrapure ion-free water subphase separately. About ~ 30 minutes was allowed for the solvent to evaporate from the water subphase before compressing the film. The surface pressure (π) - area per μg (A_w) isotherms for G-COOH+HAT5 nanocomposites were obtained by compressing the film symmetrically using the two barriers of the LB trough and recorded the π simultaneously using an integrated balance. The barrier speed during compression was maintained at 40 mm/min.

The LF of G-COOH+ HAT5 nanocomposites were transferred onto solid substrate e.g. Si/SiO_2 wafer, glass cover slip and ITO glass plates. The Si/SiO_2 and glass cover slip substrates were cleaned with ethanol and treated with piranha solution and rinsed with ultrapure ion-free water prior to any deposition. The ITO substrates were procured commercially and used after cleaning them thoroughly by ultrapure ion-free water, absolute alcohol and HPLC grade chloroform, successively. The substrates were dried by blowing hot air at about 60°C.

The monolayer of LB films of G-COOH+HAT5 nanocomposites are deposited at different value of π_t by a single upstroke motion of the dipper at a speed of 5 mm/min. The transfer ratio for LB film deposition on substrates was found to be 1 ± 0.1.

The LM of G-COOH + HAT5 nanocomposites were also transferred onto solid substrate using ILS method. In ILS method, solid substrate is kept immersed under the water subphase before spreading the monolayer. The substrate is kept tilted (~15°) with respect to the horizontal. This is to facilitate the adsorption of the LM and drainage of the entrapped water between the film and the substrate (figure 4.2).

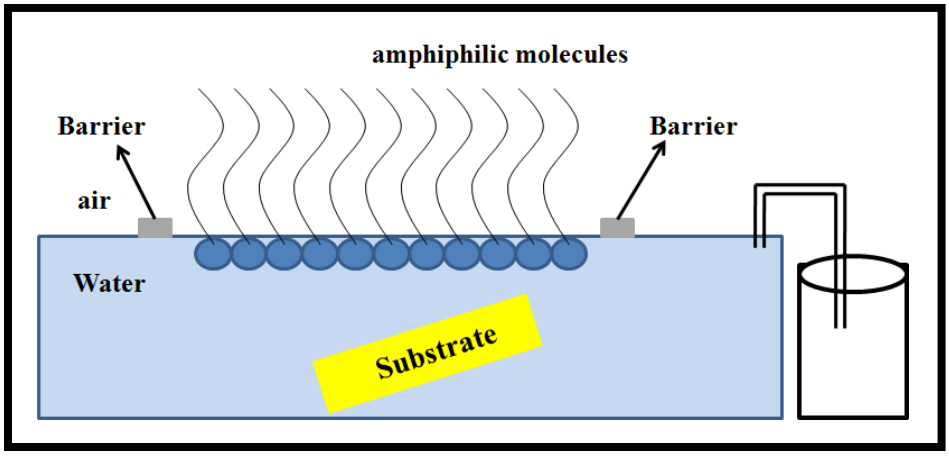

Figure 4.2: Schematic diagram of method for deposition of Inverse Langmuir Schaefer film of amphiphilic molecules at air-water interface.

The monolayer is formed by spreading the molecules on water subphase. After achieving the required π_t, the aqueous subphase is siphoned out very slowly from the other side of the barriers. As the level of water recedes, the monolayer gets adsorbed onto the substrate.

4.2.3 Characterization

The optical property of the LB films of HAT5, G-COOH and G-COOH+HAT5 nanocomposites deposited onto substrates were studied using UV-Vis spectrophotometer. The UV-Vis spectra were recorded in transmission mode. The emission spectra of LB films of HAT5, G-COOH and G-COOH+HAT5 nanocomposites were recorded using a spectro-fluorometer from Horiba Jobin Yvon (Fluoro Max-4). The charge-transport mechanism in the LB film of G-COOH+HAT5 nanocomposites were studied by using I-V characteristic measurement. The LB films of G-COOH+HAT5 nanocomposites were transferred to the scanning stage of the AFM and the films were scanned in the contact mode. The images were analyzed using the NTMDT proprietary software. The morphology of LB film of G-COOH+HAT5 nanocomposites deposited on Si/SiO_2 substrates was carried out using FESEM.

LC cells were fabricated using LB and ILS films of G-COOH+HAT5 nanocomposites deposited onto solid substrates. The dielectric constant of DLC TP10 enclosed in such LC cell was measured.

4.3 Results and discussion

4.3.1 Surface manometry of G-COOH+HAT5 nanocomposites at A/W interface

The surface manometry of G-COOH, HAT5 and G-COOH+HAT5 nanocomposites at the A/W interface was studied. The isotherm of pure G-COOH (inset of figure 4.3) shows a lift - off area (A_i) to be around ~ 2.2 $cm^2/\mu g$. Initially the π rises slowly on decreasing the area. There is a rapid increase in π at area less than 2 $cm^2/\mu g$. The region of the isotherm corresponding to the sharp rise in the π may indicate a liquid-like phase of G-COOH film at the A/W interface. The monolayer collapses at π = 11 mN/m. The collapse is indicated by a change in the slope.

The isotherm of HAT5 shows the A_i at around 8 $cm^2/\mu g$. The π rises rapidly thereafter on decreasing the area. The monolayer collapses with the collapse surface pressure (π_c) of ~ 30 mN/m. The region of the isotherm corresponding to the sharp rise in the π may indicate a liquid-like phase of HAT5 monolayer at the A/W interface. Due to the incorporation of even very small

amount of HAT5 in G-COOH, the isotherm shifts towards higher area per µg. Similar shift in the isotherms is obtained for all the composition of the G-COOH+HAT5. It is noteworthy, that the isotherm corresponding to the 20 and 50 wt% of HAT5 in G-COOH are shifted towards higher area per µg compared to that of pure HAT5 molecules. The value of A_i increases on increasing the wt.% of HAT5 in the LM of G-COOH+HAT5 nanocomposites. The A_i values obtained from isotherm are 5.6, 8, 11, 10.33 cm^2/µg for 5, 10, 20, 50 wt.% of HAT5 in G-COOH+HAT5 nanocomposites respectively. The shift in the isotherms due to incorporation of HAT5 in G-COOH towards higher area per µg is an indication of expansion of the monolayer due to some complex formation between G-COOH and HAT5.

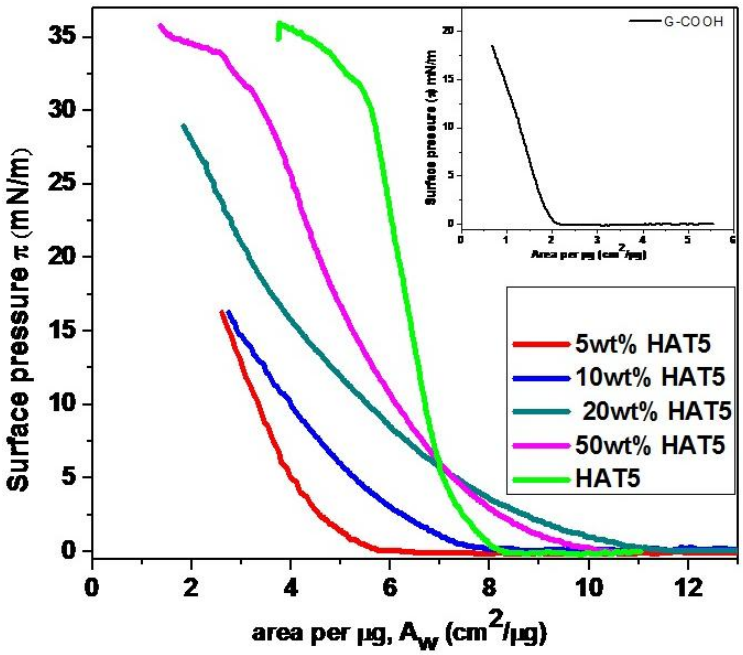

Figure 4.3: Surface pressure (π) - Area per µg (A_w) isotherms of Langmuir monolayer of the pure G-COOH (inset), HAT5 and G-COOH+HAT5 nanocomposites with different wt.% of HAT5 at air-water interface.

The rigidity and elasticity (E) of the Langmuir film (LF) can be calculated employing the eq. 4.1,

$$E = -(A_w)\, d\pi/dA_w \qquad 4.1$$

The E vs A_w curve provides insight into the elastic nature of the LF and shows weak phase transition in the LF at A/W interface.

The variation of E vs A_w for G-COOH, HAT5 and G-COOH+HAT5 nanocomposites is shown in figure 4.4. The maximum value of E for pure HAT5 and G-COOH in the liquid-like phase was

obtained ~ 120 and 25 mN/m, respectively. The maximum value of E ~ 27.3 mN/m was obtained for G-COOH +HAT5 (5 wt.%) nanocomposites in the liquid-like phase. We found the maximum value of E ~ 18.2, 20 and 42mN/m for 10, 20 and 50 wt.% of HAT5 in G-COOH+HAT5 nanocomposites in the liquid-like phase. These values are comparable to the liquid-like phase of LF of some reported hydrophobic polymers [37]. The liquid-like phase destabilizes upon further compression, leading to a decrease in the value of E indicating an initiation of the collapse of the film. Though the collapse of the LF of G-COOH and G-COOH+HAT5 nanocomposites was not evident from the isotherm, the indication of the collapse can be seen from the E vs A_w curves.

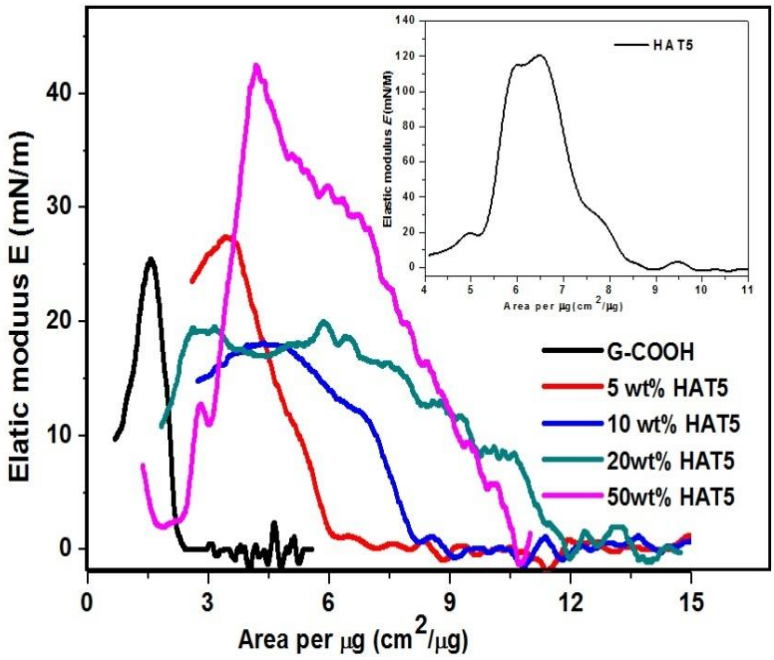

Figure 4.4: Elasticity (E) - Area per µg (A_w) curves of pure G-COOH and G-COOH+HAT5 nanocomposites at the air-water interface and E-A_w curve for the pure HAT5 is shown in inset.

The miscibility or the phase separation of two components for the study the molecular organization of the mixed monolayer at the A/W interface can be calculated on the basis of the π-A_w isotherms for various wt.% using the excess criterion and the surface phase rule [38].

For an ideal case of complete miscibility or immiscibility of two-component monolayer system, the area of the mixed monolayer is given by the rule of additivity,

$$A_{id} = A_1X_1 + A_2X_2 \qquad 4.1$$

where X_1 and X_2 are wt.% of the components 1 and 2, respectively. A_1 and A_2 are the area of the individual pure component monolayer. However, for a mixed system, the monolayer area can deviate from the ideal case. Such deviation in the monolayer area depends on the nature of the interaction between the component molecules and is known as the excess area per molecule, A_{ex}. The A_{ex} is defined as

$$A_{ex} = A_{12} - A_{id} \qquad 4.2$$

where A_{12} is the experimentally determined values of the area of the mixed monolayer. A_{id} is the ideal area value calculated from equation 4.1. The negative or positive value of the A_{ex} indicates an attractive or repulsive interaction, respectively between the component molecules in the mixed monolayer [38, 39].

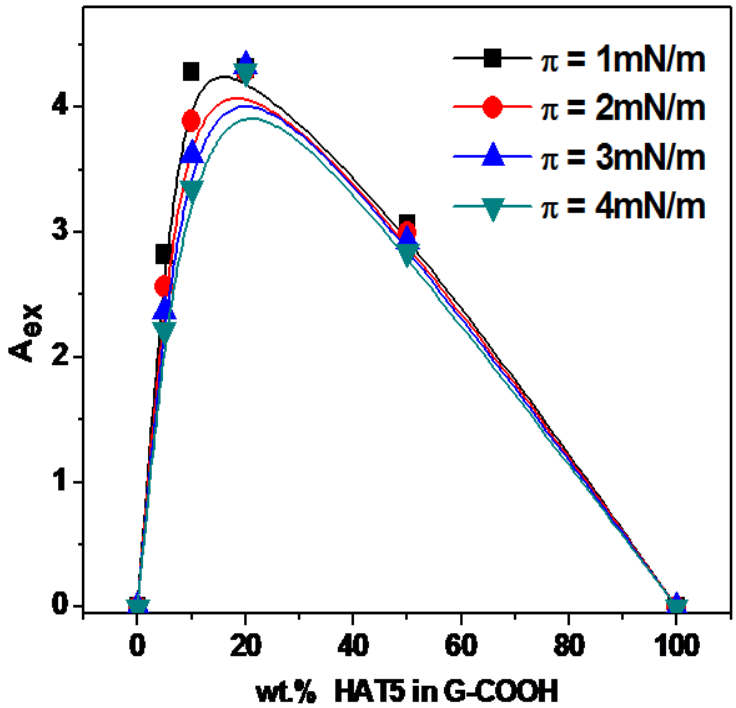

Figure 4.5: Excess area per molecule (A_{ex}) as a function of wt.% of HAT5 in G-COOH at different surface pressures (π). The points indicate the calculated values obtained from the experimental data.

The excess area per molecule A_{ex} is calculated using equation 4.2 for G-COOH+HAT5 nanocomposites at π =1, 2, 3 and 4mN/m and is shown in figure 4.5. The curve shows positive values at different π_t for all wt.% of HAT5 in G-COOH+HAT5 nanocomposites. This indicates a

repulsive interaction between HAT5 and G-COOH or expansion of the film due to some complex formation between HAT5 and G-COOH.

The LB films of G-COOH, HAT5 and G-COOH+ HAT5 nanocomposites (10, 20 and 50 wt.%) are deposited onto glass coverslips, Si/SiO_2 and ITO plate at the different values of π_t.

4.3.2 Characterization of G-COOH+HAT5 nanocomposites at A/S interface

4.3.2.1 UV-Vis Spectroscopy

The optical property of the LB films of G-COOH+HAT5 nanocomposites deposited on coverslips was investigated using UV-Vis spectroscopy. The spectra of the LB films deposited on cover slip are shown in figure 4.6. We observed a peak at 292 nm for G-COOH and at 296 nm for HAT5 system. We observe red shift in the spectrum from 293 to 296 nm for LB film of G-COOH+HAT5 nanocomposites with increase in wt.% of HAT5 in the nanocomposites. The value of absorbance reduced for 10 wt.% of HAT5 in the nanocomposites whereas it increase dramatically for the 20 and 50 wt.% of HAT5 in the nanocomposites.

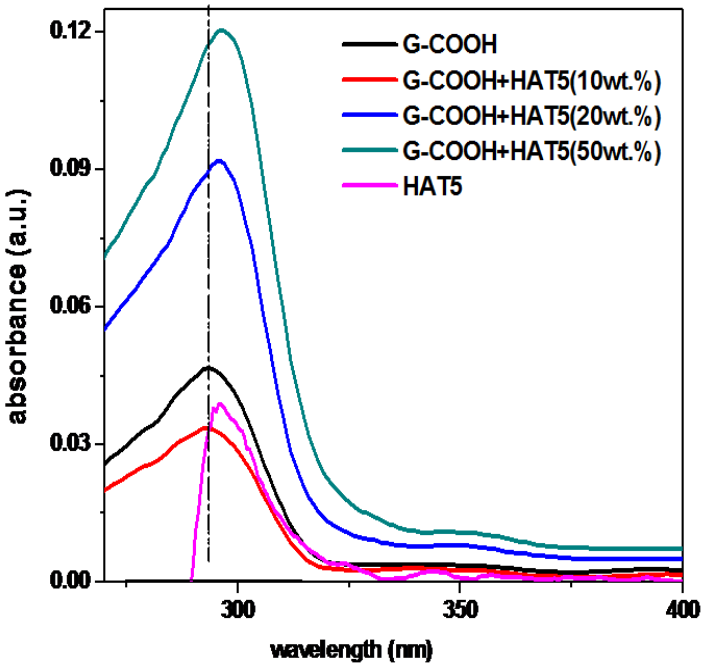

Figure 4.6: UV-Vis absorption spectra measurements for LB films of G-COOH, G-COOH+HAT5 nanocomposites with 10, 20 and 50 wt. % of HAT5 deposited on the glass coverslips.

4.3.2.2 Photoluminescence

The photoluminescence emission spectra of HAT5, G-COOH and G-COOH+HAT5 nanocomposites are shown in figure 4.7 The spectrum of G-COOH film at an excitation wavelength 350 nm shows the emission peaks at 436, 467 and 518 nm (in figure 4.7(a)). The emission spectrum of DLC HAT5 at an excitation wavelength of 330 nm is shown in figure 4.7(b). It shows the emission peaks at 473, 507 and 533 nm.

The emission spectra of LB film of G-COOH+HAT5 nanocomposites at an excitation wavelength 325 nm are also shown in figure 4.7(a). We observe red shift in the spectrum for LB film of G-COOH+HAT5 nanocomposites with increase in wt.% of HAT5 in G-COOH+HAT5 nanocomposites.

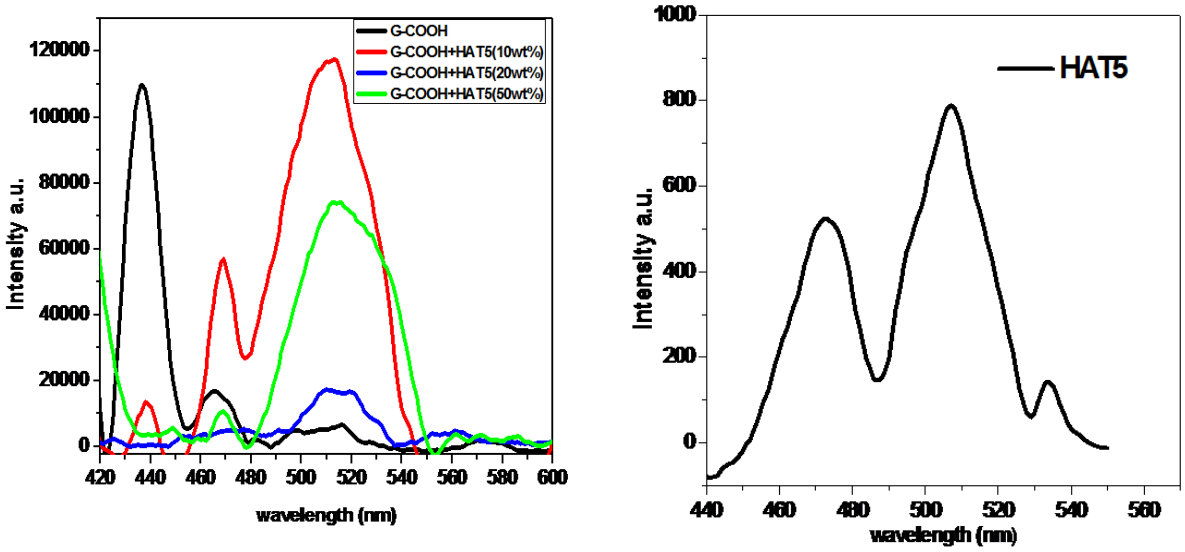

(a) (b)

Figure 4.7: The emission spectra of LB film of (a) G-COOH, G-COOH+HAT5 nanocomposites (b) HAT5 deposited on the glass.

The emission curve of G-COOH+HAT5 nanocomposites shows the features of HAT5 as well as G-COOH. The emission peaks were observed for G-COOH+HAT5 (10 wt.%) nanocomposites at 439, 470, 513 nm. For 20 wt.% HAT5 in G-COOH+HAT5 nanocomposites, the emission peak were observed at 432, 469, 480 and 513 nm. The spectra for G-COOH+HAT5 (50 wt.%) nanocomposites shows the emission peaks at 448, 468 and 515 nm. The intensity of G-COOH+HAT5 nanocomposites increases with increase in wt.% of HAT5 in G-COOH+HAT5 nanocomposites.

4.3.2.3 Current-Voltage (I-V) Characteristics

The charge - transport mechanism in the LB film of G-COOH+HAT5 nanocomposites was investigated by the current-voltage (I-V) measurement in current-in-plane (CIP) geometry.

We fabricated LB film of HAT5, G-COOH, G-COOH+HAT5 (10 and 50 wt.%) nanocomposites at different π_t on gold deposited electrodes on Si substrate, and the charge - transport mechanism was studied. The I-V curves for the LB film of G-COOH, HAT5 and G-COOH+HAT5 nanocomposites were recorded at different temperature (T).

The conductivity (G = dI/dV) versus T curves of LB film of G-COOH, HAT5 and G-COOH+HAT5 (10 and 50 wt.%) nanocomposites are shown in figure 4.8. The value of G increases monotonically with the increase in temperature. The curves show an increment in conductivity of G-COOH+HAT5 nanocomposites as compared to the pure HAT5 and G-COOH.

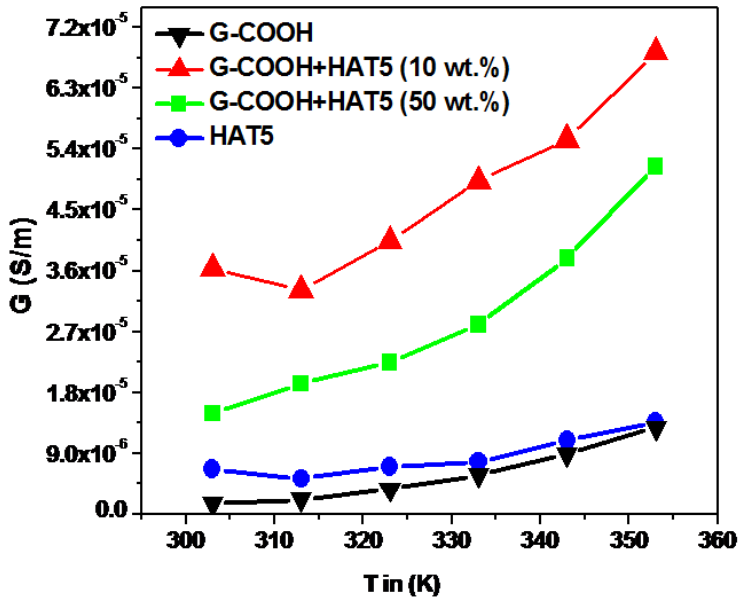

Figure 4.8: Conductivity curve as a function of temperature for the pure G-COOH, pureHAT5 and G-COOH+HAT5 nanocomposites.

A plot of ln (G) versus 1/T for G-COOH, HAT5 and G-COOH+HAT5 nanocomposites is shown in figure 4.9. A linear fit to the data corresponding to an LB film of G-COOH, HAT5 and G-COOH+HAT5 nanocomposites indicates an Arrhenius behavior of charge transport. The activation energy (E_A) was calculated from slope of the curve. The E_A corresponding to LB films of G-COOH, HAT5 and G-COOH+HAT5 nanocomposites for 10 and 50 wt.% of HAT5 are 1.23, 0.15, 0.12 and 0.22 eV, respectively.

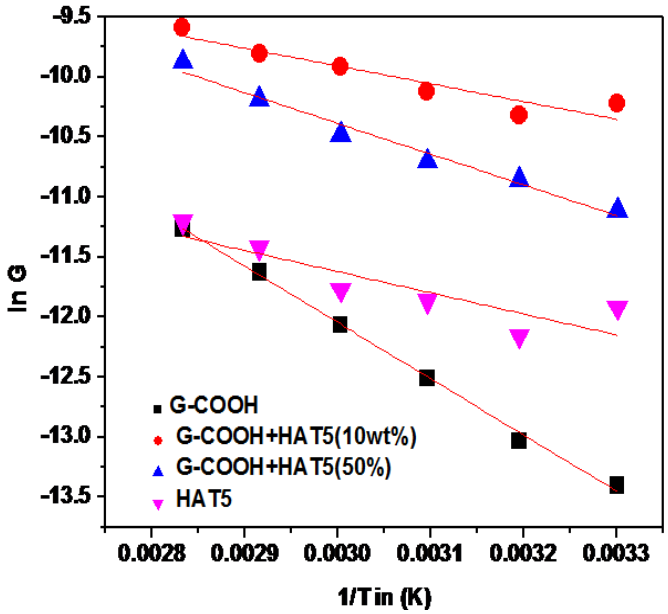

Figure 4.9: The plot of ln G as a function of 1/T for LB films of pure G-COOH, pure HAT5 and G-COOH+HAT5 nanocomposites. The solid line is a linear fit to the data.

4.3.2.4 Atomic Force Microscopy

A single layer of LB film of G-COOH+HAT5 nanocomposites (10, 20 and 50 wt.%) were transferred on Si/SiO_2 substrates at different values of π_t and scanned using AFM. The topography of LB film of G-COOH+HAT5 nanocomposites are shown in figure 4.10

The topographic images of LB film of G-COOH+HAT5 nanocomposites (10 wt.%) deposited on Si substrate at π_t = 5 mN/m shows stacks or network of G-COOH with small bright oval domains (in figure 4.10(a)). These small bright domains may represent the HAT5 molecules. The density of these bright domain increases with increase in the wt.% of HAT5 in G-COOH+HAT5 nanocomposites. Figure 4.10(b) shows the topographic images of LB film of G-COOH+HAT5 (20 wt.%) deposited on Si/SiO_2 substrate at π_t = 10 mN/m. It shows the bright domains with uniform film in the background. The topographic images of LB film of G-COOH+HAT5 (50 wt.%) deposited on Si/SiO_2 substrate at π_t = 15 mN/m is shown in figure 4.10(c). As the wt.% of HAT5 increases in G-COOH+HAT5 nanocomposites the bright dots get arranged in a ring pattern. The HAT5 molecules assemble in a circular ring pattern with ~ 180 to 300 nm size of inner diameter. The width of these circular rings lies in the range of 60 to 80 nm. The patches due to G-COOH can be observed in the background (figure 4.10(c)).

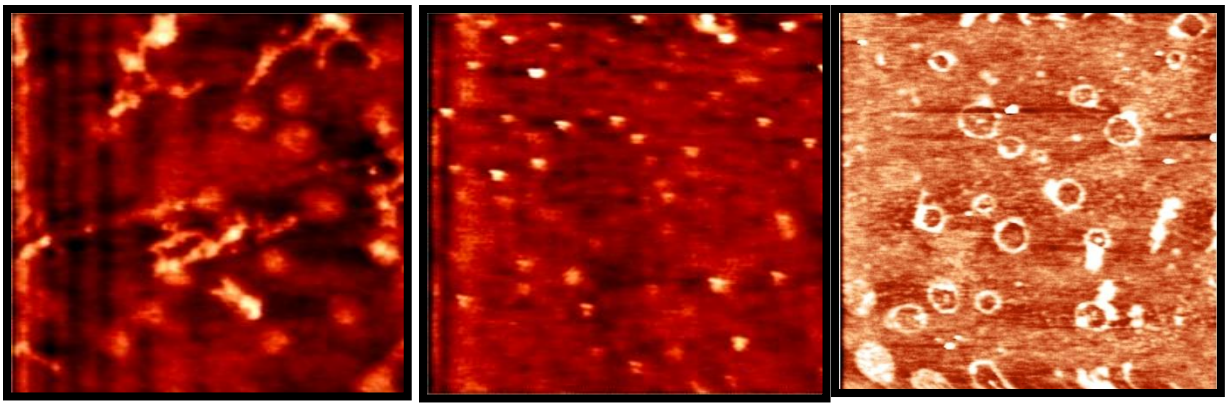

(a) (b) (c)

Figure 4.10: The AFM images of LB films of G-COOH+HAT5 nanocomposites for (a) 10 wt.% of HAT5 deposited at target surface pressure (π_t) = 5 mN/m, (b)20 wt.% of HAT5 deposited at π_t = 10 mN/m and (c)50 wt.% of HAT5 deposited at π_t =15 mN/m. The size of images (a) and (c) is 5x5 and (c) is 2x2 μm^2 respectively.

4.3.2.5 Field Emission Scanning Electron Microscopy

The surface morphology of LB film of G-COOH+HAT5 nanocomposites is obtained using FESEM. Figure 4.11 shows the FESEM images of LB film of G-COOH+HAT5 nanocomposites deposited on Si/SiO_2 substrates at different π_t.

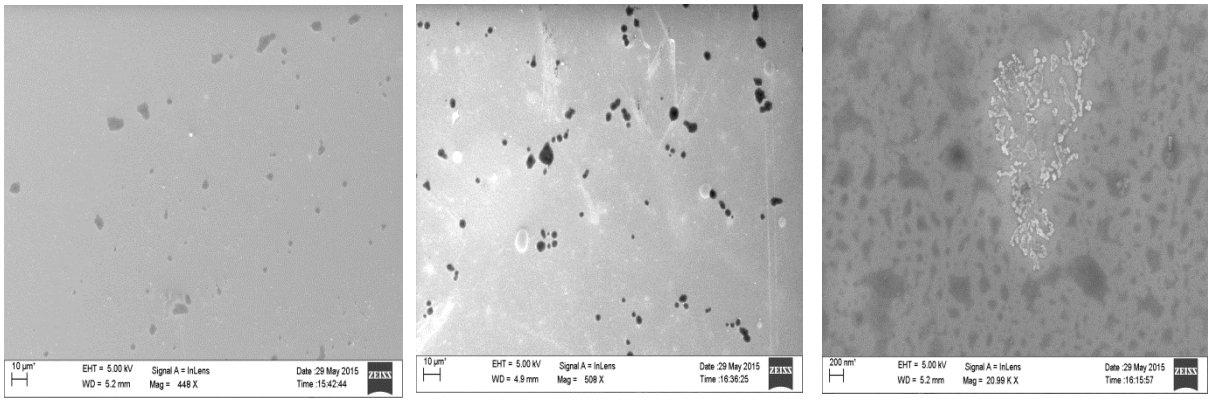

Figure 4.11: The FESEM images of LB films of G-COOH+HAT5 nanocomposites for (a) 10 (b) 20 and (c) 50 wt.% of HAT5 in G-COOH+HAT5 nanocomposites deposited on S/SiO_2 substrate.

The FESEM image (figure 4.11(a)) of LB film of G-COOH+HAT5(10 wt.%) at π_t = 5 mN/m shows a black region with gray bright region in the background. The black region may

represent the HAT5 molecules. As the wt.% of HAT5 increases in G-COOH+HAT5 nanocomposites, the density of black region increases (figure 4.11(b) and 4.14(c)). The thick domain of G-COOH (bright gray region) are clearly visible in the figure 4.11(b) and 4.11(c).

4.3.3 Dielectric constant measurement

We have fabricated LC cell using ITO coated glass plates. We have prepared LC cell using unidirectional rubbed polyimide coated ITO substrates. The LC cells are also fabricated by depositing LB and ILS film of G-COOH+HAT5 nanocomposites (50 wt.%) on the ITO substrate. All the LC cells were ~ 8 μm thick. The DLC exhibiting rectangular columnar phase (TP10) was filled in these LC cells. The phase sequence of TP10 is Cr-45°C-Col_h-69°C-Iso. The optical texture of TP10 in such LC cells is shown in figure 4.12. The optical texture indicates the columnar phase exhibited by TP10 enclosed in the cells. Dielectric constant measurements were carried out all of these LC cells.

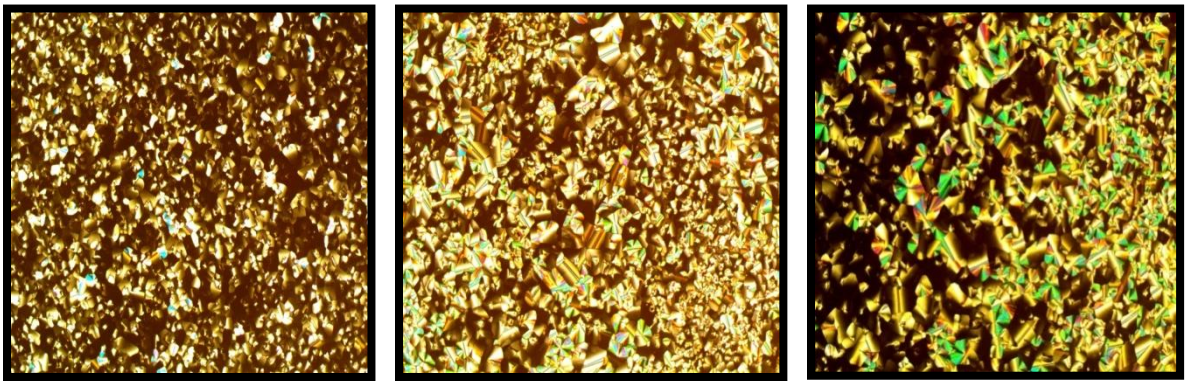

(a) (b) (c)

Figure 4.12: The polarizing optical microscopy textures of the TP10 in LC cell fabricated using (a) polyimide coated ITO (b) bare ITO and (c) LB film of G-COOH+HAT5 nanocomposites (50 wt.%) on the ITO substrate.

The temperature variation of dielectric constant (ε) for LC cells fabricated using bare ITO, polyimide coated ITO and LB & ILS film of G-COOH+HAT5 nanocomposites deposited on ITO substrates are shown in figure 4.13. The value of dielectric constant of TP10 is slightly enhanced in LC cell fabricated using LB film of G-COOH+HAT5 nanocomposites as an alignment layer in comparison to all other cells. The LB film of G-COOH+HAT5 nanocomposites seems to be a better alignment layer in comparison to all other alignment layers

used in this study.

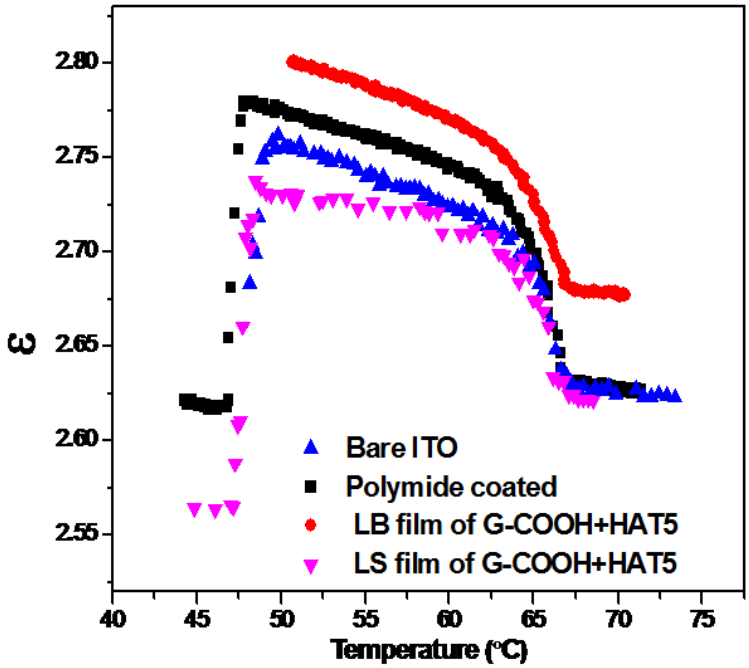

Figure 4.13: Dielectric constant (ε) of TP10 measured in LC cell fabricated using bare ITO substrate, polyimide coated ITO and LB and ILS film of G-COOH+HAT5 (50 wt.%) nanocomposites deposited ITO substrate.

4.4 Conclusion

The surface manometry on HAT5, G-COOH and their composites shows very interesting result. The LM of G-COOH exhibits gas and a liquid-like phase. Structurally similar organic discotic liquid crystal molecule (HAT5) was incorporated in the monolayer matrix of G-COOH. The surface manometry of such mixed monolayer system indicated the evidence of repulsive interaction or complex formation between the components. The UV-Vis spectroscopy on the LB films of the nanocomposite reveals red shift in the characteristic peak and thereby leading to a systematic decrease in energy gap due to incorporation of HAT5 in G-COOH monolayer matrix. The in-plane conductivity of the LB films of the nanocomposites enhances as compared to that of pure components. The surface morphology obtained using FESEM shows uniform film over the 2D surface. The signature of both HAT5 and G-COOH were seen from the images. The dielectric measurements indicate that the LB film of the nanocomposites provide better

alignment of discotic liquid crystals as compared to some other mechanism of obtaining the alignment layer in the LC cells.

The morphology of LB films depends on various factors including the π_t, temperature, pH, and ion contents in the subphase. The stress exerted by the monolayer onto the Wilhelmy plate was found to be dependent on the direction of compression of the monolayer at the A/W interface. In the next chapter, we will discuss the effect of such stress on the morphology of LB films of stearic acid deposited onto solid substrate. Such LB film are employed for aligning bulk LC.

References

1. K. S. Novoselov, A. K. Geim, S. V. Morozov, D. Jiang, M. I. Katsnelson, I. V. Grigorieva, S. V. Dubonos, A. A. Firsov, Nature 197,438, **2005**.
2. T. Ohta, A. Bostwick, T. Seyller, K. Horn, E. Rotenberg , Science 313, 951, **2006**.
3. A. K. Geim, K. S. Novoselov, Nat Mater. 6, 183, **2007**.
4. R. F. Service, Science 324, 875, **2009.**
5. A. A. Balandin , S. Ghosh,W. Bao, I. Calizo, D. Teweldebrhan, F. Miao, C. N. Lau, Nano Letters 8, 902, **2008.**
6. C. Lee, X. Wei, J. W. Kysar, J. Hone, Science 321, 385, **2008**.
7. K. S. Novoselov, V. I. Falko, L. Colombo, P. R. Gellert, M. G. Schwab, K. Kim, Nature 490, 192, **2012**.
8. F. Bonaccorso, Z. Sun, T. Hasan, A. C. Ferrari, Nat Photon 4, 611, **2010**.
9. Y. Dan, Y. Lu, N. J. Kybert, Z. Luo, A. T. C. Johnson, Nano Letters 9, 1472, **2009**.
10. S. Borini , R. White, D. Wei, M. Astley, S. Haque, E. Soigone, N. Harris,J.Kivioja, T.Ryhanen, ACS Nano 7, 11166 , **2013**.
11. F. Schedin, A. K. Geim, S. V. Morozov, E. W. Hill, P. Blake, M. I. Katsnelson, K.S. Novoselov, Nat. Mater. 6, 652, **2007**.
12. A. K. Geim, K. S.Novoselov, Nat. Mater. 6, 183, **2007.**
13. M. I. Katsnelson, Mater. Today 10, 20, **2007**.
14. L. A. Ponomarenko, F. Schedin, M. I. Katsnelson, R. Yang, E. W. Hill, K.S. Novoselov, A. K. Geim, Science 320, 356, **2008**.
15. Y. W. Son, M. L. Cohen, S.G. Louie, Nature**,** 444, 347, **2006**.
16. Y. Yang , S. Li, L. Zhang, J. Xu, W. Yang, Y. Jiang, ACS Applied Materials & Interfaces 5, 4350, **2013.**
17. B. Wang, D. Su, J. Park, H. Ahn, G. Wang, Nanoscale Research Letters 7, 215, **2012.**
18. T. Kuila, S. Bose, A. K. Mishra, P. Khanra, N. H. Kim, J. H. Lee *"Chemical functionalization of graphene and its applications",* Progress in Materials Science 57,1061**, 2012.**

19. I.Y. Jeon, Y.R. Shin,G. J. Sohn, H. J.Choi, S.Y. Bae, J. Mahmood, S. M.Jung, J. M. Seo, M. J. Kim, D. W. Chang, L. Dai, J. B. Baek, Proceedings of the National Academy of Sciences 109, 5588, **2012.**
20. V. A. Chhabra, A. Deep, R. Kaur, R. Kumar, International Journal for Science and Emerging Technologies with Latest Trends 4, 13, **2012**.
21. G. Bharath, V. Veeramani, S. M. Chen, R. Madhu, M. M.l Raja, A. Balamurugan, D. Mangalaraj, C. Viswanathan, N. Ponpandian, RSC Adv. 5, 13392, **2015**.
22. C. G. Salzmann, V. Nicolosi, M. L. H. Green, J. Mater. Chem. 20, 314, **2010.**
23. M. J. Ju, I.Y. Jeon, K. Lim, J. C. Kim, H.J. Choi,I. T. Choi, Y. K. Eom, Y. J. Kwon, J. Ko, J. J. Lee, J.B. Baek, H. K. Kim. Energy Environ. Sci. 7, 1044, **2014**.
24. B. Avinash, Shivanandareddy, S. Krishnamurthy, V. Lakshminarayanan, S. Kumar, Chem. Commun. 50,710, **2014**.
25. S. Kumar, Chem. Soc. Rev. 35, 83, **2006.**
26. S. Sergeyev, W. Pisula, and Y. H. Geerts, Chem. Soc. Rev. 36,1902 , **2007**.
27. L. S. Mende, A. Fechtenkotter, K. Mullen, E. Moons, R. H. Friend, J. D. MacKenzie, Science 293, 1119, **2001.**
28. P. Suresh Kumar, S. Kumar, V. Lakshminarayanan, J. Appli. Phy. 106,093701 , **2009.**
29. S. Kumar, S. K. Gupta, Tetrahedron Letters 52, 5367, **2011.**
30. C. Catry, M. V. der Auweraer, F. C. De Schryver, H. Bengs, L. Haussling, O. Karthaus, H. Ringsdorf, Mac. Chem. Phy. 194, 2985**, 1993.**
31. R. K. Gupta, V. Manjuladevi, C. Karthik, S. Kumar, Journal of Physics., 417, 012068, **2013**.
32. O. Albrecht, W. Cumming, W. Kreuder, A. Laschewsky , H. Ringsdorf, Coll. Polym. Sci. 264, 8, 659, **1986**.
33. N. C. Maliszewskyj, P. A. Heiney, J. K. Blasie, J. P. McCauley Jr, A. B. Smith III, J. de Phys. II, 2, 75, **1992**.
34. A. Nayak, K. Suresh, S. Kumar Pal, and S. Kumar, J. Phys. Chem. B 111, 11157, **2007**.
35. D. Gidalevitz, O. Y. Mindyuk, P. A. Heiney, B. M. Ocko, P. Henderson, H. Ringsdorf, N. Boden, R. J. Bushby, P. S. Martin, J. Strzalka, J. Phys. Chem. B 101, 10870, **1997**.
36. S. Kumar, "*Chemistry of Discotic Liquid Crystals: From Monomers To Polymers*", Taylor and Francis, US, **2010**.

37. D. Langevin, F. Monroy, Current Opinion in Colloid & Interface Science 15, 283, **2010.**
38. G. L. Gains, "*Insoluble Monolayers at Liquid-Gas Interface*", Interscience, New York, USA, **1996.**
39. A. Angelova, M. A. Van der, R. Ionov, D. Vollhardt, F.C.de Schreyver, Langmuir 11, 316, **1995.**

Chapter-5

Morphological Transformation in Langmuir-Blodgett Films of Stearic Acid and its Effect on Alignment of Bulk Liquid Crystal

5.1 Introduction

The alignment layer plays crucial role in the liquid crystal (LC) based devices. The surface morphology/functionality can induce the alignment of the interfacial layer of the LC molecules which in turn can govern the growth of the bulk LC in the LC cell. The surface morphology or functionality can tailored by the deposition of thin films using self-assembly or Langmuir-Blodgett (LB) techniques. LB technique can provide numerous advantages including the control over the surface density, number of layers and functional properties. Hence, a thin layer of LB films can be deposited over substrate and the role of different film parameters on the alignment of bulk nematic liquid crystal (NLC) in the LC cells can be studied. There are some reports wherein LB films were employed for aligning the bulk LC in the LC cell [1,2]. In this chapter, we propose the LB films of stearic acid deposited under different condition at a given surface pressure can be employed for both homeotropic and homogeneous alignment of the LC. This is the first report where LB film of a material deposited in different condition can be employed for both the alignment of the LC in LC cells.

Langmuir monolayer (LM) at an air-water (A/W) interface can be considered as a two dimensional (2D) system wherein the 2D plane is provided by the water surface. Stearic acid (octadecanoic acid) is one of the classical molecules for studying LM at the A/W interface [3,4].

Conventionally, the surface pressure (π) - area (A) isotherm of any such system is obtained with surface normal of the Wilhelmy plate parallel (or antiparallel) with respect to the compression direction. Traditionally, the monolayer at the A/W interface is compressed unidirectionally by using a single barrier or bidirectionally by symmetric compression of the monolayer employing two barriers. The π - A isotherm of a surfactant is dependent on the way the monolayer is compressed at the A/W interface. In order have an isotropic compression; the monolayer at the A/W interface can be compressed by employing a circular trough with compression barrier made up of teflon tape [3].

The LM at the A/W interface can exert stress onto Wilhelmy plate which are dependent on the compression and shear moduli at a given area per molecule (A_m) [5]. The stress tensor is found to be dependent on the relative direction of compression. The stress tensor exhibits large value in the direction of compression whereas least value in the perpendicular direction [6]. Such difference in stress in different direction has a significant effect in the π - A isotherm when measured in the different directions [6,7]. The morphology of LB films was found to be dependent on target surface pressure (π_t), temperature, pH and ion-contents in the subphase. During the LB deposition, the line tension at the interface of three media e.g. air/substrate/organic layer on water surface plays a crucial role [8,9]. Recently, Poonia et al. demonstrated that single walled carbon nanotubes can be aligned parallel or perpendicular to interdigitated electrodes by LB technique if the direction of substrate normal changes from 0^o to 90^o with respect to the compression direction [10].

In this chapter, we present the investigation of the effect of different stress on the morphology of the LB films of stearic acid deposited at π_t with different orientation angle of substrate normal with respect to the monolayer compression direction. The morphology of LB film of stearic acid was studied using Atomic Force Microscopic (AFM).The LB films show a morphological transformation from granular texture with large and compact grains to granular texture with very small grains to completely uniform texture. The surface morphology can induce ordering in the bulk material [11,12]. Here, we present the effect of surface morphology of LB films of stearic acid deposited at a given π_t but in different direction of substrate normal relative to the compression direction on the alignment of a NLC. The LC cells were fabricated using such LB films deposited substrates. Alignments of NLCs in these cells were observed under a Polarizing Optical Microscope (POM). These LC cells show different alignments (planar to homeotropic)

due to difference in morphology of stearic acid in the LB films.

5.2. Materials and Experimental Methods

Stearic acid ($C_{17}H_{35}COOH$) was purchased from Sigma Aldrich and used without any further purification. The molecular structure of stearic acid is shown in figure 5.1. A solution of stearic acid was prepared in high performance liquid chromatography grade chloroform with a concentration on 3.51 mM. The filter paper was hanged from the pressure sensor using magnetic wire loops such that the surface normal of plate is either made parallel ($\theta = 0^o$) or perpendicular ($\theta = 90^o$) to the compression direction during the π - A_m measurement. The solution (100 µl) was spread on the water sub phase between the two barriers of an LB trough. The solvent was allowed to evaporate for 15 minutes before starting the compression. The film at the A/W interface is compressed by symmetric motion of barriers with the speed of 20 mm/min and π - A_m was recorded. The π - A_m isotherm measurements were carried out at temperature of 20ºC.

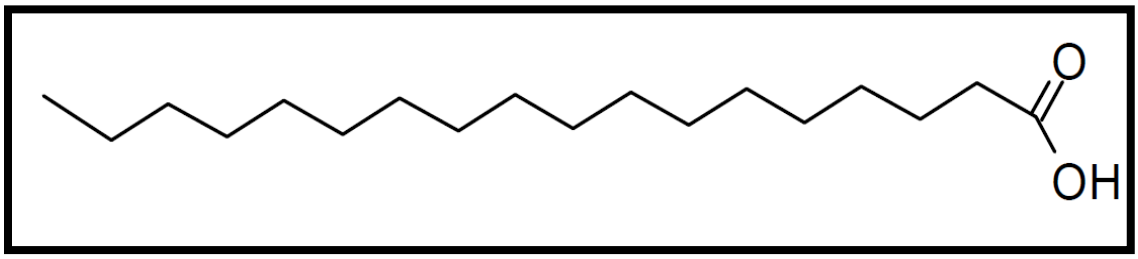

Figure 5.1: Molecular structure of Stearic acid ($C_{18}H_{36}O_2$).

The LB films of stearic acid were deposited onto hydrophilic (HPL) substrates by withdrawing them vertically out of subphase. Such substrates were found to be very smooth possessing an average roughness of ~1 nm [13]. The glass substrates were kept immersed at different orientations angles with respect to compression axis (θ) as shown in figure 5.2 in the subphase (water) prior to spreading the solution. The LB films were deposited with the orientation of the substrate normal parallel, perpendicular and 45^o with respect to the direction of compression. The π_t for the LB film deposition was 15 mN/m. Once the π_t achieved, the monolayer was allowed to equilibrate for about 2 - 5 min. Single layer of stearic acid was transferred on the HPL substrates at different orientation angles with respect to compression axis ($\theta_a = 0°$, $\theta_b = 90°$, $\theta_c = 45°$) using the LB technique. The dipping speed was maintained at 5 mm/min during upstroke of the dipper.

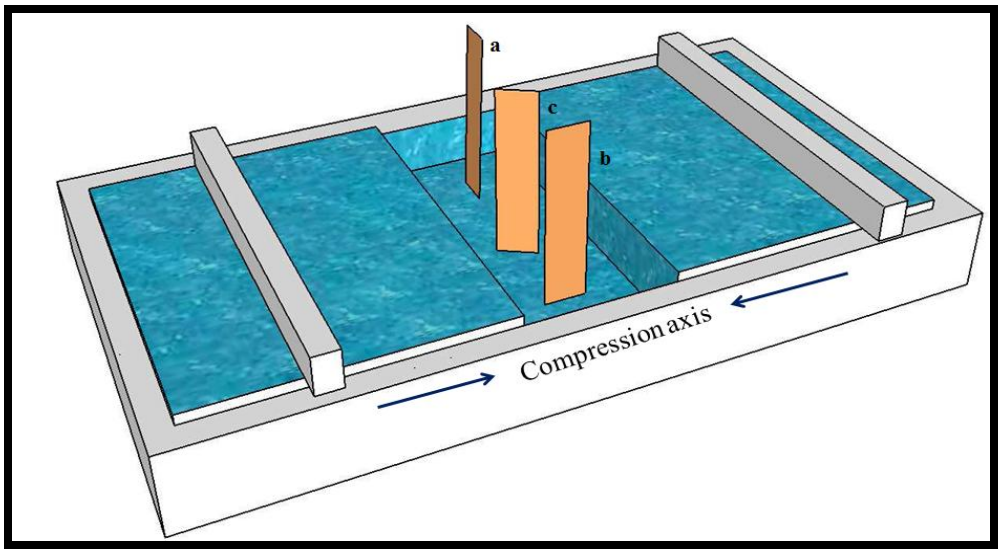

Figure 5.2: Schematic diagram of Langmuir trough with three substrates to be deposited at different orientation angles with respect to the compression axis (θ_a = 0°, θ_b = 90°, θ_c = 45°).

The topography and morphology of LB film of stearic acid was carried out using AFM in contact mode. The Si tips with a spring constant ~ 0.2 N/m was employed for scanning. The images were analyzed using WSxM software [14]. LB film of stearic acid was deposited on glass plate at different orientation angles with respect to compression axis (θ_a = 0°, θ_b = 90°, θ_c = 45°) at π_t = 15 mN/m. LC cells of ~ 8 μm thickness were fabricated using such LB deposited substrates and cured by heating at 80°C. A NLC (E7) was filled in such fabricated cells at room temperature. These cells filled with E7 were observed under POM and the images were captured using a digital camera. A laser of wavelength 633 nm was incident on these E7 filled cells placed between crossed polarizers and the transmitted intensity was recorded using a photodiode. The polar plot of the transmittance as a function of angle of rotation of the cell is plotted.

5.3 Results and Discussion

5.3.1 Surface manometry of stearic acid at A/W interface

The π - A_m isotherm of stearic acid monolayer at A/W interface for two different orientations of Wilhelmy plate (filter paper) with respect to the compression direction are shown in figure 5. 3. The LM of stearic acid exhibits liquid expanded (L_1) and liquid condensed (L_2) phase [2]. The isotherms recorded in the orthogonal directions are found to be different. The isotherm recorded

using Wilhelmy plate oriented with $\theta = 0^o$ is identical to most of the isotherms of stearic acidreported in literature [4].

The isotherm for $\theta = 0^o$, shows a lift-off area (A_i) at 0.3 nm^2. The isotherm indicates the gradual rise in π due to appearance of L_1 phase. The isotherm shows a kink at π = 21 mN/m indicating a phase transition from L_1 to L_2 phase. The isotherm shows a steep rise in π till it collapses at π = 50 mN/m. The steep region of the isotherm is due to L_2 phase of LM of stearic acid. Limiting area per molecule (A_o) can be estimated by extrapolating the steep region of the isotherm curve to zero π. The value of A_o is found to be ~ 0.24 nm^2.

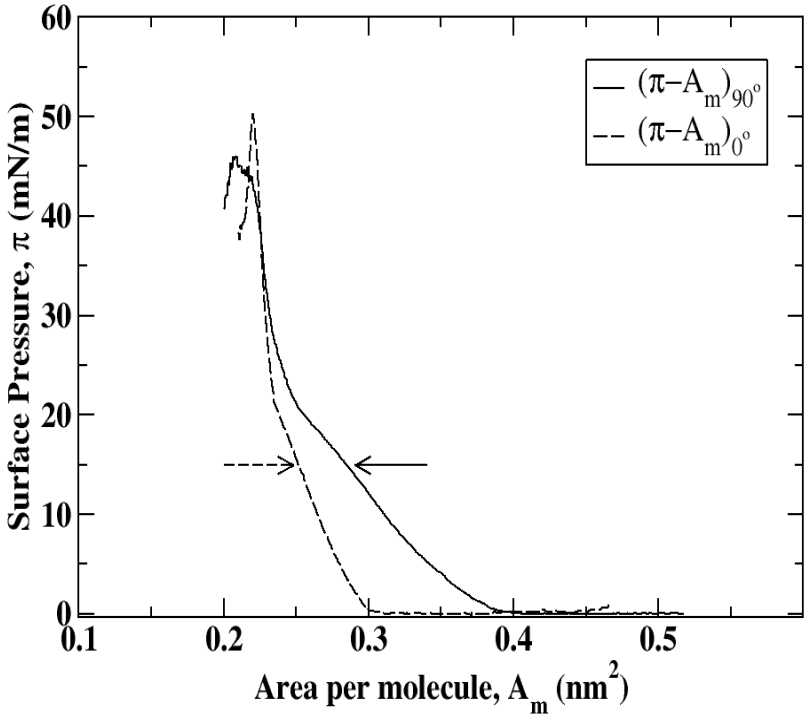

Figure 5. 3: Surface pressure (π) - area per molecule (A_m) isotherms of stearic acid monolayer at the air-water interface recorded using the Wilhelmy plate oriented 0^o and 90^o with respect to the compression direction. The LB films were deposited at π_t =15 mN/m as indicated by the arrows.

The trend of the isotherm changes drastically when the π is measured with the surface normal of the Wilhelmy plate 90^o with respect to the compression direction (i.e. $\theta = 90^o$). The L_1 phase appears at the higher A_m (i.e. lift-off A_m = 0.38 nm^2). The slope of the isotherm in the L_1 phase increases. The kink indicating the L_1 - L_2 phase transition appears at π = 20 mN/m. The slope of

the isotherm in the L_2 phase also appears increasing as compared to that of the isotherm obtained for $\theta = 0^o$. A_0 estimated from the isotherm for $\theta = 90^o$ is approximately 0.25 nm^2. Such value corresponds to the cross-sectional area of the stearic acid for its normal orientation [15].

The in-plane elastic modulus (E) is an appropriate parameter to understand the elastic nature of the monolayer in different surface phases. This can also be employed for identifying the discontinuity in the isotherm due to weak phase transition. The value of E can be estimated from isotherm using the equation 2.2. The variation of E as a function of A_m for the isotherms recorded for $\theta = 0^o$ and 90^o is shown in figure 5.4. When the isotherm is recorded with $\theta = 0^o$, the maximum value of E (E_p) in L_1 and L_2 phases are ~ 120 and 725 mN/m, respectively whereas the isotherm recorded with $\theta = 90^o$ yields the E_p values in the L_1 and L_2 phases to be ~ 55 and 258 mN/m, respectively. The E is found to be reduced in both L_1 and L_2 phase when the measurement is performed with $\theta = 90^o$ as compared to that of $\theta = 0^o$. It can be observed from the figure 5.3 that the range of A_m for L_1 phase has increased largely due to the measurement with $\theta = 90^o$. The peak position of E_p in the L_2 phase is found to be invariant.

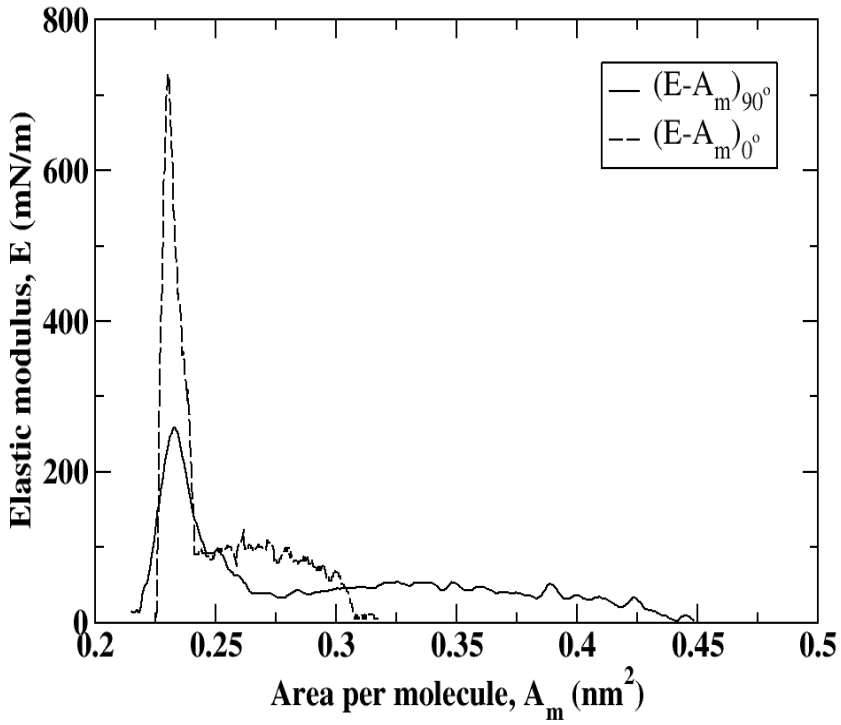

Figure 5.4: *The variation of elastic modulus (E) as a function of area per molecule (A_m) for two different orientation of Wilhelmy plate, $\theta = 0^o$ and 90^o with respect to the compression direction.*

A single layer of stearic acid was deposited on HPL substrates at π_t = 15 mN/m at different orientation angles of the substrate normal w. r. t. compression axis (i.e. at $\theta = 0^o$, 45^o and 90^o).

5.3.2 Characterization of LB film of Stearic acid at A/S interface using AFM

The topography and 3D views of LB films of stearic acid are shown in figure 5.5. The morphology of the LB films of stearic acid deposited at different θ is found to be different. The film deposited with the orientation of the substrate planar to the compression direction ($\theta = 0^o$) shows granular texture with compact grains (figure 5.5(a)). As the orientation angle of the substrate changes to 45^o with respect to the compression direction during LB deposition, the morphology of the film shows granular texture with smaller grain size (figure 5.5(b)). The granular texture vanished and a uniform texture with fewer defects was obtained in the LB film deposited at the orientation angles of 90^o with respect to compression axis (figure 5.5(c)).

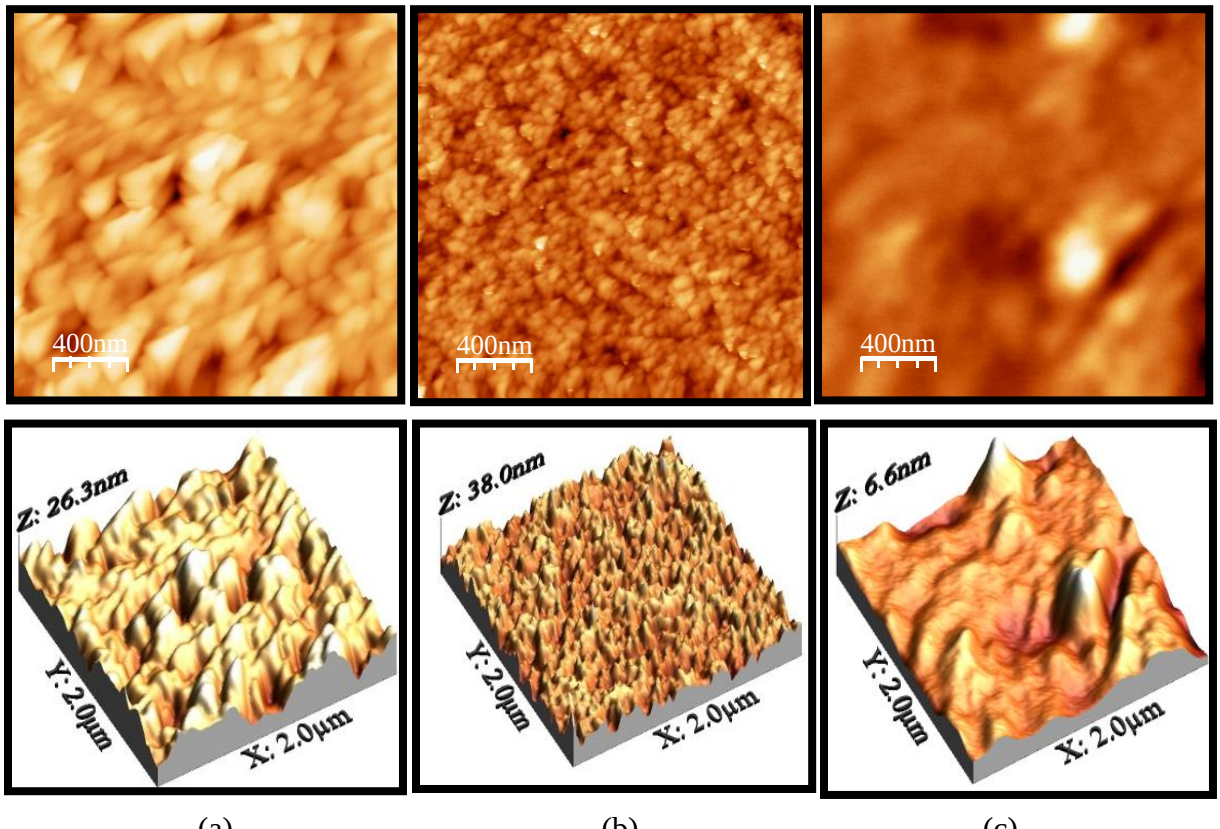

(a) (b) (c)

Figure 5.5: AFM images of LB film of stearic acid deposited on HPL substrates at different orientation angles and their 3-dimensional view (a) $\theta_a = 0°$,(b) $\theta_b = 45°$,(c) $\theta_c = 90°$ with respect to the compression axis.

Therefore, it is found that there is a morphological transformation in the LB films deposited at a given π_t but at different orientational angles of the substrate with respect to the compression direction. The granular texture with large grain size transforms to granular texture with smaller grain size and finally to uniform layer with the change in the orientation angle from planar to 45^o and finally perpendicular to the compression direction, respectively.

The average roughness (S_a) of the films was calculated and is shown as bar diagram in figure 5.6. The films deposited with the orientation of the substrates perpendicular to the compression direction ($\theta = 90^o$) was found to be smoothest. This is in consistence with that of the obtained morphology of the LB film. The S_a value for the LB film deposited with $\theta = 45^o$ is the largest because of the formation of large number of smaller grains in the given area.

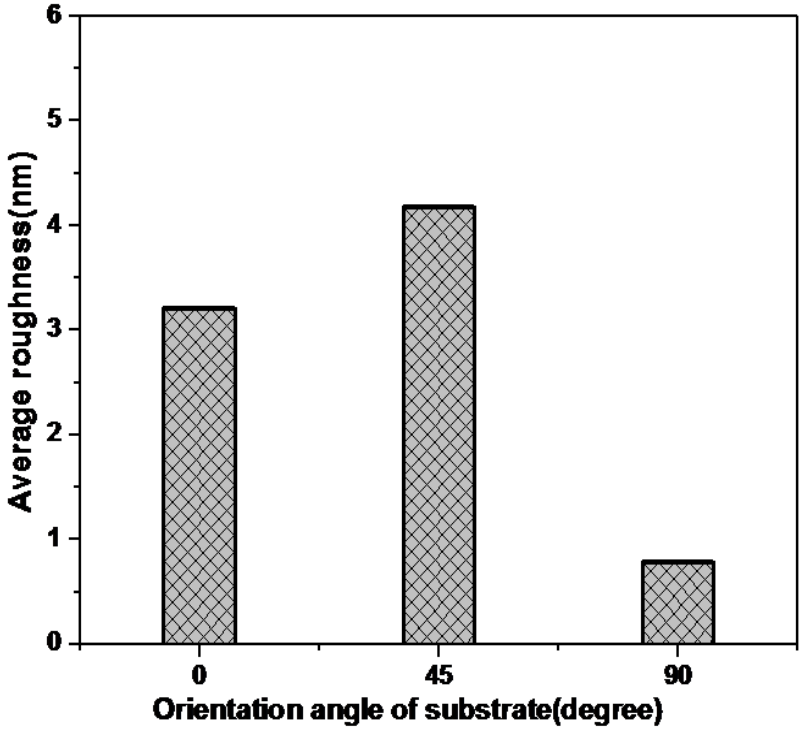

Figure 5.6: Average roughness of LB films of stearic acid deposited at 15 mN/m with different orientation angles of the substrates with respect to the compression direction (θ).

It has been reported that the π measured with the surface normal of Wilhelmy plate parallel and perpendicular to the compression axis were found to be remarkably different [5,6]. The component of the stress tensor measured along the direction of compression (i.e. $\theta = 0^o$) is largest due the additive nature of compression and shear moduli whereas it is smallest when

measured along the direction perpendicular to the compression (i.e. $\theta = 90^o$) due to differential nature of compression and shear moduli [6]. The stress tensor components along off-diagonal (i.e. $\theta = 45^o$) can expected to be an intermediate value between those measured along perpendicular and parallel to the direction of compression. At a given A_m, the monolayer of stearic acid exert least stress with $\theta = 90^o$ whereas it is largest for $\theta = 0^o$. Therefore, for $\theta = 45^o$, the monolayer may exert an intermediate stress onto the substrate or the Wilhelmy plate. Such difference in stress onto the substrate or Wilhelmy plate has remarkable effect onto the morphology of the LB film deposited for different orientations of the substrates with respect to the compression direction. The LB film deposited with $\theta = 0^o$ shows granular texture with compact and larger grain size. For this orientational state of the substrate, the monolayer of stearic acid exerts largest stress. On changing the orientation of the substrate to $\theta = 45^o$, the stress reduces which leads to the formation of granular texture in the LB film but with very small grain size. On further changing the orientation of the substrate to $\theta = 90^o$, the stress reduces to minimum for the given A_m and hence the morphology of the LB film shows a uniform texture with fewer defects.

5.3.3 Fabrication of Liquid Crystal cell and characterization

The effect of surface morphology of these LB films of stearic acid on aligmnent of bulk NLC was studied. The LB film of stearic acid was deposited on glass plate at $\pi_t = 15$ mN/m with $\theta = 0^o$, 45^o and 90^o. The LC cells were fabricated using such substrates and NLC (E7) was filled in such cells at room temperature. The photomicrographs of optical textures of these E7 filled cells as observed under the POM between crossed polarizers are shown in figure 5.7. In case of cells prepared using LB films deposited with $\theta = 0^o$ and $\theta = 45^o$, the bright state observed under the crossed polarizers is shown in figure 5.7(A) and (C), respectively. The dark state observed on rotation of the cell mounted on the POM stage is shown in figure 5.7 (B) and (D), respectively. It can be clearly noticed that these two LC cells exhibit a planar orientation, whereas the one fabricated with $\theta = 90^o$ shows a dark state at all angles of rotation of the POM stage indicating a homeotropic alignment as shown in figure 5.7 (E) and (F). The image (D) appears more darker than that of (B) which indicates that the homogenous alignment of the LC molecules in the cell fabricated using LB film of stearic acid deposited with $\theta = 45^o$ is better than that of $\theta = 0^o$.

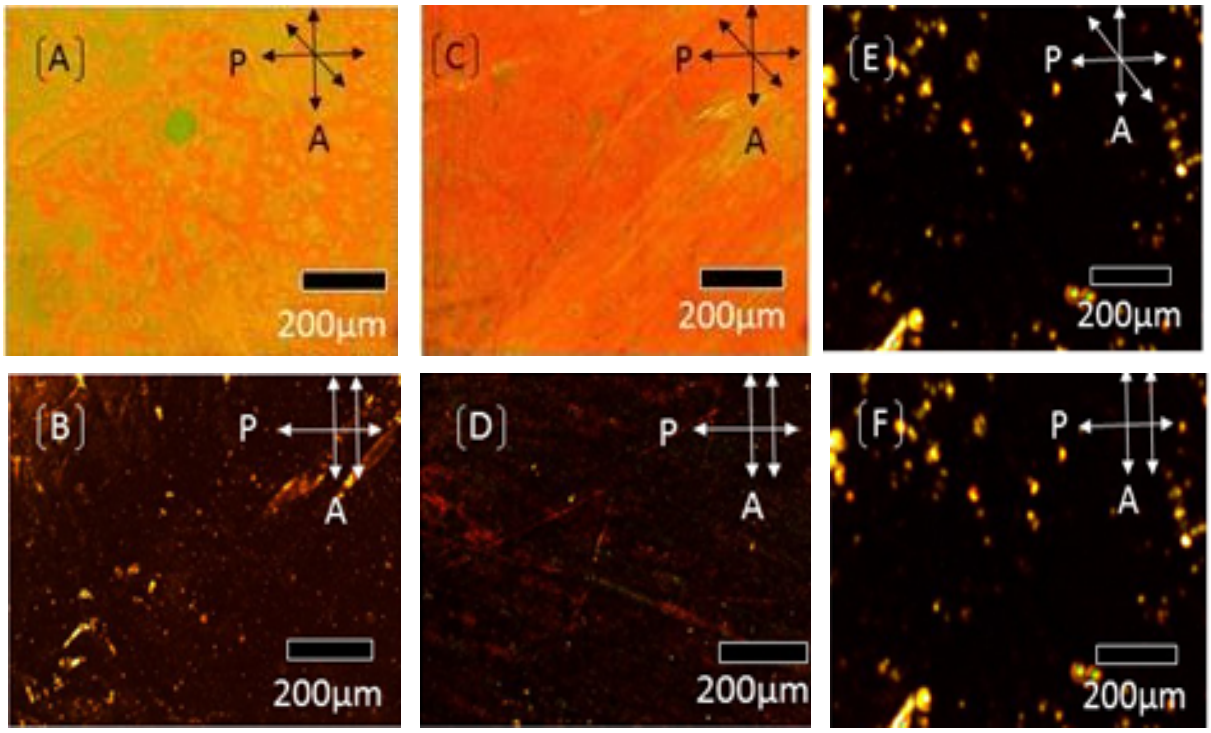

Figure 5.7: Polarizing optical microscope (POM) images of the nematic LC (E7) filled in LC cells fabricated using glass plates deposited with LB films of stearic acid at π_t=15 mN/m with θ =0°(A,B) , θ = 45°(C, D) and θ = 90° (E, F). The bright and dark state images have been taken by rotating the sample cell under polarising microscope with crossed polariser condition.

Further to confirm these observed alignments, we have carried out the transmittance intensity measurements. A polar plot of transmittance as a function of rotation angle of the cells placed between the crossed polarizers is shown in figure 5.8. The alternating maxima and minima in the transmittance at intervals of 90^o indicates that a uniform azimuthal direction of the nematic director in LC cells prepared using LB films deposited with $\theta = 0^o$ and 45^o. Whereas in case of cells prepared using LB film deposited with $\theta = 90^o$, the polar plot shows no such feature as already observed under the microscope indicating a homeotropic alignment. It can be further noted that the dark state of the LC cell of LB film deposited with $\theta = 45^o$ is more significant than that of LC cell of LB film deposited with $\theta = 0^o$.

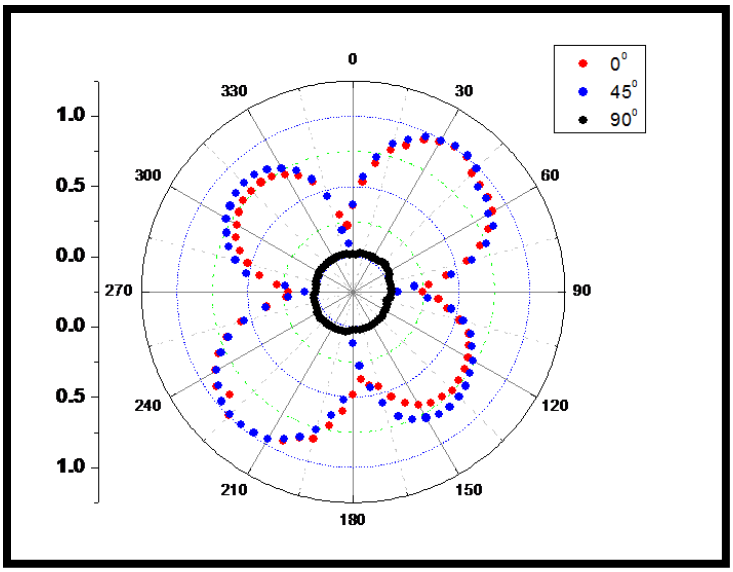

Figure 5.8: Polar plot of transmittance of the cells prepared with stearic acid deposited on substrate at different orientation angles of the substrates with respect to the compression direction between the two crossed polarizers.

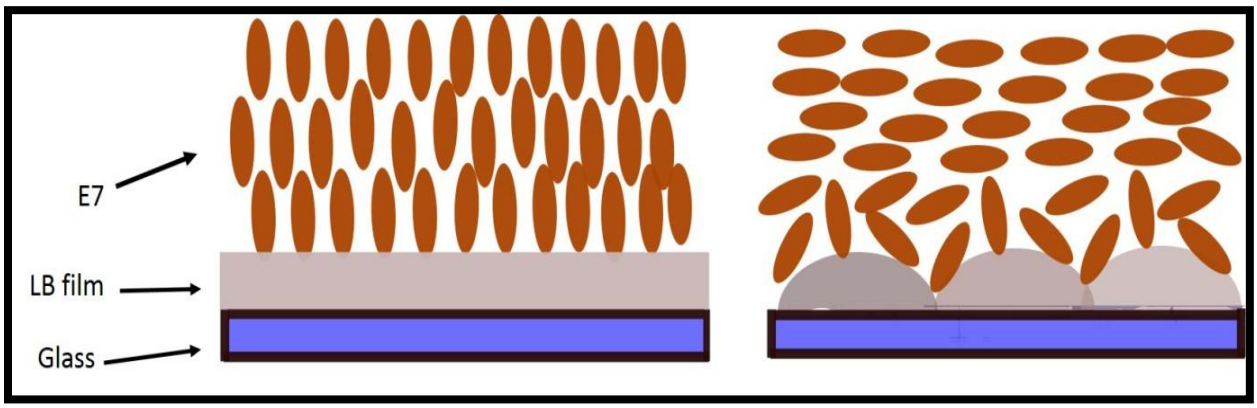

(a) (b)

Figure 5.9: Schematic representation of the alignment of liquid crystals on the LB films of stearic acid deposited onto glass substrate with (a) $\theta = 90^o$ and (b) $\theta = 0$ or 45^o.

Therefore, it is found the granular texture of the LB film (figures 5.5(a) and 5.5(b)) supports the planar orientation whereas the uniform layer of the LB (figure 5.5(c)) supports homeotropic orientation of the NLC in the LC cells. If the aligning layer (i.e. LB films of stearic acid) is uniform, the first layer of LC molecules onto the LB films follow the morphology and yield a smectic layer wherein the LC molecules may align perpendicular to the surface. This geometry

may be followed by the LC molecules in bulk yielding a homeotropic geometry (figure 5.9 (a)). Due to the granular texture of the LB films of stearic acid, the first layer of LC molecules may follow the surface morphology. Therefore, the first layer of LC molecules adsorbed to the LB films supported onto the glass plate exhibit large bend and twist. Such large bend and twist may be followed up by the LC molecules in the bulk which finally yield a homogenous or planar orientation of LC molecules (figure 5.8(b)) in the cells.

5.4 Conclusion

The morphology of LB films deposited onto substrates depends on various factors including the value of π_t, temperature, pH, and ion contents in the subphase. The stress exerted by the monolayer onto the Wilhelmy plate was found to be dependent on the direction of compression of the monolayer at the A/W interface. In this chapter, we have presented the result of our experiment on the effect of such stress on the morphology of LB films of stearic acid deposited onto solid substrate. The LB films were deposited at a π_t = 15 mN/m with different orientation of substrates with respect to the film compression direction. Due to large stress, the film deposited at $\theta = 0^o$ shows granular texture with very large size and compact grains. The large grains change to smaller size and finally vanish due to reduction of the stress by changing θ from 0° to 45^o and then 90^o. LC cells using such LB films deposited at different θ are found to yield a well aligned planar or homeotropic modes for the NLC.

In the next chapter we will discuss the effect of LB film of banana-shaped LC molecules as an alignment layer for the alignment for NLCs.

References

1. V. S. U. Fazio, F. Nannelli, L. Komitov , Phys. Rev. E 63, 061712,**2001**
2. H.Ichinose, M.Suzuki , T.Goto. Molecular Crystals and Liquid Crystals 203, 1, **1991.**
3. G. L. Gaines, "*Insoluble Monolayers at Gas-Liquid Interfaces*" Wiley: New York, **1966.**
4. V. M. Kaganer, H. Mohwald , P. Dutta, Rev. Mod. Phys. 71, 779, **1999**.
5. D. Y. Zang, E. Rio, D. Langevin, B. Wei , B. P. Binks, Eur. Phys. J. E 31, 125, **2010.**
6. J. T. Petkov, T. D. Gurkov, Langmuir. 16, 3703, **2000.**
7. P. Cicuta, E. M. Terentjev, Eur. Phys. J. E 16,147, **2005.**
8. P. G. de Gennes, Colloid Poly. Science, 264, 463, **1986**.
9. R. L. Cerro, J. Colloid Interf. Sci. 257, 276, **2003.**
10. M. Poonia, V. Manjuladevi, R. K. Gupta, S. K. Gupta, J. Singh, P. B. Agarwal, J. Akhtar, Sci. Adv. Mater.**7**, 455, **2015.**
11. P. Ruffieux, O. Groning, M. Bielmann, C. Simpson, K. Mullen, L. Schlapbach, P. Groning, Phys. Rev. B 66, 073409, **2002.**
12. R. Friedlein, X. Crispin, C.D. Simpson, M.D. Watson, F. Jackel, W. Osikowicz, S. Marciniak, M. P. de Jong, P. Samori, S.K.M. Jonsson, M. Fahlman, K. Mullen, J. P. Rabe, W. R. Salaneck, Phys. Rev. B 68, 195414, **2003**.
13. R. K. Gupta, V. Manjuladevi, International Journal of Nanoscience & Nanotechnology (IRPH) 2, 171, **2011.**
14. I. Horcas, R. Fernandez, J. M. Gomez-Rodriguez, J. Colchero, J. Gomez-Herrero, A. M. Baro, Review of Scientific Instruments 78, 013705, **2007**.
15. R. K. Gupta, V. Manjuladevi, "*Ultrathin Films, in Comprehensive Guide for Nanocoatings Technology",* edited by M. Aliofkhazraei, NOVA Publishers, USA, Ch 10, **2014.**

Chapter - 6

Alignment of Liquid Crystals Using Langmuir-Blodgett and Inverse Langmuir-Schaefer Films of Unsymmetrical Bent-Core Liquid Crystals

6.1 Introduction

In the previous chapter, we have demonstrated that the morphology of Langmuir-Blodgett (LB) film is dependent on the orientation angle of substrate normal with respect to the monolayer compression direction. The LB film of stearic acid deposited under different experimental conditions was used as alignment layer in the liquid crystal (LC) cell. The alignment of nematic LC (NLC) in LC cell also show different alignments due to difference in morphology. It will be interesting to study the role of LB film of bent-core LC (BCLC) as an alignment layer.

BCLCs have attracted the researchers due to their unique properties such as chirality [1], ferroelectricity [2] and antiferroelectricity [3]. These properties of BCLCs make them suitable candidates for practical applications like switching devices, storage device [4], electromechanical devices [5] and electro-optical display devices [6].

The ability to control the alignment of the LC molecules at interface is very important for the fabrication of LC display devices. Alignment layer in any LC based device is the main driving point which determines the switching behavior on application and removal of external electric and magnetic fields. Thin films fabricated from organic materials serve as alignment layer in the

devices; so the study of growth mechanism of thin film, molecular ordering and the overall film morphology are highly important for device fabrication [5]. Photo aligned polymers films [7-8], evaporated oxides [9], LB technique [10], self assembled monolayer [11-13] and unidirectional mechanical rubbing [7] are used for alignment of calamitic LC. BCLCs cannot be aligned with conventional techniques such as rubbed polyimide or nylon due to their characteristic bent shape [14, 15]. Thin films of BCLCs can be formed by vacuum deposition [16-17], self-assembly [18] or LB techniques. LB technique provides a precise control over the orientation and ordering of the molecules at the substrate.

There are few studies which show that BCLCs can form a stable Langmuir monolayer (LM) at the air - water (A/W) interface and such LMs are transferred onto solid substrates [19-26] by LB or Inverse Langmuir - Schaefer (ILS) technique. Kinoshita et al.[19] have reported the first article based on a LM of BCLC. They formed LM of 1, 3-phenylene bis[4-(((4-dodecylphenyl) imino) methyl) benzoate] BC molecules at A/W interface and transferred LB film onto solid substrate. They studied the molecular orientation in LB films by using surface second harmonic generation measurements and they also investigated the optical symmetries and nonlinear optical susceptibility of monolayer of BCLC molecules.

Blinov et al. [20-22] have reported the dielectric, ferroelectric and antiferroelectric properties of LB films of symmetric BCLCs. They investigated antiferroelectric and ferroelectric switching in thin films of an achiral BCLC compound in sandwich geometry. A LB film of achiral BCLC (antiferroelectric) compound was transferred onto a conductive glass. They reported that the thin films of achiral BCLC compound in sandwich geometry exhibited ferroelectric, antiferroelectric and electro-optic properties (which depends on the film thickness) similar to those in bulk samples even up to a high-temperature in B_2 phase.

Zou et al. [23] have reported the LM of five different symmetric BCLCs at A/W interface in 2004 wherein both the core and end-chains were varied while maintaining the molecular symmetry. They observed that the properties of these LM are dependent on the end group of chains of the molecules. The molecules with amphiphilic chains lie quite flat on the surface, and the molecules with hydrophobic (HPB) end chains form multilayer structures.

In 2006, Wang et al. [24] have characterized the LM of a symmetric BC molecule with hydrocarbon end chains and two chlorine atoms substituted on the central phenyl ring of the BC

molecule by a combination of isotherms, Brewster angle microscopy (BAM) and surface potential measurements. These LMs were found to be optically anisotropic.

In 2010, ILS film of symmetric BC molecules was used as alignment layer for nematic BCLC molecules (4-chloro-1, 3-phenylene bis [4-(10-decenyloxy) benzoyloxy] benzoate) in LC cell [25]. They found that ILS film of a symmetric BC molecules can serve as effective planar alignment layer for a nematic BCLC cell. But even at very low pressure, the LM of symmetric BC molecule was unstable and formed multilayer [25].

In 2011, Iglesias et al. [26] have investigated the films of BC molecules with one hydrophilic (HPL) end group connected to the bent-core by a short aliphatic chain as alignment layer for LC. They found that HPL end group led to much more stable LM. A molecular tilt at the surface can be controlled by varying molecular area. The ILS films were used as alignment layers for alignment of a bulk rod-like nematic, 4-pentyl-4-cyanobiphenyl (5CB) and BCLCs. It was the first report based on the alignment of BC nematic with highly-compressed films. They found BCLC molecules in the nematic phase are aligned perpendicular to the surface. Such interpretation of the molecular behavior was also supported by a combination of atomically accurate molecular dynamics simulations of up to 36 BC molecules at the water surface, and the continuous variation of tilt induced by ILS films of BC molecules in a LC cell filled with calamitic LCs [26].

In this chapter, we present an investigation on the surface behavior of unsymmetrical BCLCs with either cyano (CN) or nitro (NO_2) polar end groups at one end of bent-core molecule at A/W and air-solid (A/S) interfaces. We will refer to these compounds (4-((4-(tetradecyloxy) benzoyl) oxy) phenyl 3-((4-((4-cyanobenzoyl) oxy) benzoyl) oxy) benzoate) ($C_{49}H_{49}NO_9$) as B-CN, 4-((4-(tetradecyloxy) phenoxy) carbon) phenyl 3-((4-((nitrobenzoyl) oxy) benzoyl)oxy) benzoate ($C_{48}H_{49}NO_{11}$) as BN1 and 4-((4-(octadecyloxy)phenoxy)carbonyl)phenyl3-((4-((4-nitrobenzoyl) oxy) benzoyl) oxy) benzoate ($C_{52}H_{57}NO_{11}$) as BN2 now onwards in this chapter.

We formed a LM of B-CN, BN1 and BN2 at A/W interface. The LM of B-CN, BN1 and BN2 at A/W interface were found to be stable. The LM of these BCLCs at A/W interface was characterized by BAM. A single layer of these BCLCs were transferred onto various solid substrates at different target surface pressures (π_t) using the LB and ILS method. Films fabricated by both the methods at A/S interface were characterized using Atomic Force Microscopy (AFM)

and Field Emission Scanning Electron Microscopy (FESEM).

Using the force - distance spectroscopy of AFM, the HPL and HPB nature of the LB film was studied. To confirm the orientation of BC molecules on solid substrate, the adhesion force between an AFM tip and LB film of BN2 molecules deposited on HPL treated Si/SiO_2 substrates was calculated. The adhesion force between an AFM tip and different substrates has been reported through several studies. It was found that the adhesion force strongly depends on the nature of the film on the substrate and the AFM tip [27-30].

The alignment of the LC molecules at interface plays a vital role in display devices [31-32]. We have studied the effect of molecular aggregation in the LB and ILS films on the alignment of LC molecules in the LC cell. The alignment of LC can be controlled using the LM deposited on substrate at various π_t as aligning layer. LC cells were fabricated using these LB and ILS film deposited substrates. Alignments of NLC in these cells were observed under a Polarizing Optical Microscope (POM).

6.2 Materials and Experimental Methods

6.2.1 Materials

All the banana molecules B-CN, BN1 and BN2 were synthesized in the laboratory by Prof. Sadashiva et al. at RRI, Bengaluru [33]. B-CN molecules with CN end group and 14 alkyl chains exhibits the phase sequence: partial bilayer uniaxial smectic A phase (SmA_d) - Isotropic (Iso). BC molecules with NO_2 end group and 14 and 18 alkyl chains exhibit the phase sequence: partial bilayer biaxial antiferroelectric smectic A (SmA_dP_A) - bilayer smectic A (SmA_d) - Isotropic (Iso). The –CN and $–NO_2$ groups of the molecules act as hydrophilic polar group and facilitate in stabilizing the monolayer at the A/W interface [34].

The molecular structure and phase sequence of all molecules are shown in figure 6.1. The molecular length of B-CN, BN1 and BN2 are ~ 4.7, 4.7 and 5.2 nm respectively. The bent-core angles are around ~ 144.1°, 142.53° and 142.84° for B-CN, BN1 and BN2 molecules, respectively. All these values were calculated using ACD/ChemSketch software. The cross sectional molecular area of B-CN, BN1 and BN2 were estimated to be $0.5nm^2$.

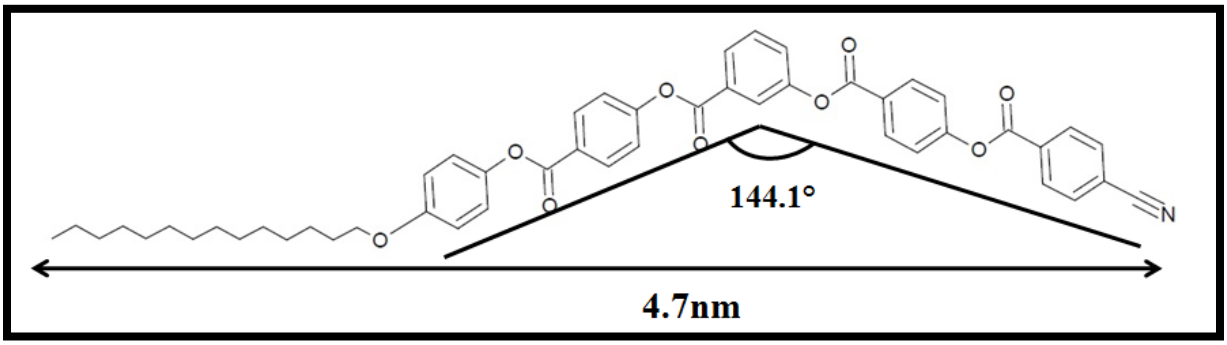

Cr 158.0°C S_mA_d 154.0°C Iso

(a)

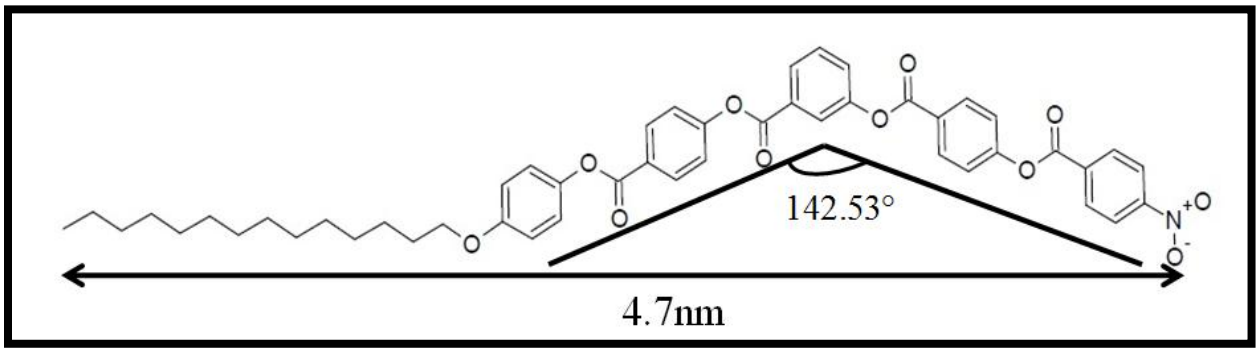

Cr 146.5° SmA_dP_A 145.8° SmA_d 153.0° Iso

(b)

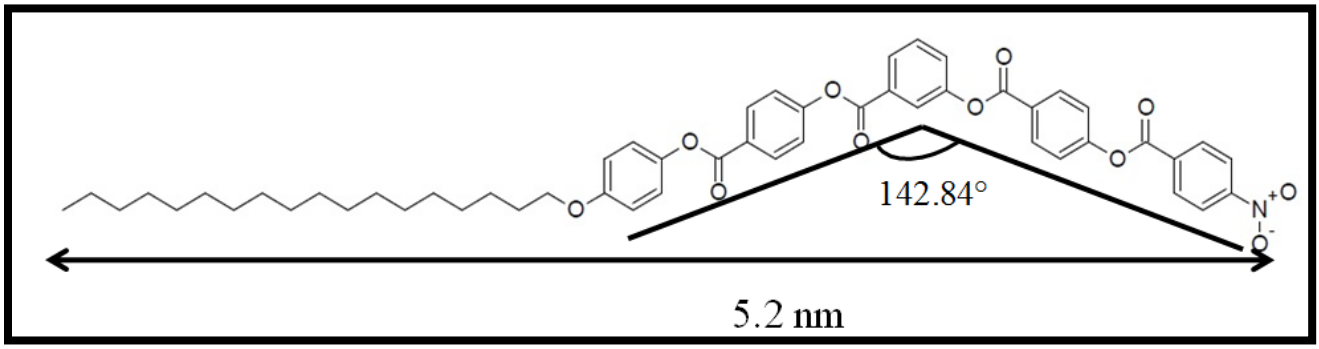

Cr 144.0° SmA_dP_A 151.0° SmA_d 166.0° Iso

(c)

Figure 6.1: Molecular structure and phase sequence exhibited by

(a) B-CN, (b) BN1 and (c) BN2 molecules.

6.2.2 Experimental Methods

Chloroform solutions of all BCLCs having a concentration of 0.5 mg/ml were prepared separately. A known quantity of these individual solutions of BC molecule was spread onto the ion-free water subphase between the barriers of the LB trough and solvent was allowed to evaporate by waiting for ~30 minutes before performing the measurements. The monolayer of BCLCs at the A/W interface in a LB trough was compressed symmetrically using the two barriers of the LB trough at a speed of 20 mm/min and the surface pressure (π) as a function of area per molecule (A_m) was recorded using an integrated balance simultaneously. The LM of BC molecules at the A/W interface was imaged in real time using a BAM. The stability of the LM of the BC molecules is studied by recording isocycles during repeated compression and expansion of the monolayer. Small hysteresis and retraceable isocycles indicate stable and reversible phase of the LM. The shift in the isocycles curves towards the lower or higher A_m indicates unstable LM. The instability may arise due to dissolution of the molecules or the formation of irreversible aggregates on the water surface.

The LM of BC molecules was transferred onto solid substrates using the LB technique. Indium tin oxide coated (ITO) glass plates, quartz plates, microscopic glass slides and Si/SiO_2 wafer were used as solid substrates. The glass slides and Si substrates were treated successively with ethanol, piranha solution and ultrapure ion free water prior to any deposition. The ITO and quartz plates were procured commercially and used after cleaning them thoroughly by ultrapure ion-free water, absolute alcohol and high performance liquid chromatography (HPLC) grade chloroform, successively. The substrates were dried by blowing hot air at about 60°C. Prior to the LB deposition, the LM of BC molecules is compressed to a π_t, and about ~ 5 minutes time is allowed for the equilibration of the film. The single layers of LB films are deposited at different π_t by a single upstroke motion of the dipper at a speed of 5 mm/min. The transfer ratio for LB deposition on ITO and Si substrates were found to be 1±0.2.

The LM of B-CN molecule was also transferred onto solid substrate using the ILS method as discussed in section 4.2.2 of chapter 4.

The topography of thin film of BCLC molecules transferred onto solid substrates (A/S interface) at different π_t was examined using AFM. The images were analyzed using the WSxM software. The interaction forces between the tip and LB film was estimated using the force-distance

spectroscopy of AFM. FESEM is used for obtaining the information of morphology of the films of BC molecules deposited on the solid substrates. LC cells of ~ 8µm thickness were fabricated by using the two solid substrates on which LB/ ILS film of banana molecules were deposited. The alignments of these LC cells filled with NLC were observed under a POM. All the experiments were carried out in ambient at room temperature (~20°C).

6.3 Results and Discussions

6.3.1 Surface manometry of banana shaped molecules at A/W interface

The surface manometry of BCLCs was studied at A/W interface. The π - A_m isotherms of BCLCs are shown in figure 6.2 and 6.3. The corresponding elastic moduli *(E)* as a function of *Am* are also plotted in figure 6.2 and 6.3. The π - A_m isotherm was obtained by compressing the monolayer on the water surface.

The π - A_m isotherm of B-CN molecule is shown in figure 6.2. The isotherm of B-CN has a shoulder region of very low surface pressure (~ 0 mN/m) within A_m = 1 to 0.6 nm^2 (figure 6.2). This region can be treated as a co-existence of gas and a liquid phase. The isotherm shows a lift-off area (A_i) at around ~ 0.6 nm^2. This is the onset of liquid condensed (L_2) phase.

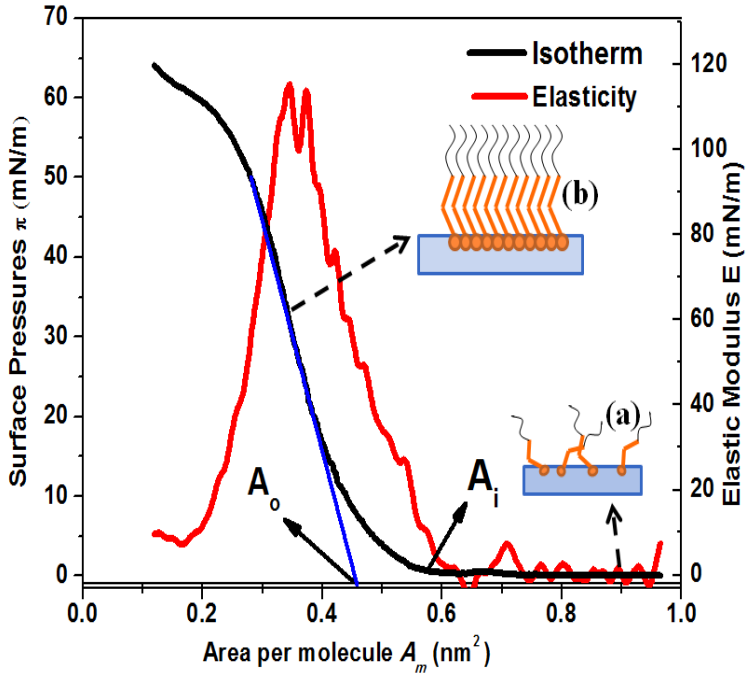

Figure 6.2: Surface pressure (π) – area per molecule (A_m) isotherm and the variation of the in-plane elastic modulus (E) as a function of A_m of the B-CN at the air-water interface.

On further reduction in A_m, the π rises monotonically and sharply till the monolayer collapses. This region of the isotherm corresponds to L_2 phase. The monolayer collapses with a collapse surface pressure (π_c) of ~ 58 mN/m. Unlike the case of sharp collapse of stearic acid [35] or plateau type collapse of octylcyanobiphenyl [36], here the collapse is indicated by a relatively slow change in the slope. The extrapolation to the zero π of the sharp region of the isotherm yields a limiting area of around 0.46 nm^2(=A_o). The schematic for a possible molecular arrangement in the different phases is shown in the inset (a) and (b) of figure 6.2.

The in-plane *E* of the LM was calculated by employing the equation 2.2. The *E* vs A_m curve provides insight into the elastic nature of the LM and shows weak phase transition in the LM at A/W interface. The value of *E* is varying for the large area and it increases with variation at the onset of L_2 phase. We obtained the maximum value of *E* ~ 114 mN/m in L_2 phase for B-CN molecule as shown in figure 6.2. The L_2 phase destabilizes upon further compression, leading to a decrease in the value of *E*, which is an indication of the initiation of the collapse of the film.

The isotherm of BN1 and BN2 are shown in figure 6.3(a) and (b). Isotherms of both molecules exhibit a shoulder region at very large A_m, and π remains nearly zero mN/m. This is co-existence of gas and a liquid phase of BN1 and BN2 molecules. The isotherm shows A_i at 0.66 and 0.63 nm^2 for BN1 and BN2, respectively.

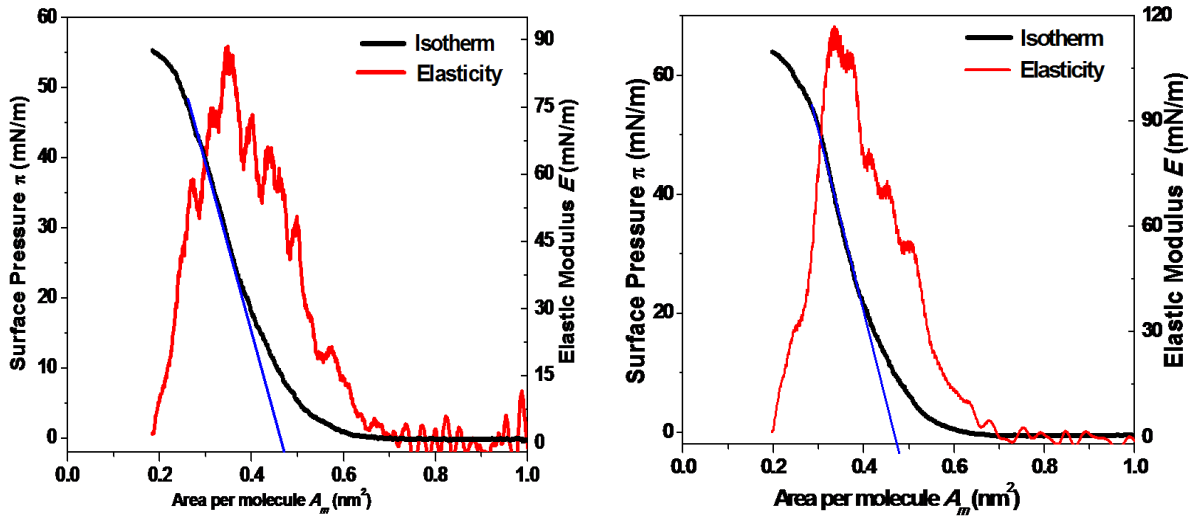

Figure 6.3: Surface pressure (π) – area per molecule (A_m) isotherm and the variation of the in-plane elastic modulus (E) as a function of A_m of the (a) BN1 and (b) BN2 at the air-water interface.

On decreasing the A_m, the value of π rises sharply until the film is compressed completely in the trough. The isotherms indicate collapse at π ~ 50 and 53 mN/m for BN1 and BN2, respectively. This region corresponds to L_2 phase of the both BC molecules. The values of A_o for BN1 and BN2 molecule were estimated to be 0.48 and 0.47 nm^2, respectively. The maximum values of E in the L_2 phase is obtained as ~ 88 and 117 mN/m for BN1 and BN2 molecules, respectively as shown in figure 6.3(a) and (b).

The different length of alkyl chains at the end of the molecules affects configuration, stability and monolayer formation at A/W interface. The value of A_i and A_o are smaller for BN2 molecule in comparison to BN1 molecule due to longer alkyl chain length of BN2 molecule. The value of E increases with increase in alkyl chain length. The value of E for BN2 molecules is large as compared to BN1 molecule. Stability of molecules is also dependent upon length of alkyl chains. Molecules having longer alkyl chains will form a more stable monolayer as compared to smaller alkyl chain molecules due to stronger Van der Waals interaction between the chains [37]. Thus, LM of BN2 molecules is more stable at A/W interface than that of LM of BN1 molecules.

The stability and reversibility of LM of BCLCs is studied by recording the isocycles of the LM at the A/W interface. Figure 6.4 shows the isocycles of the LM of BCLCs at A/W interface. The isocycles are obtained by repeated compression and expansion of the LM with a speed ~ 20 mm/min. The maximum π was maintained at 30 mN/m for B-CN and BN1 respectively and 20 mN/m for BN2.

The isocycles for B-CN shows small hysteresis in the compression and expansion curve of a given cycle as shown in figure 6.4(a). The expansion curve almost follows the compression curve. The expansion and compression curve of 2^{nd} and 3^{rd} cycles are almost overlapping the expansion and compression curve of 1^{st} cycle. The 2^{nd} and 3^{rd} cycles are shifted on y-axis by 10 mN/m relative to each other for visual clarity. The isocycles curve indicates that the LM of banana molecule at the A/W interface is stable. The zero π is achieved at large area during the expansion. This indicates that though the liquid-like phase is completely reversible, the gas phase appears at very large area during the expansion of LM. The isocycles measurement show not only a reversible but also a stable LM of B-CN molecules at the A/W interface.

For BN1 and BN2 molecules, the first isocycle shows some hysteresis in the compression and expansion curve of both the BCLCs (in figure 6.4(b) and (c)). The hysteresis in the isocycles

indicates the irreversible nature of the L_2 phase A/W interface due to expansion. The expansion and compression curve of 2nd and 3rd cycles for both BC molecules (BN1 and BN2) are almost overlapped. This indicates that the molecules may attain some stable conformation during repeated compression and expansion. The hysteresis in the 1st isocycle is small for BN2 molecules as compared to BN1 molecules. This reveals that BN2 molecules form a more stable LM at A/W interface as compared to BN1 molecule.

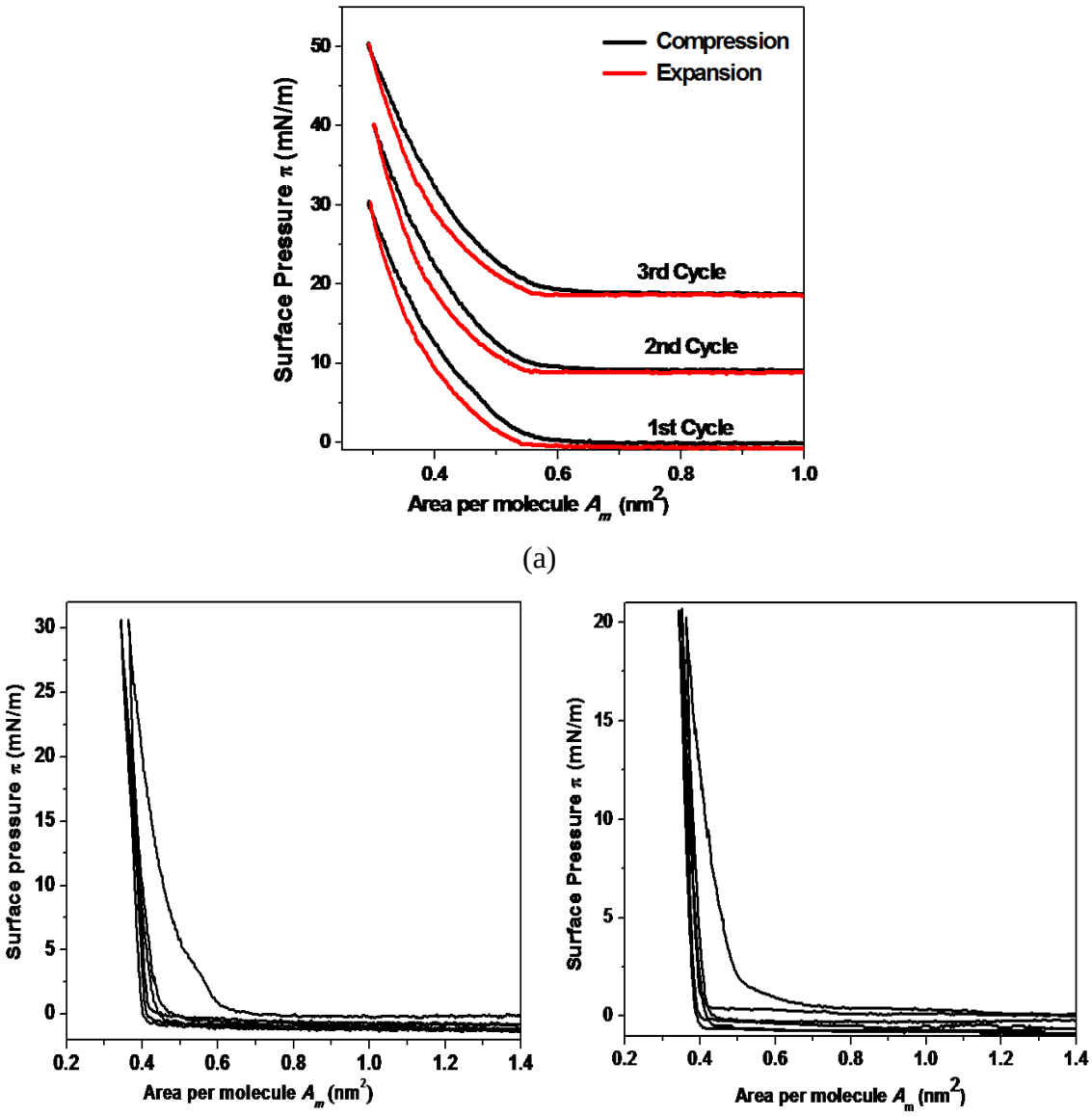

Figure 6.4: Isocycles of LM of (a) B-CN, (b) BN1 and (c) BN2 molecules at the air-water interface.

6.3.2 Characterization of Langmuir monolayer of BCLCs at A/W interface using BAM

The LM of BCLC molecules at A/W interface was imaged in real time using BAM. The BAM images of LM of B-CN at A/W interface are shown in figure 6.5. In figure 6.5(a), the black region represent the water subphase before spreading the molecules. The BAM image captured in gas + L_2 phase shows gray region in the dark background (in figure 6.5(b)). This gray region represents the domain of L_2 phase of B-CN molecules at A/W interface. The dark region represents the gas phase. The surface coverage of gray region increases with compression of the LM. These gray regions of B-CN molecule grows and form a large gray region in the dark background with compression of the LM on water surface. The BAM image captured in L_2 phase shows the complete uniform gray texture on water surface (figure 6.5(c)). The BAM image (figure 6.5(d)) captured in the collapsed state shows cracks in the film at water surface.

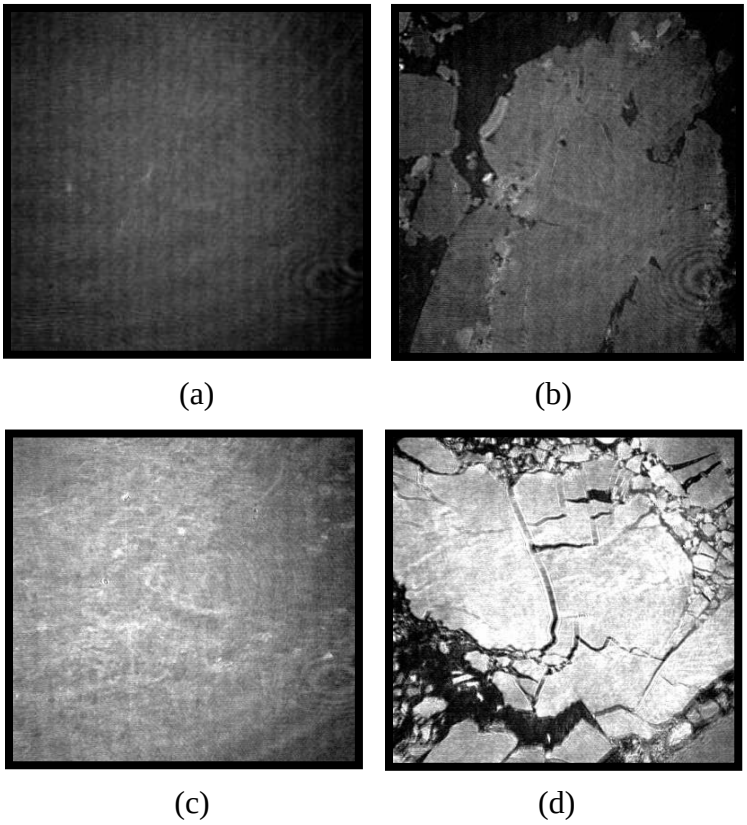

Figure 6.5: Brewster angle microscope images of Langmuir monolayer of B-CN at air-water interface. Images a-d were captured over monolayer areas (A) of 1, 0.9, 0.4 and 0.1 nm^2. The size of the images is 4.8 x 4.8mm^2.

The BAM images of LM of BN1 at A/W interface are shown in figure 6.6. The gray region with the dark background is observed at a large area as shown in figure 6.6(a). This gray region represents the domains of L_2 phase of LM of BN1 molecules. The surface coverage of gray region increases with the compression of LM on water surface (as shown in figure 6.6(b)). The BAM image captured in L_2 phase shows almost complete uniform gray region of LM of the BN1 molecules on water surface (figure 6.6(c)). The BAM image (figure 6.6(d) captured in the collapsed state shows cracks in the film on the water surface.

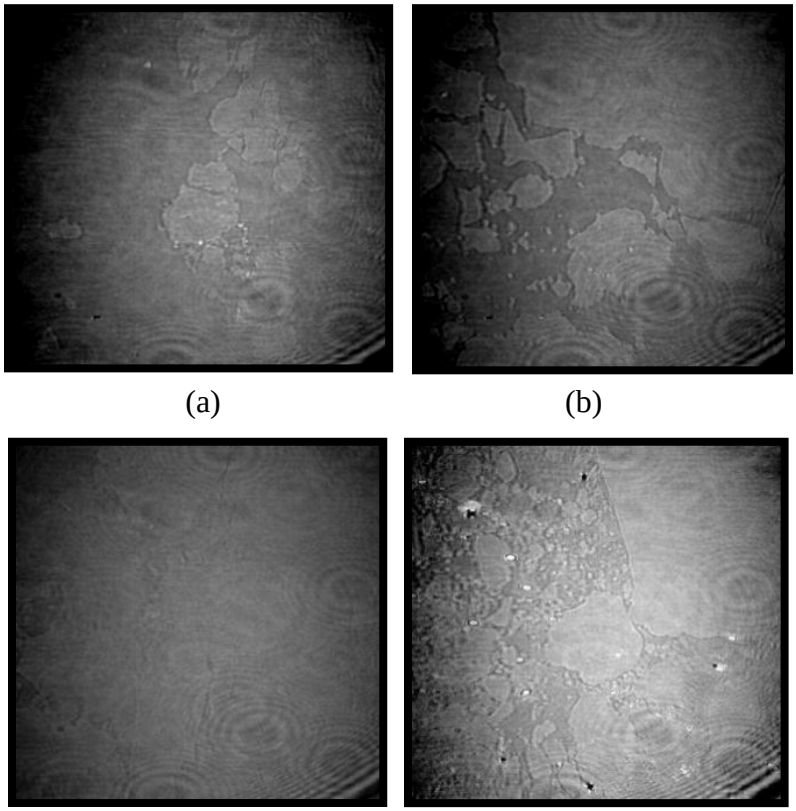

Figure 6.6: Brewster angle microscope images of Langmuir monolayer of BN1 at the air-water interface. Images a-d were captured over monolayer areas (A) of 1, 0.7, 0.4 and 0.2 nm^2. The size of the images is 4.8x4.8mm^2.

The BAM images of LM of BN2 at A/W interface are shown in figure 6.7. The BAM image captured at large area displays bright gray region in the dark background (figure 6.7(a)). This gray region represents the domains of L_2 phase of LM of BN2 molecules at A/W interface. The surface coverage of the gray region increases on compression of LM. Figure 6.7(b) shows a large

gray region of BN2 molecules on water surface with the compression of LM on water surface. The BAM image recorded in L_2 phase presents the complete uniform film of banana molecules on water surface (figure 6.7(c)). The BAM image (figure 6.7(d)) captured in the collapsed state shows very bright crack - like feature in the film.

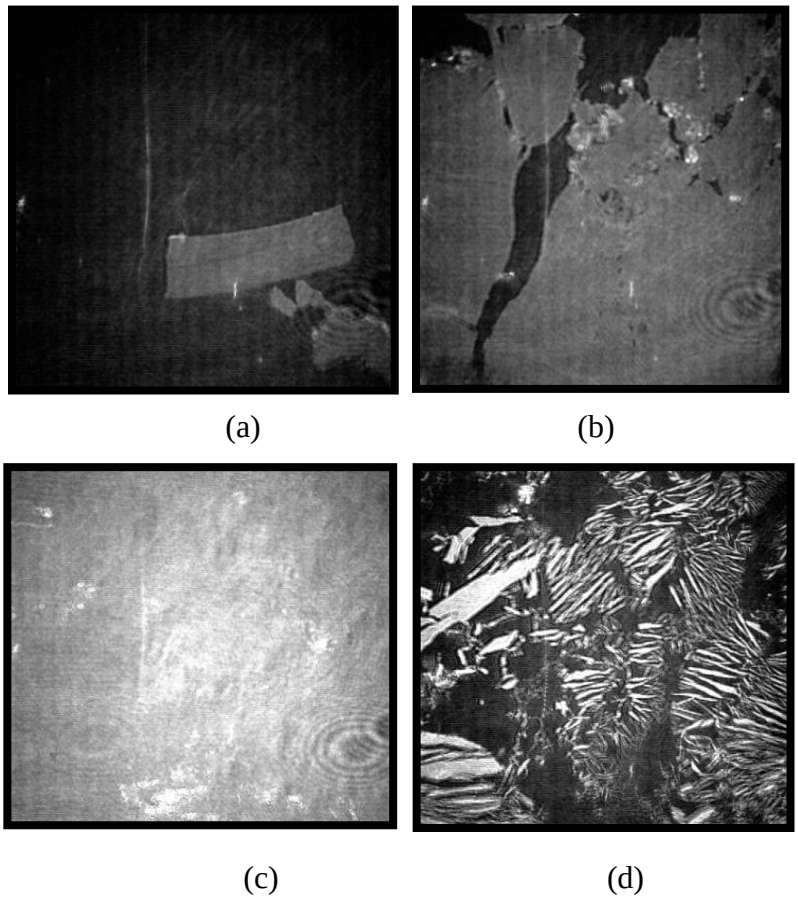

(a) (b)

(c) (d)

Figure 6.7: Brewster angle microscope images of Langmuir monolayer of BN2 at air-water interface. Images a-d were captured over monolayer areas (A) of 1, 0.6, 0.4 and 0.2 nm^2. The size of the images is 4.8x4.8mm^2.

6.3.3 Characterization of LB film of BCLCs at A/S interface using FESEM and AFM

6.3.3.1 Field Emission Scanning Electron Microscopy (FESEM)

The LB films of BCLCs are deposited on HPL Si/SiO_2 substrate (A/S interface) at different value of π_t. The morphology of LB film of B-CN, BN1 and BN2 molecules on the Si/SiO_2 substrates at various π_t was carried out using FESEM.

The FESEM images of LB film of B-CN molecules at π_t = 3 mN/m shows the irregular droplet

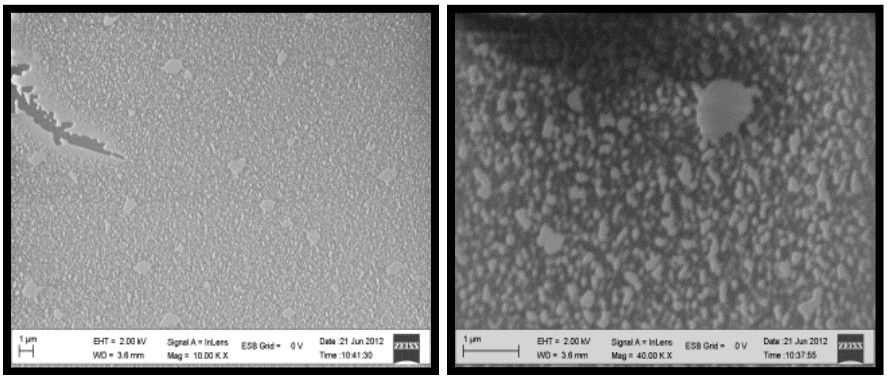

(a) (b)

Figure 6.8: FESEM images of LB film of B-CN on Si/SiO_2 substrates deposited at target surface pressures π_t = 3 mN/m. The size of these (a) and (b) images are 34x25µm^2 and 7.5x5.5µm,^{2} respectively.

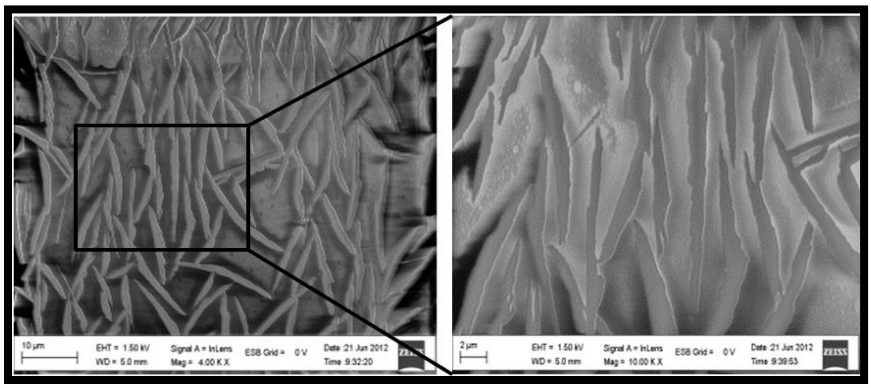

(a) (b)

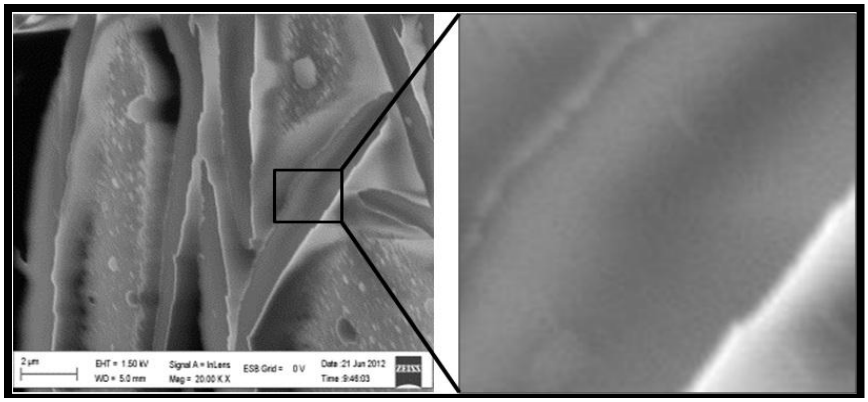

(c) (d)

Figure 6.9: FESEM images of LB film of B-CN on Si/SiO_2 substrates deposited at target surface pressures π_t = 30 mN/m. The size of these (a),(b),(c) and (d) images are 76 x51µm^2, 30x22µm^2, 15x11µm^2 and 2x2µm^2, respectively.

like structure on Si/SiO_2 substrate (in figure 6.8). The size of the small droplets lies in the range of 100 ~ 200 nm. LB film of B-CN molecules transferred at π_t = 30 mN/m shows the large bent leaf - like crystalline flakes on Si/SiO_2 substrate (in figure 6.9(a) and (b)). The average length and width of leaf shape domain is around ~ 1x12 μm^2. It is observed that each bent leaf crystalline flake exhibits uniform texture (figure 6.9(d)) on Si/SiO_2 substrate.

The FESEM images of LB film of BN1 molecules on Si/SiO_2 substrate at π = 5 mN/m, shows uniformly deposited irregular network like pattern on substrate (figure 6.10(a)). The FESEM images of BN1 deposited on Si/SiO_2 substrate at higher π = 30 mN/m, show streak like pattern with grainy background as shown in figure 6.10(b). The length of streaks lies in the range of ~ 2.6 to 4.48 µm. These streaks are the aggregation of molecules in L_2 phase on substrate.

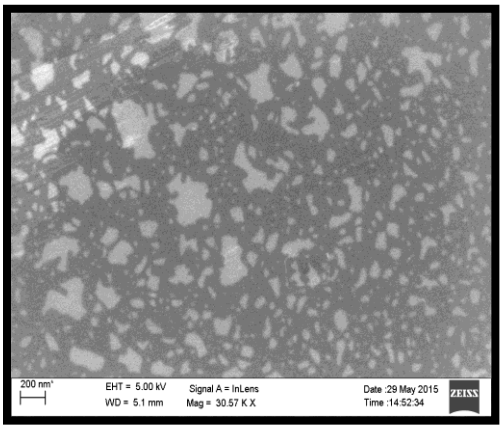

(a)

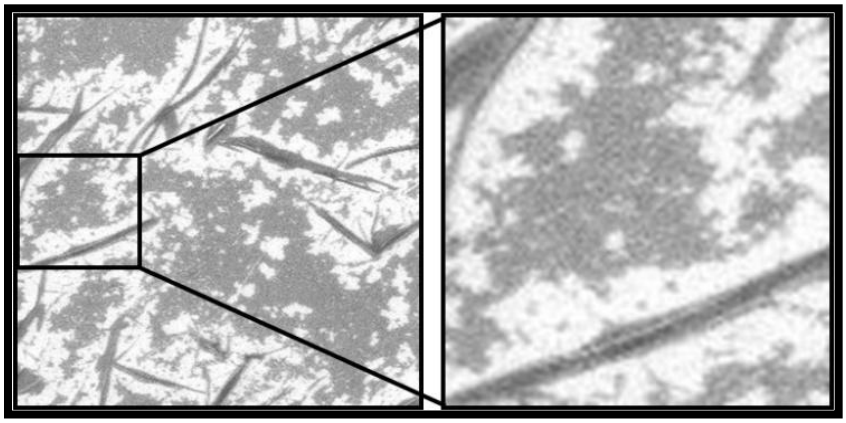

(b) (c)

Figure 6.10: The FESEM images of LB film of BN1 molecule deposited on Si/SiO_2 substrate at (a) π_t = 5 mN/m, (b& c) π_t = 30 mN/m target surface pressures. The size of images (a),(b) and (c) are 4x3μm^2, 12x12μm^2 and 4x4μm^2, respectively.

The FESEM images of LB film of BN2 molecule deposited on Si/SiO_2 substrate at different π_t = 5 and 30 mN/m are shown in figure 6.11. The film deposited at π_t = 5 mN/m, shows some network of small and large grains on substrate (figure 6.11(a)). The film deposited at higher π_t = 30 mN/m is in L_2 phase, shows highly dense network like structure on substrate (figure 6.11 (b)). This network is the aggregation of BN2 molecules in highly dense liquid condensed phase.

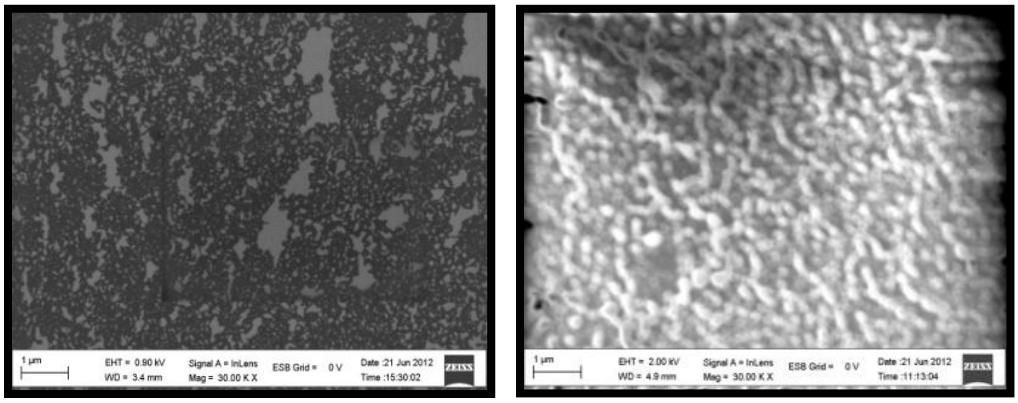

(a) (b)

Figure 6.11: *FESEM images of LB film of BN2 molecule deposited on Si/SiO_2 substrates at (a) π_t = 5 mN/m (b) π_t* = 30 mN/m *target surface pressures. The size of each image is 10x7μm^2.*

6.3.3.2 Atomic Force Microscopy (AFM)

The topography of the LB films of BCLC molecules was studied at low length scale using AFM. The films were scanned in the contact mode using silicon tip having the spring constant ~ 0.2 N/m. The images were analyzed using the WSxM software.

(a) LB and ILS film of B-CN molecules on Si/SiO_2 substrates

The AFM images and height profile of the LB film of B-CN molecules deposited on HPL Si/SiO_2 substrates at π_t = 2, 20 and 30 mN/m are shown in figure 6.12.

The topographic image of LB film of B-CN molecules deposited onto Si/SiO_2 substrate at lower π_t (= 2 mN/m) is shown in figure 6.12(a). It is clear from both 2-dimensional (2D) and 3D images that the coverage of molecules at lower π_t on the substrate is less with large voids. The variation in height is ~ 4 to 5 nm. The domain size lies in the range 150 ~ 350 nm. On increasing the π_t (= 20 mN/m), the coverage of substrate increases (figure 6.12(b)) and the domain size is found to be very small. With further increase in π_t, void disappears and a uniform film of B-CN molecules on substrate can be observed.

The average roughness (S_a) at low π_t = 2mN/m is ~ 0.9 nm whereas for π_t = 20, 30 mN/m, S_a values are ~ 0.43, ~ 0.46 nm, respectively. The value of S_a is less for the LB film of B-CN deposited at higher π_t which indicates that the monolayer deposited at higher π_t (20 and 30 mN/m) forms a uniform coverage over the Si/SiO_2 substrate.

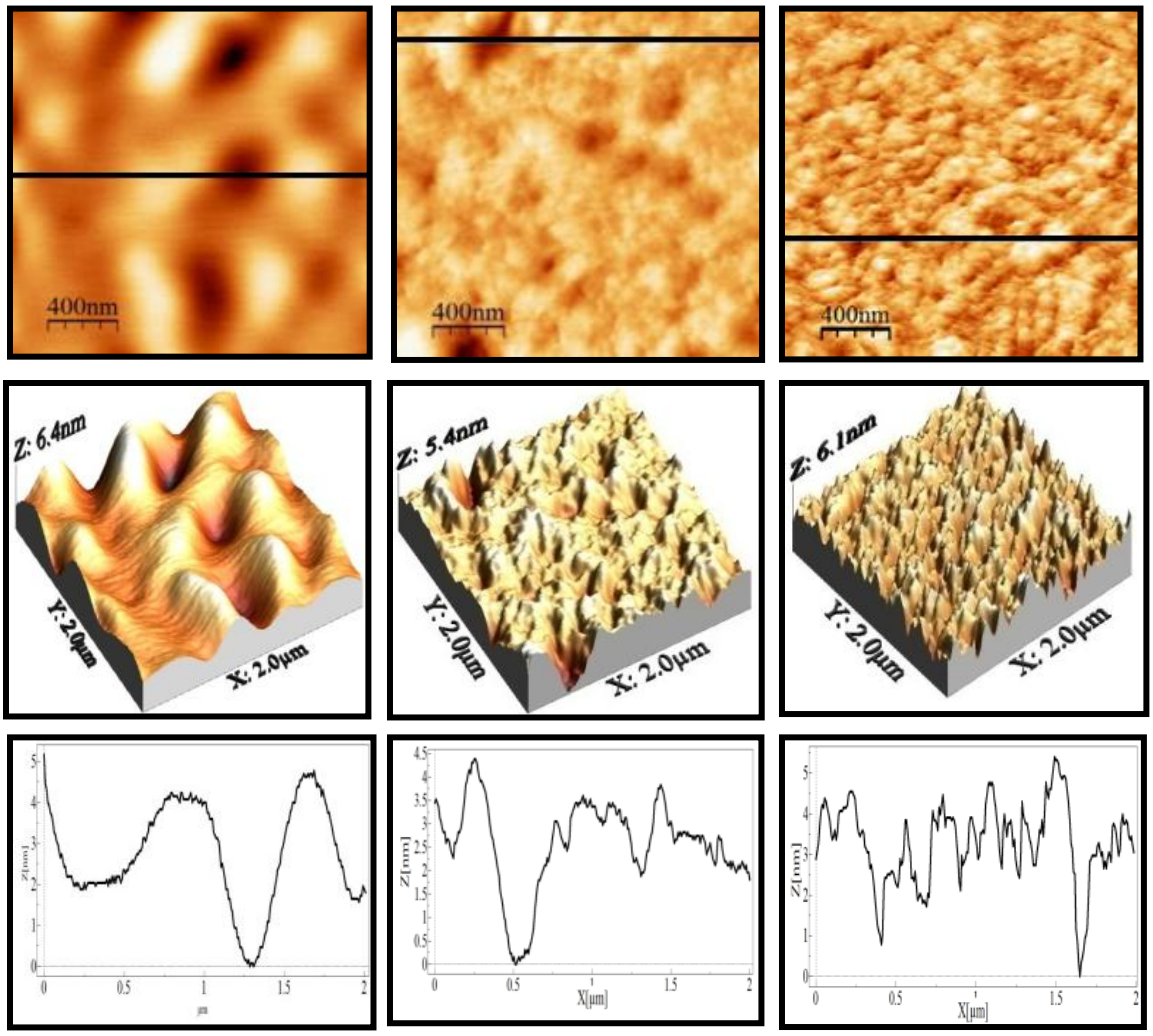

(a) (b) (c)

Figure 6.12: Atomic force microscope images of LB of B-CN on Si/SiO_2 substrates deposited at different target surface pressures π_t = (a) 2 (b) 20 (c) 30 mN/m.

The maximum height of the film is around ~ 5 nm which lies in the range of length of molecule (4.7 nm). It indicates that a single monolayer of B-CN molecules is transferred on Si/SiO_2 substrates with a normal orientation of the molecules. The bar diagram of S_a as a function of π_t (figure 6.13) of LB film of B-CN on the substrate indicates that the film is more uniform at

higher π_t as compared to lower π_t.

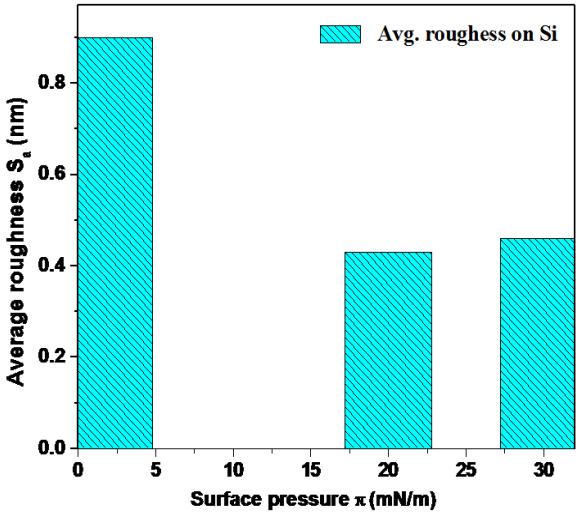

Figure 6.13: Average roughness (S_a) as a function of target surface pressure (π_t) of LB film of B-CN on Si/SiO_2.

By using the ILS method, a single layer of B-CN molecules is transferred on to Si/SiO_2 substrates at π_t = 10 mN/m. The topography of ILS film of B-CN molecules on Si/SiO_2 substrates at π_t = 10 mN/m were recorded using AFM in non-contact mode. The topographic image (figure 6.14) of ILS film of B-CN on Si/SiO_2 substrates at π_t = 10 mN/m shows uniform deposition on substrates similar to the LB film deposited at higher π_t. The value of S_a is ~ 0.3 nm indicating the smooth film of B-CN molecules on the substrate.

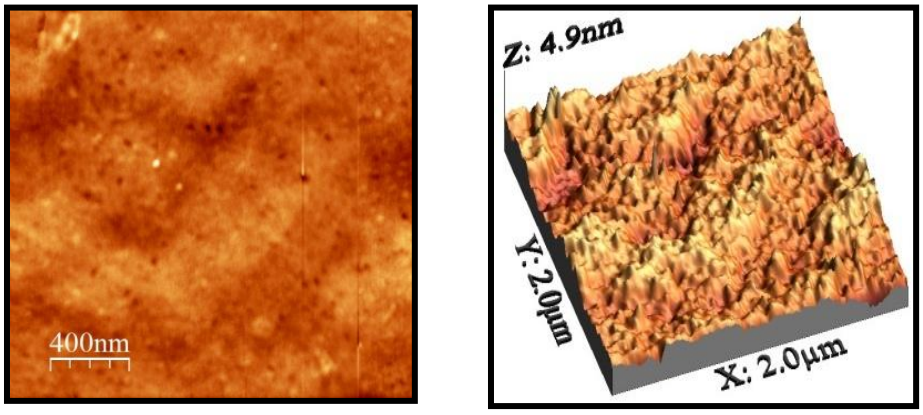

(a) (b)

Figure 6.14: Topographic image of Inverse Langmuir- Schafer (ILS) film of B-CN on Si/SiO_2 substrates deposited at target surface pressures π_t =10 mN/m (a)2D and (b)3D representation.

This indicates that the topography of the single layer of LB film is similar to the single layer deposited using ILS method.

(b) LB film of BN1 molecules on Si/SiO_2 substrates

The topography images along with the height profile of LB film of BN1 deposited on Si/SiO_2 at π_t = 2, 10 and 20mN/m are shown in figure 6.15. The topographic images of LB film of BN1 deposited on Si/SiO_2 substrate shows uniform film with some defects.

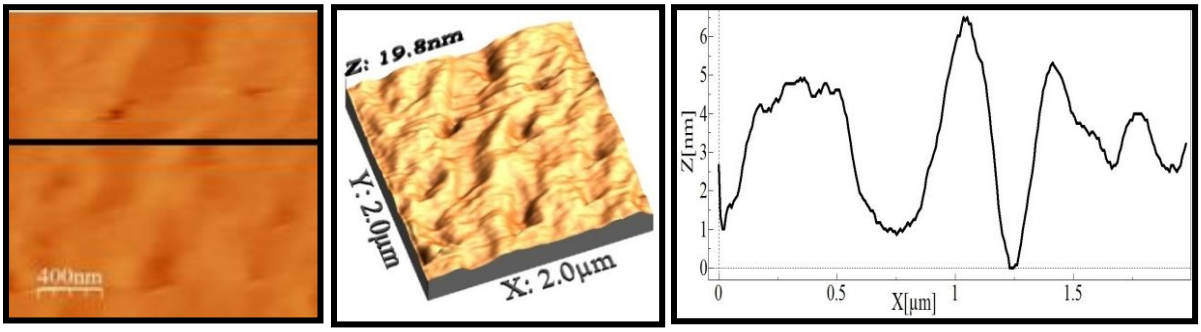

(a) At π_t = 2 mN/m

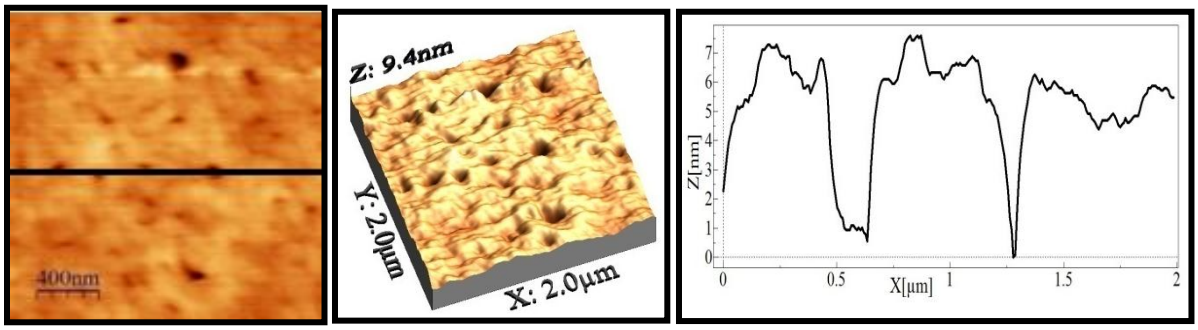

(b) At π_t = 10 mN/m

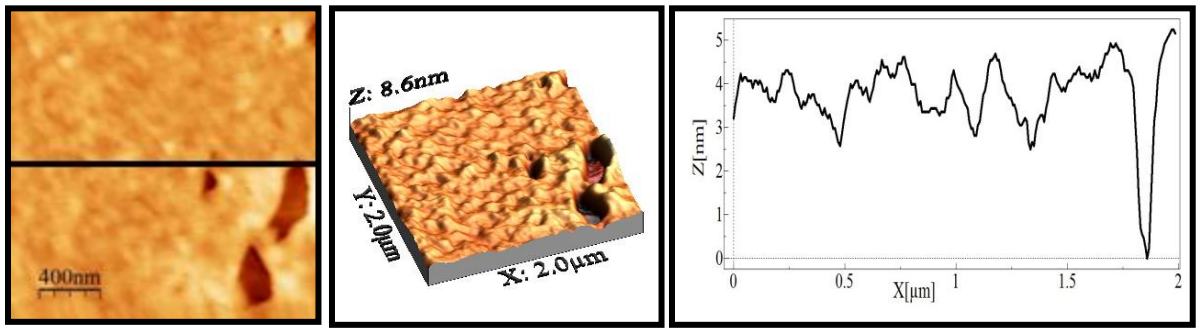

(c) At π_t = 20 mN/m

Figure 6.15: Atomic force microscope images of LB Film of BN1deposited on Si/SiO_2 substrates at different target surface pressures.

Both 3D and height profile suggest that the density w.r.t coverage of molecules on the substrate at lower π_t (= 2 mN/m) is found to be less with voids in between the region covered with molecules, and the variation in height is around 4-5 nm. On increasing π_t, the coverage of substrate increases and the number of defects as voids reduces (figure 6.15(b) and(c)). The average thickness of the film is around 5-7 nm.

(c) LB film of BN2 molecules on Si /SiO_2 substrates

The AFM image of LB film of BN2 deposited on Si/SiO_2 substrate at π_t = 2, 10, 20 and 30 mN/m are shown in figure 6.16. The topographic images of LB film of BN2 deposited on Si/SiO_2 substrate show triangular shaped domains with some defects (figure 6.16(a)). The topography and height profile images of LB film of BN2 molecules onto Si/SiO_2 substrate indicates that at lower π_t, the average thickness of thin film is around ~ 6 nm. This is larger than the length of molecule (5.2 nm). There are some irregular patterns of triangular domains in the film, which shows a variation in height from ~ 4 - 6 nm. It indicates that BN2 molecules may assemble on Si/SiO_2 substrate in a layering pattern with some non-uniformity. With increase in value π_t, the density of these triangular domain increases (figure 6.16(b) to (d)) and the film appears more and more uniform at this length scale. The height profile of LB film of BN2 deposited on Si substrates at different π_t (2, 10, 20 and 30 mN/m) shows average height of the LB film is around ~ 5 nm.

The voids in the LB film for π_t = 2, 10 and 20 mN/m can be clearly seen from the images in figure 6.16 (a), (b) and (c). The AFM image of the LB film deposited at π_t = 30 mN/m shows uniform texture with no voids. However, some triangular domain can be seen from the image. The height of these triangular domains on film lies in the range of ~ 4 to 5 nm which is less than the bilayer of the molecules. It indicates that there may be a partial bilayer formation of BN2 molecules on the Si/SiO_2 substrate.

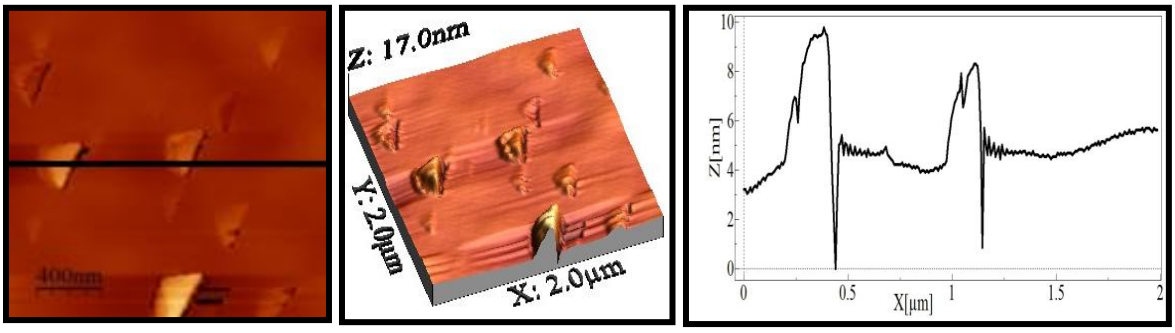

(a) At π_t = 2 mN/m

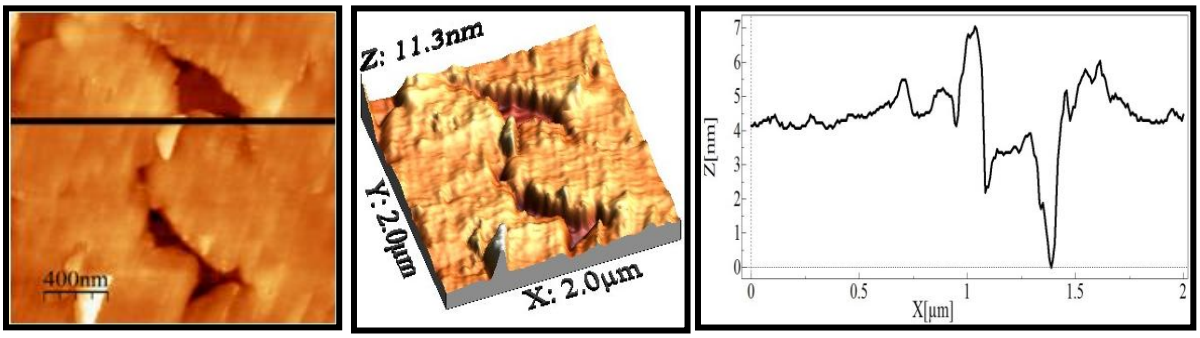

(b) At π_t = 10 mN/m

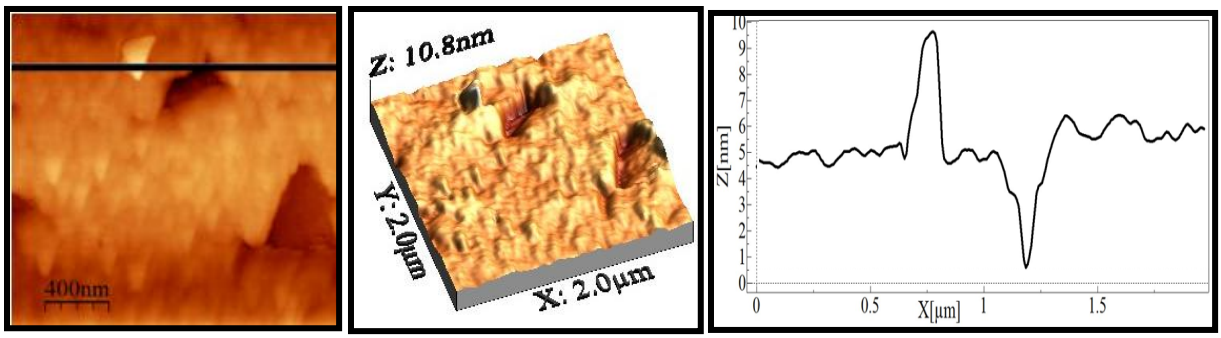

(c) At π_t =20 mN/m

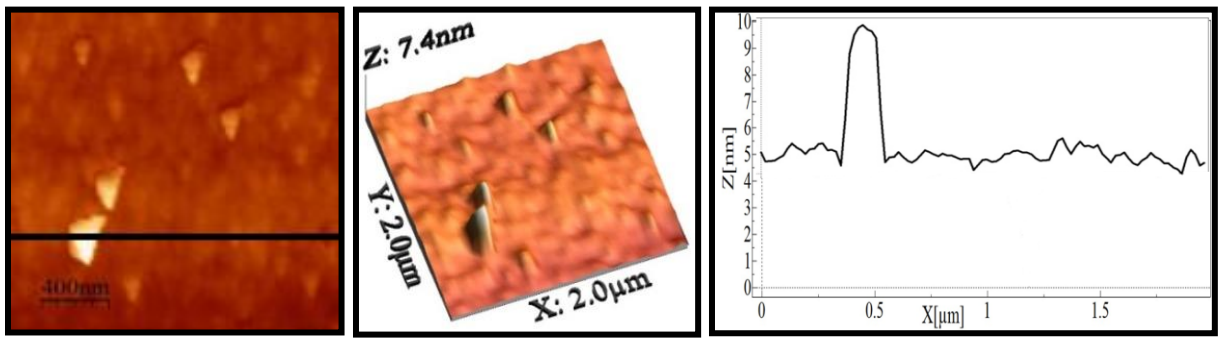

(d) At π_t =30 mN/m

Figure 6.16: Atomic force microscope images of LB film of BN2 on Si/SiO_2 substrate deposited at different (2, 10, 20 and 30 mN/m) target surface pressures.

(d) LB film of B-CN molecules on ITO substrates

The LB films of B-CN molecules is also transferred onto ITO plates at different value of π_t and scanned using AFM. The AFM image of bare ITO plate is shown in figure 6.17. The topography images along with the corresponding height profiles of the LB film of B-CN molecules deposited on ITO plate at π_t = 2, 10 and 30 mN/m are shown in figure 6.18. The AFM images of LB film on ITO plate shows granular texture. The granular texture may arise due to the underlying grains of ITO domains on the glass plate (figure 6.17).

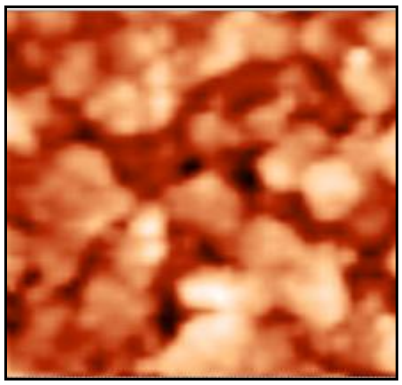

Figure 6.17: Atomic force microscope images of bare ITO. The size of image is 2x2μm^2.

The AFM image at π_t = 2 mN/m shows wide grains with the approximate size of 150 ~ 360 nm. On increasing π_t to 10 mN/m, the density of grains increases and their size lies between 140 ~ 300 nm. On further increasing π_t, a large density of small and large size grains are observed.

The height profile of the B-CN molecules at lower π_t shows that there are fewer voids in between the region covered with molecules in the film. The number of such voids increases with increasing π_t. This indicates that the film becomes less uniform at high π_t. The height of the film lies in the range ~ 5 to 9 nm which is larger than the length of molecule (4.7 nm) and less than bilayer of the molecules. It indicates that there may be a partial bilayer formation of the B-CN molecules on ITO plate.

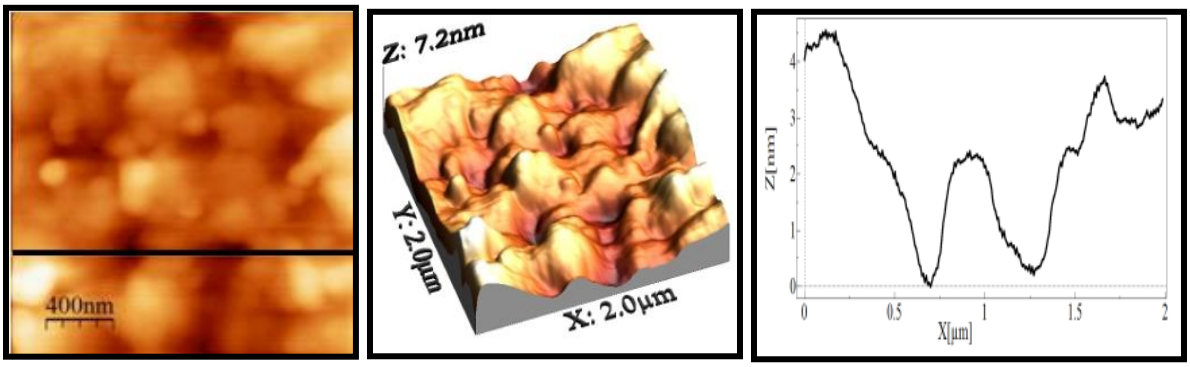

(a) at π_t = 2 mN/m

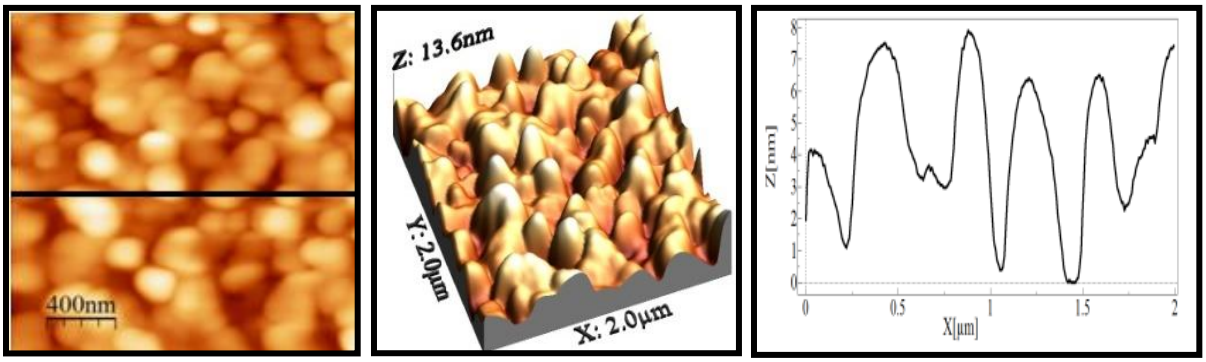

(b) at π_t = 10 mN/m

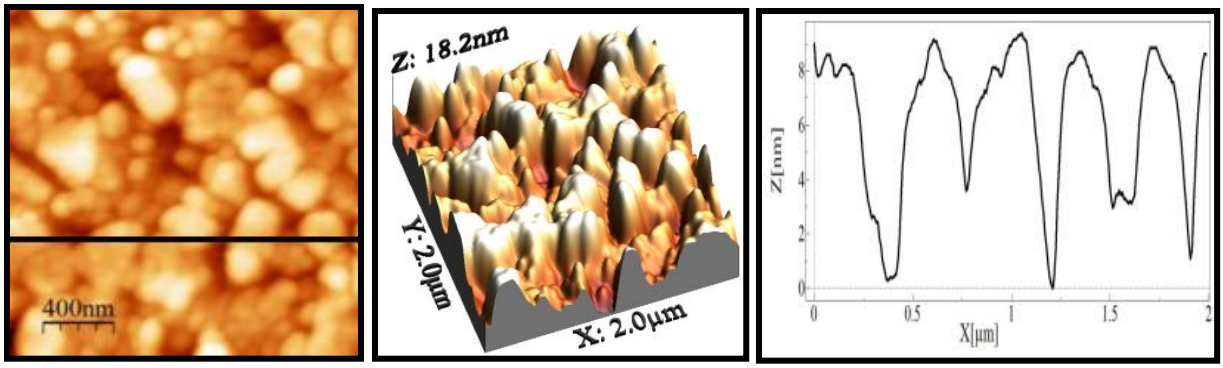

(c) at π_t = 30 mN/m

Figure 6.18: Atomic force microscope images of LB of B-CN on ITO substrate deposited at different target surface pressures (a) π_t = 2 mN/m (b) π_t = 10 mN/m and (c) π_t = 30 mN/m.

The plot S_a as a function of π_t is shown in figure 6.19. The value of S_a at π_t = 2 mN/m is 0.58 nm whereas S_a value are 1.63 and 2.34 nm for LB film of B-CN deposited on ITO at π_t = 10 and 30 mN/m, respectively. It reveals that the film deposited on ITO substrate is more uniform at lower π_t as compared to higher π_t.

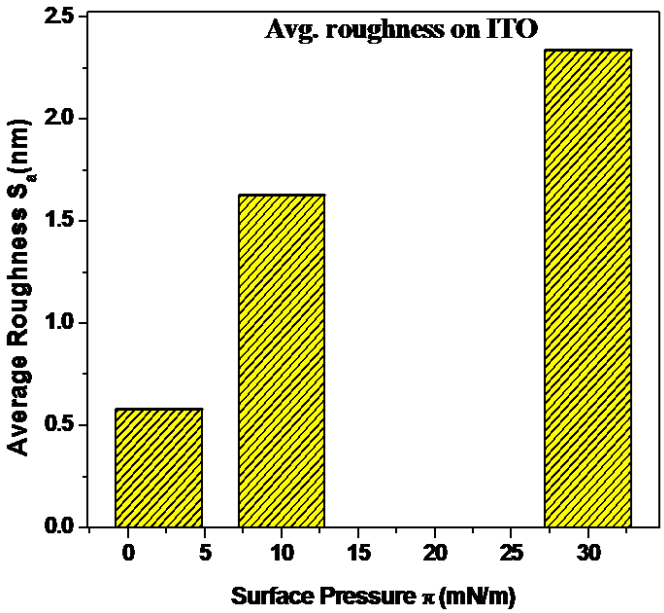

Figure 6.19: Average roughness (S_a) as a function of target surface pressure(π_t) of LB film of B-CN on ITO substrate.

We also transferred the LB film of both BN1 and BN2 molecules onto ITO plate at π_t = 2, 10, 20 and 30 mN/m and scanned using AFM in contact mode. We observed the similar granular texture on ITO plate for LB film of both BN1 and BN2 molecules at different π_t.

The height profile images show that the banana molecules are forming partial bilayer on the solid substrate. The HPL and HPB nature of the LB film of banana molecules on Si/SiO_2 substrate was investigated using force - distance spectroscopy of AFM. The orientation of polar or non-polar part of the molecule on Si/SiO_2 substrate can be studied by calculating the adhesion force between an AFM tip and the LB film. AFM has the ability of measuring the interaction forces between the cantilever and the substrate with force-distance spectroscopy. The interaction force between the tip and the sample is affected by the orientation of the molecules in the LB film as well as by the environment [38-40]. Therefore, by studying the interaction between AFM tip and sample, the orientation of molecules can be estimated qualitatively. Such studies can be made by recording the force-distance characteristic curve using the AFM probe. The adhesion force can be calculated by assuming the force as a linear function of the probe displacement relative to the sample surface along the Z-axis.

Figure 6.20 (a) shows the DFL-height curve of HPL Si/SiO_2 with HPL Si/Si_3N_4 tip. Here DFL is

the difference in signal between top and bottom halves of the photodiode in the AFM. The value of DX and DY in the curve 6.20 (a), are Δheight and ΔDFL, respectively. The adhesion force is calculated using Hooke's law:

$$F = k \times \Delta X \qquad 6.1$$

Here k is the cantilever stiffness and ΔX is the Δ height of the curve. In our case the value of k is ~0.2 N/m. The adhesion force was calculated using average of Δ height measured at different positions. The average value of adhesion force with HPL tip, for Si/SiO_2 substrate is ~ 45.34 nN. Similarly, we have also calculated adhesion force of LB film of BN2 on Si/SiO_2 substrate with HPL tip. Figure 6.20 (b) shows the DFL-height curve of LB film of BN2 on Si/SiO_2 substrate with HPL tip. The average value of adhesion force for LB film of BN2 on Si/SiO_2 with HPL tip is ~ 204 nN.

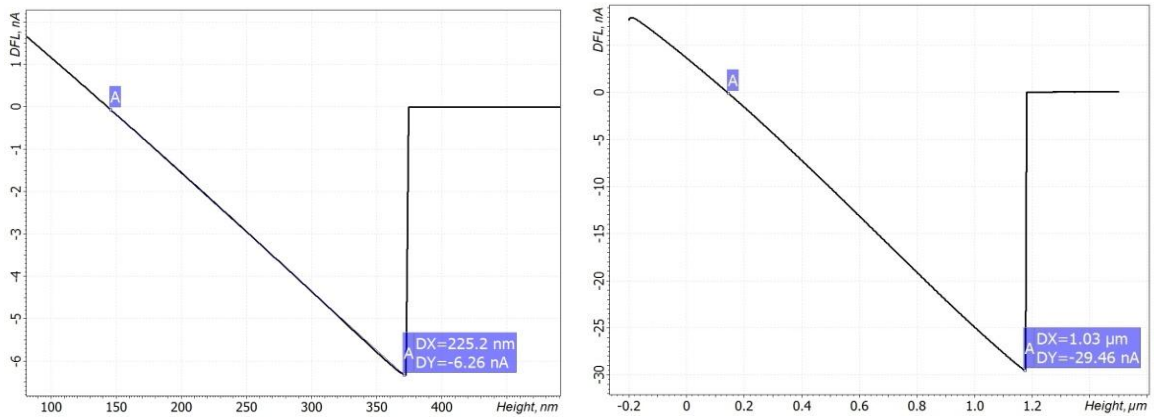

(a) (b)

Figure 6.20: The DFL-Height curve of (a) bare Si/SiO_2 substrate and (b) LB film of BN2 on Si/SiO_2 substrate with Si/Si_3N_4 tip.

We also estimated the adhesion force of HPL Si/SiO_2 substrate and LB film of BN2 on Si/SiO_2 substrate with HPB functionalized tip. To functionalize the tip, the Si/Si_3N_4 tip (HPL in nature) was dipped into the solution of HMDS (Hexamethyldisilazane) and chloroform (1:9) solution for ~3 hours. Figure 6.21 shows the DFL-height curve of bare HPL Si/SiO_2 substrate and LB film of BN2 on Si/SiO_2 substrate with HPB functionalized tip. The average value of adhesion force with HPB functionalized tip, for Si/SiO_2 substrate and LB film of BN2 on Si/SiO_2 are ~ 33.2 and ~ 272 nN, respectively.

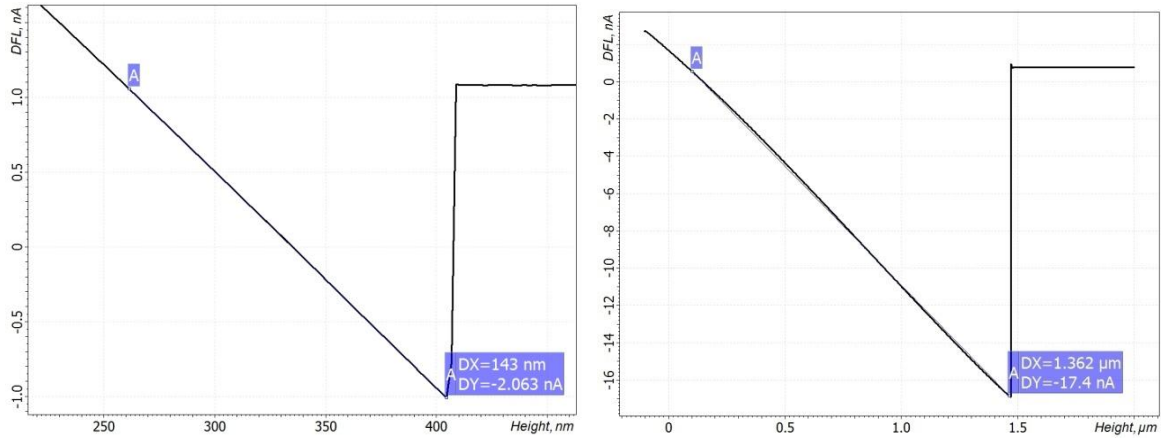

(a) (b)

Figure 6.21: The DFL-Height curve of (a) bare Si/SiO_2 substrate and (b) LB film of BN2 on Si/SiO_2 substrate with HPB functionalized tip.

The average value of adhesion forces for Si/SiO_2 substrate and LB film of BN2 on Si/SiO_2 with Si/Si_3N_4 HPL tip and HPB functionalized tip are listed in Table 6.1.

Table 6.1: Value of Adhesion forces of pure Si and LB film on Si substrate using different tips.

	adhesion force for HPL Si substrate (nN)	**adhesion force for LB film of BN2 on Si substrate (nN)**
with HPL Si/Si_3N_4 tip	45.34	204
With HPB functionalized tip	33.23	272

The value of adhesion force is found to be maximum when probed using HPB tips. This suggests that there may exist a strong van der walls attractive force between the tip and the sample. Such strong attractive force may arise due to interaction between methyl group of the tip with the alkyl chain to the BN2 molecules.

Thus our studies indicate that the LB film of BN2 exhibits a partial bilayer structure with the alkyl chain projected in the air-medium (figure 6.23)

6.3.3.3 X-ray diffraction

To confirm the partial bilayer formation of BCLC on Si/SiO_2 substrate, the LB film of BN2 molecules on Si/SiO_2 substrate was characterized using the X-ray diffraction (PAN alytical XPERT-PRO). A single layer of LB film of BN2 was transferred at π_t = 30 mN/m on HPL Si/SiO_2 substrate. The X-ray diffraction curve obtained using such LB film is shown in figure 6.22.

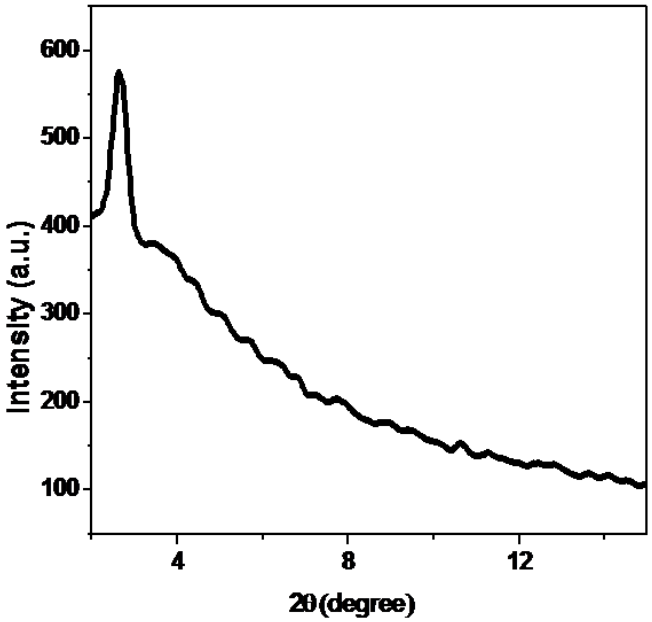

Figure 6.22: X-ray diffraction from the LB film of BN2 deposited on HPL Si substrate.

The d-spacing of LB film of BN2 was found to be ~ 3.2 nm for 2θ = 2.7°. The reported value of d-spacing in bulk material are 5.9 and 2.9 nm for θ = 0.8° and 1.4° corresponding to partial bilayer smectic A (smectic A_d) phase [33]. The obtained value of d-spacing of LB film of BN2 is almost similar to the reported value of this molecule in bulk. This reveals that the LB film of BN2 molecules on Si/SiO_2 substrate exhibit partial bilayer similar to smectic A_d phase. We could not measure another d-spacing value for lower value of θ = 0.8°, due to the lack of accessibility of small angle in XRD system.

On the basis of the AFM images, X-ray result and the values of adhesive force, we propose a model for the orientation of BN2 molecule on Si/SiO_2 substrate. The BN2 molecules get aligned on to the substrates in such a manner that the polar part NO_2 gets attached to the surface of HPL Si/SiO_2 substrate and non-polar part remains in the air as shown in the figure 6.23. The BN2

molecules in the bulk exhibit partial bilayer antiferroelectric smectic A phase; and the LB film of BN2 molecules on Si/SiO_2 exhibit partial bilayer smectic A phase. The molecules in second layer get aligned in opposite direction with respect to the polarization direction of the first layer as shown in figure 6.23.

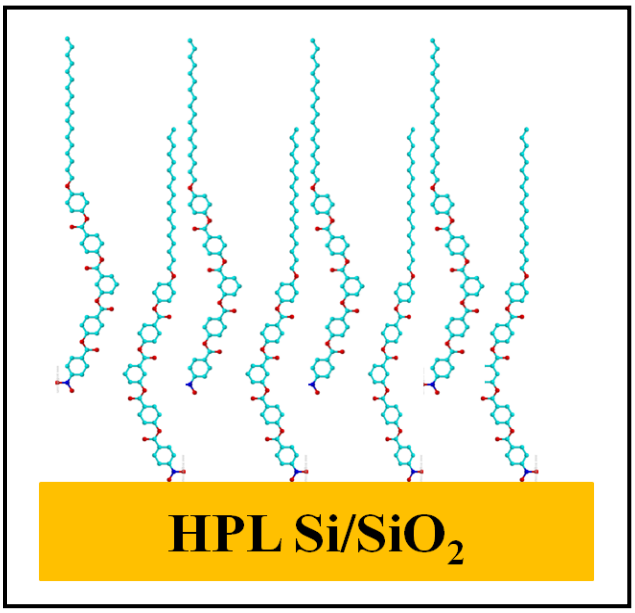

Figure 6.23: The proposed model of LB film of BN2 molecule for the orientation of molecules on substrate.

6.3.4 Fabrication of Liquid Crystal cell and Characterization

A single layer of B-CN molecule was deposited onto quartz, ITO and glass plates at different π_t using the both LB and ILS methods. LC cells of ~ 8 μm thickness were fabricated using such substrates. The NLC (E7) was filled in such cells at room temperature. These LC cells prepared using LB films deposited at different π_t were placed on the POM stage and textures were observed.

In LC cells prepared using LB films of B-CN molecules deposited on quartz plates at π_t = 2 mN/m, a complete dark state was observed at all angles of rotation of the sample stage of POM indicating a homeotropic alignment of NLC. For π_t = 30 mN/m, we observed a change in intensity through sample placed between crossed polarizer which indicates planar tendency of NLCs, but the alignment was not uniform.

We also fabricated the LC cell using LB film of B-CN molecules deposited on ITO plates at π_t =

2, 20 and 30 mN/m. The alignment of NLCs in these LC cells prepared show a planar tendency of alignment of NLCs, but they do not show good alignment.

We also fabricated the LC cells using ILS films of B-CN deposited on ITO at π_t = 10 and 30 mN/m and then the cells were examined under POM. The optical texture of NLC in these cells is shown in figure 6.24 (a) and (b). At π_t = 10 mN/m, under the crossed polarizers, we observed bright and dark state on rotation of the POM stage for ILS film deposited on ITO plate (as shown in figure 6.24 (a)). It can be clearly noticed that these LC cells exhibit a planar orientation. At higher π_t = 30 mN/m, complete dark state was observed on rotating POM stage for cells prepared using the ILS films deposited on ITO plate as shown in figure 6.24 (b) .This represents homeotropic alignment of NLCs.

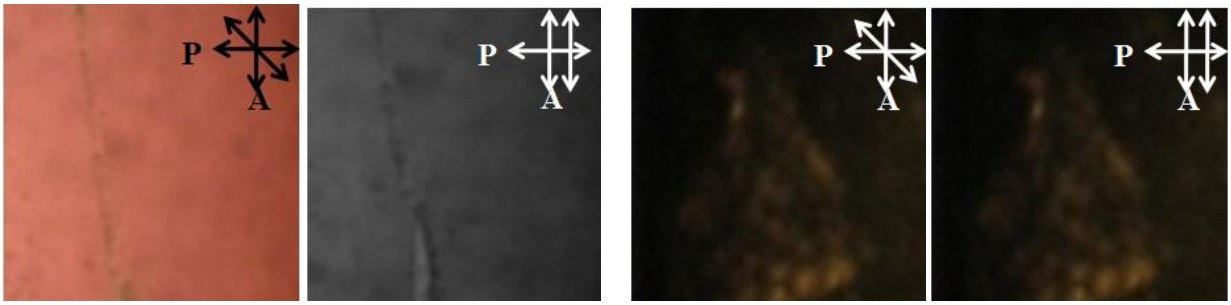

(a) (b)

Figure 6.24: The polarizing microscopy textures of the LC cell fabricated using Inverse Langmuir-Schafer film of B-CN on ITO plates at target surface pressures (a) π_t =10 (b) π_t = 30 mN/m.

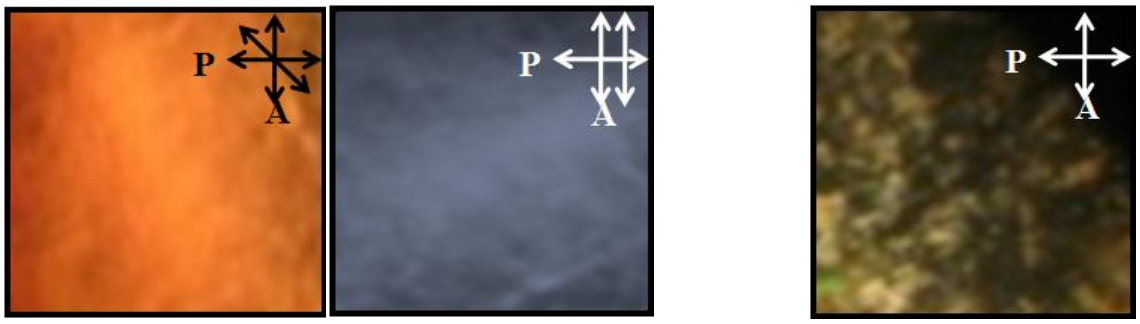

(a) (b)

Figure 6.25: The polarizing microscopy textures of the LC cell fabricated using Inverse Langmuir-Schafer film of B-CN on glass plates at target surface pressures (a) π_t =10 (b) π_t = 30 mN/m.

ILS film of B-CN molecules were also transferred on microscopic glass slide at π_t = 10 and 30 mN/m. The LC cells prepared using such ILS deposited glass substrates shows planar and homeotropic alignment of NLCs at π_t = 10 and 30 mN/m, respectively as shown in figure 6.25(a) and (b).

LB film of BN1 molecules was deposited on ITO substrate at different target pressure (π_t = 2, 30 and 40 mN/m). The LB film of BN2 molecules was also deposited on ITO substrate at different target pressure (π_t = 2, 10, 20 and 40 mN/m). These substrates were used for the fabrication of LC cell with ~ 8 µm thickness. The NLC, E7 was filled in these cells. The textures of E7 in these cells were observed using POM.

Figure 6.26 (a), (b) and (c) show the optical textures of E7 in the cell fabricated using LB film of BN1 deposited onto ITO at π_t = 2, 30 and 40 mN/m respectively. These textures are obtained between the crossed polarizers of POM.

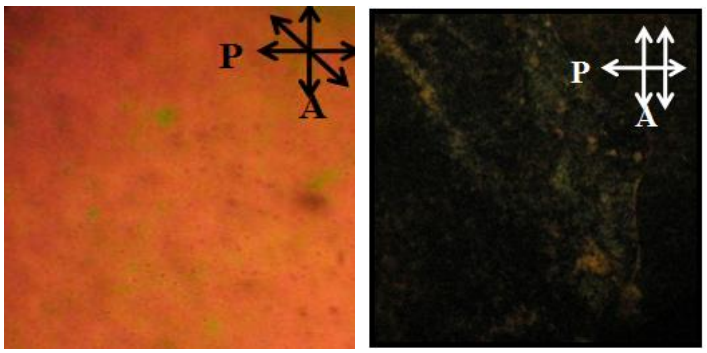

(a)

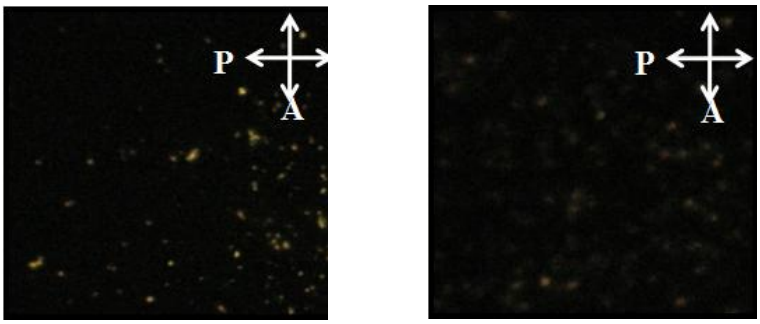

(b) (c)

Figure 6.26: The polarizing microscopy textures of the LC cell fabricated using Langmuir-Blodgett film of BN1 on ITO substrates at different target surface pressures (a) π_t = 2 mN/m (b) π_t = 30 mN/m (c) π_t = 40 mN/m.

At π_t = 2 mN/m, we observed bright and dark state on rotating the sample by 45 degree between the crossed polarizers which confirms the planar alignment of NLC, whereas the cell fabricated at π_t = 30 and 40 mN/m shows complete dark state at all angle of rotation of the POM stage indicating homeotropic alignment of NLC as shown in figure 6.26 (b) & (c).

LC cells fabricated using LB film of BN2 molecules which were deposited on ITO at π_t = 2, 10, 20 and 40 mN/m. E7 LC was filled in these cells. The optical textures of NLC in these cells are shown in figure 6.27 (a), (b), (c) and (d). In all cells, bright and dark states were observed with rotating POM stage. This represents a planar alignment of LCs.

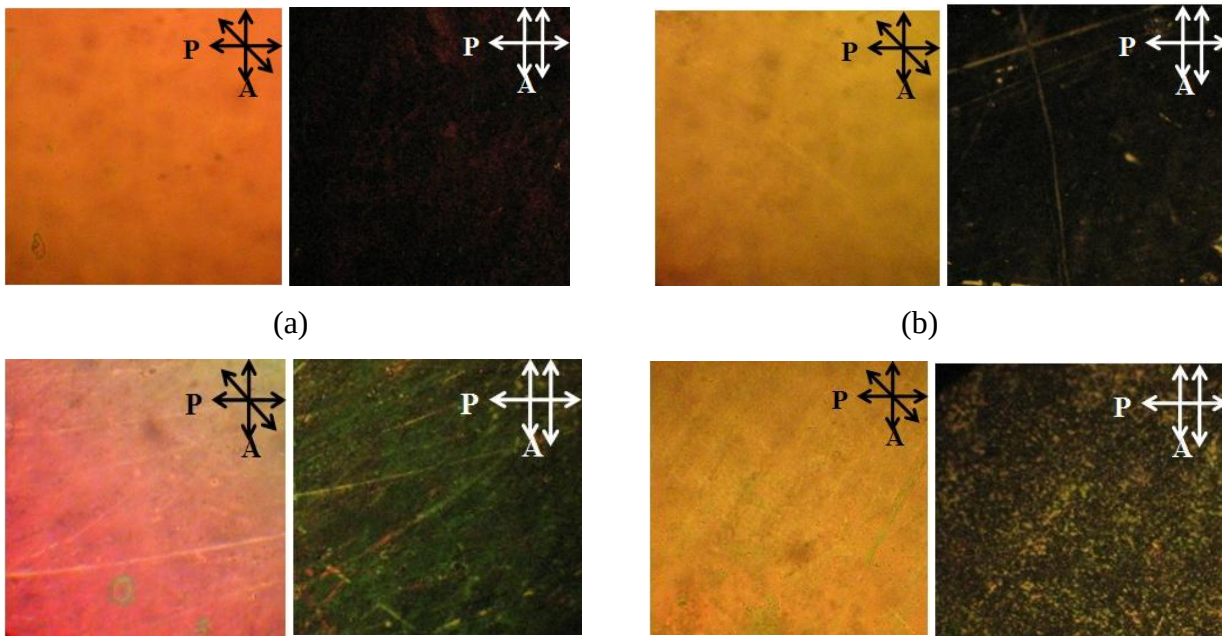

Figure 6.27: The polarizing microscopy textures of the LC cell fabricated using Langmuir-Blodgett film of BN2 on ITO substrates at different target surface pressures (a) π_t =2 mN/m (b) π_t = 10 mN/m (c) π_t = 20 mN/m (d) π_t =40 mN/m.

LB film of BN1 molecules was also deposited on quartz plate at π_t = 20, 30 and 40 mN/m. We fabricated the LC cell using such LB deposited quartz plates. E7 LC was filled in these cells. We obtained homeotropic alignment of LCs in all cell.

LC cells fabricated using LB film of BN2 molecules which were deposited on quartz plate at π_t = 2, 30 and 40 mN/m. E7 LC was filled in these cells. We obtained planar alignment of NLCs.

In summary, it was found that LC cell fabricated using LB film of B-CN deposited onto ITO and quartz plates do not support uniform alignment of the bulk LC. ILS film of B-CN molecule as an aligning layer on ITO favors the planar alignment of the bulk LC. It was also found that the granular texture of LB film of BN2 molecules on ITO and quartz plate favors the planar orientation whereas the uniform layer of the LB of BN1 molecules on quartz and ITO plates support homeotropic orientation of the nematic LC in the LC cells. Such technique for aligning bulk LC can be employed in LC display industries.

If the aligning layer (i.e. LB/ILS films of BCLCs) is uniform, the first layer of LC molecules onto the LB films follow the morphology and yield a smectic layer wherein the LC molecules may align perpendicular to the surface. This geometry may be followed by the LC molecules in bulk yielding a homeotropic geometry (figure 6.28 (a)).

Due to the granular texture of the LB/ILS film of BCLC, the first layer of E7 LC molecules follows the surface morphology. Therefore, the first layer of LC molecules adsorbed to the LB films supported onto the ITO exhibit large bend and twist. Such large bend and twist may be followed up by the LC molecules in the bulk which finally yield a planar orientation of LC molecules (figure 6.28 (b)) in the cells.

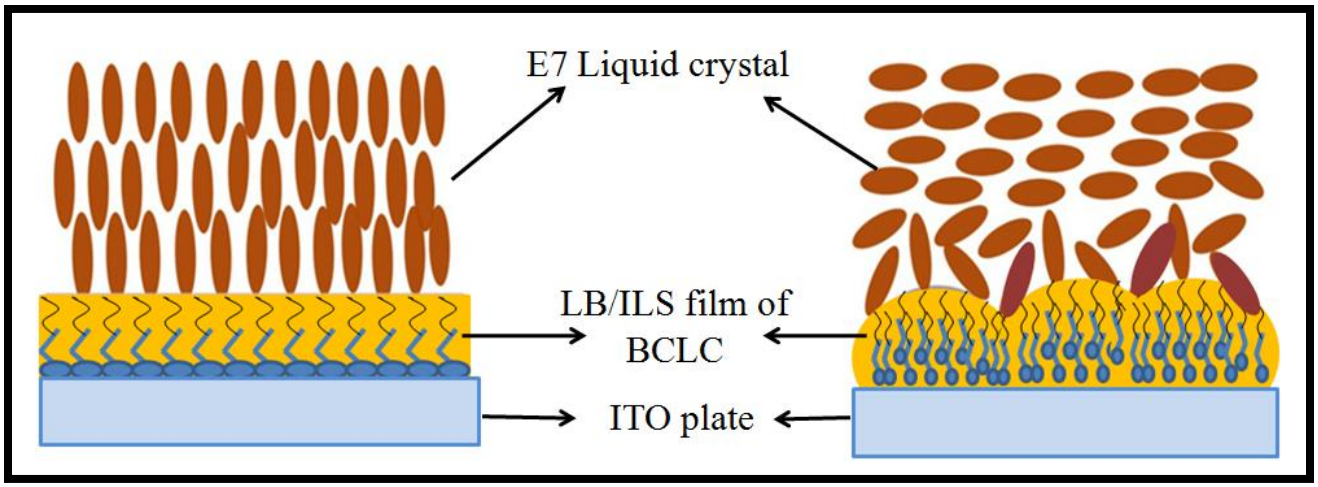

(a) (b)

Figure 6.28: Schematic representation of the (a) homeotropic and (b) planar alignment of liquid crystals on the LB films BCLCs deposited onto ITO substrate.

6.4 Conclusion

The alignment of LC molecules at interface is important in display devices. We studied the role of interfacial LC layers on the alignment of bulk LC.

We formed a stable monolayer of different unsymmetrical B-CN, BN1 and BN2 BC molecules at A/W interface. We transferred the monolayer onto solid substrate (Si/SiO_2 and ITO) using both LB and ILS techniques at different π_t and characterized them using AFM and FESEM. Both LB and ILS film of B-CN molecule on Si/SiO_2 substrate was found to be uniform. We observed a uniform film of BN1 molecules on Si/SiO_2 substrate. The topographic images of LB film of BN2 deposited on Si substrate shows triangular shaped domains with some defects. AFM results show that BN2 molecules get non-uniformly assembled in a layered pattern on Si substrate. With increases in π_t, the density of these triangular shaped domains increases. LB film of banana molecules deposited onto ITO plate shows granular texture with partial bilayer formation of the molecules on substrate.

The force-distance spectroscopy was also studied for the LB film of BN2 molecule on Si/SiO_2 substrate. The adhesion force for LB film of BN2 molecules was measured with HPL Si/Si_3N_4 tip and HPB functionalized tip. The LB film of BN2 was also characterized using the X-Ray. We proposed a model for the orientation of BN2 molecules in the LB film on substrate.

Both LB and ILS film of BC molecules on different substrates (quartz, ITO, glass plate) were employed as alignment layer for the fabrication of LC-cell. The alignment of bulk NLC E7 is studied using POM. The ILS film of B-CN molecules on ITO and glass plates favors the planar alignment of E7 at π_t = 10 mN/m. The uniform LB film of BN1 molecules deposited onto ITO substrate supports the homeotropic alignment whereas the LB film of BN2 molecule supports the planar alignment of NLC in the LC cell. Future work involves a comparative study of electro-optic measurement of LB and ILS film of B-CN molecule as alignment layer.

In the next chapter we will discuss about the formation of LM of achiral symmetric banana molecules at A/W interface and also investigate the behavior of mixed monolayer of the BC molecules with rod shaped molecules.

References

1. T. Niori, T. Sekine, J. Watanabe, T. Furukawa, H. Takezoe, J. Mater. Chem. 6, 7, 1231, **1996**.
2. T. Sekine, T. Niori, M. Sone, J. Watanabe, S.W. Choi, Y. Takanishi, H. Takezoe, Jpn. J. Appl. Phys. 36,6455, **1997**.
3. D. R. Link, G. Natale, R. Shao, J. E. Maclennan, A. N. D. Clark, E. Korblova, D. M. Walba, Science 278, 1924, **1997**.
4. A. Jakli, D. Kruerke, H. Sawade, L. C. Chien, G. Heppke, Liquid Crystal, 29, 377, **2002**.
5. A. Jakli, D. Kruerke, G. G. Nair, Phys. Rev. E 67, 051702, **2003**.
6. Y. Tong, Y. Wang, G. Wang, H. Wang, L. Wang, D. Yan, J. Phys. Chem. B 108, 12921, **2004**.
7. M. O. Neill, S. M. Kelly, J. Phys. D: Appl. Phys. 33, R67, **2000**.
8. J. M. Geary, J. W. Goodby, A. R. Kmetz, J. S. Patel, J. Appl. Phys. 62, 4100, **1987**.
9. J. L. Janning , Appl. Phys. Lett. 21, 173, **1972**.
10. G.L. Gains, "*Insoluble Monolayers at Liquid-Gas Interface*" Interscience: New York. NY, USA, **1996**.
11. R. A. Drawhorn, N. L. Abbott, J. Chem. Phys. 99, 16511, **1995**.
12. Y. L. Cheng, D. N. Batchelder, S. D. Evans, J. R. Henderson, J. E. Lydon, S. D. Ogier, Liquid Crystal 27, 1267, **2000**.
13. J. P. Bramble, S. D. Evans, J. R. Henderson, C. Anquetil, D. J. Cleaver, N. J. Smith, Liquid Crystal 34, 1059, **2007**.
14. C. Mauguin, Bull. Soc. Fr. Mineral. 34, 71, **1911.**
15. J. Cognard, Mol. Cryst. Liq. Cryst. Suppl. Ser. 1, 1, **1982.**
16. T. H. Tang, Y. Wang, G. Wang, H. B. Wang, L.X. Wang, D. H. Yan, J. Phys. Chem. B 108,12921, **2004.**
17. Y. H. Tang, Y. Wang, X. D. Wang, X. D. Xun, C.Y. Mei, L. X. Wang, D. H. Yan, Phys. Chem. B 109,8813, **2005**.
18. J. R. Gong, L. J. Wan, J. Phys. Chem. B 109,18733, **2005**.
19. Y. Kinoshita, B. Park, H. Takezoe, T. Niori , J. Watanabe, Langmuir 14, 6256, **1998**.
20. L. M. Blinov, A. R. Geivandov, V. V. Lazarev, S. P. Palto,S. G. Yuding, G. Pelzl ,W.

Weissflog, Appl. Phys. Lett. 87, 241913, **2005**.

21. L. M. Blinov, P. Palto, V. B. Lazarev, A. R. Geivandov, S. G. Yuding, Crystallography 51, 843, **2006**.
22. A. R. Geivandov, S. P. Alto, S. G. Yudin, L. M. Blinov, G. Pelzl , W. Weissflog, Ferroelectrics 344, 3, **2006**.
23. L. Zou, J. Wang, V. J. Beleva, E. Kooijman, S. V. Primak, J. Risse, W. Weissflog, A. Jakli , E. K. Mann, Langmuir 20, 2772, **2004**.
24. J. Wang, L. Zou, W. Weissflog, A. Jakli, E. K. Mann, Langmuir 22, 3198, **2006**.
25. J. Wang, L. Qiu, A. Jakli, W. Weissflog , E. K. Mann, Liquid Crystal 37, 1229, **2010**.
26. W. Iglesias, T. J. Smith, P. B. Basnet, S. R. Stefanovic, C. Schierske, D. J. Lacks, A. Jakli, E. K. Mann, Soft Matter 7, 9043, **2011**.
27. M. Binggeli, C. M. Mate, Appl. Phys. Lett. 65, 415, **1994**.
28. T. Thundat, X. Y. Zheng, G.Y. Chen, S. L. Sharp, R. J. Warmack, L. J. Schowalter, App. Phys. Lett. 63, 2150, **1993**.
29. T. Thundat, X.Y. Zheng, G.Y. Chen, R. J. Warmack, Surf. Sci. 294, 939, **1993.**
30. T. Eastman, D. M. Zhu, Langmuir 12, 2859, **1996**.
31. M. Schadt, Ann. Revi. Mat. Sci. 27, 305, **1997**.
32. L. E. Tannas, W. E. Glenn, J. W. Doane, Knovel (firm) "*Flat-Panel Display Technologies-Japan, Russia, Ukraine and Belarus"* Noyes Publications: Park Ridge, N. J. **1995.**
33. H. N. S. Murthy, B. K. Sadashiva, Liquid crystal 31,4,567, **2004**.
34. R.K. Gupta, V. Manjuladevi, Ultra thin films, "Comprehensive Guide for Nanocoatings Technology", NOVA Publishers, USA, **2014.**
35. R. K. Gupta, V. Manjuladevi, Israel Journal of Chemistry 52, 809, **2012**.
36. R. K. Gupta, V. Manjuladevi, "*Molecular Interactions at Interfaces"* INTECH Open Access Publisher, **2012.**
37. M. C. Petty, "*Langmuir-Blodgett Films: An Introduction",* Cambridge University Press: Cambridge, U. K. **1996.**
38. E. Meyer, H. Heinzelmann, "*Scanning Tunneling Microscopy II* " Springer, Berlin, **1992.**

39. R. Guckengerger, T. Hartmann, W. Wiegrabe, W. Baumeister, "*Scanning Tunneling Microscopy II* " Springer, Berlin, **1992**.
40. N. A. Burnham, D. D. Dominguez, R. L. Mowery, R. J. Colton, Phys. Rev. Lett. 64, 1931, **1990.**

Chapter-7

Mixed Monolayers of Rod Shaped Liquid Crystals and Bent-Core Liquid Crystals

7.1 Introduction

In the previous chapter we have discussed about the alignment of liquid crystal (LC) using Langmuir - Blodgett (LB) and inverse Langmuir - Schafer (ILS) film of a pure system consisting of bent - core LC (BCLC) molecules. The LB and ILS film of BCLC induces different alignment of bulk LC in the LC cell. It will be interesting to study alignment of LCs using the mixed monolayer of BCLC and calamitic LC as an alignment layer.

LC materials are mostly used in display devices [1-2] and photonic devices [3-5].The ability to control the alignment of the LC molecules at interface is very important from the device fabrication point of view. There are different methods used for LC alignment like rubbing, photo aligned polymers films [6-7], evaporated oxides [8], LB technique [9], self-assembly [10-12]. Among these methods, LB technique is the only technique in which a thin film of LCs or their mixtures can be deposited onto substrates in a highly controlled manner [9] and can be used for aligning bulk LC. The nematic phase of calamitic LCs is most commonly used in large number of devices e.g LCDs. There are few reports in which the bent shaped molecules are used as alignment layer [13].

BCLCs have unique properties like polarity, chirality, biaxiality and ferroelectricity [14-15]. Due to these unique properties bent core molecules can be employed in the fabrication of electro-optical [16], electromechanical [17], and other interesting organic devices [18]. However, the applications of BCLCs are limited because BCLC phases appear at a temperature higher than the room temperature. The mixture of BC and calamitic molecules can show interesting properties

like improvement of the chirality in cholesterics phase and induction of antiferroelectric order in smectics [19-21], and can expand the mesophase temperature range [22-24].There are some studies based on the miscibility of fatty acids in thermotropic LCs [25-27].

Hall et al. [25] studied the miscibility of the guest molecule (dodecylcyanobiphenyl LC (12CB)) in the host of long chain fatty acid molecules (arachidic acid (AA) and oleic acid (OA)) at an air-water (A/W) interface using surface pressure - area (π - *A*) isotherm and spectroscopic techniques. They found that the guest 12CB was immiscible in AA and miscible in OA over a wide range of compositions [25].

Martynski et al.[26] have studied the two-component films of 4-4-octyl-4'-cyanobiphenyl (8CB) and a non amphiphilic azo dye on an A/W interface by means of π - *A* isotherm measurement, Brewster angle microscopy (BAM) and absorption spectroscopy. Their thermodynamic and BAM study indicate that the molecules of 8CB and azo dye are partially miscible **[**26].

Anna et al. [27] have investigated the miscibility of AA with fluoro substituted LCs (4-cyano-3-fluorophenyl 4'-n-octyloxybenzoate (8OCFPB) LC and six other LCs (Nnm)) at A/W and air-solid (A/S) interface.

In the previous chapter we have discussed about the behavior of unsymmetrical BC molecules with either polar CN or NO_2 group at one end of the bend-core at A/W and A/S interfaces. There are few studies showing that symmetric BC molecules can form Langmuir film (LF). These LF were unstable forming multilayer even near zero pressure [28-31], however these LB films were used to align nematic bent core LC. In this chapter we present the results of our investigation on the interaction of symmetric BC molecules (((((5-cyano-1, 3-phenylene) bis(oxy)) bis(carbonyl))bis (2-fluoro-4,1-phenylene) bis(4'-nonyl-[1,1'-biphenyl]-4-carboxylate))) at A/W and A/S interfaces. In this molecule, the CN group is attached at the fifth position on the central phenyl ring and a fluorine substituent on the phenyl ring adjacent to it in the arms of the seven-ring esters. Now onwards we will refer to this ($C_{65}H_{63}F_2NO_8$) compound as 5CNBC in this chapter. The surface behavior of 5CNBC molecules at A/W and A/S interface was studied. The study reveals that the LF of 5CNBC molecules at A/W interface exhibits gas and liquid - condensed (L_2) phases. A single layer LF of 5CNBC was transferred onto a solid substrate and then it was characterized by using Atomic Force Microscope (AFM). The AFM images reveal a uniform granular texture of 5CNBC molecule for the LB film deposited in the L_2 phase.

In this chapter, we also present the investigation on behavior of mixed monolayer of bent core LC 5CNBC with a range of mole fractions (X_M) of calamitic LC 4-octyloxy-4-cyanobiphenyl (8OCB) at the A/W and A/S interfaces. The information about the miscibility of these two molecules is obtained on the basis of π - *A* isotherms for various X_M and estimating excess area, excess Gibbs free energy criterion. Mixed monolayer of 5CNBC and 8OCB molecules with different X_M was transferred onto solid substrates. Morphology of the mixed LB film was characterized by using AFM. There are no studies available in the literature based on the miscibility of BCLC with calamitic LC at A/W and A/S interface till now.

The alignment of the LC molecules at an interface is important in display devices [32-33]. We have employed LB films of LCs as the alignment layer to align bulk LCs in the LC cell. The alignment of LC can be controlled using the LB films deposited under different conditions employing different LC molecules. LC cells were fabricated using the LB films of 5CNBC and mixed monolayer of 5CNBC and 8OCB molecules. Alignment of calamitic LCs in these cells was observed under a Polarizing Optical Microscope (POM). The dielectric constant measurement of a LC enclosed in such cells was also performed.

7.2 Materials and Experimental Methods

7.2.1 Materials

The banana shaped 5CNBC molecule was synthesized in the laboratory by Prof. Sadashiva et al. at RRI Bengaluru [34]. The 5CNBC molecule is achiral symmetric BCLC. The 5CNBC molecule consists of two hydrophobic end chains and a hydrophilic central core with CN group, which exhibits the phase sequence: Two dimensional columnar (B_1 phase) - Isotropic (Iso). The calamitic 8OCB molecule is purchased from Sigma Aldrich. 8OCB molecule exhibits Smectic A phase (Sm A) as well as Nematic phase (N). The molecular structures of both the molecules and their phase sequence are shown in figure 7.1. The molecular length of 8OCB is ~ 2.24 nm. The molecular length of 5CNBC is ~ 5.96 nm. The bent-core angle is around ~ 143.48° for 5CNBC molecule and cross sectional molecular area of 5CNBC was estimated 0.5nm^2. All these values were calculated using ACD/ChemSketch software.

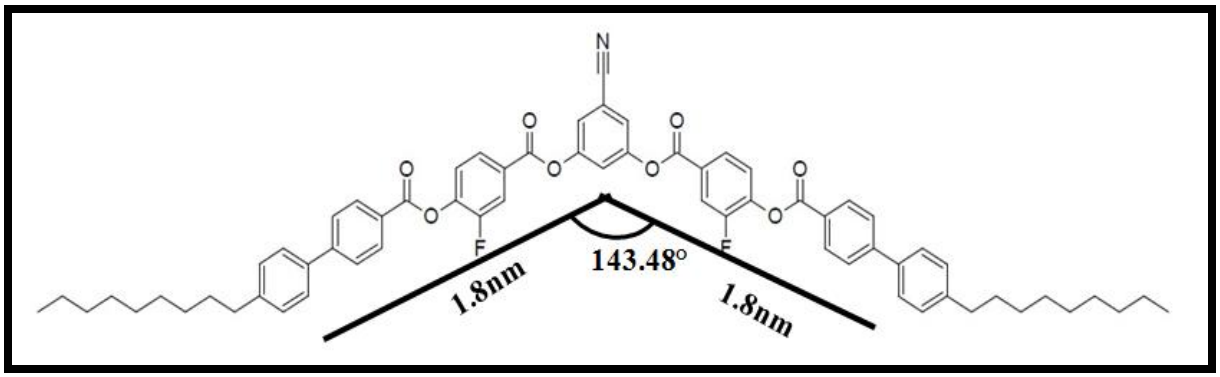

(a)

Cr 157.0°C B_1 201.0° Iso

5CNBC (Bent -Core Molecule)

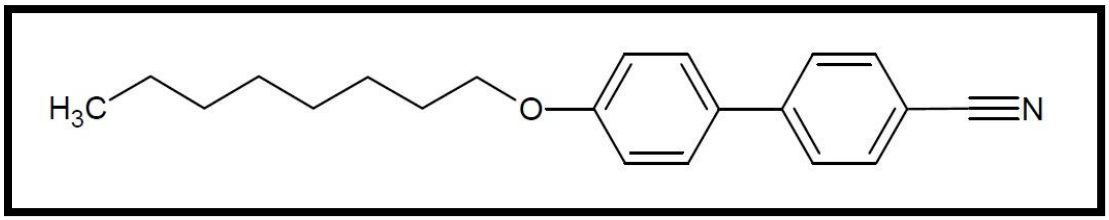

(b)

Cr 56.3°C Sm A 66.5°C N 79.8°C Iso

4-octyloxy-4-cyanobiphenyl (8OCB)

Figure 7.1: Molecular structure and phase sequences exhibited by (a) 5CNBC and (b) 4-octyloxy-4-cyanobiphenyl (8OCB).

7.2.2 Experimental Methods

The solutions of 5CNBC and 8OCB molecules were prepared in chloroform solvent with concentration 0.5 mg/ml each. These solutions were then mixed in an appropriate quantity to obtain different mole fractions (X_M = 0, 0.1, 0.25, 0.50, 0.75, 0.9 & 1) of 8OCB in 5CNBC. An appropriate volume of these above were spread onto the ultrapure ion - free water between the barriers of LB trough separately. The solvent was allowed to evaporate on waiting for ~ 20 minutes, before conducting the measurements. The Langmuir monolayer (LM) was compressed with a barrier speed of 5 mm/min at the A/W interface and simultaneously the surface pressure (π) - area per molecule (A_m) isotherm was recorded.

The LM of 5CNBC and the mixed monolayer of both molecules with different X_M were transferred onto solid substrates by using LB technique at various π_t. Indium tin oxide coated (ITO) glass plates and hydrophilically treated silicon (Si/SiO_2) wafer were used as solid

substrate. The ITO substrates were cleaned thoroughly by ultrapure ion-free water, absolute alcohol and chloroform, successively. The substrates were dried by blowing hot air at about 60°C. Prior to the LB deposition, the LM is compressed to a π_t and a time of ~5 min was allowed for equilibration the film.

A single layer of 5CNBC and the mixed monolayer of 5CNBC with different X_M of 8OCB were deposited onto such substrates by one upstroke of the dipper at a withdrawal speed of 5mm/min. The transfer ratio of the LB film deposition was found to be 1 ± 0.2. The topography of LB film transferred onto solid substrates was examined using AFM. In AFM, the LB films were scanned in contact mode using silicon tip. The images were analyzed using the WSxM software. LC cells were fabricated using LB film deposited on ITO substrate. The alignment of these LC cells filled with 8OCB was observed under a POM and further confirmed by the dielectric constant measurement.

7.3 Results and Discussion

7.3.1 Surface Pressure - Area isotherm of 5CNBC molecule

The π - A_m isotherm of pure 5CNBC (X_M = 0 of 8OCB in 5CNBC) is shown in figure 7.2. The isotherm was obtained by compressing the monolayer at A/W interface. The isotherm of 5CNBC molecules shows zero π at very large A_m. This region of the isotherm corresponds to gas phase. The isotherm shows a lift-off area at (A_i) ~ 0.53 nm^2. This is the onset of pure L_2 phase. On decreasing the A_m, molecular rearrangement takes place and the π rises gradually. On further reduction in A_m, the π rises sharply till the monolayer collapses at around collapse surface pressure (π_c) of 35 mN/m. The collapse is indicated by a change in the slope. The region of the isotherm corresponds to the steep rise in the π may represent the L_2 phase. We assume that in this phase the molecules are closely packed (inset level (b)). The extrapolation to the zero π of the sharp region of the isotherm yields a limiting area ~ 0.40 nm^2 (=A_o). The value is less than the cross-sectional area of the 5CNBC molecule. In order to account for this, the molecules may arrange with aliphatic chain on the water surface, in closed pack geometry as shown in the schematic (b) in figure 7.2. According to the traditional concept of a LM, one might easily assume that the 5CNBC molecule will form a monolayer with its CN polar group embedded in the water and the two alkyl tails intruded to the air. According to this configuration, the limiting molecular area of 5CNBC should be very large instead of the observed 0.40 nm^2. There is a

report on the formation of a nontraditional LM of disubstituted urea lipid molecule where the hydrophilic part stays away from the water surface, whereas the hydrophobic part stays near to the water surface. The stabilization of such monolayer was attributed to the hydrogen bonding network of the urea moiety of the molecule [35]. A stable LM formed by purely hydrophobic molecules at A/W interface was also reported [36, 37]. The formations of such monolayers are attributed to the hydrophobic interaction between the molecules and the increase in overall entropy of the system. Therefore, a possible arrangement of the 5CNBC molecules in the L_2 phase is as shown in the inset (b) of figure 7.2.

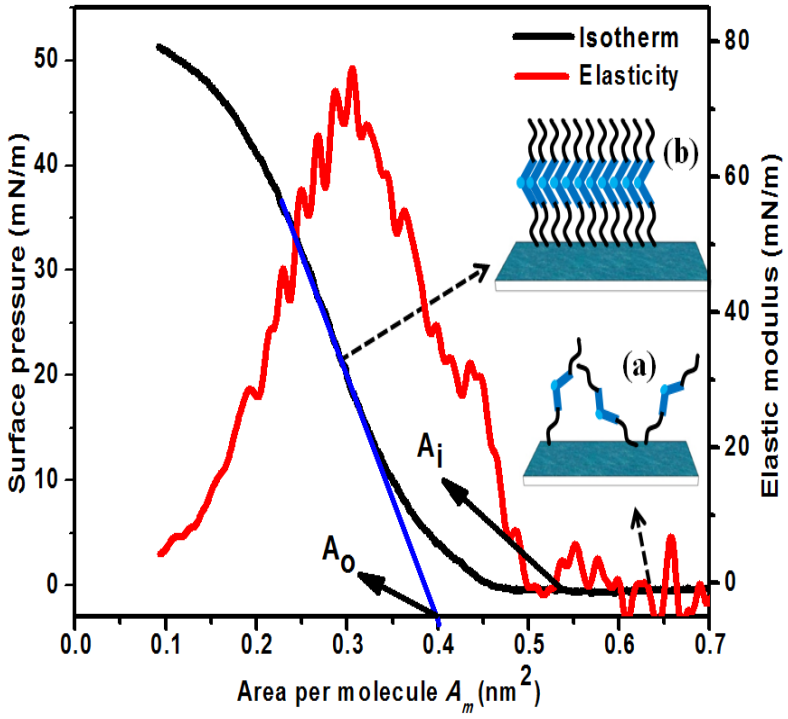

Figure 7.2: The surface pressure (π) – area per molecule (A_m) isotherm, elastic modulus and possible molecular model of 5CNBC at the air-water interface.

The isothermal in-plane elastic modulus (E) of LM can be calculated by employing the equation 2.2. The plot of E vs A_m curve provides insight into the elastic nature of the LM and shows weak phase transition in the LM at A/W interface. The E vs A_m curve is shown in figure 7.2. The value of E is negligible at large A_m and it rises sharply at the onset of L_2 phase. We obtained the maximum value of E ~ 77 mN/m in L_2 phase for 5CNBC molecule. The L_2 phase destabilizes upon further compression, leading to a decrease in the value of E. This is an indication of the initiation of the collapse of the film.

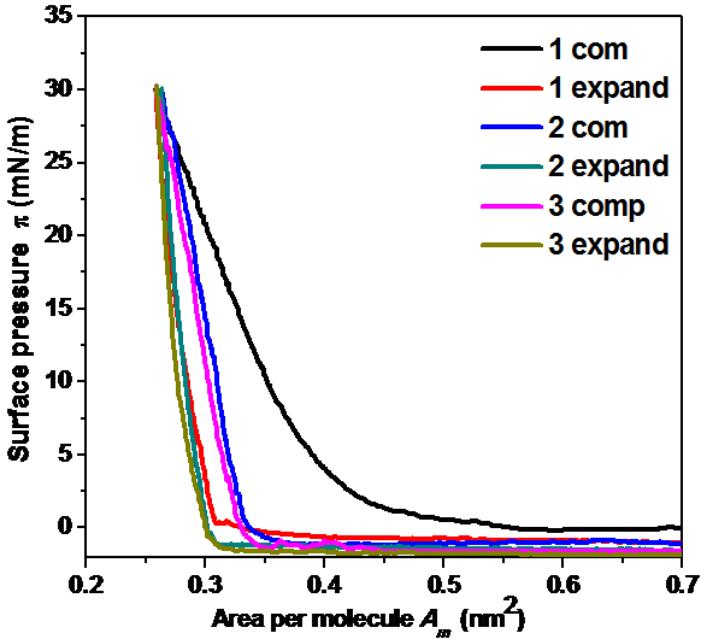

Figure 7.3: The isocycles of the LM of 5CNBC molecules at air-water interface. The film was compressed to the maximum surface pressure of 30 mN/m.

The stability and reversibility of LM of 5CNBC was studied by compressing and expanding the film repeatedly and recording the corresponding π. The isocycles of the LM of 5CNBC are shown in figure 7.3. The maximum π was maintained at 30 mN/m. The first cycle of π -A_m curve shows considerable hysteresis, and indicates that the LM is not reversible in nature. The amount of hysteresis decreases as we increase the number of cycles from 1 to 3. The compression and expansion curve of 3rd cycle are almost overlapping with the compression and expansion curve of 2nd cycle. This indicates that the molecules attain some stable conformation during repeated compression and expansion

7.3.2 Surface manometry of 8OCB and mixed monolayer of 8OBC in 5CNBC molecule

The π - A_m isotherm of 8OCB (X_M = 1 of 8OCB in 5CNBC) is shown in figure 7.4. The isotherm shows zero π at very large A_m. This is gas like phase of 8OCB molecule. The isotherm shows a lift off area (A_i) at 0.67 nm^2. Further, with decrease in A_m, there is a rapid increase in π. This was obtained corresponding to a region from a to b of the isotherm. This is a low density liquid phase (L_1). Like an amphiphilic molecule, 8OCB molecule is oriented on to the water subphase in such

a manner that polar CN part is in contact with water and non-polar part of the molecule is suspended in the air as shown in inset of figure 7.4 [38].

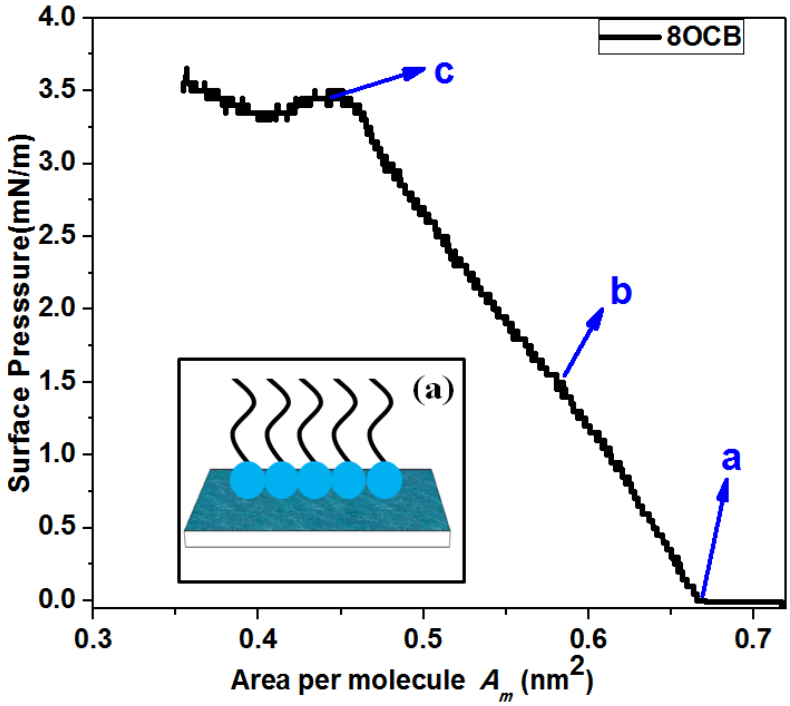

Figure 7.4: The surface pressure (π)-area per molecule (A_m) isotherm of 8OCB molecule at air-water interface.

For studying the behavior of mixed monolayer of 5CNBC and 8OCB at the A/W interface, we formed the LM of various X_M of 8OCB in 5CNBC. The π - A_m isotherms of LM of 5CNBC (curve 1), 8OCB molecule (curve 7) and their mixtures at various X_M of 8OCB in 5CNBC (curve 2- 6) on water subphase are shown in figure 7.5. It was found that when the 8OCB is added to 5CNBC, the shape of π - A_m isotherm changes. The slope of isotherm, value of A_i and π_c varies with increase in X_M of 8OCB in 5CNBC. The surface phase rule states that the value of π_c should change with composition of the mixture, if the components are miscible [9].

For X_M = 0.10 of 8OCB in 5CNBC molecule (curve 2), the isotherm almost behaves like that of 5CNBC molecule. Initially there is no change in π. The isotherm shows A_i at 0.51 nm^2. Further with compression in A_m, there is a sharp rise in π.

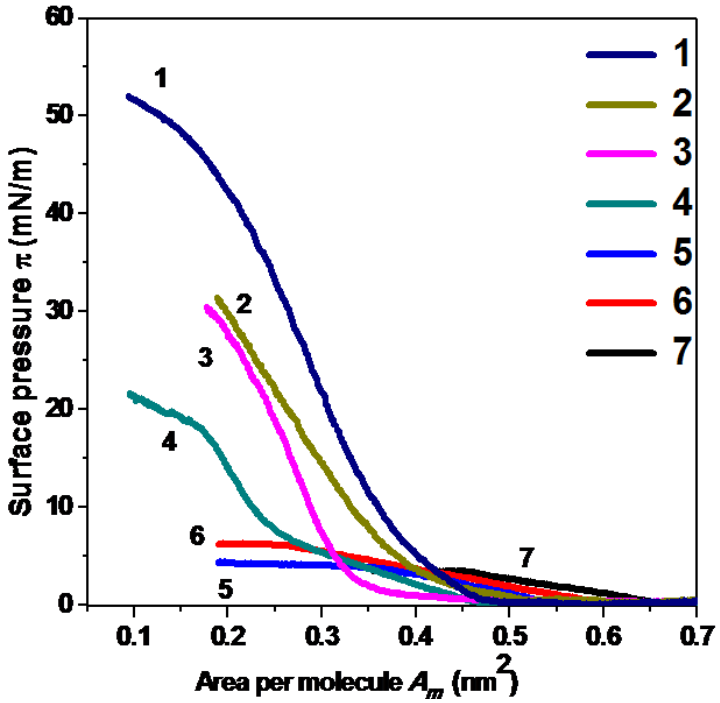

(a)

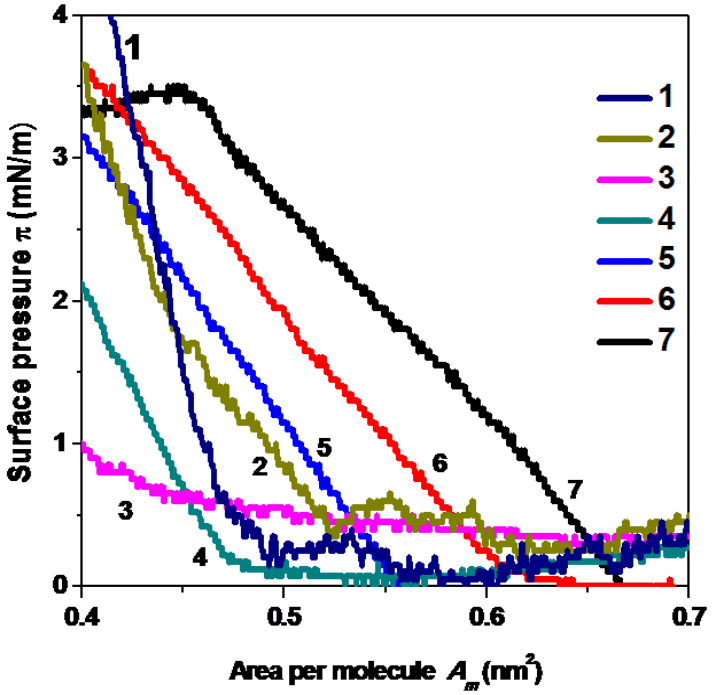

(b)

*Figure 7.5: The surface pressure (π)-area per molecule (A_m) isotherms of LF of 5CNBC (**1**), 8OCB(**7**) and for various X_M : 0.1(**2**),0.25(**3,**)0.50(**4**), 0.75(**5**) and 0.90(**6**) of 8OCB in 5CNBC molecule. (b) Isotherms of LF of 5CNBC (**1**), 8OCB (**7**) and for various X_M : 0.1(**2**), 0.25 (**3**), 0.50 (**4**), 0.75 (**5**) and 0.90 (**6**) X_M of 8OCB in 5CNBC molecule are enlarged for clear visuality.*

For X_M = 0.25 of 8OCB in 5CNBC molecule (curve 3), isotherm shows a large gas phase. It shows A_i at 0.45 nm^2. On decreasing the A_m, there is a sharp and rapid increase in π. It shows π_c at ~ 25 mN/m. For X_M = 0.50 of 8OCB in 5CNBC (curve 4), isotherm shows zero π at very large A_m. It shows A_i at 0.47 nm^2. On decreasing A_m, the π rises sharply. There is change in the slope at π = 6.14 mN/m. On further reduction in A_m, the π rises and monolayer collapse at π_c of 18.6 mN/m. For X_M = 0.75 of 8OCB in 5CNBC (curve 5), feature of isotherm is similar to that of pure 8OCB molecule. The isotherm shows A_i ~ 0.55 nm^2 and the monolayer collapses at π_c = 4.08 mN/m. For X_M = 0.9 of 8OCB in 5CNBC (curve 6), isotherm behavior is almost like 8OCB molecule. Initially the isotherm shows zero π, this indicates the gas phase. With compression in A_m, the π rises. It shows A_i at 0.62 nm^2. On further decreasing the value of A_m, there is a rapid increase in π and the monolayer collapses at 6.2 mN/m.

The variation of lift off area (A_i) and collapse surface pressure (π_c) as a function of X_M 8OCB in 5CNBC molecule are shown in figure 7.6. The π_c decreases with increase in X_M of 8OCB in 5CNBC molecule. The value of A_i increases with increase in X_M of 8OCB in 5CNBC.

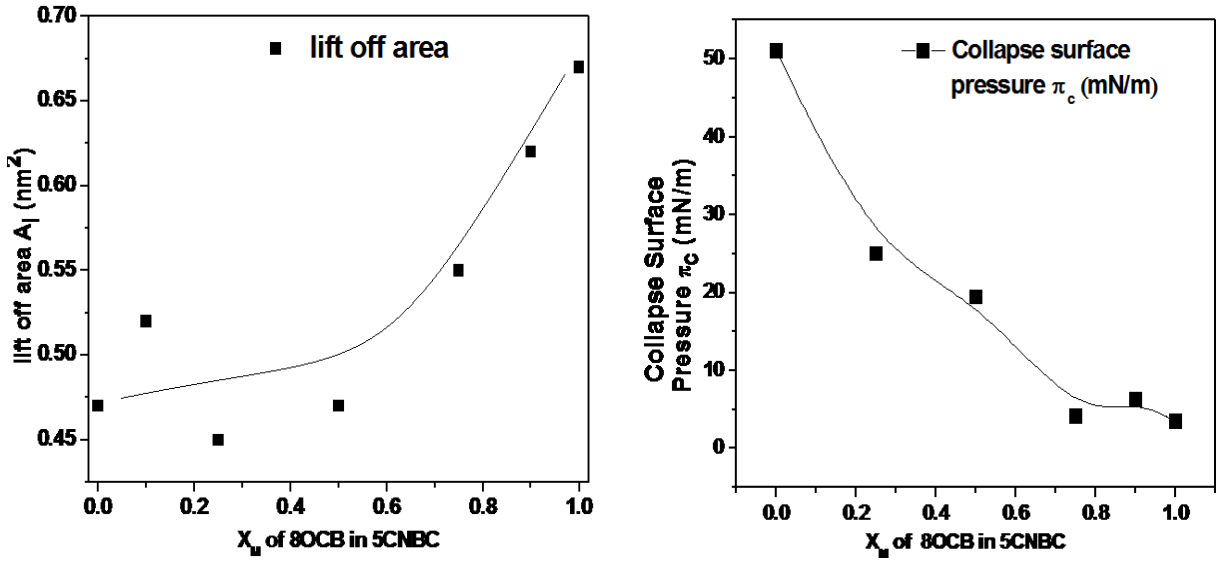

Figure 7.6: The variation of lift off area (A_i) and collapse surface pressure (π_c) as a function of X_M of 8OCB in 5CNBC molecule.

For an ideal case of complete miscibility or immiscibility of two-component monolayer system, the area of the mixed monolayer is given by the rule of additivity [9, 39].

The excess area per molecule (A_{ex}) is calculated using equation 4.2 for different X_M and at π = 1, 2, 3 mN/m. The variation in A_{ex} as a function of X_M at different π shows negative values for all

the compositions in figure 7.7. This indicates that there is an attractive interaction between both 8OCB and 5CNBC molecules in the mixed monolayer [39].

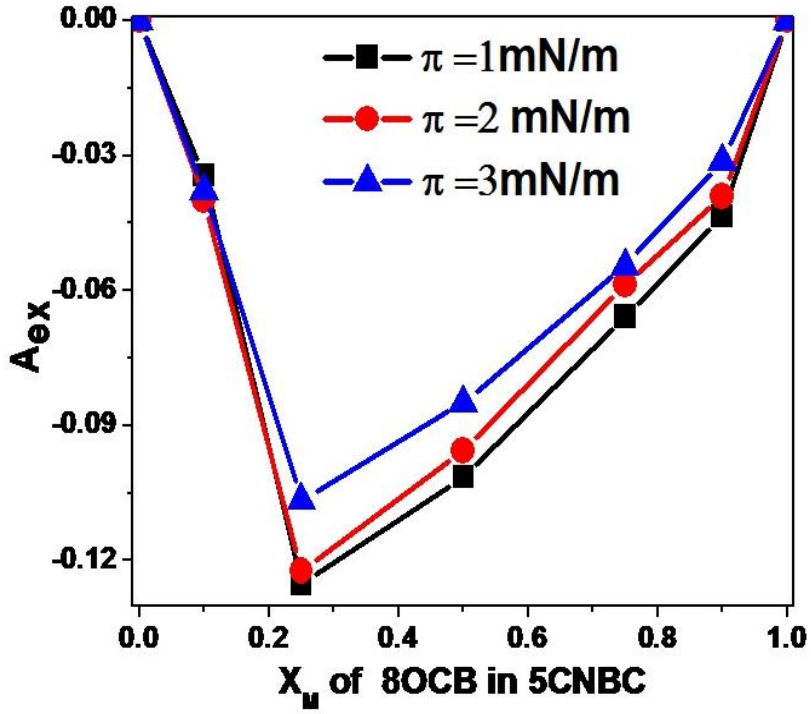

Figure 7.7: Excess area per molecule (A_{ex}) as a function of mole fraction (X_M) of 8OCB in 5CNBC at different surface pressures (π). The points indicate the calculated values obtained from the experimental data.

The stability and the degree of miscibility of a mixed monolayer were studied by calculating the excess Gibbs free energy (ΔG). The ΔG is given by

$$\Delta G = N_a \int_0^{\pi} A_{ex}\, d\pi \qquad 7.1$$

where N_a indicates the Avogadro number.

The variation of ΔG with respect to X_M at π = 1, 2, 3 mN/m shows negative values for all the compositions (in figure 7.8). It shows a minimum at around X_M = 0.25 of 8OCB in 5CNBC. This suggests a miscible nature of the component molecules 5CNBC and 8OCB in the mixed monolayer with the stable composition being at around X_M = 0.25 of 8OCB in 5CNBC. The thermodynamical studies on the mixed monolayer of 5CNBC and 8OCB LCs suggest the monolayer is miscible for all compositions.

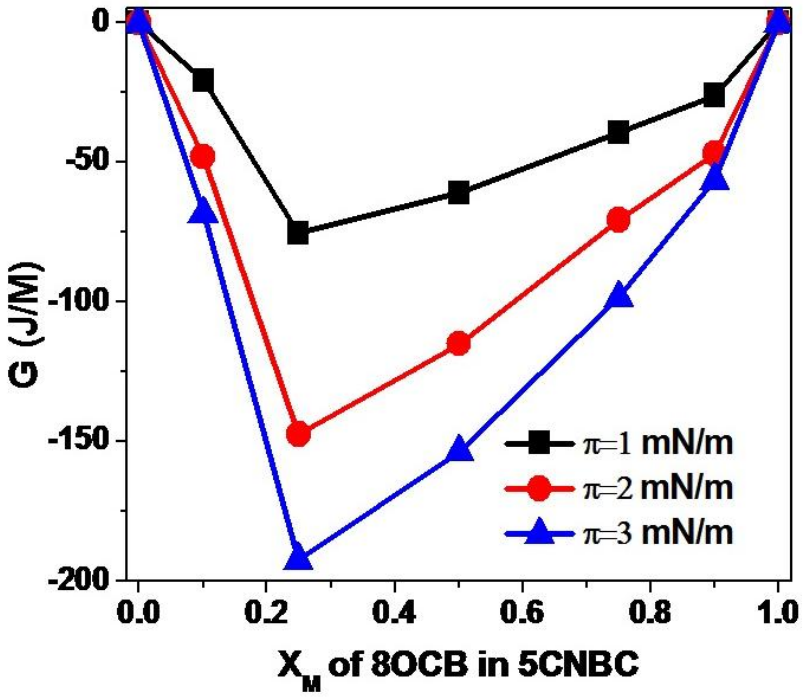

Figure 7.8: The excess Gibbs free energy (ΔG) as a function of mole fraction (X_M) of 8OCB in 5CNBC at different surface pressures (π). The points indicate the calculated values obtained from the experimental data.

7.3.3 Characterization of LB film of 5CNBC, 8OCB and mixed monolayer at A/S interface

7.3.3.1 Reflection Absorption Infrared Spectroscopy

The LB films of 5CNBC was deposited at π_t = 10 mN/m and 8OCB film was deposited at π_t = 2 mN/m onto Si/SiO_2 substrates. The RAIRS of LB films of both the LC molecules on Si/SiO_2 substrate are shown in figure 7.9. The absorption bands corresponding to O-C stretching and C=C stretching are observed at 1254 and 1650 cm^{-1} for LB film of both molecules. The C=O stretching and C≡N stretching are observed at 1735 and 2200 cm^{-1} for LB film of 5CNBC. For LB film of 8OCB, we obtained C=O stretching and C≡N stretching at 1725 and 2195 cm^{-1}[40]. In 8OCB molecule, the band corresponding to the C≡N group is shifted towards lower wavenumber as compare to that of 5CNBC molecule.

The integrated absorbance values for the C≡N group in the 5CNBC and 8OCB molecules are 25 and 32 arb unit. It is well known that the IR measurement in the reflection absorption mode is sensitive to vertical component of the transition dipole moment [36]. The difference in the integrated absorption values may indicate different orientational states of the 8OCB and 5CNBC

molecules on the substrate. The transition dipole moment associated with C≡N group of 8OCB has larger vertical component than that of 5CNBC molecules. Since the C-F group is present only in 5CNBC molecule, a strong peak corresponding to C-F band is observed at 1025 cm^{-1}.

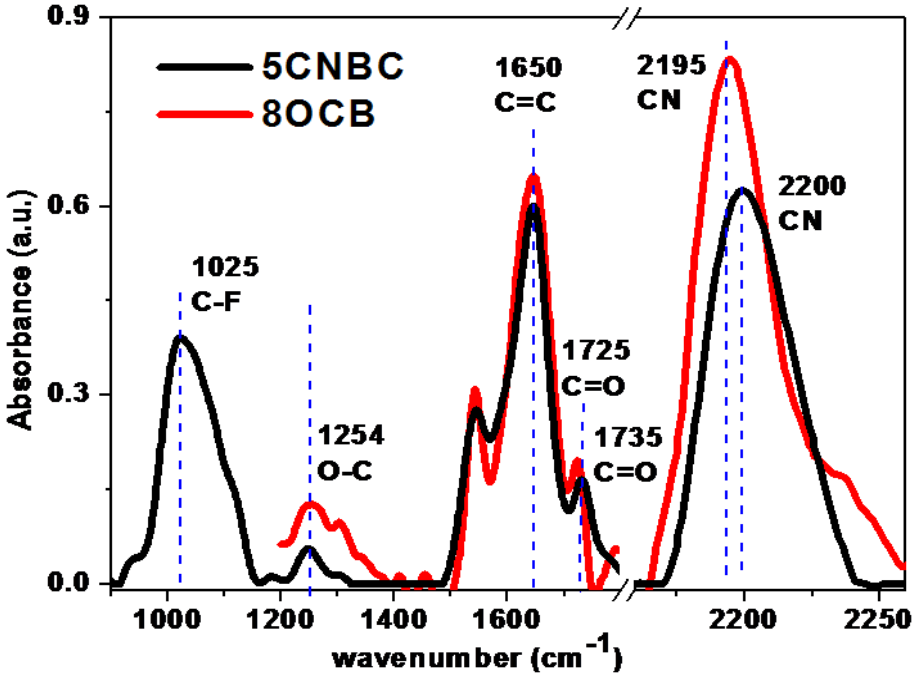

Figure 7.9: Reflection absorption infrared spectra of the LB films of 5CNBC and 8OCB molecules deposited onto Si/SiO_2 substrates.

7.3.3.2 Atomic Force Microscopy

The LM of 5CNBC, 8OCB and their mixtures with different X_M were transferred onto Si/SiO_2 substrate by LB technique at different π_t. The surface morphology of the LB films were obtained using AFM in contact mode. The AFM images are shown in figure 7.10.

The AFM image (figure 7.10 (a)) of LB film of pure 5CNBC deposited at 2 mN/m on Si/SiO_2 substrate shows granular texture. The granular feature diminishes and the film appears smoother due to the incorporation 8OCB molecules in the matrix of 5CNBC (figure 7.10 (b)-(d)). The AFM image of LB film of pure 8OCB shows a very smooth texture with few grains (figure 7.10 (e)). The images corresponding to the mixed monolayer system do not reveal any signature of phase separation in the topographic images at such length scale. This is in consistence with the surface manometry studies on such mixed monolayer system.

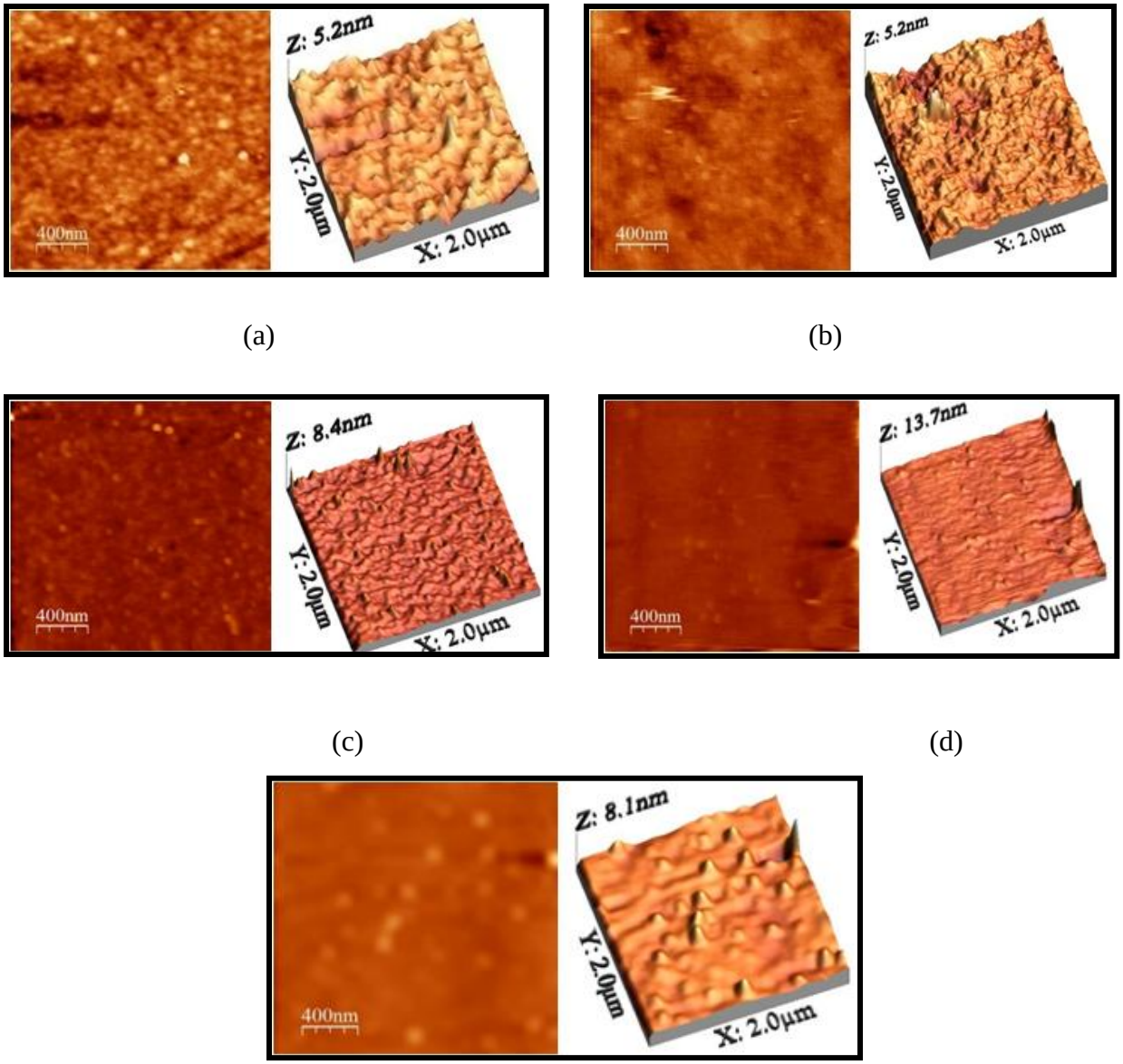

Figure 7.10: Atomic force microscope images of LB Film of (a)5CNBC, (b) 0.25, (c) 0.75, (d) 0.90 X_M = of 8OCB in 5CNBC and (e)8OCB deposited at target surface pressures π_t=2 mN/m.

7.3.4 Dielectric constant measurement

We fabricated ~ 8 μm thick LC cells using ITO substrates deposited with LB film of 5CNBC at π_t = 2 and 15 mN/m and mixed monolayer (different X_M of 8OCB in 5CNBC) at π_t = 2 mN/m and used them as an alignment layer. The LC cell was also fabricated using spin coated film of octadecyltriethoxysilane (ODSE) on ITO substrates. 8OCB was filled in such fabricated cells in isotropic phase. These cells were placed on the POM stage and a homeotropic alignment was

observed in all cells. The dielectric constant (ε) was measured at 5 volt as a function of temperature. Figure 7.11 shows the dielectric constant as a function of temperature of 8OCB filled in these LC cells.

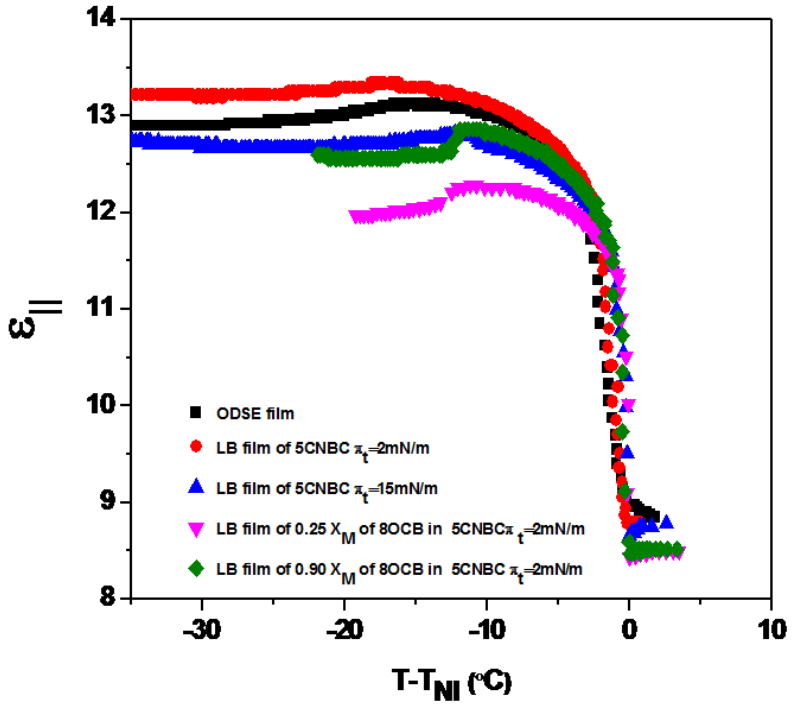

Figure 7.11: Dielectric constant (ε) as a function of temperature of 8OCB measured in LC cell fabricated using ODSE, and LB film of 5CNBC deposited at different π_t and different X_M of 8OCB in 5CNBC at π_t= 2 mN/m.

The value of dielectric constant (ε) of 8OCB measured ODSE treated LC cell corresponds to the dielectric constant ($\varepsilon_{\parallel}$) component and is in good agreement with the literature [41]. The value of dielectric constant of 8OCB measured in LC cell treated with LB film of 5CNBC molecules in L_2 phase is enhanced, which indicates that 8OCB molecules are aligning perpendicular to the substrate yielding a better homeotropic alignment of 8OCB.

In cells prepared using LB film of mixed monolayer (different X_M of 8OCB in 5CNBC), the nematic phase is suppressed and hence the smectic phase temperature range has increased.

7.4 Conclusion

We investigated the surface behavior of a mixed monolayer system of two different shape anisotropic LC molecules viz 8OCB (rod shaped) and 5CNBC (bent core LC). The π - A_m

isotherms of the mixed system was recorded by varying X_M of 8OCB in 5CNBC. The variation of excess area and excess Gibbs free energy versus X_M shows negative values for all composition in the π range of 1 to 3 mN/m. This suggests the system to be miscible and stable. The miscibility may arise due to attractive interaction between the component molecules.

The LB films of the mixed monolayer system were deposited and the morphology was obtained using AFM. The AFM image shows the miscible nature of the components on the solid substrates.

These LB films were employed as alignment layer for the fabrication of LC cell. The alignment of bulk 8OCB LC enclosed in these cells is observed using POM and the dielectric measurement was performed. The value of dielectric constant of 8OCB measured in LC cell treated with LB film of 5CNBC molecules in L_2 phase is enhanced. This indicates homeotropic alignment of 8OCB. The nematic phase of 8OCB LC is suppressed in LC cells prepared using LB film of mixed monolayer.

References

1. M. Schadt, Liquid Crystal Materials and Liquid Crystal Display, Ann. Rev. Mat. Sci. 27, 305, **1997**.
2. L. E. Tannas, W. E. Glenn, J.W. Doane, Knovel "*Flat-Panel Display Technologies-Japan, Russia, Ukraine, and Belarus*", Noyes Publications: Park Ridge N. J., **1995**.
3. T. T. Alkeskjold, L. Scolari, D. Noordegraaf, J. Laegsgaard, J. Weirih, L. Wei, G.Tartarini, P. Bassi, S. Gauza, S. T. Wu, A. O. Bjarklev, Opt. Quant. Elect. 39,1009, **2007**.
4. L. Wei, J. Weirich, T.T. Alkeskjold, A. Bjarklev, Optics. Lett. 34, 3818, **2009.**
5. L. Z. Ruan, J. R. Sambles, I. W. Stewart, Phy. Rev. Lett., 91, 033901, **2003**.
6. M. O. Neill, S. M. Kelly, J. Phys. D: Appl. Phys. 33, 67, **2000**.
7. J. M. Geary, J. W. Goodby, A. R. Kmetz, J. S. Patel, J. Appl. Phys. 62, 4100, **1987**.
8. J. L. Janning , Appl. Phys. Lett. 21, 173, **1972.**
9. G. L. Gains, "*Insoluble Monolayers at Liquid-Gas Interface*", Interscience: New York. NY, USA, **1996.**
10. R. A. Drawhorn, N. L. Abbott, J. Chem. Phys. 99, 16511, **1995.**
11. Y. L. Cheng, D. N. Batchelder, S. D. Evans, J. R. Henderson, J. E. Lydon, S. D. Ogier, Liquid Crystals 27, 1267, **2000.**
12. J. P. Bramble, S. D. Evans, J. R. Henderson, C. Anquetil, D. J. Cleaver, N. J. Smith, Liquid Crystals 34, 1059, **2007.**
13. O. Elamain, G. Hedge, L. Komitov, Applied Physics Letters 103,023301, **2013**.
14. T. Niori, T. Sekine, J. Watanabe, T. Furukawa, and H. Takezoe, J. Mater. Chem. 6, 1231, **1996.**
15. D. R. Link, G. Natale, R. Shao, J. E. Maclennan, N. A. Clark, E. Korblova, D. M. Walba, Science 278, 1924, **1997.**
16. A. Jakli, Liquid Crystals Today, 11, 1, **2002.**
17. J. Harden, B. Mbanga, N. Eber, K. Fodor-Csorba, S. Sprunt, J. T. Gleeson, A. Jakli, Phys. Rev. Lett. 97, 157802, **2006**.
18. Y. Tang, Y. Wang, G. Wang, H.B. Wang, L. X. Wang, D. H. Yan, J. Phys. Chem. B 108,12921, **2004**.

19. E. Gorecka, M. Cepic, J. Mieckowski, M. Nakata, H. Takezoe, B. Zeks, Phys. Rev. E. 67, 061794, **2003.**
20. M. Nakata, Y. Takanishi, J. Watanabe, H. Takezoe, Phys. Rev. E. 68, 041710, **2003.**
21. E. Gorecka, M. Nakata, J. Mieczkowski, Y. Takanashi, K. Ishikawa, J. Watanabe, H. Takezoe, S. H. Eichorn, T. M. Swager, Phys. Rev. Lett. 85, 2526, **2000.**
22. R. Prathibha, N. V. Madhusudana, B. K. Sadashiva, Science 288, 2184, **2000.**
23. M. W. Schroder, S. Diele, G. Pelzl, N. Pancenko, W. Weissflog, Liquid Crystal 29, 1039, **2002.**
24. G. G. Nair, C. A. Bailey, S. Taushanoff, K. Fodor-Csorba, A. Vajda, Z. Varga, A. Bota, A. Jakli, Adv. Mater. 20, 3138, **2008.**
25. R. A. Hall, P. J. Thistlethwaithe, F. Grieser, Langmuir 9, 2128, **1993.**
26. T. Martynski, J. Miyake, Molecular, Z. Naturforschung A, 58, 23, **2003**.
27. A. Modlinska, D. Bauman, Int. J. Mol. Sci. 12, 4923, **2011.**
28. J. Wang, L. Zou, W. Weissflog, A. Jakli, E. K. Mann, Langmuir 22, 3198, **2006**.
29. L. Zou, J. Wang, V. J. Beleva, E. Kooijman, S. V. Primak, J. Risse, W. Weissflog, A. Jakli , E. K. Mann, Langmuir 20, 2772, **2004**.
30. J. Wang, L. Qiu, A. Jakli, W. Weissflog , E. K. Mann, Liquid Crystal , 37, 1229, **2010**.
31. W. Iglesias, T. J. Smith, P. B. Basnet, S. R. Stefanovic, C. Schierske, D. J. Lacks, A. Jakli, E. K. Mann, Soft Matter 7, 9043, **2011**.
32. M. Schadt, Ann. Rev. Mat. Sci. 27, 305, **1997**.
33. L. E. Tannas, W. E. Glenn, J. W. Doane, "*Knovel Flat-Panel Display Technologies-Japan, Russia, Ukraine and Belarus"* Noyes Publications: Park Ridge, N. J., **1995.**
34. A. Reddy, B. K. Sadashiva, Liquid Crystals 31, 8, 1069, **2010.**
35. Q. Huo, S. Russev, T. Hasegawa, J. Nishijo, J. Umemura, G Puccetti, K. C. Russell, R. M. Leblanc, J. Am. Chem. Soc. 122, 7890, **2000**.
36. G. L. Gaines Jr., Langmuir **7**, 3054 , **1991.**
37. A. El Abed, M-C. Faure, E. Pouzet, O. Abillon, Phys. Rev. E 65, 051603, **2002.**
38. M. N. G. de Mul, J. A. Mann Jr., Langmuir 10, 2311,**1994.**
39. A. Angelova, M. A. van der, R. Ionov, D. Vollhardt, F.C. de Schreyver, Langmuir 11, 316, **1995.**

40. D. L. Pavia, G. M. Lampman, G. S. Kriz , J. A. Vyvyan "*Introduction to Spectroscopy*" fifth edition, United state of America, ISBN-10, **2015.**
41. S. J. Rzoska, A. D. Rzoska, P. K. Mukherjee, D.O. Lopez, J. C. M. Garcia, J. Phys.: Condens. Matter, 25, **2013.**

Chapter - 8

Conclusions and Future Scope of Our studies

8.1 Conclusions

Liquid crystals (LCs) are the fourth state of matter whose order lies between that of 3-dimensioanlly (3D) ordered solids and completely disordered fluids. There are two types of LCs: thermotropic and lyotropic LCs. The thermotropic LCs exhibit mesophases as a function of temperature whereas lyotropic LCs exhibit mesophases as a function of concentration, ion-contents, pH, temperature and humidity. The thermotropic mesophases are dependent on various factors including the molecular interaction and molecular shape anisotropy. Several thermotropic LCs are amphiphilic in nature and can form stable Langmuir monolayer (LM).

LM is a stable film of single layer of amphiphilic molecules at the air-water (A/W) interface. A single layer of molecules onto the substrate can be considered as thin film. The thin films of LC exhibit interesting properties. The surface to volume ratio of a material increases enormously when spread on to a substrate to form thin film. Such huge increase in surface-to-volume ratio increases the activities of the material enormously and thereby the material properties like catalysis, reactivity, adhesion, etc are enhanced remarkably. Such changes in the material properties in the state of thin films promises a wide range of applications starting from the basic science research to various device fabrications. The surface morphology and the nanostructure in the thin film can govern the growth of the bulk material deposited over it. Therefore, this provides an opportunity to alter the alignment of bulk LC molecules by altering the morphology and functionality of the interfacial layer. The formation of nanostructure in the thin film is governed by molecular interaction and external parameters like temperature, surface density etc. The surface can be patterned and the nanostructures can be controlled by an appropriate choice of thin film forming materials e.g. liquid crystals, nanomaterials and its nanocomposites. The LC based devices consist of alignment layer for aligning the bulk LC materials within a confined

geometry. Such alignment layer can determine the alignment of bulk material and thus regulates the performance of LC based devices. The study on the role of alignment layer on the bulk LCs is essential. The alignment layer can be fabricated using different techniques including a precisely controlled Langmuir-Blodgett (LB) technique for ultrathin film deposition.

This thesis mainly focuses on the LM and Langmuir-Blodgett (LB) films of LCs, nanomaterials and their composites at A/W and air-solid (A/S) interfaces. LM can be considered as a 2D system on water surface, and it is known to exhibit several interesting surface phases. Such phases can be characterized using several techniques e.g. surface manometry, Brewster angle microscopy (BAM), epifluorescence microscopy (FM), X-ray diffraction (XRD) and second harmonic generation techniques. We have employed surface manometry and BAM for our studies. The monolayer in a particular phase at the A/W interface can be transferred layer-by-layer onto a solid substrate by using the LB and inverse Langmuir-Schaefer (ILS) methods in a highly controlled manner. LB and ILS films at the A/S interfaces can be characterized using numerous techniques. We have employed atomic force microscopy (AFM), field emission scanning electron microscopy (FESEM), ultraviolet-visible (UV-Vis) spectroscopy, Fourier transform infrared (FTIR) spectroscopy, XRD and Current-Voltage (I-V) measurement for our studies.

LC cells fabricated using LB and ILS film deposited substrates can influence the overall performance of the device, as the anchoring can play a major role in switching the bulk LC medium. Substrates prepared using the LB and ILS techniques are used for the fabrication of LC cell. LC sample was filled in cells in isotropic phase through capillary action. The alignment of LCs in these cells was observed under a Polarizing Optical Microscope (POM).

This thesis comprises of the results of studies on thin films of LCs, nanomaterials and its nanocomposites. The titanium dioxide (TiO_2) nanomaterials, nanocomposites of $TiO_2$with discotic LC (DLC), different bent-core LCs (BCLCs) and calamitic LCs have been used for our studies.

Chapter 1 discusses the introduction to LC, LC phases exhibited by mesogens which are different in shape. We give a brief introduction about only those LCs and their phases which are relevant to this thesis.

Introduction to the system like LM and LB films and the techniques used for their characterization are discussed in chapter 2. The different techniques which we have used for the

formation of thin film of LCs, nanomaterials and their nanocomposites at A/W and A/S interface are described. The topography and morphology study of thin films at A/S interface was done using AFM and FESEM. Other characterization technique like FTIR, UV-Vis spectroscopy, XRD, I-V measurement etc is also described. The fabrication of LC cell using the thin film deposited substrate is described. For textural study, we have used POM. The recent development in the field and the identified research gap are also discussed.

In Chapter 3 of this thesis, we present the results of studies on LM of TiO_2 nanoparticles at A/W interface. We obtained stable Langmuir film (LF) of TiO_2 nanoparticles at A/W interface. We transferred the LB film of TiO_2 nanoparticles onto HPL substrates. The morphological, optical and electrical properties of such LB films were studied. The LB films of TiO_2 deposited at higher target surface pressure (π_t) reveal a higher surface coverage, thereby yielding a higher density of crystalline defect sites. The UV-Vis spectroscopy of LB film of TiO_2 nanoparticles reveals that with the increase in π_t of deposition the optical property of LB film of TiO_2 nanoparticles more closely approaches that of the bulk sample. The charge-transport mechanism in the LB film of TiO_2 nanoparticles was studied. We observed an Arrhenius behavior of charge transport for LB film of TiO_2 nanoparticles. Both the LB and spin coated film of TiO_2 nanoparticles are employed for ethanol sensing applications. The LB film of TiO_2 nanoparticles shows an appreciable and recoverable response toward ethanol sensing (figure 8.1) and spin-coated bulk material does not show any sensing toward the ethanol gas.

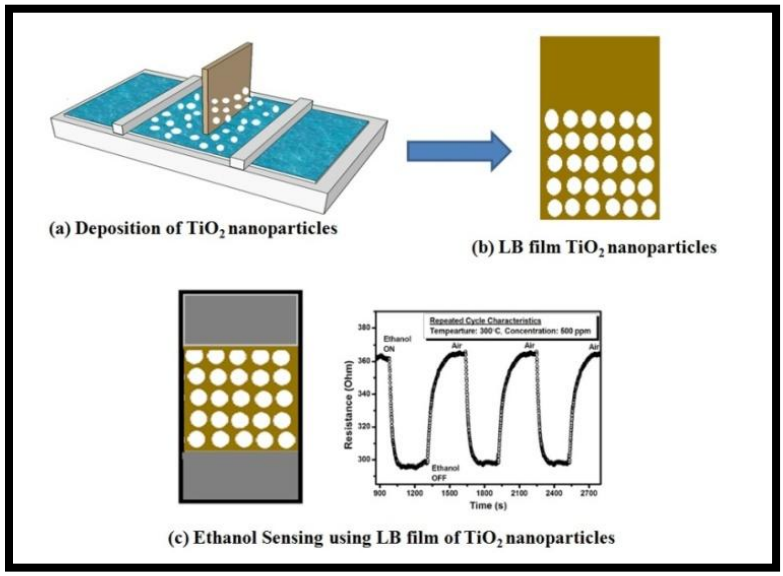

Figure 8.1: Films of TiO_2 nanoparticles at the air-water and air-solid interfaces and response of LB film of TiO_2 nanoparticles for ethanol sensing.

In this chapter, we also present the investigations on doped DLC with TiO_2 nanoparticles. We doped DLC hexa-alkoxytriphenylene (HAT5) with TiO_2 nanoparticles. We obtained stable LF of nanocomposites of HAT5+TiO_2 (with different wt. %) at A/W interface. We found a condensation effect on the monolayer of HAT5+TiO_2 nanocomposites due to the presence of TiO_2 nanoparticles. We transferred the LB film of pure HAT5 and HAT5+TiO_2 nanocomposites onto HPL substrates characterized using AFM, UV-Visible spectroscopy and I-V measurement. We observed reduction in the energy gap of the HAT5 system in a controlled manner on doping the system with TiO_2 nanoparticles. We observed an Arrhenius behavior of charge transport for LB film of TiO_2, HAT5 and HAT5+ TiO_2 (10 wt.%) nanocomposites. We observed that the even with 10 wt.% TiO_2 nanoparticles doped into HAT5 DLC leads to a change the charge-transport behavior of HAT5. The conductivity and activation energy (E_A) of HAT5+TiO_2 nanocomposites increases with increasing concentration of TiO_2 nanoparticles. The charge-transport mechanism in thin film of HAT5 can be controlled precisely by altering the π_t of LB film deposition of HAT5+ TiO_2 nanocomposites.

We present our investigation on the carboxylated graphene (G-COOH) doped with a DLC, at interfaces in chapter 4. The surface manometry on HAT5, G-COOH and their composites shows interesting results. The LM of G-COOH exhibits gas and a liquid-like phase. Structurally similar organic DLC molecule HAT5 was incorporated in the monolayer matrix of G-COOH. The surface manometry of such mixed monolayer system indicated the evidence of repulsive interaction or complex formation between the components. The LB films of G-COOH+HAT5 nanocomposites were deposited on solid substrate. The LB films were characterized using UV-Vis spectroscopy. The UV-Vis spectroscopy on the LB films of the nanocomposite reveals red shift in the characteristic peak. The charge - transport mechanisms in the LB film of G-COOH+HAT5 nanocomposites were studied. The in-plane conductivity of the LB films of the nanocomposites enhances as compared to that of pure components. The surface morphology obtained using FESEM shows uniform film over the 2D surface. The signature of both HAT5 and G-COOH were seen from the images.

LC cell were fabricated by using LB and ILS films of G-COOH+HAT5 nanocomposites deposited indium tin oxide (ITO) coated glass plates. A DLC decyloxytriphenylene (TP10) exhibiting rectangular columnar phase was filled in these LC cells. Dielectric constant measurement was carried out. The dielectric measurements indicate that the LB film of the

nanocomposites provide better alignment of discotic liquid crystals as compared to some other mechanism of obtaining the alignment layer in the LC cells.

The morphology of LB films depends on various factors including π_t, temperature, pH, and ion contents in the subphase. The stress exerted by the monolayer onto the Wilhelmy plate was found to be dependent on the direction of compression of the monolayer at the A/W interface. In chapter 5, we demonstrated the effect of such stress on the morphology of LB films of stearic acid deposited onto solid substrate (figure 8.2). The LB films were deposited at a π_t = 15mN/m with different orientation angle of substrates with respect to the film compression direction. Due to large stress, the film deposited at $\theta = 0^o$ shows granular texture with very large size and compact grains. The large grains change to smaller size and finally vanish due to reduction of the stress by changing θ from 0° to 45^o and then 90^o. LC cells using such LB films deposited at different θ are found to yield a well aligned planar or homeotropic modes for the nematic LC (NLC).

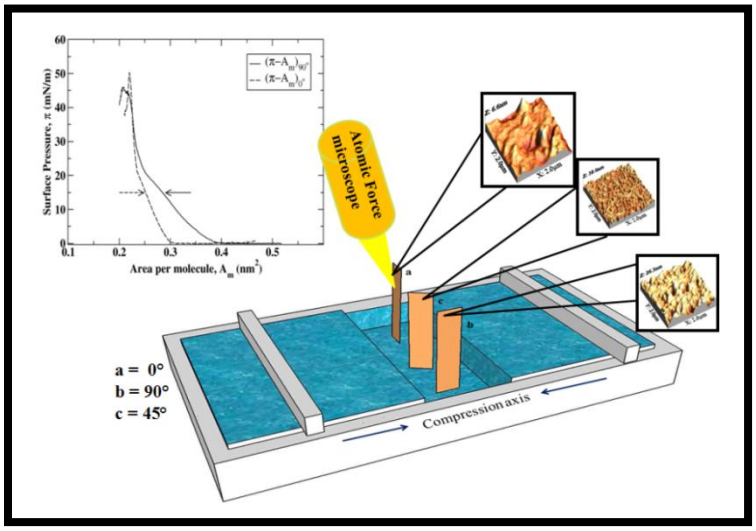

Figure 8.2: Graphical abstract of chapter 5.

In chapter 6, we have presented the results of detailed study of a stable monolayer of different unsymmetrical BC molecules4-((4-(tetradecyloxy)benzoyl)oxy) phenyl 3-((4-((4-cyanobenzoyl) oxy)benzoyl)oxy) benzoate (we referred this molecule as B-CN),4-((4-(tetradecyloxy) phenoxy) carbon) phenyl 3-((4-((nitrobenzoyl) oxy) benzoyl)oxy) benzoate (we referred this molecule as BN1) and 4-((4-(octadecyloxy) phenoxy) carbonyl) phenyl 3-((4-((4-nitrobenzoyl)oxy) benzoyl) oxy) benzoate (we referred this molecule as BN2) at A/W interface. The LM of B-CN, BN1 and

BN2 at A/W interface were found to be stable.

We transferred the LM of B-CN molecule onto Si/SiO_2substrate using both LB and ILS method at different π_t and characterized them using AFM and FESEM. Both LB and ILS film of B-CN molecule on Si/SiO_2 substrate was found to be uniform. The LB film of BN1 molecules on Si/SiO_2 substrate shows the uniform texture at different π_t. The topographic images of LB film of BN2 deposited on Si/SiO_2 substrate shows triangular shaped domains with some defects. With increases in π_t, the density of these triangular shaped domains increases and film becomes more uniform. LB film of banana molecules deposited onto ITO plate shows granular texture with partial bilayer formation of the molecules on substrate.

Using the force - distance spectroscopy, the adhesion force between LB film of BN2 molecules on Si/SiO_2 substrate with hydrophilic Si/Si_3N_4 tip and hydrophobic functionalized tip was calculated. On the basis of the value of adhesion force, we propose a model for the orientation of BN2 molecules in the LB film on substrate as shown in figure 8.3.

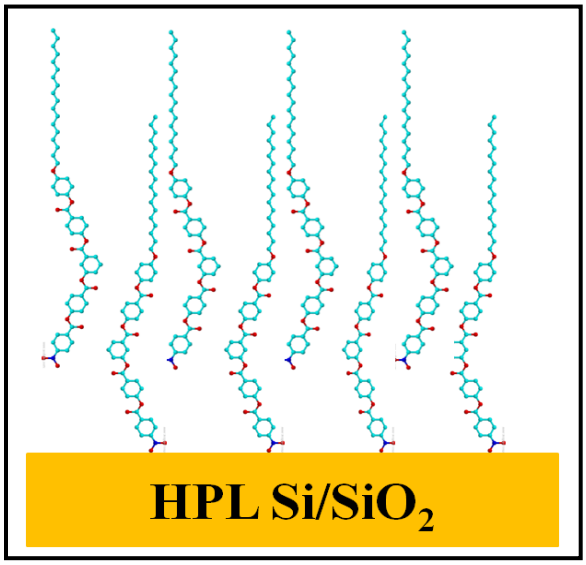

Figure 8.3:Proposed model for the orientation of LB film of BN2 molecules on Si/SiO_2 substrate.

Both LB and ILS film on different substrates (ITO, microscopic glass plate) were employed as alignment layer for the fabrication of LC cell. The alignment of bulk NLC is studied using POM. The ILS film of B-CN molecules on ITO and glass plates exhibit the planar alignment of NLC at lower π_t =10 mN/m and at higher π_t = 30 mN/m, it shows homeotropic alignment. The uniform LB film of BN1 molecules deposited onto ITO substrate supports the homeotropic alignment whereas the LB film of BN2 molecule supports the planar alignment of NLC in the LC cell.

We investigated the surface behavior of a mixed monolayer system of two different shape anisotropic LC molecules viz 4-octyloxy-4-cyanobiphenyl (8OCB calamitic LC) and bent-core ((5-cyano-1, 3-phenylene) bis(oxy)) bis(carbonyl))bis(2-fluoro-4,1-phenylene) bis(4'-nonyl-[1,1'-biphenyl]-4-carboxylate(referred as 5CNBC) in chapter 7. The $\pi - A_m$ isotherms of the mixed system were recorded by varying mole fraction (X_M) of 8OCB in 5CNBC. The variation of excess area (A_{ex}) and excess Gibbs free energy versus X_M (in figure 8.4) shows negative values for all composition in the π range of 1 to 3 mN/m. This suggests the system to be miscible and stable. The miscibility may arise due to attractive interaction between the component molecules. The LB films of the mixed monolayer system were deposited and the morphology was obtained using AFM. The AFM image shows the miscible nature of the components on the solid substrates.

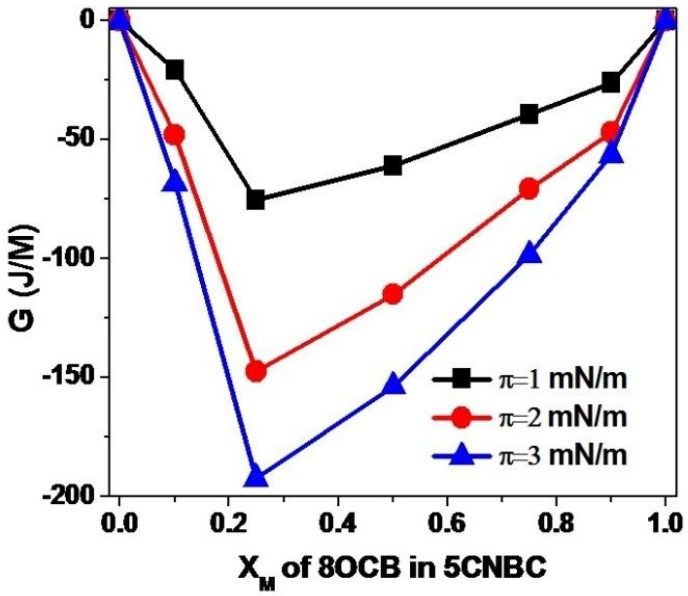

Figure 8.4: The excess Gibbs free energy (G) as a function of mole fraction (X_M) of 8OCB in 5CNBC at different surface pressures (π).

These LB films were employed as alignment layer for the fabrication of LC cell. The alignment of bulk 8OCB LC is observed using POM and the dielectric measurement was performed. The value of dielectric constant of 8OCB measured in LC cell treated with LB film of 5CNBC molecules in liquid - expanded phase is enhanced. This indicates homeotropic alignment of 8OCB. The nematic phase of 8OCB is suppressed in LC cells prepared using LB film of mixed monolayer.

8.2 Future Scope

In this thesis we have presented the results of experimental studies on the Langmuir and Langmuir-Blodgett films of LCs, nanomaterials and their nanocomposites. It will be interesting to study the role of factors like temperature, pH and substrates in the nanostructure formation at the A/S interface. In our studies, we found that the π_t of LB deposition is an important factor to control the nanostructures in the LB films.

The charge-transport mechanism in thin film of HAT5 can be controlled precisely by altering the π_t in the LB film of HAT5+TiO_2 nanocomposites. The LB film of such nanocomposites can be employed for the fabrication of organic solar cell and the performance of the device can be studied under the influence of various physical parameters.

We have demonstrated the ethanol gas sensing capability of the ultrathin films of TiO_2 (anatase : rutile (ca. 80:20)) nanoparticles deposited by LB technique. This work can be extending by comparative study of the sensing performance of LB films of N-doped TiO_2 and undoped TiO_2.

We studied the surface behavior of a G-COOH+HAT5 (with different wt.%) nanocomposites. The LB film of such nanocomposites can be employed for the fabrication of photovoltaic devices.

The molecular states of the thermotropic LCs can be significantly affected due to change in temperature. Therefore, it will be interesting to perform a systematic study of LB or ILS film of thermotropic LCs with the variation in temperature. Such LB films can be employed for the alignment of bulk LCs for display device application.

The LM of different BCLCs at the A/W interface is found to be stable and therefore, it was possible to form a well-organized LB and ILS films onto solid substrates. The miscibility of BCLCs with calamitic LC was studied. The surface behavior of BCLC molecules with different alkyl chains length at A/W and A/S interface was also studied. The surface behavior of BCLCs can be studied as a function of temperature, pH and ion contents in the subphase. It will be interesting to study the morphology of the LB film of these BCLCs onto different substrates like mica, quartz etc. The alignment of LC was observed in LC cell fabricated using such LB and ILS deposited substrates. Using such LB /ILS film deposited substrate at different π_t, the electro-optic and dielectric measurement for the LC can be carried out. It will be interesting to see the alignment of different LCs like BC, DLC in the LC cell. This can be employed for fabrication of display and optical switching devices.

List of Publications and Presentations

International journals

1. "Thin films of discotic liquid crystals and their applications"

   R. K. Gupta, V. Manjuladevi, C. Karthik & **Keerti Choudhary,** ***Liquid Crystals*** 2016 ,43,13-15,2079-2091 DOI: 10.1080/02678292.2016.1195454

2. "Ultrathin Films of TiO2 nanoparticles at interfaces"

   Keerti Choudhary, V. Manjuladevi, Raj Kumar Gupta, Partha Bhattacharyya, Arnab Hazra & Sandeep Kumar, ***Langmuir*** 2015, 31: 1385-1392 DOI: 10.1021/la503514p

3. "Studies on thin films of Hexa-alkoxy triphenylene(HAT5) and composite of HAT5-TiO_2 nanoparticles"

   C. Karthik, **Keerti Choudhary**, Aditya Joshi, Adbhut Gupta, V. Manjuladevi, and R. K. Gupta, Sandeep Kumar, ***Advanced Science Letters***, 2014, 20:1138-1142.

4. "Morphological transformation in Langmuir-Blodgett films of stearic acid due to change in orientational direction of substrate normal relative to compression direction"

   Keerti Choudhary, Jitendra Kumar ,V. Manjuladevi, Raj Kumar Gupta (communicated)

Conference proceedings

1. Studies on morphology of Langmuir-Blodgett films of stearic acid deposited with different orientation of substrates with respect to compression
   Keerti Choudhary, Manjuladevi V., and R. K. Gupta *AIP Conf. Proc. 2016,1728, 020159.*

2. Periodic Array of TiO_2 Nanoparticles on Gold Substrates
   Keerti Choudhary, Raj Kumar Gupta, Manjuladevi V, Sanjeev K. Gupta, Jamil Akhtar *AIP :Conference Proceeding, 2013, 1532:185-186.*

3. Alignment of Liquid Crystals on LB films of Stearic Acid
   Keerti Choudhary, Monika Poonia, Jitendra Kumar, Manjuladevi V, Raj Kumar Gupta, , *International Journal of Physics and Mathematical Sciences, 2012, 2: 27-29.*

4. Interaction of Octadecanoic Acid Monolayer with Divalent Cd^{2+} Ion at an Air-Water Interface
   Monika Poonia, **Keerti Choudhary**, Raj Kumar Gupta, Manjuladevi V, *International Journal of Physics and Mathematical Sciences, 2012, 2: 36-40.*

Conferences / Seminars / Workshops Attended

- Poster presentation in the International Conference Condensed Matter & Applied Physics (ICC 2015) GEC, Bikaner, INDIA October 30-31, 2015.
- Poster presentation in the National Conference on Nano- and Functional Materials, (NFM-2014) BITS Pilani, Pilani Campus, November 7-8, 2014.
- Attended a workshop and training on Current Research Trends in Condensed Matter-Material Science, BITS Pilani, Pilani Campus, March 7 - 8, 2014.
- Poster presentation in the International Conference on Applied Physics and Material Science, GCET Bikaner, INDIA Feb 1-2, 2013.
- Poster Presentation in the Symposium on Recent Trends in Chemical Science, BITS Pilani, Pilani Campus, March 25, 2012.
- Poster presentation in the National Conference on Condensed Matter Physics 2012, BITS Pilani, Pilani campus, Feb 24-25, 2012.

Brief Biography of the Candidate

Ms. Keerti Choudhary is a full time research scholar in Department of Physics, BITS, Pilani since August 2011. She obtained her Masters degree in Physics from Banasthali Vidyapith, in 2009. Her research interests are focused on surface manometry of liquid crystals with different functional groups and nanocomposites using Langmuir - Blodgett Technique. She also works on fabrication and characterization of ultra-thin films of different nanomaterials, and nanostructures in the thin films. She is currently pursuing Ph.D. from BITS, Pilani in soft condensed matter physics (experimental) as "**Study of Liquid Crystals and Nanocomposites at Interface**". She has published papers in international reputed journals and few are under review. In addition to this, she has participated and presented her work in several national and international conferences of high repute.

Brief Biography of the Supervisor

Prof. V. Manjuladevi has acquired her Ph.D. from Raman Research Institute, Bengaluru in the field of physical properties of thermotropic liquid crystals in the year 2004. She has carried out research in the field of ferroelectric liquid crystals as a post doctoral fellow in Trinity College, Dublin, Ireland from 2005–2006. She joined BITS Pilani in December 2006 and currently, she is an associate professor in the department of physics, BITS Pilani. Her main research interests are electro-optic switching measurement and dielectric studies on liquid crystals and their nanocomposites, thin films of liquid crystals and sensors. She has completed three DST funded research projects either as PI or Co-PI. She has published more than 30 papers in reputed international journals.